The Journal of Gemmology

Volume 37 / No. 4 / 2020

Investigating the Black Prince's Ruby

Emeralds from Davdar, China

Flower-Shaped Trapiche Ruby from Myanmar

Characterisation of Pink-to-Red Spinel

Emeralds from Madagascar

SSEF SCHWEIZERISCHES GEMMOLOGISCHES INSTITUT SWISS GEMMOLOGICAL INSTITUTE INSTITUT SUISSE DE GEMMOLOGIE

Gem-A THE GEMMOLOGICAL ASSOCIATION OF GREAT BRITAIN

SSEF

SCHWEIZERISCHES GEMMOLOGISCHES INSTITUT
SWISS GEMMOLOGICAL INSTITUTE
INSTITUT SUISSE DE GEMMOLOGIE

ORIGIN DETERMINATION · TREATMENT DETECTION

DIAMOND GRADING · PEARL TESTING

EDUCATION · RESEARCH

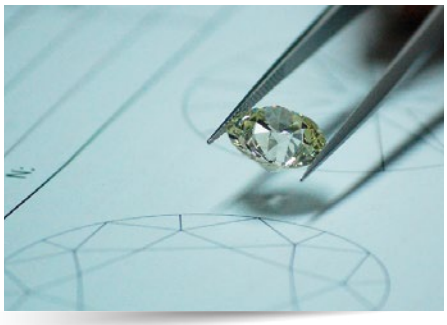

THE SCIENCE OF GEMSTONE TESTING™

Aeschengraben 26, 4051 Basel, Switzerland Tel. +41 61 262 06 40 Fax + 41 61 262 06 41 admin@ssef.ch www.ssef.ch

The Journal of Gemmology

Volume 37 / No. 4 / 2020

Cover photo: *Burmese rubies are prized for their bright red colouration, and these 1.39 and 2.19 ct stones also contain interesting inclusions, which are described in a Gem Note on pp. 346–348 of this issue. Photo by Bilal Mahmood, American Gemological Laboratories.*

COLUMNS

Photo by B. Williams

ARTICLES

Royal Collection Trust/© Her Majesty Queen Elizabeth II, 2016 (RCIN 3170)

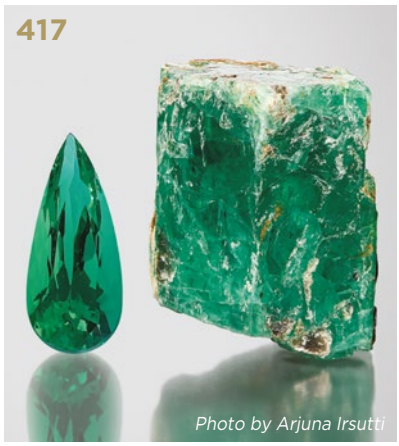

Photo by Arjuna Irsutti

The Journal is published by Gem-A in collaboration with SSEF and with the support of AGL.

Gem-A THE GEMMOLOGICAL ASSOCIATION OF GREAT BRITAIN

SSEF SCHWEIZERISCHES GEMMOLOGISCHES INSTITUT SWISS GEMMOLOGICAL INSTITUTE INSTITUT SUISSE DE GEMMOLOGIE

AGL AMERICAN GEMOLOGICAL LABORATORIES

The Journal of Gemmology

COVERED BY THE FOLLOWING ABSTRACTING AND INDEXING SERVICES:

Clarivate Analytics' (formerly Thomson Reuters/ISI) Science Citation Index Expanded (in the Web of Science), *Journal Citation Reports (Science Edition)* and *Current Contents (Physical, Chemical and Earth Sciences)*; Elsevier's Scopus; Australian Research Council's Excellence in Research for Australia (ERA) Journal List; China National Knowledge Infrastructure (CNKI Scholar); EBSCO's Academic Search Ultimate; ProQuest (Cambridge Scientific Abstracts); GeoRef; CrossRef; Chemical Abstracts (CA Plus); Mineralogical Abstracts; Index Copernicus ICI Journals Master List; Gale Academic OneFile; British Library Document Supply Service; and Copyright Clearance Center's RightFind application.

Science Citation Index Expanded
Web of Science Clarivate Analytics

CONTENT SUBMISSION

The Editor-in-Chief is glad to consider original articles, news items, conference reports, announcements and calendar entries on subjects of gemmological interest for publication in *The Journal of Gemmology*. A guide to the various sections and the preparation of manuscripts is given at https://gem-a.com/membership/journal-of-gemmology/submissions, or contact the Editor-in-Chief.

SUBSCRIPTIONS

Gem-A members receive *The Journal* as part of their membership package, full details of which are given at https://gem-a.com/membership. Laboratories, libraries, museums and similar institutions may become direct subscribers to *The Journal*; download the form from *The Journal*'s home page.

ADVERTISING

Enquiries about advertising in *The Journal* should be directed to advertising@gem-a.com.
For more information, see https://gem-a.com/membership/media-pack-2020.

DESIGN & PRODUCTION

Zest Design, London. www.zest-uk.com

PRINTER

DG3 Group (Holdings) Ltd, London. www.dg3.com

FSC Mixed Sources
Product group from well-managed forests and other controlled sources
www.fsc.org Cert no. TT-COC-002454
© 1996 Forest Stewardship Council

ISSN 1355-4565 (Print), ISSN 2632-1718 (Online)

Gem-A
THE GEMMOLOGICAL ASSOCIATION OF GREAT BRITAIN

21 Ely Place
London EC1N 6TD
UK
t: +44 (0)20 7404 3334
f: +44 (0)20 7404 8843
e: information@gem-a.com
w: https://gem-a.com

Registered Charity No. 1109555
A company limited by guarantee and registered in England No. 1945780
Registered office: Palladium House, 1–4 Argyll Street, London W1F 7LD

What's New

INSTRUMENTATION

Presidium ARI

In September 2020, Presidium released its ARI diamond verification instrument. It uses UV radiation absorption to help identify natural versus CVD- and HPHT-grown synthetic diamonds, as well as synthetic moissanite. The handheld unit measures only 190 × 46 × 25 mm and tests colourless (D–J) samples, loose and mounted, as small as 0.02 ct. For additional information, including a video demonstration and downloadable user handbook, visit https://presidium.com.sg/psdproduct/ari-by-presidium.

NEWS AND PUBLICATIONS

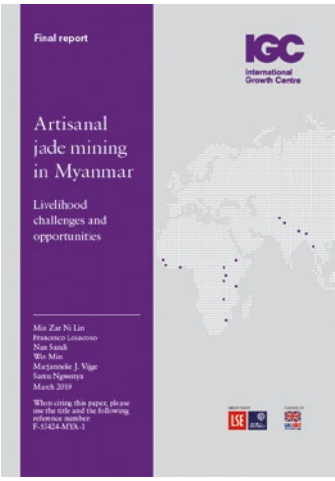

Artisanal Jade Mining in Myanmar

This 51-page report from the International Growth Centre in London was originally issued in March 2019 and made available online in April 2020. It provides an overview of Myanmar's jade sector, its political economy, characteristics of the artisanal 'hand-pickers', labour and social conditions at the mines, and conflicts between the artisanal miners and larger companies. It concludes with suggestions to improve the working conditions for the artisanal jade mining sector in Myanmar. Download the report at www.theigc.org/wp-content/uploads/2020/04/Lin-et-al-2019-Final-Report.pdf.

Consumer and Trade Report on Synthetic Diamonds

In October 2020, USA-based MVI Marketing LLC released *Gaining Critical Mass: 2020 Lab Grown Diamond Consumer & Trade Research Report*, which was prepared in association with the International Grown Diamond Association and *Instore* magazine. Some key findings include: (1) in 2020, 80% of jewellery consumers have heard about lab-grown diamonds, up from only 58% in 2018; (2) many diamond retailers report that up to 50% of customers ask about lab-grown diamonds; and (3) 8% of the 1,027 jewellery consumers surveyed had purchased synthetic diamonds. The report can be purchased for USD125.00 at www.themveye.com/premium-reports.php.

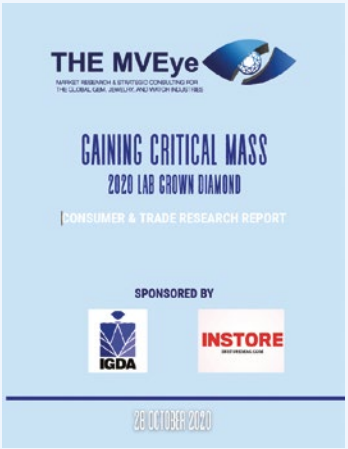

Gem Testing Laboratory (Jaipur, India) Newsletter

The September 2020 (Vol. 77) issue of GTL Jaipur's *Lab Information Circular* is available to download at https://gtljaipur.info/lab-information-circular1.aspx. It reports on strands of red-brown type Ib HPHT-grown synthetic diamond beads, a 43 ct yellow-brown phenakite, azurite in K-feldspar, a 149 ct violet Maxixe-type beryl, 'caramel spice' variegated opal, yellow-green magnesite sold as 'lemon chrysoprase' and amethyst with inclusions of goethite (not 'cacoxenite').

ISO Report on Grading Polished Diamonds

In September 2020, the International Organization for Standardization (ISO, Geneva, Switzerland) released ISO standard 24016:2020, titled *Jewellery and Precious Metals — Grading Polished Diamonds — Terminology, Classification and Test Methods*. The 55-page document 'specifies the terminology, classification and the methods that are used for the grading and description of single unmounted polished diamonds over 0,25 carat (ct)'. It applies only to natural, unmounted, polished diamonds and not to fancy-coloured, synthetic or treated diamonds (except as specified in the document) or assembled stones. The report is available for CHF178.00 in electronic or hardcopy format. Visit www.iso.org/standard/79795.html.

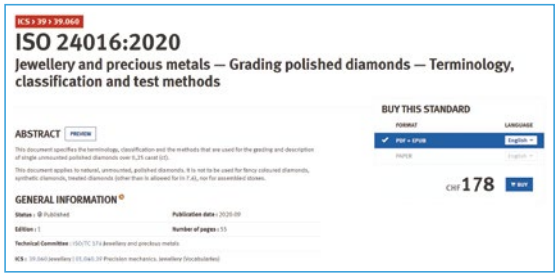

GIT Lab Reports on Blue Jadeite and Colourless Garnet

In August–September 2020, The Gem and Jewelry Institute of Thailand (GIT, Bangkok) posted reports at www.git.or.th/articles_technic_en.html about two unusual gem materials. In the first report, two samples of greenish blue to blue-green jadeite were found to be coloured by a combination of Ti and Fe, while Cr—the primary chromophore in green jadeite—was essentially absent. The second report describes a 0.38 ct grossular that lacked any chromophores (as shown by EDXRF and UV-Vis spectroscopy) and was therefore colourless, which is rare for garnet.

NAJ White Paper on Jewellery and UK Consumers

In July 2020, the National Association of Jewellers (NAJ) in London released a report supported by the Company of Master Jewellers and the Goldsmiths' Company titled *The Role of Jewellery in the Lives of UK Consumers*, which profiles opinions gathered in autumn 2019 from more than 2,500 UK consumers. The findings indicate that 70% of consumers had purchased jewellery in the previous five years, and only 7% would consider purchasing online. Many, however, spend less than GBP100.00, well below the mean price for a 'significant jewellery purchase'. Download the report at www.thegoldsmiths.co.uk/company/today/news/2020/07/29/naj-research.

OTHER RESOURCES

Webinars and Other Online Resources for Gemmological Education

Since the arrival of the COVID-19 pandemic, various educational and gem industry organisations have provided webinars and other archived video content of interest to gemmologists. Additionally, recordings of some conferences that have streamed online during the pandemic have been made available for public viewing. The following items add to the list of such resources that have been featured in previous issues of *The Journal*.

- The **39th World Diamond Congress**, co-hosted by the World Federation of Diamond Bourses and the International Diamond Manufacturers Association, was held online 14–15 September 2020. Recordings of the opening session, closing session, a guest lecture on 'Marketing Diamonds to Future Generations' and the 2020 Young Diamantaires Meeting that took place during the conference are available at www.youtube.com/channel/UChzc3v8PFSZVpZYYc2Qqu7w.

- The **African Diamond Conference** webinar series was held online in October 2020 in lieu of its postponed second conference. Three webinars cover: (1) the state of the diamond market, (2) creating shared value in the future and (3) 'Telling the Real Diamond Story'. A closing statement is provided by Namibia's Minister of Mines, who is also chair of the African Diamond Producers Association. The videos can be viewed on the Antwerp World Diamond Centre's website at www.awdc.be/adc20.

- The **American Opal Society**, in conjunction with the Muzeo Museum and Cultural Center (Anaheim, California, USA), organised three webinars in September–October 2020 under the theme 'Opals Unveiled'. The first one, called 'Intro to Opal: Featuring Opals of Australia', is now available online. The others, titled 'Opals in the Americas' and 'How to Purchase Opal and Opal Jewelry', will be uploaded in the future. Visit https://muzeo.org/event/opalsunveiled.

- **Branko Gems** (Vancouver, British Columbia, Canada) and **Analytical Gemology & Jewelry** (New York, New York, USA) teamed up to present a webinar series on synthetic diamonds in October–December 2020. The videos feature experts who contributed to the recently released 3rd edition of the book *Laboratory-Grown Diamonds*. View the webinars at www.youtube.com/channel/UCtL81xZ4k7vDZtiF79UYZPg and www.brankogems.com/shop/product-category/webinars.

- **The Gem and Jewelry Institute of Thailand** has a webinar series called 'GIT Talk', which is available at www.youtube.com/playlist?list=PL2WH62cAeZKjGWF6T2MKSu9MyUbFB4qky. Most of the recordings are in Thai, but some are in English. They cover topics such as coloured stone marketing and colour terminology.

- **Initiatives in Art and Culture** (IAC, New York), in collaboration with De Beers, organised a virtual event in October 2020 titled 'All That Glitters'. A panel discussion covered responsible mining in the jewellery supply chain and leadership in responsible practice, and was followed by an awards presentation. Register and watch the 2.5-hour video at www.wirestream.tv/customer/iac/2020/10-28.

- **JewelleryNet.com** (Hong Kong) hosts numerous webinars on its 'Jewellery & Gem Knowledge Community' web page at https://jewellerynet.com/en/webinar. Most of the webinars were posted in September–October 2020, in conjunction with the Jewellery & Gem Digital World online event that took place 27–29 October. Others form a series titled 'Return & Recovery' about business strategies for dealing with challenges posed by the COVID-19 pandemic. The webinars feature various industry experts and are mostly in English.

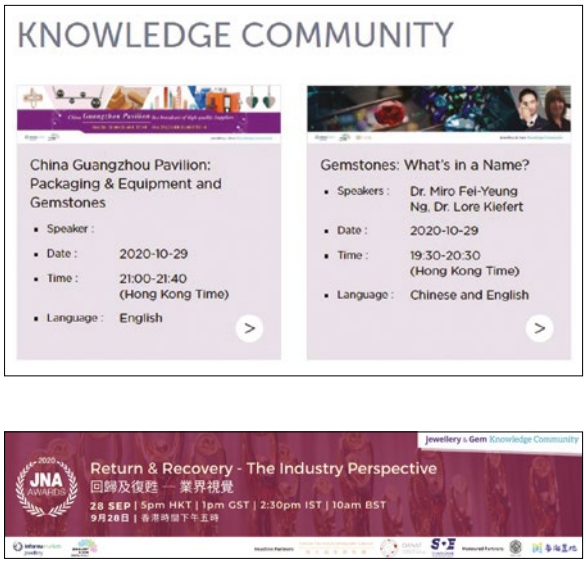

- ***National Jeweler***'s 'My Next Question' webinar series started in September 2020 and is available at www.nationaljeweler.com/webinars/recorded-webinars. The recordings feature insights on topics such as marketing, photomicrography, gem legends and royal jewels.

- The **South Orange County Gem and Mineral Society** (San Clemente, California, USA) offers videos of several online presentations from a variety of speakers at www.youtube.com/channel/UCp1119BoRsRpsAqx6o0dwmg/videos. Topics include opal, rare and unusual gems of California, Native American jewellery, coloured diamonds, Montana sapphires and the Cheapside Hoard.

- **Vicenzaoro** (Vicenza, Italy), in collaboration with the Italian Gemmological Institute, offers a series of 'Gem Talks' webinars at www.youtube.com/playlist?list=PLrsoaKqEfAlVzHw4ayR9V_82ueY9fWdCO. Many were recorded at the January 2020 Vicenzaoro gem fair, where presentations (in English or Italian) covered topics pertaining to quartz, ruby and tanzanite.

MISCELLANEOUS

Peretti Museum Foundation

The Peretti family founded this Swiss-based non-profit foundation in 2020 to showcase the scientific contributions of Dr Adolf Peretti, including his collection of more than 2,000 gems, minerals and fossils. The Foundation plans to build a public museum devoted to paleontology, mineralogy and earth sciences, and supports research and collaboration with other scientists. The foundation's website (www.pmf.org) has videos on ruby, amber and perettiite-(Y) from Myanmar, as well as charity work done by Dr Peretti. It also contains extensive information about perettiite-(Y), and hosts a new publication titled *Journal of Applied Ethical Mining of Natural Resources and Paleontology (PMF Journal)*, with the first issue covering 'Ethics, Science and Conflict in the [Burmese] Amber Mines'.

Peretti Museum Foundation

What's New provides announcements of new instruments/technology, publications, online resources and more. Inclusion in What's New does not imply recommendation or endorsement by Gem-A. Entries were prepared by Carol M. Stockton, unless otherwise noted.

Gem Notes

COLOURED STONES

Celestine from Madagascar

Celestine (or celestite, coelestite) is named after the Latin *caelestis*, alluding to the colour of the sky. It is a strontium sulphate ($SrSO_4$) of the baryte group, where the other isostructural members are baryte ($BaSO_4$), anglesite ($PbSO_4$) and anhydrite ($CaSO_4$). A solid-solution series exists between celestine and baryte, and the name *baritocelestine* is sometimes used for barium-rich celestine. Celestine is colourless to pale blue, although rare orange material has been found in Ontario, Canada (Bernstein 1979).

Although celestine occurs worldwide, Madagascar is the main source and has produced many hundreds of tons of geodes showing pale blue colour, including the world's finest specimens. The mining area is located north and west of Sakoany village in the Mahajanga (Majunga) region on the north-western coast of Madagascar, near the mouth of Betsiboka River (Pezzotta 1999; Wilson 2010; Pezzotta & Pezzotta 2020). Celestine is most commonly seen on the market as tumbled stones and mineral specimens, and is sometimes fashioned into cabochons. It is rarely encountered as faceted stones; its low hardness (Mohs 3–3½), perfect cleavage and brittleness make it difficult to facet.

The 4.22 ct faceted celestine in Figure 1 is reportedly from Madagascar and was characterised by the author to add more gemmological data to the literature on this collector's stone. It showed the following properties: colour—almost colourless with a very faint greyish blue tint; pleochroism—light green-blue, light bluish violet and colourless; lustre—vitreous; diaphaneity—transparent; RI—1.620–1.631; birefringence—0.011; optic character—biaxial positive; hydrostatic SG—3.98; magnetism—diamagnetic (repelled by an N52 neodymium magnet); Chelsea Colour Filter reaction—none; and fluorescence—inert to long- and short-wave UV radiation. These characteristics are consistent with those previously reported for celestine (O'Donoghue 2006). Microscopic observation (up to 40×) showed no visible inclusions.

Infrared (IR) reflectance spectra were collected from several spots on the stone's table and pavilion facets, and a representative spectrum is provided in Figure 2. Although the anisotropy of the material significantly modified the pattern in the 1300–1000 cm^{-1} range, overall the data matched the reference spectrum published by Hainschwang and Notari (2008). It is possible to distinguish celestine from baryte using IR spectroscopy because the ν_1 band (stretching mode) is at 991 cm^{-1}, versus 981 cm^{-1} for baryte. Three bands (ν_4) at 614–618, 643 and 654 cm^{-1} for celestine (compared to 610–614, 635 and 648 cm^{-1} for baryte) can also be used, but the patterns of these bands are sensitive to anisotropy. The bands' assignments were reported by Lane (2007).

Visible-range spectra (Figure 3) were collected for each polarisation direction corresponding to the three pleochroic colours, and the path lengths were used to calculate absorption coefficients. The E||b spectrum (green-blue) consisted of two broad bands at 425 and 618 nm that created a transmission window at about 510 nm. The E||c spectrum (bluish violet) was similar to E||b, but one of the broad bands (605 nm) was somewhat shifted towards the blue region and it lacked

Figure 1: This 4.22 ct celestine (9.4 × 7.6 × 6.4 mm) is reportedly from Madagascar. It was fashioned by Ottorino Invernizzi from a crystal taken from a mineral specimen. Photo by T. Cathelineau.

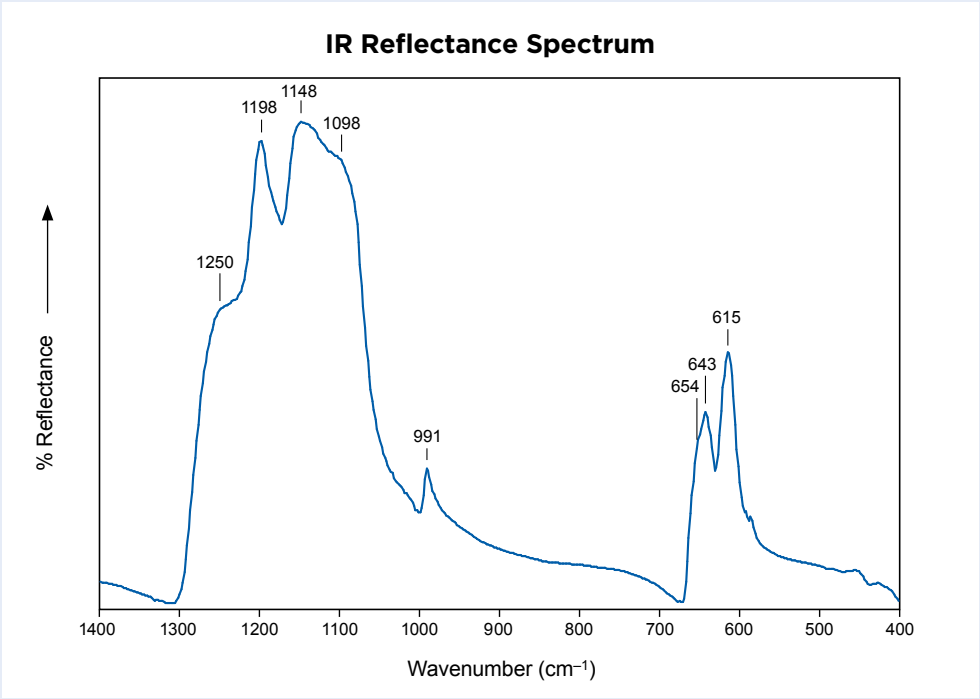

Figure 2: The IR reflectance spectrum of celestine is characterised by bands in the ranges 1200–1080 and 680–580 cm^{-1}, as well as a ν_1 band at 991 cm^{-1}.

the 425 nm band. An asymmetric band (shoulder) on the low-wavelength side of the 605–618 nm absorption is due to an underlying band at around 575–585 nm. The E||a spectrum (colourless) was rather flat.

The causes of colour in celestine were studied with EPR spectroscopy by Bernstein (1979), who reported the presence of colour centres due to radiation damage; no more recent work appears to have been published. Bernstein (1979) indicated that the 425 nm band is related to SO_2^-, the 575–585 nm band might be due to SO_3^- and the 605–618 nm feature is associated with O^-. These centres are stabilised by the presence of trace components, primarily K^+ substituting for Sr^{2+}. Bernstein (1979) also performed heat-treatment experiments and found that thermal bleaching occurred at just 200°C for heating durations of a minute to several days; the colour could be restored by irradiation.

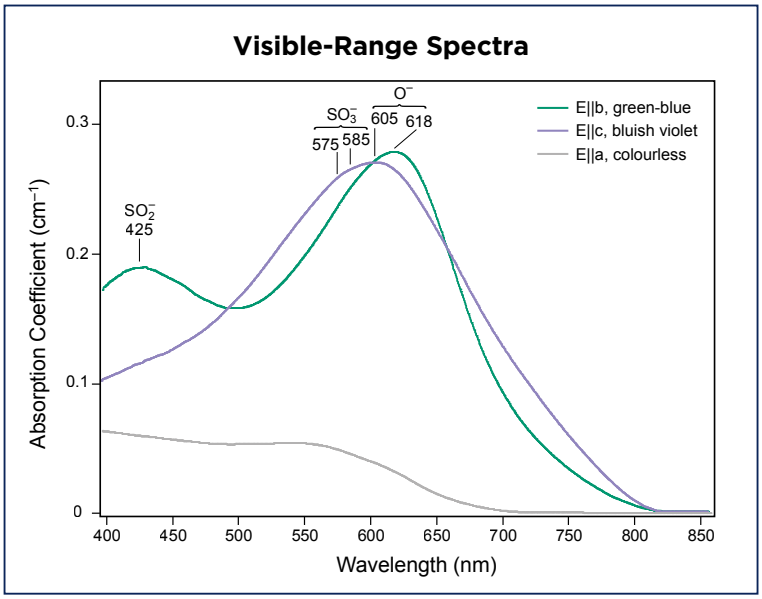

Figure 3: Polarised visible-range spectra are shown for the green-blue (E||b), bluish violet (E||c) and colourless (E||a) pleochroic directions of the 4.22 ct celestine. The major absorption bands are due to O^-, SO_3^- and SO_2^-.

Celestine has been reported in the literature to be sometimes 'fluorescent', with a white, blue or even red reaction to UV radiation. A broad photoluminescence (PL) emission band usually peaking between 430 and 500 nm has been possibly connected to Pb^{2+} centres, but this has not been confirmed (Gaft *et al.* 2015). Other studies have proposed several other possible luminescence causes, such as organic impurities and Eu^{2+} (Tarashchan 1978), and at low temperature (77 K), O_2^-, VO_4, TiO_4 and MoO_4 (Gaft *et al.* 1985). The stone described here was analysed by PL spectroscopy using 254, 375 and 405 nm excitations at room temperature, but no photoluminescence was detected.

Thierry Cathelineau
(thierry.cathelineau@spec4gem.info)
Paris, France

References

Bernstein, L.R. 1979. Coloring mechanisms in celestite. *American Mineralogist*, **64**(1–2), 160–168.

Gaft, M.L., Bershov, L.V., Krasnaya, A.R. & Yaskolko, V.Y. 1985. Luminescence centers in anhydrite, barite, celestite and their synthesized analogs. *Physics and Chemistry of Minerals*, **11**(6), 255–260, https://doi.org/10.1007/bf00307403.

Gaft, M., Reisfeld, R. & Panczer, G. 2015. *Modern Luminescence Spectroscopy of Minerals and Materials*. Springer, Cham, Switzerland, xix + 606 pp., https://doi.org/10.1007/978-3-319-24765-6.

Hainschwang, T. & Notari, F. 2008. Specular reflectance infrared spectroscopy — A review and update of a little exploited method for gem identification. *Journal of Gemmology*, **31**(1), 23–29, https://doi.org/10.15506/JoG.2008.31.1.23.

Lane, M.D. 2007. Mid-infrared emission spectroscopy of sulfate and sulfate-bearing minerals. *American Mineralogist*, **92**(1), 1–18, https://doi.org/10.2138/am.2007.2170.

O'Donoghue, M. 2006. *Gems*. Butterworth-Heinemann, Oxford, xxix + 873 pp.

Pezzotta, F. 1999. Heavenly: Madagascar's celestite. *In: Madagascar—A Mineral and Gemstone Paradise*. extraLapis English No. 1, Christian Weise Verlag, Munich, Germany, and Lapis International, East Hampton, Connecticut, USA, 88–89.

Pezzotta, F. & Pezzotta, S. 2020. La celestina, un classico della mineralogia del Madagascar. *Rivista Mineralogica Italiana*, **44**(2), 94–108 (in Italian).

Tarashchan, A.N. 1978. *Luminestsentsia Mineralov [Luminescence of Minerals]*. Naukova Dumka, Kiev, Ukraine, 296 pp. (in Russian).

Wilson, W.E. 2010. The Sakoany celestine deposit, Mahajanga Province, Madagascar. *Mineralogical Record*, **41**(5), 405–416.

Vesuvianite (Idocrase) and Apatite Inclusions in Ruby Identifiable by Infrared Spectroscopy

Recently, two rubies weighing 1.39 and 2.19 ct (see the cover of this issue) were submitted to the American Gemological Laboratories (AGL) separately for testing, and they provided an opportunity to expand the range of inclusions identifiable in corundum using infrared spectroscopy. Routine origin testing indicated that both samples originated from Myanmar (Burma).

The 2.19 ct ruby contained a variety of internal features, including groups of near-colourless to slightly greenish crystals (Figure 4). Raman micro-spectroscopy identified several of the surface-reaching inclusions as vesuvianite (also known as idocrase). While all of the ruby's standard gemmological properties were consistent with those of natural corundum, the mid-infrared (IR) spectra showed several anomalous features, which we suspected were due to the vesuvianite inclusions: a dominant compound structure between approximately 3700 and 2700 cm^{-1} with bands at approximately 3580, 3475, 3260, 3180 and 3086 cm^{-1}, as well as a series of weaker bands positioned at approximately 5018, 4515, 4235, 4200 and 4105 cm^{-1} (Figure 5). Analysis of

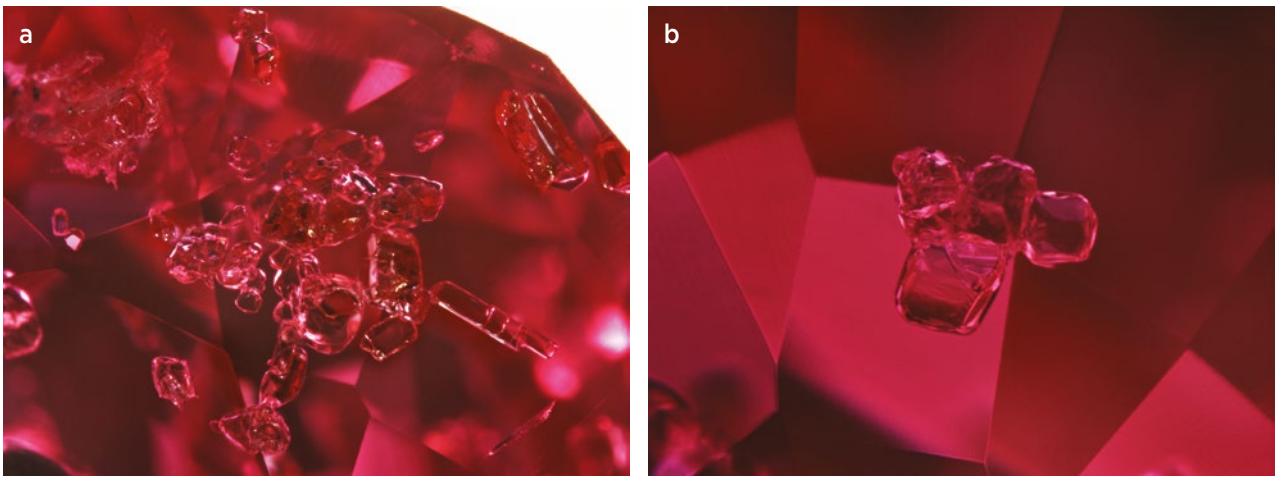

Figure 4: These groups of near-colourless to slightly greenish crystals in the 2.19 ct Burmese ruby were initially identified by Raman micro-spectroscopy as vesuvianite. Photomicrographs by C. P. Smith; magnified (a) 38× and (b) 78×.

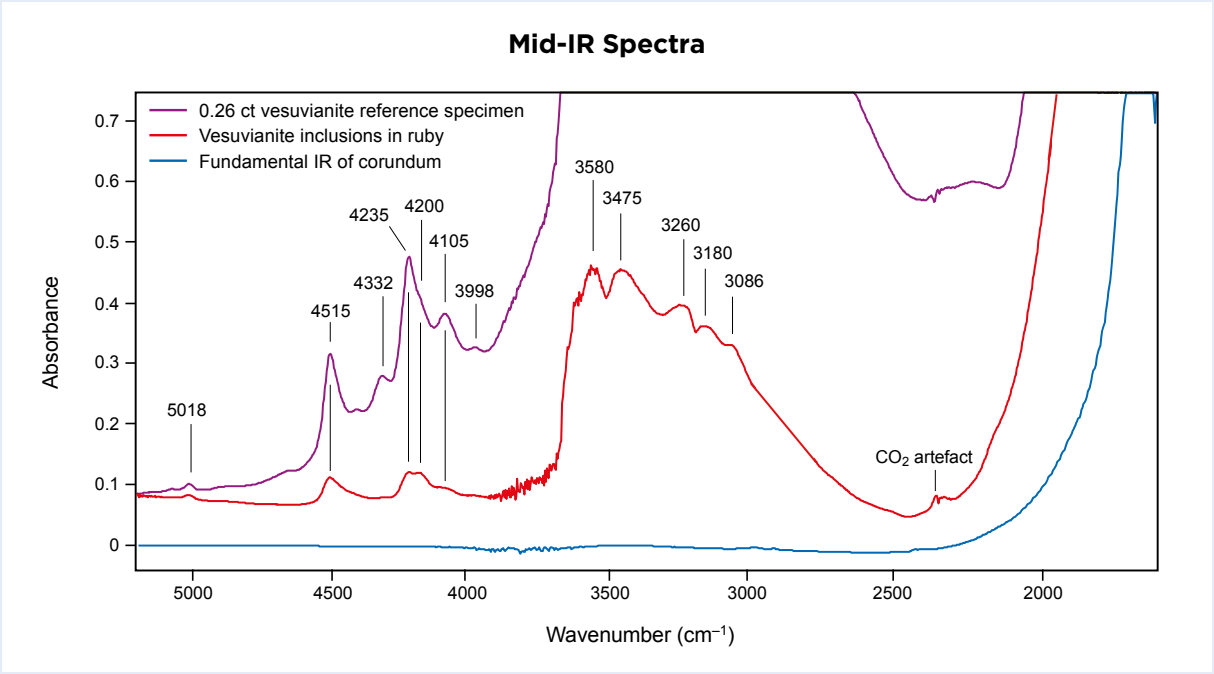

Figure 5: The mid-IR spectrum of the 2.19 ct ruby reveals a series of absorption bands that identified the presence of vesuvianite inclusions. Shown for comparison is the reference spectrum for a 0.26 ct vesuvianite (path length 2.5 mm). The vesuvianite spectrum shows total absorption between approximately 3700 and 2700 cm^{-1}, whereas the small size of the vesuvianite inclusions in the ruby permitted the features in this region to be fully resolved. Corundum is anhydrous and is therefore typically free of such bands.

a vesuvianite from the AGL reference collection (again, see Figure 5) proved that the anomalous features in the ruby spectrum were indeed due to these inclusions.

Because vesuvianite absorbs strongly in the mid-IR region of the spectrum, even minute inclusions can give a distinct IR signal. In fact, when collecting our reference spectra for vesuvianite it was necessary to analyse a small sample (0.26 ct) because larger ones yielded spectra that saturated significant regions of the spectrum, making the comparison with our ruby spectrum difficult. The area of the spectrum in which the 0.26 ct reference vesuvianite showed total absorption corresponded to the region of the compound band structure in the 2.19 ct ruby, and a comparison with published literature (e.g. Groat *et al.* 1995; Bellatreccia *et al.* 2005) also showed that the anomalous peaks resolved in this ruby were consistent with IR features reported for vesuvianite.

Vesuvianite is a hydrous sorosilicate that commonly forms in skarns as a result of the regional metamorphism of limestone (Groat *et al.* 1992). Marble units resulting from metamorphosed limestone are well known to host ruby mineralisation in the Mogok Valley region of Myanmar. Vesuvianite was first identified in ruby (from Myanmar) by Renfro and Koivula (2017). One of the present authors (CPS) has previously observed the IR features described above in a few other rubies, but until now their relation to the presence of vesuvianite inclusions was not recognised.

The 1.39 ct ruby contained several colourless euhedral mineral inclusions, including one particularly large crystal directly under the table (Figure 6). The crystals

Figure 6: Shown here is a particularly large near-colourless apatite crystal located just under the table facet of the 1.39 ct Burmese ruby. Photomicrograph by C. P. Smith; magnified 28×.

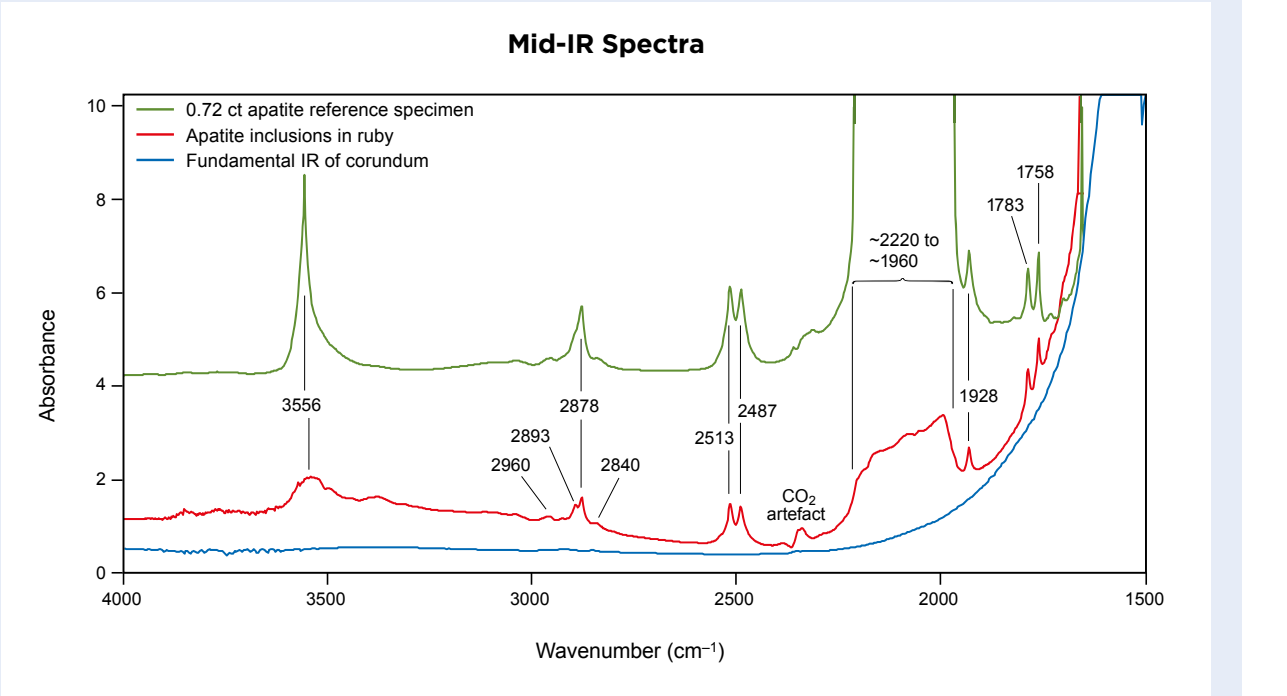

Figure 7: The mid-IR spectrum of the 1.39 ct Burmese ruby reveals a series of absorption bands related to the presence of a large apatite inclusion. Shown for comparison is the reference spectrum for a 0.72 ct apatite (path length 4.5 mm). While the apatite spectrum shows total absorption between approximately 2220 and 1960 cm^{-1}, the structure of this band can be seen for the apatite inclusion in the ruby. Corundum is anhydrous and is therefore typically free of such bands.

exhibited a morphology common for apatite inclusions in ruby. Infrared spectroscopy of this sample displayed a series of bands not typically associated with corundum, at approximately 3556, 2960, 2893, 2878, 2840, 2513, 2487, 1928, 1783 and 1758 cm^{-1}, as well as a compound structure between about 2220 and 1960 cm^{-1}. Comparison with the mid-IR spectrum of a faceted apatite from the AGL reference collection proved that these features were related to apatite (Figure 7). Apatite occurs as a protogenetic inclusion in rubies and sapphires from a number of sources around the world (see, e.g., Gübelin & Koivula 2008; Hughes 2017).

With this research, the catalogue of minerals identifiable by FTIR spectroscopy as inclusions in corundum continues to expand (see, e.g., Smith *et al.* 2020). This emphasises the usefulness of applying a range of analytical techniques to help identify and recognise inclusions occurring within a host gemstone.

Christopher P. Smith FGA
(chsmith@aglgemlab.com)
and Dr Riadh Zellagui
American Gemological Laboratories Inc.
New York, New York, USA

References

Bellatreccia, F., Della Ventura, G., Ottolini, L., Libowitzky, E. & Beran, A. 2005. The quantitative analysis of OH in vesuvianite: A polarized FTIR and SIMS study. *Physics and Chemistry of Minerals*, **32**(1), 65–76, https://doi.org/10.1007/s00269-004-0437-4.

Groat, L.A., Hawthorne, F.C. & Ercit, T.S. 1992. The chemistry of vesuvianite. *Canadian Mineralogist*, **30**(1), 19–48.

Groat, L.A., Hawthorne, F.C., Rossman, G.R. & Ercit, T.S. 1995. The infrared spectroscopy of vesuvianite in the OH region. *Canadian Mineralogist*, **33**(3), 609–626.

Gübelin, E.J. & Koivula, J.I. 2008. *Photoatlas of Inclusions in Gemstones*, Vol. 3. Opinio Publishers, Basel, Switzerland, 672 pp.

Hughes, R.W. 2017. *Ruby & Sapphire: A Gemologist's Guide*. RWH Publishing, Bangkok, Thailand, 734 pp.

Renfro, N. & Koivula, J. 2017. *G&G* Micro-World: Vesuvianite in Burmese ruby. *Gems & Gemology*, **53**(4), 469.

Smith, C.P., Hartley, A. & Zellagui, R. 2020. Gem Notes: Titanite (sphene) inclusions in ruby identified by infrared spectroscopy. *Journal of Gemmology*, **37**(1), 11–12, https://doi.org/10.15506/jog.2020.37.1.11.

Tourmaline with Cassiterite Inclusions

Tourmaline is well known for its range of colours, but not so much for its variety of inclusions. Most of the time it simply contains elongated filamentary two-phase fluid inclusions referred to as 'trichites'. While cataloguing some older samples in the collection of the French Gemmological Laboratory, we came across a tourmaline of unknown geographical origin that contained some unusual octahedral inclusions (Figure 8).

The 0.90 ct tourmaline was a medium dark, slightly greenish blue, and was fashioned as a buff top. The gem's RI was about 1.62–1.64 and its hydrostatic SG was 3.08, confirming it was a tourmaline. It contained a number of small, almost perfectly octahedral-appearing crystals with slightly rounded shiny faces (Figure 9). In some observation directions they appeared dark brownish green, but when reflected light was added they looked more brownish. The brownish green appearance probably resulted from the surrounding tourmaline colour combined with the colour of the inclusions.

A Raman spectrum of a surface-reaching inclusion was obtained with a Renishaw InVia Raman spectrometer using 514 nm excitation and a standard resolution of 4 cm^{-1}. The spectrum showed major peaks at about 1061, 718, 635, 375 and 224 cm^{-1}, and the CrystalSleuth software associated with the RRUFF database revealed a match for cassiterite (SnO_2). One common shape of cassiterite crystals—the tetragonal bipyramid—looks very much like a regular octahedron, and the typical brown colour of cassiterite is also consistent with this identification.

To obtain confirmation, we performed chemical analysis of the surface-reaching inclusion (which measured up to 50 µm in dimension) using a JEOL JSM-5800LV scanning

Figure 8: This 0.90 ct tourmaline (approximately 7.6 × 5.9 × 3.3 mm) contains unusual crystal inclusions, which are visible here in brightfield illumination in the left part of the stone. Photo by E. Fritsch.

electron microscope equipped with a SANx EDS SDD detector. The analysis revealed Sn and O, the components of cassiterite, and a small Si signal, likely from the matrix. Qualitative analysis of the tourmaline host indicated the presence of Si, Al and Na, with traces of Fe and Mn. This is consistent with an elbaite composition, although B and Li are too light to be detected with this instrument. In addition, Fe is known to contribute to the dark blue colour of tourmaline (i.e. indicolite). Backscattered-electron (BSE) mode showed high contrast between the inclusions and the matrix, confirming the presence of heavy elements such as Sn (Figure 10).

The association of gem-quality tourmaline with cassiterite is uncommon. Gübelin and Koivula (1986, p. 241) mentioned acicular inclusions of tourmaline in gem cassiterite, but not the reverse. They described inclusions

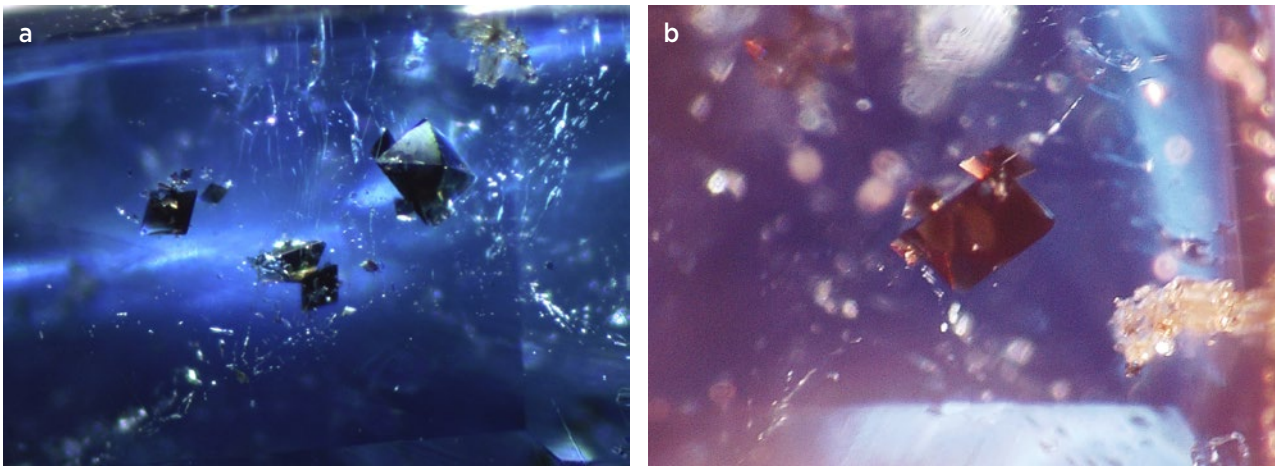

Figure 9: (**a**) In some observation geometries, the octahedral-appearing crystals look brownish green. (**b**) With the addition of reflected light, the inclusions look dark brown. Photomicrographs by A. Delaunay; image widths (a) 1.8 mm and (b) 1.5 mm.

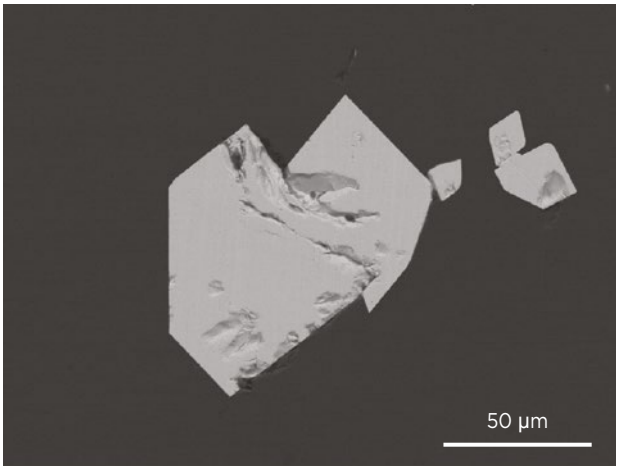

Figure 10: In this BSE image, the surface-reaching cassiterite inclusions appear much lighter grey than the surrounding tourmaline host, confirming the presence of heavy elements—in this case Sn. Image by N. Stephant.

of cassiterite mostly in quartz but also, in one case, in beryl. Subsequently, Gübelin and Koivula (2005, p. 585) showed cassiterite inclusions in quartz that displayed a well-formed octahedral shape.

The association of cassiterite with tourmaline (typically schorl) is known in granitic pegmatites, and Sn is one of the high field-strength elements (i.e. high valence: Sn^{4+}) to be incorporated latest in pegmatite minerals, occurring further from the granitic source than most others. It forms in moderately to highly evolved complex pegmatites with spodumene or petalite, and is typically associated with Sn, Ta and Cs mineralisation (Simmons *et al.* 2003). Grassi (2014) described cassiterite crystals from the Usakos tourmaline mine in Namibia that are very close in size and shape to the ones described here. In addition, Usakos is well known for producing gem-quality blue elbaite, so it is a possible locality of origin for this unusual gem.

Aurélien Delaunay
Laboratoire Français de Gemmologie
Paris, France

Dr Emmanuel Fritsch FGA
(emmanuel.fritsch@cnrs-imn.fr)
and Nicolas Stephant
IMN-CNRS and University of Nantes, France

Ugo Hennebois
Laboratoire Français de Gemmologie
Paris, France

References

Grassi, L.R. 2014. *A geochemical investigation of the Usakos gem pegmatite, Namibia*. MS thesis, University of New Orleans, Louisiana, USA, 203 pp.

Gübelin, E.J. & Koivula, J.I. 1986. *Photoatlas of Inclusions in Gemstones*. ABC Edition, Zurich, Switzerland, 532 pp.

Gübelin, E.J. & Koivula, J.I. 2005. *Photoatlas of Inclusions in Gemstones*, Vol. 2. Opinio Publishers, Basel, Switzerland, 829 pp.

Simmons, W.B., Webber, K.L., Falster, A.U. & Nizamoff, J.W. 2003. *Pegmatology: Pegmatite Mineralogy, Petrology & Petrogenesis*. Rubellite Press, New Orleans, Louisiana, USA, 176 pp.

DIAMONDS

Pale Yellow Type IIa Diamond Coloured by H4 Centres

Type IIa diamonds are generally colourless, brown or pink, and some can turn yellow after HPHT annealing by the formation of substantial nitrogen-related defects (Wang *et al.* 2003). In addition, Lu and Wang (2010) described an untreated greenish yellow type IIa diamond coloured by the H3 centre.

Recently, the National Gemstone Testing Center's (NGTC) Shenzhen laboratory examined a 1.29 ct cushion modified brilliant-cut diamond with a pale yellow (M) colour (Figure 11). It had no detectable nitrogen-related absorptions in the mid-infrared region, but the near-

Figure 11: This 1.29 ct pale yellow type IIa diamond owes its colour to H4 centres. Photo by W. Zhu.

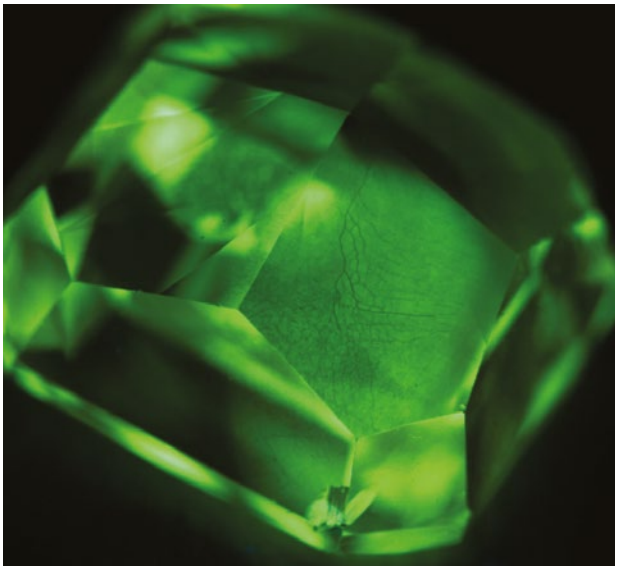

Figure 12: This DiamondView image of the 1.29 ct diamond in Figure 11 shows strong green fluorescence and a well-developed polygonal pattern associated with natural type II diamonds. Photo by Z. Song.

infrared spectrum revealed an obvious radiation-related absorption at 9280 cm^{-1}. This line is equivalent to the 1.149 eV centre and anneals out at temperatures above 1000°C (Zaitsev 2001). Such intense absorption often appears in irradiated blue and green diamonds.

The UV-Vis-NIR absorption spectrum, collected at liquid-nitrogen temperature, revealed a relatively high concentration of the H4 defect, with its zero-phonon line at 495.8 nm. The H4 centre consists of four nitrogen atoms separated by two vacancies, and can produce a yellow body colour and green fluorescence (Shigley & Breeding 2013).

DiamondView imaging (Figure 12) showed strong green fluorescence and a well-developed polygonal pattern associated with lattice dislocations characteristic of natural type II diamonds. We therefore concluded that the present diamond was natural and not synthetic. A similar fluorescence structure was observed in a type II diamond containing the H3 centre (Johnson 2010).

Microscopic observation revealed a fracture near the girdle (Figure 13) that displayed etch patterns. There were also brown radiation stains along its edge, presumably caused by radioactive fluids penetrating into the fracture (again, see Figure 13; cf. Breeding *et al*. 2018). Photoluminescence (PL) spectroscopy with 473 and 532 nm excitation showed radiation-related defects such as the GR1, 3H and other vacancy-related centres, including H4, H3 and NV. Multiple PL analyses of various spots on the stone showed a greater intensity of the 3H centre in the areas with radiation stains than in the rest of the diamond, while the H3 centre showed the reverse trend (Figure 14). The H3 centre is composed of two nitrogen atoms separated by a single vacancy. Photoluminescence related to the 3H centre is associated with isolated self-interstitials and disappears after heating to about 420°C (Steeds *et al*. 1999).

The strong PL intensity of the H4 centre provided good evidence for the origin of the diamond's yellow body colour. This is the first pale yellow type IIa diamond coloured by H4 centres caused by natural irradiation that has been seen in NGTC's laboratories.

Wenfang Zhu (zhu_wenfang@163.com), Zhonghua Song, Dr Taijin Lu and Huihuang Li
National Gemstone Testing Center Shenzhen and Beijing, China

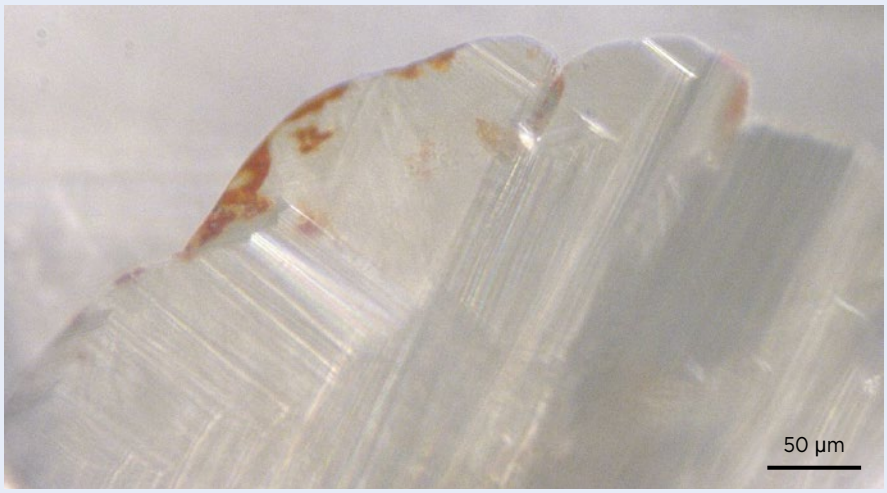

Figure 13: Radioactive fluids penetrated into this fracture in the diamond and caused brown radiation stains. Photomicrograph by W. Zhu.

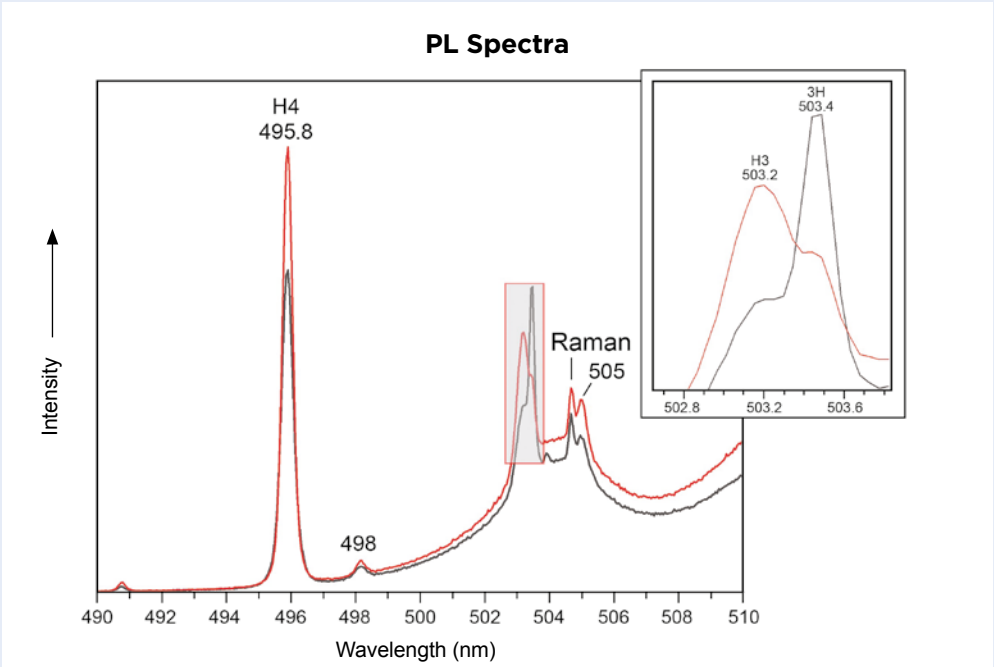

Figure 14: PL spectroscopy with 473 nm excitation shows a reverse in the relative intensity of the H3 and 3H defects between areas containing radiation stains (black trace) and other parts of the diamond (red trace).

References

Breeding, C.M., Eaton-Magaña, S. & Shigley, J.E. 2018. Natural-color green diamonds: A beautiful conundrum. *Gems & Gemology*, **54**(1), 2–27, https://doi.org/10.5741/gems.54.1.2.

Johnson, P. 2010. Lab Notes: Diamond with rare green fluorescence. *Gems & Gemology*, **46**(1), 49–50.

Lu, R. & Wang, W. 2010. Lab Notes: Type IIa greenish yellow diamond colored by IR-inactive nitrogen. *Gems & Gemology*, **46**(1), 52–53.

Shigley, J.E. & Breeding, C.M. 2013. Optical defects in diamond: A quick reference chart. *Gems & Gemology*, **49**(2), 107–111, https://doi.org/10.5741/gems.49.2.107.

Steeds, J.W., Davis, T.J., Charles, S.J., Hayes, J.M. & Butler, J.E. 1999. 3H luminescence in electron-irradiated diamond samples and its relationship to self-interstitials. *Diamond and Related Materials*, **8**(10), 1847–1852, https://doi.org/10.1016/s0925-9635(99)00144-2.

Wang, W., Hall, M. & Moses, T.M. 2003. Gem Trade Lab Notes: Diamond—Intensely colored type IIa, with substantial nitrogen–related defects. *Gems & Gemology*, **39**(1), 39–41.

Zaitsev, A.M. 2001. *Optical Properties of Diamond*. Springer-Verlag, Berlin and Heidelberg, Germany, 502 pp., https://doi.org/10.1007/978-3-662-04548-0.

SYNTHETICS AND SIMULANTS

History Revisited—A Quartz 'Soudé Emerald'

Synthetic emeralds have become more affordable and prevalent, so one might expect to see fewer emerald imitations. However, in recent years, various types of assembled or composite imitations (triplets known as 'soudé emeralds' in the past) have continued to appear. These have traditionally been composed of crown and pavilion layers of colourless synthetic spinel or quartz that are bonded together with a thin green-coloured layer (Anonymous 1940; Webster 1952). Other materials that have been reported for triplets imitating emeralds include natural or synthetic beryl, glass or petalite, but almost any light-coloured or colourless material could be used.

Recently submitted to the Stone Group Laboratories was an emerald-cut green specimen set in a ring with two round brilliant diamonds (Figure 15). The colour was what might be expected for emerald. The specimen was inert

Figure 15: The emerald-cut green specimen (approximately 9.0 × 13.2 mm) set with diamonds in this ring turned out to be a classic type of quartz triplet known as 'soudé emerald'. Photo by B. Williams.

to long-wave UV radiation and no reaction was observed with a Chelsea Colour Filter. Observation with 10× magnification revealed surface scratches and abrasions, as well as partially healed, fluid-filled fissures, as are commonly seen in emeralds, but these were noticeably less complex in structure (Figure 16). Further observation revealed that the inclusions did not continue across the girdle plane. A side view with immersion readily revealed the composite structure of the sample (Figure 17). Abrasions at the exposed girdle edges drew attention to apparent separations along the bonding plane between the crown and pavilion due to wear and, perhaps, cleaning.

We were curious as to the exact components of the triplet, and a GemmoRaman-532SG spectrometer confirmed both the crown and pavilion to be quartz. The natural (i.e. not synthetic) origin of the quartz was indicated by the presence of natural inclusions and confirmed by FTIR spectroscopy. UV-Vis spectroscopy performed with a GemmoSphere instrument showed a broad band centred at about 730 nm and a strong absorption in the violet to UV region of the spectrum, which together produced a transmission window in the green region at about 520 nm (Figure 18). A spectrum of a Brazilian emerald shown for comparison displays a transmission window at a similar wavelength formed by distinct absorptions due mainly to Cr^{3+} with contributions from V^{3+}, Fe^{2+} and Fe^{3+}.

It seems possible that this triplet could have been a 'soudé emerald' that was inherited or otherwise recycled from old jewellery, presumed to be natural and then re-set into the present ring. In any case, this quartz triplet serves as a reminder that old-fashioned emerald imitations may still be encountered in today's market.

Cara Williams FGA and Bear Williams FGA
(info@stonegrouplabs.com)
Stone Group Laboratories
Jefferson City, Missouri, USA

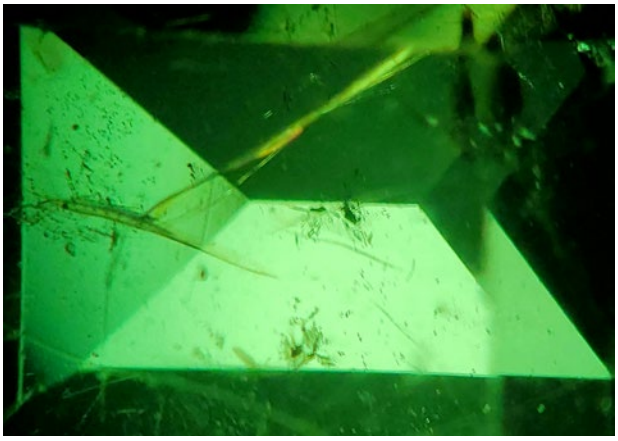

Figure 16: Fluid inclusions in the triplet resemble those seen in emeralds but are less complex. Photomicrograph by B. Williams; image width 7 mm.

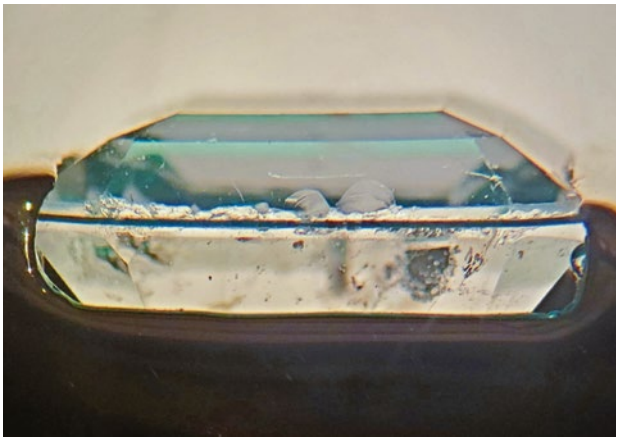

Figure 17: A side view of the girdle of the triplet clearly reveals a coloured intermediate layer. Photo by B. Williams, using darkfield illumination and immersed in water.

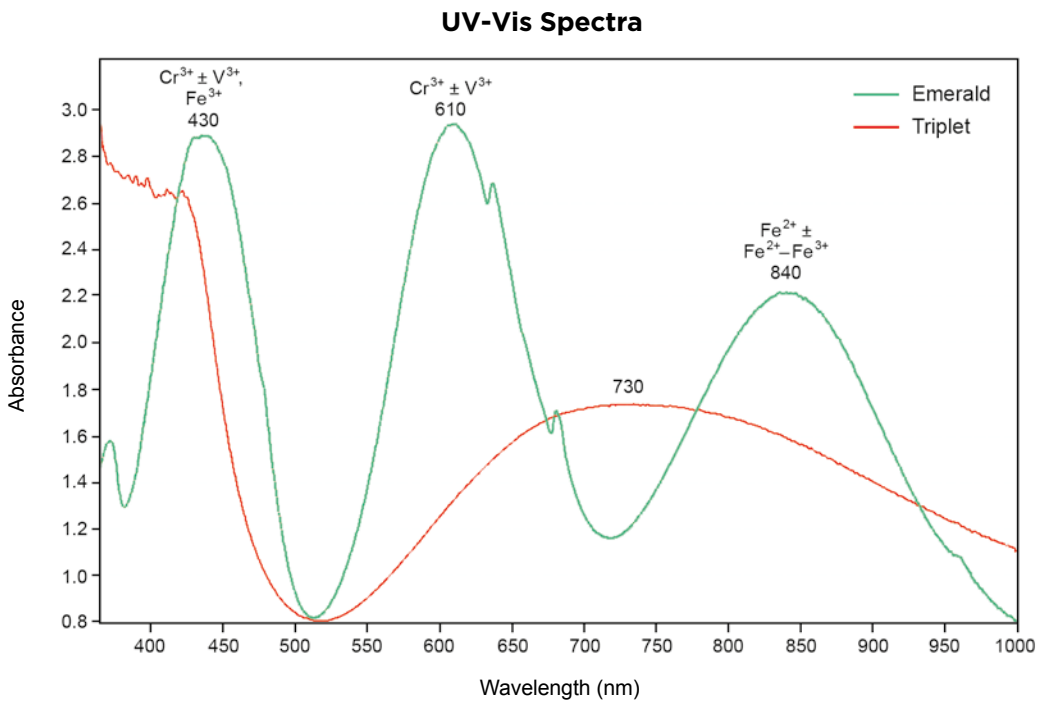

Figure 18: UV-Vis spectroscopy of the triplet shows a transmission window in the green region at about 520 nm, similar to that seen in the spectrum of a Brazilian emerald. While the absorption features recorded for the emerald are mainly due to Cr^{3+}, those of the triplet are attributed to a dye in the coloured layer.

References

Anonymous 1940. Gemmology for beginners: 11.—Composite stones and artificially induced colour. *The Gemmologist*, **10**(110), 18–22.

Webster R. 1952. New spinel doublet. *Journal of Gemmology*, **3**(5), 199–201, https://doi.org/10.15506/jog.1952.3.5.199.

Synthetic Rock Crystal Clusters on the Chinese Market

In recent years there have been various reports of synthetic quartz containing inclusions that would be expected in natural quartz (e.g. Ng-Pooresatien 2015; Skalwold 2016), which show ongoing developments in such laboratory-grown material. However, little has been published on the presence of synthetic quartz crystal clusters (see, e.g., Clifford & Klipov 2015; JGGL 2019).

In June 2020, a team from NGTC visited China's largest crystal market, located in Jiangsu Province. The group obtained a 1.24 kg crystal specimen—sold as natural quartz—that consisted of numerous transparent colourless crystals pointing in different directions that contained local areas of green colouration (Figure 19). The crystals were composed of a hexagonal prism and a rhombohedron, with horizontal parallel striations and polygonal etchings on the surfaces of the hexagonal prism, which are similar to those typically seen on natural quartz crystals. The green-coloured areas were produced by abundant particles of different sizes, with a clear boundary between green and colourless zones, as might be expected for chlorite-included quartz. However, on one side of the cluster, a group of crystals displayed unusual colour banding that was perpendicular to the direction of crystal growth (Figure 20). This aroused suspicion that the sample was not composed of natural rock crystal quartz.

Several colourless crystals were removed from the cluster for further examination. Their RIs were 1.544–1.550 (birefringence 0.006) and their hydrostatic SG values were in the range of 2.56–2.58. The upper RI value and birefringence were slightly lower than those expected for quartz, and the SG range was also low. With magnification, we observed a large number of 'fingerprint'-like

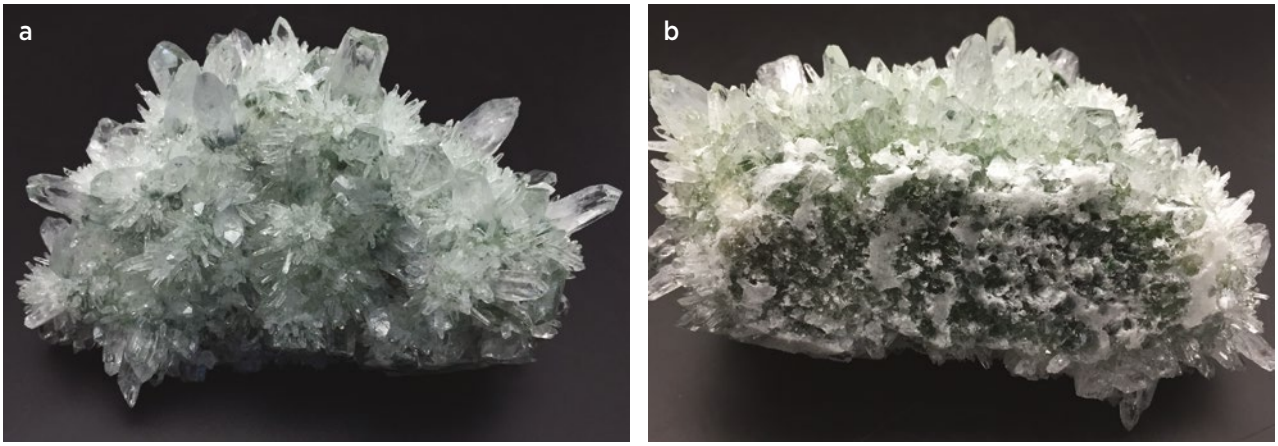

Figure 19: (**a**) This 1.24 kg specimen, which proved to consist of synthetic quartz, displays many colourless crystals oriented in different directions that locally contain green areas. (**b**) Viewed from the reverse side, the cluster exhibits additional areas of green colouration. Photos by H. Dai.

Figure 20: This group of crystals (160 mm long) on one side of the synthetic quartz cluster displays conspicuous colour banding perpendicular to the direction of crystal growth. Photo by H. Dai.

gas-liquid inclusions, arranged in indistinct, irregular curved planes that extended in various directions (Figure 21), as typically seen in natural quartz. No 'breadcrumb' inclusions typical of synthetic quartz were seen. The green areas of the crystals remained green when viewed with a Chelsea Colour Filter, while natural green quartz appears light red (Ma *et al.* 2011).

IR absorption spectra were recorded for the colourless and green areas of the crystals in transmission mode using a Thermo Nicolet 6700 infrared spectrometer (Figure 22). The colourless crystals lacked the bands at 3379, 3483 and 3595 cm^{-1} that are characteristic of natural quartz, and displayed bands at 3585, 3432, 3294 and 3194 cm^{-1} that are typical of synthetic quartz (Zecchini & Smaali 1999; Ng-Pooresatien 2015). The green areas of the crystals showed an additional absorption band at 5520 cm^{-1}, but lacked the band at 4455 cm^{-1} that has been reported in natural green quartz (Ma *et al.* 2011).

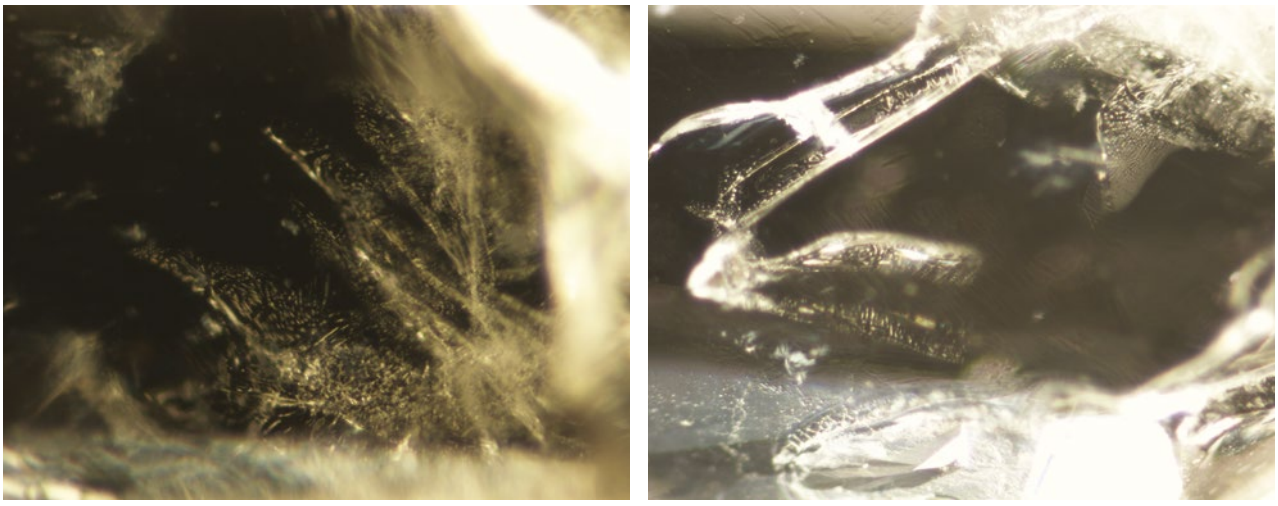

Figure 21: The synthetic quartz contains numerous gas-liquid inclusions, which appear similar to those seen in natural quartz. Photomicrographs by H. Dai; magnified 30×.

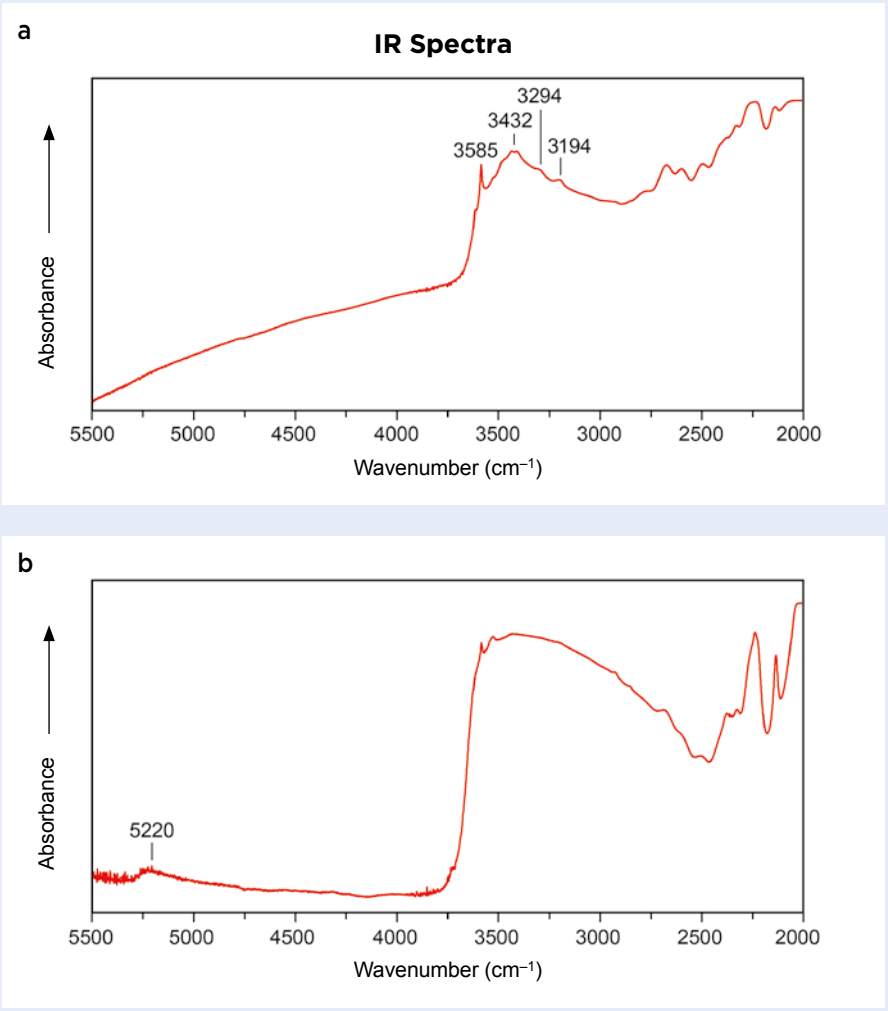

Figure 22: (**a**) The IR absorption spectrum of a colourless crystal from the specimen shows bands at 3585, 3432, 3294 and 3194 cm^{-1} that are typical of synthetic quartz. (**b**) The spectrum of a green portion of a crystal from the specimen shows an additional band at 5220 cm^{-1} and lacks the feature at 4455 cm^{-1} previously reported in natural green quartz.

Therefore, we concluded that the sample was composed of synthetic rock crystal quartz.

This specimen is similar to some of those pictured in the brief report by JGGL (2019), and it also resembles certain crystal clusters being offered (as natural) by various sellers on the internet. The appearance on the market of such material is an important reminder that not all synthetic quartz crystals consist of single columnar plates, but they also can be grown as clusters. Furthermore, such natural and synthetic quartz crystals can have a very similar visual appearance, with identical inclusion features. Therefore, IR absorption spectroscopy may be necessary to separate them.

Huiru Dai (478202834@qq.com), Danyi Zhou, Zhonghua Song, Jun Su, Haibo Li, Dr Taijin Lu and Yongwang Ma
National Gems & Jewelry Technology Administrative Center, National Gemstone Testing Center, Beijing, China

References

Clifford, J.H. & Klipov, V.A. 2015. A marriage of science and art: Creating quartz specimens in the laboratory. *Rocks & Minerals*, **90**(4), 379–385, https://doi.org/10.1080/00357529.2015.1012958.

Japan Germany Gemmological Laboratory (JGGL) 2019. Synthetic green quartz cluster. *Gem Information*, No. 46, 14.

Ma, Y., Li, H., Lu, T., Shen, M. & Zhou, J. 2011. Identification of irradiated green quartz and synthetic green quartz. *2011 China Gems & Jewelry Academic Conference*, Beijing, China, 22–23 November, 126–129.

Ng-Pooresatien, N. 2015. Lab Notes: Synthetic rock crystal quartz bangle with unusual inclusions. *Gems & Gemology*, **51**(4), 439–440.

Skalwold, E.A. 2016. *G&G* Micro-World: Synthetic quartz: A designer inclusion specimen. *Gems & Gemology*, **52**(4), 425–426.

Zecchini, P. & Smaali, M. 1999. Identification de l'origine naturelle ou artificielle des quartz. *Revue de Gemmologie A.F.G.*, Nos. 138–139, 74–80.

TREATMENTS

Cobalt Glass-Filled Sapphires and the Chelsea Colour Filter: A New Technique

The Chelsea Colour Filter (CCF) was developed in 1934—initially as a means to separate natural and synthetic emerald (Popley 1934)—by Basil Anderson and James Payne at the gem testing laboratory of the London Chamber of Commerce. It works by transmitting certain wavelengths of light in the green-yellow and the extreme red end of the visible spectrum. Although it is less effective today for separating emeralds than when it was first introduced, the CCF remains an essential part of a gemmologist's basic kit for quickly distinguishing between similarly coloured gem materials. The CCF can be used to rapidly separate simulants in stone parcels, particularly blue ones. For example, blue sapphires show no reaction to the CCF (and therefore appear green), while blue glass coloured by cobalt will appear red.

At the February 2020 Accredited Gemologists Association (AGA) Tucson Conference in Arizona, USA, Gem-A Instruments Manager Sam Lloyd presented a workshop called 'Gem-Fun with Filters!', and the new CCF technique described here was discovered when setting up for the workshop, as a curiosity, following the demonstration of other filters used to detect the presence of foreign substances in gemstones. For example, a colour filter can help identify dye in jadeite because it creates greater contrast between the dye and the jadeite. In the case of cobalt glass-filled sapphires, the Co-bearing glass and the sapphire have different responses under the CCF, so the contrast between them becomes obvious.

The CCF is typically held up to the eye to view samples laid on a white background that are illuminated with oblique incandescent light. With the new technique described here, the incandescent light is transmitted through the sample, and the stone is viewed from above with the aid of a loupe or microscope (Figure 23).

Two of the sample sets used at the AGA conference workshop were blue parcels: one consisted mostly of synthetic sapphires mixed with samples of Co-bearing glass, and the other contained mostly synthetic sapphires with some Co glass-filled sapphires. The results observed when using the CCF in the traditional way were very similar for each set: the synthetic sapphires appeared green, while the Co-bearing glass imitations and the Co glass-filled sapphires appeared red (e.g. Figure 24). The results for the glass-filled sapphires varied slightly depending on how much filling they contained. The stones with a light to moderate amount of glass filling showed a less distinct brownish red colour, while those with a higher percentage of glass filling showed a red response similar to that of Co glass.

As seen in Figure 25, the amount of Co-bearing glass filler in a sapphire can be observed because the filled fractures appear distinctly red against the green colour of the host sapphire. This works regardless of the amount of filling within a sapphire, although if a stone is heavily filled then sometimes the contrast is not as clear and a brighter light source is required. It is also important

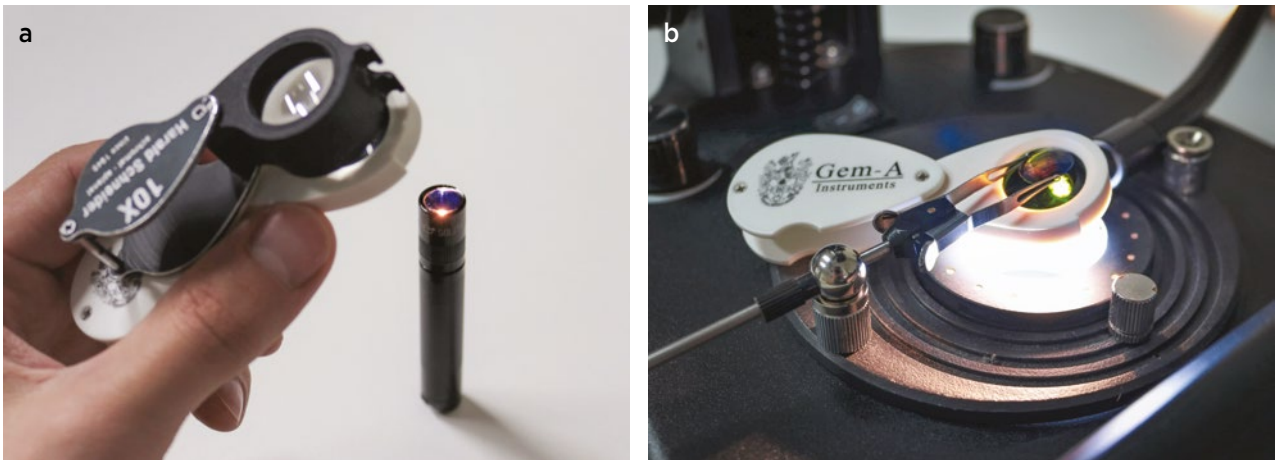

Figure 23: The new CCF technique described here for Co glass-filled sapphires involves the use of transmitted incandescent light. (**a**) A pen torch can be employed to transmit light through the sample, with the CCF positioned between the sample and a loupe. (**b**) The same method can be used with a gemmological microscope, with the CCF between the stone and the light source. Stronger illumination (such as fibre-optic lighting) works better for more heavily filled stones. Photos © C. D. Bexfield.

Figure 24: A Co glass-filled sapphire in this parcel of synthetic sapphires (1.05–2.23 ct) stands out due to its red appearance when viewed through the CCF in the traditional way with oblique incandescent light. Photo © C. D. Bexfield.

to rotate the stone and view it from all angles. In our samples we noticed the presence of gas bubbles in some areas of the glass filling that did not show a red response, suggesting that portions of the sapphires may have been filled with Pb-bearing glass before or after filling with Co-bearing glass.

The use of a microscope (with higher magnification than a loupe) can make it easier to see the colour differences, and therefore can help with estimating the percentage of Co-bearing glass filling within a sapphire, which is otherwise challenging due to the similarity in RI between the sapphire and the glass filling.

Charles D. Bexfield FGA DGA
(CharlieBexfield@gem-a.com)
Gem-A, London

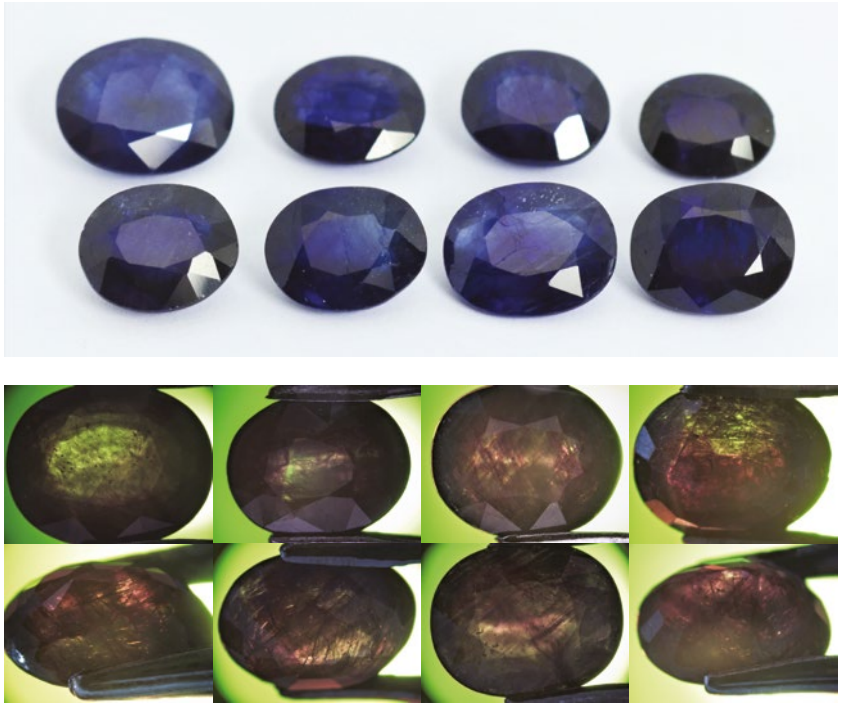

Figure 25: (Top image) These sapphires (3.27–6.73 ct) contain varying amounts of Co-bearing glass filler. (Bottom images) The same stones are shown with the new transmitted-lighting CCF technique, using a microscope with 15× magnification and brightfield illumination with fibre-optic incandescent lighting. The distribution of red colouration corresponds to the presence of Co glass-filled fractures, and more heavily filled stones show an overall darker red appearance. Photos © C. D. Bexfield.

Reference

Popley, A.R. 1934. A useful colour-filter to distinguish real from imitation emeralds. *The Gemmologist*, **4**(33), 57.

ERRATA

1. In the Gem Note titled 'Chrysocolla from the Ray Mine, Arizona, USA' (see *The Journal*, Vol. 36, No. 6, 2019, p. 499), *chrysocolla* should have been referred to as *chrysocolla chalcedony*.
2. In the Literature of Interest section of *The Journal*, Vol. 37, No. 2, 2020, the articles from *Rivista Italiana di Gemmologia/Italian Gemological Review* should have been indicated as being published in issue No. 9.
3. In the Gem Note titled 'Rhodonite from Southern Iran' (see *The Journal*, Vol. 37, No. 3, 2020, pp. 246–247), the correct spelling of the first author's surname is Rahimzadeh.

An innovator in gemstone reporting

• Identification of colored gemstones • Country of origin determination • Full quality and color grading analysis

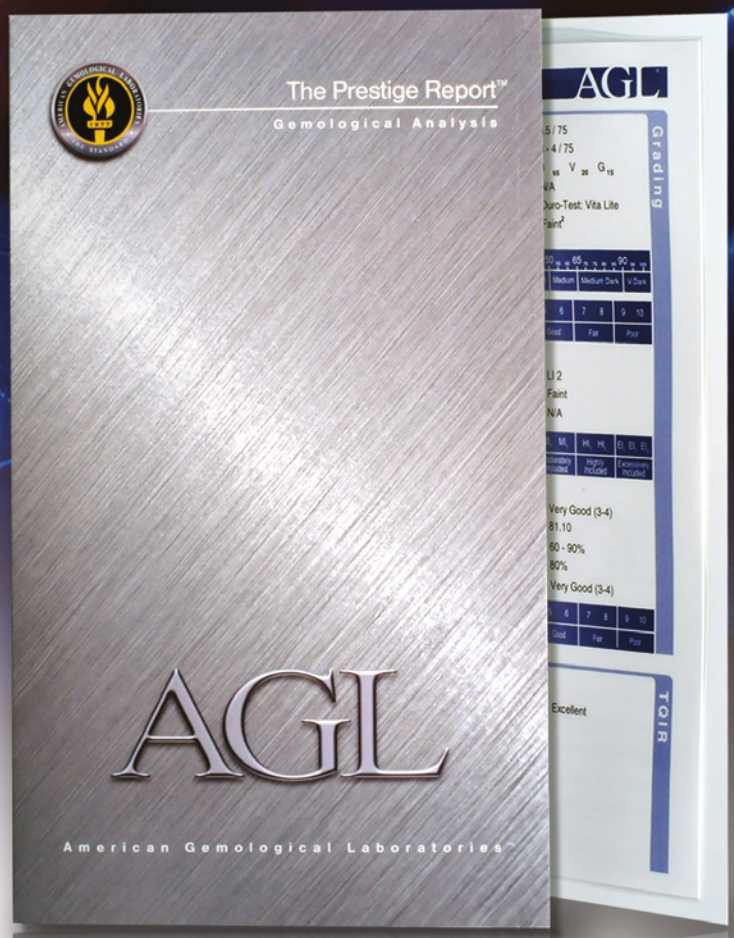

AMERICAN GEMOLOGICAL LABORATORIES AGL

580 5th Ave • Suite 706 • New York, NY 10036, USA
www.aglgemlab.com • +1 (212) 704 - 0727

Figure 1: This image of the Imperial State Crown in the British Crown Jewels shows the 'Black Prince's Ruby' (a 170 ct red spinel) and, below it, the Cullinan II diamond weighing 317.40 ct. Royal Collection Trust/© Her Majesty Queen Elizabeth II, 2016 (RCIN 3170).

The Black Prince's Ruby: Investigating the Legend

Jack M. Ogden

ABSTRACT: A 170 ct red spinel set in the Imperial State Crown in the crown jewels of the United Kingdom has long been called the 'Black Prince's Ruby' and is one of Britain's best-known gems. It has been popularly associated with Edward the Prince of Wales—the 'Black Prince'—who lived in the 1300s. This article reconsiders available evidence to substantiate the elements of its supposed early history. While the Black Prince almost certainly obtained one or more large spinels in Spain, other large spinels (generally known in the past as *balas*) reached English royal treasuries at around this same time, and no specific surviving gem can be conclusively associated with the prince. The spinel now in the crown has certainly been a part of royal regalia since the later 1600s, and probably for a century before that, but its earlier history cannot be traced. Its link with the Black Prince was suggested only in the 1760s, based on an unsubstantiated, and later disputed, identification of the gem in a portrait.

The Journal of Gemmology, **37**(4), 2020, pp. 360–373, https://doi.org/10.15506/JoG.2020.37.4.360

The 'Black Prince's Ruby', a 170 ct red spinel set in the Imperial State Crown (Blair 1998; see Figures 1 and 2), is associated with one of the best-known tales about a gemstone. It links history with a beautiful gem, and gives gemmologists the opportunity to expound on how it is actually not a ruby, but rather a red spinel. The recent history and a gemmological study of the gem published in 1998 treated its connection with Edward the Prince of Wales (also known as the Black Prince) as no more than legendary (Blair 1998, Vol. 2, p. 57). However, myriad repetitions of the story still appear in print and online, with little consideration of its veracity or source.

The story is that in 1367 Peter I—the king of Castile and León on the Iberian Peninsula (1350–1369)[1], who was sometimes known as Don Pedro, Pedro the Cruel or Pedro the Just—gave the gem to the Black Prince in return for English military support. From the Black Prince the gem supposedly passed down to King Henry V of England (1413–1422), who wore it in a crown over his helmet at the famous Battle of Agincourt in 1415. According to the legend, it eventually ended up in its present prominent place in the British Imperial State Crown.

Even some influential writers recount the story as fact. One such was George John Younghusband, Keeper of the Jewel House at the Tower of London from 1917 to 1944, who told the story in his books on the crown jewels with no caveats as to its veracity (Younghusband & Davenport 1919, pp. 55–56; Younghusband 1921, pp. 144–151). To help separate fact from fiction, this article looks at original information sources where possible. These documents generally use the term *balas* (with myriad spellings) for what we know as red spinel.

RED KING TO CRUEL KING

The first 'episode' in the usually recounted legend of the Black Prince's Ruby is its supposed transfer from Don Pedro to the Black Prince in 1367. Fourteenth-century Spain was divided between rival Christian and Nasrid Muslim kingdoms. Muhammad VI, the Muslim king of the emirate of Granada, known in Spanish as *El Rey Bermejo* ('The Red King') due to his red hair, was fighting both his second cousin Muhammad V and Don Pedro, and then he decided to side with the latter. In 1362, Muhammad VI went to meet with Don Pedro and took with him—to smooth the way—what historian José Antonio Conde described as 'the richest and most precious jewels he had, as well as emerald and balas stones' (Conde 1874, p. 298).[2] Lisan Al-Din Ibn Al-Khatib, in his *The Complete Source on the History of Granada* written in 1369, commented 'He might just as well have thrown himself into the mouth of a hungry tiger thirsting for blood; for no sooner had the infidel dog [Don Pedro] cast his eye over the countless treasures which Mohammed and the chiefs…brought with them, than he conceived the wicked design of murdering them and appropriating their riches' (Gayangos 1843, p. 361).

More details were provided by Pedro López de Ayala, a contemporary of Don Pedro, whose chronicles on the kings of Castile included a comprehensive account of Don Pedro's life.[3] López de Ayala reported that upon his arrival, Muhammad VI was seized and then 'searched separately to see if he had some jewels with him and

Figure 2: This computer rendering of the Black Prince's Ruby (which measures approximately 4.3 cm long) is based on the photographs and drawings in Blair (1998). Image © J. Ogden.

[1] The years given in parentheses after the names of monarchs are the dates of their reigns.

[2] *…las mas ricas joyas y preciosas alhajas que tenia, así en pedrería de esmeraldas y baláges…*

[3] Pedro López de Ayala lived from 1332 to 1407 and this copy of his text (MSS/10219, Biblioteca Nacional de España, Madrid, Spain) dates to within a century after his death.

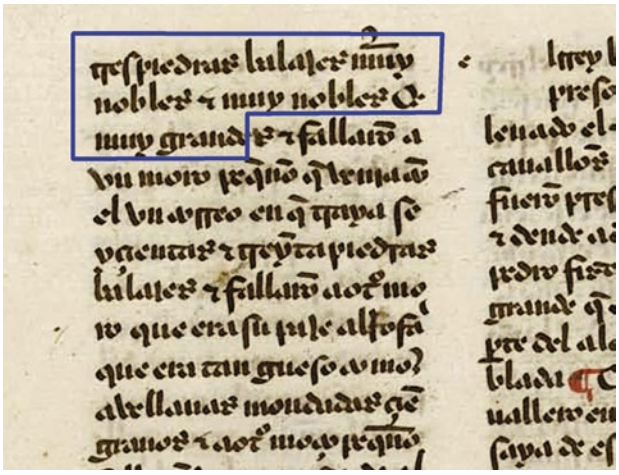

Figure 3: The top three lines on this page from *Crónica del Rey Don Pedro* by Pedro López de Ayala, held in the Biblioteca Nacional de España (MSS/10219, f. 166v), says *tres piedras balaxes muy nobles – muy nobles e muy grandes* ('three balas stones very noble – very noble and very large'). © Biblioteca Nacional de España.

they found on him three balas, very noble and very large…each as big as a pigeon's egg…' (Llaguno Amirola 1779, p. 346, 346 n.).[4] The vast number of other gems with his companions included a collection of 730 balas in the baggage of one pageboy (Llaguno Amirola 1779, pp. 346–347, 346 n.). A portion of the relevant passage in a manuscript of López de Ayala's chronicle is shown in Figure 3. Muhammad VI was soon killed and the treasures appropriated. Barely had the blood dried than Pedro wrote a will which listed numerous jewels set with balas, including two collars (neck ornaments), each with a 'very large balas' (*un balax muy grande*), specifically noted as coming from Muhammad VI. These two collars were bequeathed to Don Pedro's eldest daughters Beatrice and Constanza, who also were each to receive a second collar with 'a large balas stone' (*una piedra balax grande*), and thus presumably smaller than those from Muhammad VI (Llaguno Amirola 1779, pp. 562, 563–564).

THE BLACK PRINCE

King Edward III of England (1327–1377) supported Don Pedro by sending an army to Spain in 1366 with his eldest son, Edward Prince of Wales, popularly known as the 'Black Prince', reputedly because of his black armour.[5] In 1845, Richard Ford published his monumental *A Hand-Book for Travellers in Spain*, in which he briefly mentioned the Black Prince. He also described the assassination of Muhammad VI and the seizure of his treasures including 'a huge ruby' which 'Don Pedro gave to the Black Prince after the Victory at Navarete' (Ford 1845, p. 258). The Battle of Navarrete (more correctly the Battle of Nájera) took place on 3 April 1367 near Nájera in La Rioja, northern Spain (Figure 4). In his second edition, Ford gave more detail: among the gems was specified '"three huge rubies," big as a pigeon's egg — *huevo de Paloma*' (Ford 1855, p. 186). The specific words used and the quote in Spanish show that Ford had based this information from López de Ayala's chronicle. It is unclear, however, where the story in both these additions came from, that one particularly large ruby had been given to the Black Prince after the Battle of Navarrete and that this was the gem now in the Imperial State Crown (Ford 1845, p. 258). Ford also mentioned another contemporary account of Muhammad VI's assassination and seizure of his riches that 'Gayangos found, in an Arabic MS. [manuscript] in the British Museum' (Ford 1845, p. 258). This was Pascual Gayangos's translation of Algerian historian al-Maqqari's history of Muslim Spain, written in around 1600, based on a text in the British Museum (Gayangos 1840 & 1843). This text mentioned the bare facts of the assassination and seizure, but it said nothing about any ruby/balas or the Black Prince.

Prosper Mérimée, a French historian and author, wrote a description of Don Pedro's life, largely based on López de Ayala's account but also drawing on a wider range of other chronicles, including many unpublished ones (Mérimée 1848). In 1849 James Pearse translated Mérimée's work into English and added a footnote in which he mistakenly assumed that Ford had said that the Arab manuscript translated by Gayangos specifically mentioned Don Pedro giving the large 'ruby' to the Black Prince (Mérimée 1849, p. 76 n.). Pearse also mentioned the pigeon's-egg size of the gems, but derived this from Sir John Talbot Dillon's history of Don Pedro where 'balas' was mistranslated as 'pearls' (Dillon 1788, p. 190).

The present author has found no certain indication that one of the Red King's balas was given to the Black Prince by Don Pedro, but we do hear of another that, supposedly, was. Bertrand du Guesclin (also known as 'The Black Dog of Brocéliande') was a French military commander who fought against Don Pedro and the Black

[4] *E luego que el Rey Bermejo fué preso , fué catado á parte si tenia algunas joyas consigo , é falláronle tres piedras balaxes muy nobles é muy grandes…tan grande cada una como un huevo de paloma…*

[5] Other explanations have been given. John Hughes (1706, p. 215 n.) says 'he was call'd the *Black Prince*, not from his Colour, but Fierceness in Battel'.

Figure 4: In this painting of the Battle of Nájera (or Battle of Navarrete) on 3 April 1367, the Black Prince is heading the troops on the left, in a brightly coloured tunic, clasping the hand of Don Pedro to show their allegiance. Image courtesy of Wikimedia Commons, from a 15th century manuscript of Jean Froissart's *Chronicles*, Bibliothèque nationale de France, FR 2643, f. 312v.

Prince, and was captured at the Battle of Navarrete. He indicated that Don Pedro's most valuable treasure had been a large, gem-encrusted gold-and-silver table of amazing beauty and inestimable value that took four men to carry (Le Febvre 1692, pp. 153–154, 163). Don Pedro's great-grandfather (presumably Alfonso X) had received it in payment of ransom for a king of Granada. In its centre was *une grosse escarboucle* (a big carbuncle, i.e. red stone) that was described as having two remarkable properties: it shone at night with as much brightness as the sun in broad daylight and it turned black when near poison (Le Febvre 1692, p. 154). According to du Guesclin, Don Pedro presented this extraordinary table to the Black Prince to help enlist his support (Le Febvre 1692, pp. 165, 180).

Du Guesclin's description of the table, while perhaps not entirely reliable, at least supports the existence of a particularly noteworthy red gem, and that it may have ended up in the Black Prince's hands. The Black Prince's will included '…our large table of gold and silver full of precious relics, and in the middle a cross of the wood of the Holy Cross, and the said table garnished with gems and pearls, that is, twenty-five balas, thirty-four sapphires, fifty large pearls and many other sapphires, emeralds and small pearls…' (Nichols 1780, p. 71).[6] This table was bequeathed to a college at Ashridge in Buckinghamshire, England. There is nothing in the will to say that it came from Don Pedro, but Francis Godwin mentioned that 'a wonderful sumptuous and costly table decked with gold and precious stones' had been given by Don Pedro to the Black Prince (Godwin 1601, p. 218). This one, however, was sold by him to Thomas Arundel, Bishop of Ely and later Archbishop of Canterbury (1353–1414) for 300 marks (Godwin 1601, p. 275). The table was to stay in Ely in perpetuity, but it disappeared, 'devoured', in Joshua Barnes' words, by 'time, or avarice, or sacrilege' (Barnes 1688, p. 683). If there had been a central huge spinel in the table, perhaps the Black Prince had extracted it.

[6] *…notre grand table d'or & d'argent tout pleyn dez precieuses reliques, et en mylieu un croiz de ligno sancte crucis, et la dite table est garniz de pierres et de perles cest assavoir vingt cynk balois, trentquartre safirs, cinquant perles grosses et pluso's outres safirs, emeraudes, et perles petitz…*

BACK IN ENGLAND

The Black Prince returned to England in 1371. Then, in 1377, what were called the 'Jewels of Spain' were pledged by his father Edward III to raise money (Stratford 2012, p. 13). The Jewels of Spain were gold and gem-encrusted royal military accoutrements consisting of a crown, a helmet (*palet*), a sword with belt and a saddle with stirrups. They were perhaps brought to England by the Black Prince, but there is no confirmation of this, and they may also have reached England through the marriage of Constanza, daughter of Don Pedro, to John of Gaunt, the Black Prince's brother, in 1371. The first object listed in a valuation of this treasure, in handwriting of the period, was a 'Spanish Crown' set with numerous gems including a large balas weighing 181 ct (Palgrave 1836, Vol. 3, pp. 309–312).

It should be noted that several large balas were already in royal hands in England by this time, including at least one coming from Spain. A manuscript in the possession of the Society of Antiquaries, London, includes a list drawn up in the period 1299–1300 of the jewellery and other treasures owned by Edward I (1272–1307). This list includes a large gold crown with balas once owned by 'Blanche of Spain' (Topham 1787, p. 353); it is one of the earliest uses of the term *balas* (here spelled *baleis*) in an English document. It refers to Blanche of Castile (1188–1252), wife of Louis VIII of France and niece to King John of England. In addition, an inventory from 1303 listed what might be a different gold crown with several large balas, which Edward I had used at his coronation, and another royal inventory from 1324 included *Un baleise bele et grosse* (a balas beautiful and large) among the unset gems (Palgrave 1836, Vol. 3, p. 137; Cole 1844, p. 277). A treasury inventory from the time of Edward II (1307–1327) mentioned several balas, two of which sound important—one forming the pommel of a gold cup and another described as 'beautiful' (Palgrave 1836, Vol. 3, pp. 124, 137). There is another very large balas which might have reached England at around this time: via Don Pedro's daughter Constanza, wife of John of Gaunt, to whom he had bequeathed a collar set with a very large balas.[7] One might doubt whether Don Pedro had managed to keep much of his treasure intact to pass on to his daughters, but when he was assassinated by his brother in 1369, his chambers were found to contain a huge quantity of gems, jewellery and other treasures (Llaguno Amirola 1779, p. 557). Whether any of this actually reached his intended beneficiaries is unknown.

The 181 ct balas in the crown from the Jewels of Spain was valued at 5 marks per carat. (This is seemingly the earliest recorded use of 'carat' for a gem weight in England.) The *mark* (the gold Noble coin) was two-thirds of an English pound in value, making the gem worth £603.33, the value of about 7 kg of gold.[8] This indeed might have been the Black Prince's Ruby, as several have suggested over the years (see Stratford 2012, p. 3). The weight of the medieval carat in modern terms is not known exactly, but 181 ct for the balas in the Spanish Crown would be in the same order of magnitude as 170 ct reported for the Black Prince's Ruby when it was examined out of its setting in the 1980s (Blair 1998, Vol. 2, p. 55).[9]

The Spanish Crown pledged by Edward III in 1377 was redeemed in 1378 (Stratford 2012, p. 12), by which time both Edward III and the Black Prince were dead and the latter's son, Richard II, was on the English throne. In 1399 Richard II was deposed, and around this time a detailed list of his treasures was written on a parchment roll that is 28 m long. This extraordinary record was only rediscovered in the National Archives in Kew in the 1990s (Stratford 2012). The 1,206 entries in this list include all the Jewels of Spain, named as such, apart from the crown. The *ca.* 1377 valuation of the Jewels of Spain had noted that six large balas and 40 small pearls from the Spanish Crown had been (or were intended to be) redeployed in a 'Grand Crown', so perhaps it was broken up (Palgrave 1836, Vol. 3, pp. 309–310). This would not be surprising, as English royalty would hardly wish to wear a Spanish crown. There were 11 crowns listed in Richard II's extensive inventory containing some three hundred balas in total (Stratford 2012, pp. 145–147). The seventh on the list is the crown of Blanche of Lancaster recently discussed in this journal (Schmetzer & Gilg 2020). Many of the balas in these crowns are described as large (*grosses balays*), but none is noted as being particularly huge and the sheer number of them suggests that they were

[7] One of the gems specified in John of Gaunt's own will was 'the good ruby' (*le bonne rubie*; Nichols 1780, p. 155).

[8] This can be calculated because the gold Noble coin of Richard II weighed about 7.6 g.

[9] The medieval carat has been equated to 1/150 of a troy ounce, or 0.207 g in modern terms, but exact comparisons are impossible. Collins (1955, pp. 12–13 n.) rightly observed that this recording of the weight of a gem is unique for its period and must show that the stone was considered truly exceptional.

of relatively modest size. The Grand Crown (*une grand coronne*), number nine in the inventory, was valued at £33,584, an extraordinarily high price for the time (Stratford 2012, p. 263). The gems made up all but £250 of this value and must have been something special, but they are described in far briefer terms than those in the other crown. The only gems in it described as large are two rubies (*ii grosses rubies*), while the other gems are listed in the most cursory of terms—balas, sapphires, emeralds and Scottish pearls (*balays, saphirz, emeraudes et perles d'Escoce*; Stratford 2012, p. 147). It would seem that even if some of the gems in the Spanish Crown had been used to spruce up the Grand Crown, these did not include the 181 ct balas.

HENRY V AND THE BATTLE OF AGINCOURT

The next episode in the usually recounted story of the Black Prince's Ruby its association with King Henry V (1413–1422). Henry V was a skilful military leader and at the Battle of Agincourt in 1415 he defeated the French. The king fought in the thick of it and, so the legend goes, the Black Prince's Ruby was set in a gold crown over the king's helmet and it survived when the crown was hacked from his helmet. As George John Younghusband said, with patriotic zeal but no reservations, 'Thus went forth Henry V on the morn of Agincourt, and glittering on the front of his coroneted helmet was the great ruby' (Younghusband 1921, pp. 146–147).

An early account of the Battle of Agincourt from Thomas Elmham, in his *Life of Henry V*, was written about three years after the battle. He said, 'The crown of the king was broken off his helmet by an axe' (Curry 2000, p. 47).[10] Two teenage heralds present at the battle—Jean Le Fèvre on the English side and Jehan de Waurin on the French side—later wrote almost identical accounts of the battle. The relationship between their accounts, and to an earlier one, is unclear. Although each of their versions differs slightly, both say that a group of 18 French knights had sworn to knock the crown off the King's head or die in the attempt. And, in Le Fèvre's words, 'one of them with an axe in his hand struck on the king's basinet [a helmet with visor] such a heavy blow that it knocked off one of the fleurons of his crown' (Morand 1876, p. 250; Curry 2000, p. 157).[11] All these knights were killed. A slightly later chronicle from around 1340 adds that at the battle '1 pece [piece] of his croune was broken, which afterward was founden and broughte to hym' (British Library Harley MS 53; Brie 1908, p. 555). Some accounts of the battle refer to the crown on Henry V's helmet as having gems, and from the reign of his son, Henry VI (1422–1461), there is a 1423 valuation that includes 'the golden crown for the basinet' (*la Corone d'or pur les Basinet*; Strachey & Blyke 1767–1777, p. 215). This is described as set with numerous gems and pearls with four of the balas valued at £133 6s 8d (£133.33). This may have been the one Henry V wore at Agincourt. Martin Holmes has suggested that the relatively high price listed for the four balas on this crown was 'evidence that one at least of them must have been of particular size and value' (Holmes 1937, p. 80). (Nevertheless, the single large balas in the Spanish Crown had been valued much higher, at just over £600.) Of course, kings had more than one crown; as we have seen, the long inventory of Richard II's treasure mentioned above listed 11 of them. An anonymous *ca*. 1417 account of the Battle of Agincourt—the *Gesta Henrici Quinti*, the earliest we have—notes that when it started, 'the negligence of the royal servants' allowed the French to plunder 'the kings' valuable treasure, his sword and crown…' (Curry 2000, p. 35).[12] The author here, a chaplain, who should know, said 'I, who am now writing this and was then sitting on a horse among the baggage at the rear of the battle' (Curry 2000, p. 35). Other sources say much the same thing. For example, a chronicle from Ruisseauville Abbey, near the site of the battle, probably dating to within 15 years of the battle, said that Henry V wore a gold crown on his helmet in the battle and that 'two crowns of gold and of precious stones' (*deux courons d'or et de pierres pretieuses*; Anonymous 1834, p. 141) were stolen from his baggage.

There might be no specific mention of a particularly large balas in connection with Henry V and the Battle of Agincourt, but there is a record of 'a large fleur-de-lys, garnished with one great balays, and one other balays, one ruby, three great sapphires, and ten great pearls';

[10] For the original Latin text of Elmham's account, see Cole (1858). All the sources quoted in this paragraph, and more, are discussed in detail in Curry (2000).

[11] *…l'un d'eux, d'une hache qu'il tenoit, le féry sur son bachinet ung si grant cop qu'il luy abaty l'un des flourones de sa couronne…*

[12] For the original Latin text of the *Gesta Henrici Quinti*, see Taylor and Roskell (1975). The stolen sword supposedly belonged to King Arthur.

this was one of the crown segments pledged to provide the money to pay Henry V's brother (the Duke of Clarence) and his retinue during the French campaign (Nicolas 1832, appendices on p. 15; Stratford 2013). This pledge was made on 12 July 1415, which was three months before Agincourt, so it cannot have been the one chopped off the crown during the battle (British Library MS Add. 4600). It was redeemed in 1429–1430 during the reign of Henry VI (Nicolas 1832, appendices on p. 15; Palgrave 1836, Vol. 2, p. 131). It was also listed with another smaller segment from the same crown in an undated inventory of the time of Henry VI (Palgrave 1836, Vol. 2, p. 245). Pledging the crown in several segments does not imply that it had been broken; it was more likely disassembled. Crowns of the period were often composed of several sections hinged together, such as the famous crown of Blanche of Lancaster (Schmetzer & Gilg 2020).

A MULTIPLICITY OF LARGE SPINELS

The great balas in Henry V's pawned crown segment might have been brought back from Spain by the Black Prince, and it may even be the one that is now in the Imperial State Crown, but as we have seen already there were several large balas present in late medieval England. Two are particularly relevant here. Biagio Dolfin was a Venetian merchant in the early 1400s trading gems between Venice, Alexandria and London. Two letters relating to his trade, discovered by Maria Pia Pedani in the State Archives in Venice, concern two large spinels offered for sale via his brother-in-law and another Venetian merchant in London (Pedani 2002). The first letter from Venice, dated 2 April 1413, revealed that a large balas was being offered to a London customer of whom Dolfin notes, 'I think he is a person who has the mint there [in London]' (Pedani 2002, p. 6). Presumably this was someone close to royalty, if not buying on behalf of them. The weight was not recorded, but based on its selling price of 1,200 ducats, Pedani suggested that it likely weighed between about 150 and 225 ct.

Even more pertinent is the letter from Dolfin at the beginning of the following year, 1414, concerning another large balas, this time offered directly to Henry V. The letter stresses that the king was particularly keen to buy this gem because he wanted two large balas for a new crown to wear for his upcoming marriage to Catherine, the French king's daughter. There was haggling—opening at £240 asked, with £120 offered—but sadly we have no record of whether a deal was eventually made. Here Pedani calculated the likely weight to be between about 138 and 207 ct (Pedani 2002, p. 6). Henry V's wedding was postponed because the war with France—and thus with his betrothed's father—intervened. The second Dolfin letter indicates that Henry V already had one large balas, but was this the one that had been in English royal hands for some time, perhaps from the Spanish Crown, or the one Dolfin had sold the year before? In either case, both Dolfin letters predate the pawning of the crown segment with its 'great balays'.

The quantity of spinels in Europe around that period should not be underestimated. The 1423 inventory mentioned above also included a collar, the parts set with numerous gems, the clasp set with 'the largest cut balas' (*la pluis 'gros Baleis d'entaille*; Strachey & Blyke 1767–1777, p. 214). The combined value of the large balas and four large pearls in the clasp was £800, thus comparable to the balas in the Spanish Crown, but the balas was described as cut, which would seemingly rule out the gem we know as the Black Prince's Ruby. An inventory of Edward VI dated 1446 lists 'the Rich Crown of King Edward' that was garnished with four large balas, four balas 'of a lesse sorte' and 38 balas 'of dyvers sorte' (Palgrave 1836, Vol. 3, pp. 2–3). In 1503, when Henry VII's daughter Margaret married James IV of Scotland (1488–1513), the Scottish Herald John Young accompanied her from London to Edinburgh.[13] In his account of the wedding, he described the king as wearing a 'Bonnet Blak, with a ryche Balay', but no further details are given for this gem (Leland 1774, p. 293).

Meanwhile in France, in 1417 Bartholomew Sac loaned the French Crown 23,000 *livre tournois*, taking as security several balas. These included a pear-shaped gem weighing 175 ct, a pierced one of 142 ct, another of 102 ct and a further one called *tête de coq* ('the rooster head') which weighed 174 ct and was also described as being pierced (Mirot 1940, p. 139). Also in 1408 the Duc de Berry purchased the *balai d'Orange*, and the duchess of Orléans the *balay de Venise* (Coville 1888, p. 47; Guiffrey 1894, p. XCIII; Mirot 1940, p. 147). In other medieval inventories we hear of more, such as the *balai de la châtaigne*, the *balai du pape* and the *balai de David* (Guiffrey 1894, p. XCIII). This naming of large spinels continued. Jean Baptiste Tavernier later illustrated three large balas owned by King Louis XIV in

[13] England and Scotland had different monarchs then. The union came with James VI of Scotland, who became James I of Britain in 1603.

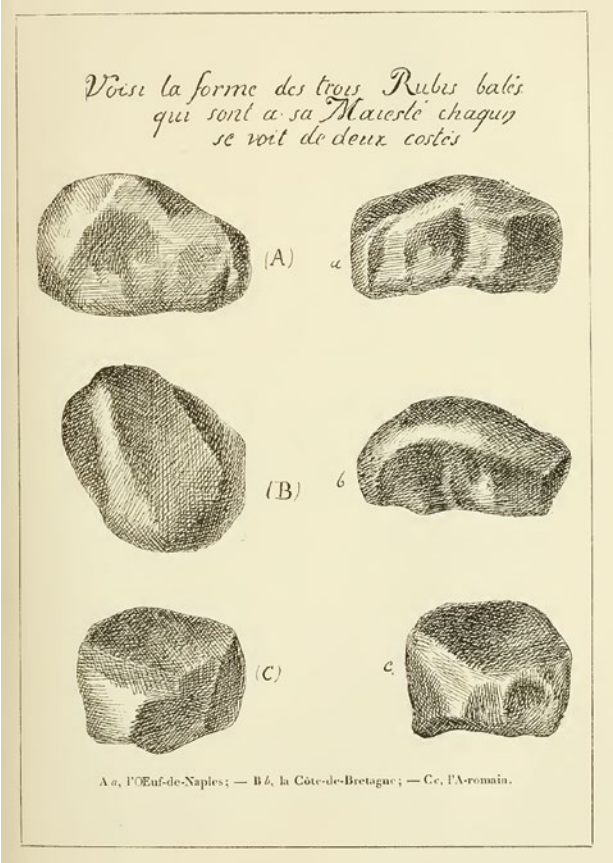

Figure 5: This drawing by Jean Baptiste Tavernier shows three large balas of King Louis XIV, annotated by Germain Bapst to give their names: *l'OEuf-de-Naples, la Côte-de-Bretagne* and *l'A-romain*. From Bapst (1889, p. 249).

the 17th century: *l'OEuf-de-Naples, la Côte-de-Bretagne* and *l'A-romain* (Figure 5; Tavernier 1677, pl. 2 facing p. 338; Bapst 1889, pp. 247–272). If the English had named their royal spinels, unravelling the story of the Black Prince's Ruby might have been a far easier task.

FIRMER GROUND IN THE 1500S

There are two surviving manuscripts of the so-called Jewel Book of Henry VIII (1509–1547), one written in 1521 and the other undated but perhaps a few years later (Palgrave 1836, Vol. 2, pp. 259–298; Trollope 1884).[14] These list the royal jewels and silver in the Tower of London at that time. They are largely identical, although there are spelling differences. Both start with 'the kingis crowne of golde' and among the large number of gems on this was 'a greate balance broken' or 'a greate balace brooken' (Palgrave 1836, Vol. 2, p. 259; Trollope 1884, p. 158). The description of the balas in Henry VIII's crown as 'broken/brooken' is a possible hint that we might now be looking at the Black Prince's Ruby. This gem has been fixed in a backed setting for much of its recent history, but it was removed for study in 1965 and 1986 (Blair 1998, Vol. 2, p. 61). The report of the 1986 examination said: 'The back is crudely cut away, as if a section of the stone had been sheered [*sic*] off by accident' (Blair 1998, Vol. 2, p. 55).

Possibly this balas in Henry VIII's crown had passed down from earlier kings, perhaps even from the Black Prince, but this is by no means certain. At least one other important balas had arrived in England early in Henry's reign, and from Spain. In 1515, an ambassador from King Ferdinand of Aragon had presented Henry VIII's wife Catherine of Aragon with a balas 'large and very precious' (*un balax grande muy rico*; Zurita y Castro 1610, f. 397 v). Catherine's mother, Queen Isabella I of Castile, had owned a considerable amount of impressive jewellery including 'two balas, the size of a pigeon's egg' (*deus ballais dela granfeur de ung heuf de colon*) and 'a large balas the size of a tennis ball' (*ung grant ballais del grandeur d'ung esteus [esteuf]*).[15] Perhaps the gem brought to England was one of these. It might also be relevant that Isabella was the great-granddaughter of Constance, the daughter of Don Pedro to whom he had bequeathed one of the large balas he had taken from Muhammad VI.

Descriptions of the Great Crown during the reign of Queen Elizabeth I (1588–1603) describe it in almost identical terms to those in Henry VIII's inventory, but whereas the latter says the great balas was broken, three inventories of Elizabeth's say, with typical variations in spelling, that it was 'whole', 'hole' or 'hoole' (Figure 6; British Library Harley NS 1650; British Library Stowe MS

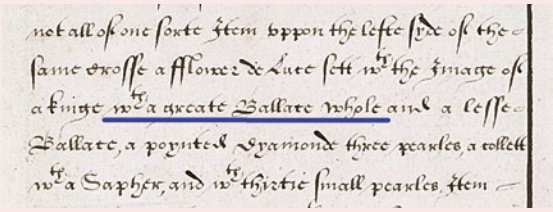

Figure 6: The description of the 'Greate Crown' in the 1596 inventory of jewels and other goods of Queen Elizabeth I says 'with a greate Ballace whole'. © British Library Board, Stowe MS 556.

[14] In the 1521 inventory, the few gems missing from the crown are named and described as 'with the king'; the other inventory just mentions the empty settings. This may suggest that this latter inventory was compiled later when the then-current whereabouts of the gems was unknown.

[15] The details of Queen Isabella's spinels can be found in Roger Machado's 1488–1489 report of the embassy to Spain and Portugal (Gairdner 1858, pp. 171, 178).

555; British Library Stowe MS 556; Collins 1955).[16] This may suggest that the damaged balas had been replaced with a whole one that was not broken.

It is just as possible, however, that 'broken/brooken' in the Henry VIII inventories really meant 'broached', that is pierced, as suggested by Shakespeare's use of *broken* for 'broached' in, aptly, his *Henry VIII* (Act 5, Scene 1). The Black Prince's Ruby is pierced, with several drill holes probably dating back to its far earlier history. It is unlikely that 'whole', 'hole' and 'hoole' in the Elizabethan inventories meant the great balas then in the crown had a hole through it.

Almost a year to the day after Elizabeth I died, an inventory was drawn up of the 'Jewelles remayninge in an yron cheste in the secrete jewelhouse wth in the Tower of London', and first on the list was 'a Crowne Imperyall' with 'uppon the top a verye greate ballace perced' (Palgrave 1836, Vol. 2, pp. 299–300). In the so-called Ditchley portrait of Elizabeth painted by Marcus Gheeraerts the Younger *ca.* 1592 (Figure 7), she wore a large red gem surmounting her elaborate headdress that appears to have a pin passing through it. Scottish diplomat Sir James Melville mentioned the 'fair ruby, gret lyk a racket [tennis] ball' (presumably a balas) that Elizabeth showed him in 1564 (Melville 1827, p. 122). Although Melville makes no mention of either a break or a piercing, it is noteworthy that he uses the same size comparison as had been applied to one of Queen Isabella I of Castile's gems, not impossibly the one that had been sent to Catherine, wife of Henry VIII. The Black Prince's Ruby in the Imperial State Crown today is 4.3 cm high, its largest dimension (Blair 1998, Vol. 2, p. 55).

Figure 7: A detail of a portrait of Queen Elizabeth I shows a large red gem, probably a spinel, surmounting her head. Portrait by Marcus Gheeraerts the Younger, *ca.* 1592. National Portrait Gallery, London, inv. no. NPG 2561.

[16] Two of the British Library manuscripts can be viewed online: www.bl.uk/manuscripts/FullDisplay.aspx?ref=Stowe_MS_555 and www.bl.uk/manuscripts/FullDisplay.aspx?ref=Stowe_MS_556.

By comparison, a tennis ball discovered in the rafters of Westminster Hall in the 1920s, dated to the late 15th to very early 16th century and now in the Museum of London (A23402), is 4 cm in diameter (see https://collections.museumoflondon.org.uk/online/object/119138.html).

POSSIBLE LOSS AND RETRIEVAL

Even if the balas in Henry VIII's crown and that in Elizabeth I's was one and the same, it cannot be traced down to today's Imperial State Crown with complete certainty. In 1649, Oliver Cromwell interrupted the monarchy. Charles I was executed that same year, and much of the royal regalia were broken up and sold. The often-repeated story is that the Black Prince's Ruby was sold under Cromwell for just £4, but this is almost certainly incorrect (Brand 1806, p. 286; Holmes 1937, p. 84; Collins 1955, p. 12 n.; Blair 1998, Vol. 2, pp. 58–59). No clear record exists of the large balas being sold in Cromwell's time, and it might have been fortuitously 'saved' by being among the crown jewels pawned by Henrietta Maria (Charles I's wife) in the early 1640s to help fund the fight against the Parliamentarians, although it proved difficult to sell some of the more valuable pieces (White 2017, pp. 62–63).

With the restoration of the monarchy and the arrival of Charles II (1660–1685) on the throne in 1661, two new crowns were made for his coronation. Of these, the Crown of State was 'most remarkable for a Wonderful large Ruby, set in the midle of one of the four Crosses, esteemed worth Ten Thousand Pounds' (Sandford 1687, p. 41). Although he was writing about the coronation of James II, who was Charles II's brother and successor, Sandford makes it clear that the Crown of State illustrated in his book (Figure 8) was made for 'the Coronation of His late Majesty King Charles the Second'. The large red gem might have been among the crown jewels earlier pawned and later redeemed, or it could have been the 'large Orientall ruby' sold to Charles II for his coronation (Blair 1998, Vol. 2, p. 58). In either case, its identification with the Black Prince's Ruby in today's Imperial State Crown is clear, as proven by a painting of the Crown of State as remade for George I (1714–1727), the first certain colour illustration of the gem (Figure 9). The only question comes from the text below the painting, which says that 'the Balass in the cross in front was ~~put~~ given to the Crown by King James II'. James was Charles II's successor. This might have come from a misunderstanding of Sandford's 1687 account, or it may reflect some now-forgotten part of the gem's history.

It seems reasonable, if not certain, to equate the large gem in Charles II's crown with Queen Elizabeth I's 'racket ball' and perhaps Henry VIII's 'broken balas', but what prompted the story that it could be traced back a further 200 years to the Black Prince's campaign in Spain?

Figure 8: A drawing of the Crown of State used at the coronation of Charles II in 1661 shows 'a Wonderful large Ruby, set in the midle of one of the four Crosses' (Sandford 1687, p. 41). Used with permission of the New York Public Library, Digital Collections.

THE BIRTH OF THE LEGEND

It was only during Elizabeth I's reign, in 1569, that Richard Grafton provided us with the first recorded use of the name 'Black Prince', whom he described as 'a noble and famous man' and says was reckoned 'the Flower of all Chyualrye [chivalry] throughout all the worlde' (Grafton 1809, p. 332). In the succeeding century, the Black Prince obtained almost mythical status. A play titled *The Black Prince*, by Irish statesman and dramatist Roger Boyle the Earl of Orrery, premiered in 1667 and extolled this hero's virtues: 'An English prince, whose fame appear'd so bright, as never any since his time was known' (Boyle 1669, p. 62). If there was any written or oral tradition then that a spectacular gem in the royal crown had belonged to the Black Prince, surely it would have been mentioned somewhere in the many books of the period that praised him.

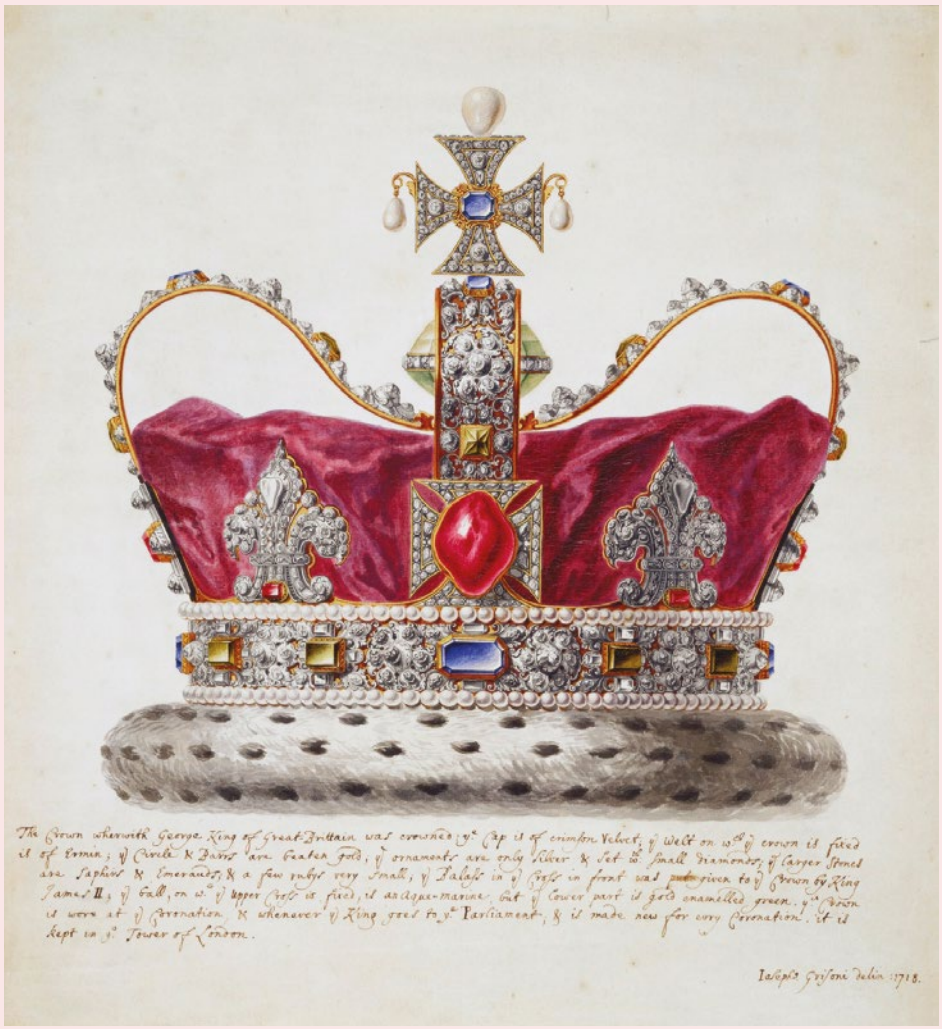

Figure 9: A watercolour of King George I's Crown of State, with a description by John Talman written below, is signed and dated on the lower right with 'Iosephs Grisoni delin: 1718.' The red gem is the same size and shape as the Black Prince's Ruby (spinel) now in the Imperial State Crown. Royal Collection Trust/© Her Majesty Queen Elizabeth II, 2016 (RCIN 913015).

The first suggestion of a link between the large spinel in the Imperial State Crown and the Black Prince only came a century after Charles II's coronation. British politician Horace Walpole was an eminent art historian with a keen interest in engraved gems and jewels. In 1765 he described a painted portrait with a hand-written note on the back saying that it depicted the Black Prince (Walpole 1765, p. 26). This note was written by the English politician Arthur Onslow (1691–1768), who had obtained the painting from Betchworth Castle in Surrey (Grose & Astle 1775, p. 169).[17] In 1775, *The Antiquarian Repertory* printed an engraving of this portrait (Figure 10), but the present author has been unable to trace the original painting. No further documentation was cited to substantiate the identification of the man as the Black Prince, but Walpole considered 'there is great reason to believe [it] was painted at the time' seemingly because 'It represents him in black armour…with a golden lion on his breast', and 'He has a hat with a white feather, and a large ruby, exactly in the shape of the rough ruby still in the crown' (Walpole 1765, p. 26 n.).

But this identification as the Black Prince was soon doubted. In 1786 Richard Gough pointed out that 'the lion rampant, as here [on his tunic], is neither the Black Prince's coat [of arms] nor crest', and also that he was not actually shown wearing armour (Gough 1786, p. cxliii). A generation later, the antiquary James Dallaway said 'The claim of this, as a genuine portrait of the Black Prince, is at least apocryphal. I cannot but consider it as of a much later age…' (Dallaway 1826, p. 45 n.).

Unfortunately, there is no way to uncover the basis for Onslow's identification. Later authorities have been equally sceptical of the portrait's dating on various

[17] Betchworth Castle was destroyed in the 1830s by none other than Henry Thomas Hope, who inherited the Hope diamond from his uncle Henry Phillip Hope.

stylistic grounds. In addition, identification of the man depicted is hindered by the lack of any surviving certain portraits of the Black Prince to use for comparison (see, e.g., Blair 1998, Vol. 2, p. 57). Also note that the gem shown in the portrait is hardly what Walpole described as 'exactly in the shape' of the Black Prince's Ruby, since it lacks its characteristic pear-shaped form. However, its generic oval shape does look very much like the stone in Sandford's drawing of the Crown of State (Figure 8), which was probably the only representation Walpole had seen. Nevertheless, Walpole seems to be the first to have suggested a possible link between the gem in the Imperial State Crown and the Black Prince. Not surprisingly, this appealing possibility was soon quoted widely. In the 18th and 19th centuries, the increasing nationalism in Britain coupled with idealised views about medieval chivalry had again made the Black Prince a hugely appealing hero (Gribling 2017).

We can note that the rampant lion on the tunic in the portrait might be more expected for a Scottish prince. So, ironically, the gem shown could still be that now in the Imperial State Crown if it was the one that James IV of Scotland had worn in his bonnet at his wedding (see above) and which, perhaps, had passed down to his great-grandson James I of Britain.

Figure 10: This etching shows a painting once in Betchworth Castle, which Horace Walpole suggested represented the Black Prince wearing the gem. From *The Antiquarian Repertory* (Grose & Astle 1775, p. 169).

CONCLUSIONS

It is possible that the Black Prince obtained a large spinel while he was in Spain and then brought it to England in the 14th century, which long after was set in the Imperial State Crown in the crown jewels of the United Kingdom. However, there was more than one large spinel in royal circles in England in the late medieval period which might have passed down to the present crown jewels. There is no evidence that the English King Henry V wore a large spinel in the crown above his helmet at the Battle of Agincourt in 1415, as often stated. So, although we can trace the Black Prince's Ruby back to the 1600s with some certainty and agree that it likely was set in royal crowns in the 1500s, its association with the Black Prince is far more speculative. Historically, there is the likelihood that the Black Prince returned from his Spanish campaign with at least one large red spinel, and whether or not the painting described by Horace Walpole in 1765 actually shows the prince or if he is wearing such a gem is irrelevant. To suggest, however, that one of his gems is the one now in the Imperial State Crown, as Walpole did, is still no more than appealing speculation.

A surprisingly high number of large red spinels circulated in late medieval European royal circles. Most of these would have had a polished form similar to that of the Black Prince's Ruby, with their origin in the medieval Islamic world. Nevertheless, the weight of the large balas in the Spanish Crown (181 ct) described in an English inventory in 1371 is close enough to make it a particularly strong contender, and perhaps further research and discoveries will allow us to link this gem more certainly with the Black Prince. This is not an impossibility; the 28-m-long treasure inventory of Richard II was only rediscovered in the 1990s. It would be exciting to be able to establish a firm historical link back from the Imperial State Crown to the Black Prince, perhaps even to the *grosse escarboucle* (big carbuncle) that supposedly shone as bright as the sun and was literally once worth a Spanish king's ransom.

An unresolved issue is what happened to the numerous spinels of significant size that once circulated in medieval Europe. A possible answer is that some of them went back to the East. By the 17th century they were in high demand among the Mughal Indian rulers, and there is plenty of documentary evidence that this demand was profitably catered to by the East India Company and other European trading companies, which brought them from Europe (Ogden 2019, p. 542). Some of the magnificent Mughal spinels now in Western collections therefore could have made the East-to-West journey not once, but twice.

REFERENCES

Anonymous 1834. Chronique de Ruisseauville. *Archives Historiques et Littéraires du Nord de la France et du Midi de la Belgique*, Ser. 1, **4**, 136–144.

Bapst, G. 1889. *Histoire des Joyaux de la Couronne de France d'après des Documents Inédits*. Librairie Hachette, Paris, France, 695 pp.

Barnes, J. 1688. *The History of that Most Victorious Monarch, Edward III[d]. King of England and France, and Lord of Ireland (…)*. John Hayes, Cambridge, 911 pp.

Blair, C. (ed) 1998. *The Crown Jewels: The History of the Coronation Regalia in the Jewel House of the Tower of London*, Vols. 1 and 2. Stationery Office Books, London, 811 pp. and 629 pp.

Boyle, R. 1669. *Two New Tragedies: The Black Prince and Tryphon*. H. Herringman, London, 127 pp. (*Note*: Some of the page numbers are misprinted; the reference for the quote gives the number shown on the page.)

Brand, J. 1806. An inventory and appraisement of the plate in the Lower Jewel House of the Tower, Anno 1649. Communicated by the Rev. John Brand, secretary, from the original MS. in his possession. *Archaeologia*, **15**, 271–290, https://doi.org/10.1017/s0261340900018415.

Brie, F.W.D. 1908. *The Brut or the Chronicles of England*, Pt. 2. Early English Text Society, Original Series 136, Kegan Paul, Trench, Trübner & Co. Ltd, London, 607 pp.

Cole, C.A. (ed) 1858. *Memorials of Henry the Fifth, King of England*. Longman, Brown, Green, Longmans, and Roberts, London, lxii + 186 pp.

Cole, H. 1844. *Documents Illustrative of English History in the Thirteenth and Fourteenth Centuries*. Eyre and Spottiswoode, London, 431 pp.

Collins, A.J. 1955. *Jewels and Plate of Queen Elizabeth I: The Inventory of 1574*. British Library, London, 605 pp.

Conde, J.A. 1874. *Historia de la Dominación de los Árabes en España: Sacada de Varios Manuscritos y Memorias Arábigas*. Marin and Co., Madrid, Spain, 327 pp.

Coville, A. 1888. *Les Cabochiens et l'Ordonnance de 1413*. Hachette, Paris, France, xix + 456 pp.

Curry, A. 2000. *The Battle of Agincourt: Sources and Interpretations*. The Boydell Press, Woodbridge, Suffolk, xiv + 474 pp.

Dallaway, J. 1826. *Anecdotes of Painting in England; with Some Account of the Principal Artists; and Incidental Notes on Other Arts; Collected by the Late Mr. George Vertue; Digested and Published from his Original Mss. by the Honourable Horace Walpole; with Considerable Additions*, Vol. 1. John Major, London, xxii + 367 pp.

Dillon, J.T. 1788. *The History of the Reign of Peter the Cruel, King of Castile and Leon*, Vol. 1. W. Richardson, London.

Ford, R. 1845. *A Hand-Book for Travellers in Spain, and Readers at Home (…)*, Pt. 1. John Murray, London, 1,064 pp.

Ford, R. 1855. *A Handbook for Travellers in Spain*, 3rd edn, Pt. 1. John Murray, London, 459 pp.

Gairdner, J. 1858. *Historia Regis Henri Septime (…)*. Longman, Brown, Green, Longmans, and Roberts, London, lxiv + 477 pp.

Gayangos, P. 1840 & 1843. *The History of the Mohammedan Dynasties in Spain (…) in Two Volumes*. Oriental Translation Fund of Great Britain and Ireland, London, xcv + 548 pp. and clxxii + 544 pp.

Godwin, F. 1601. *A Catalogue of the Bishops of England, Since the First Planting of Christian Religion in This Island Together with a Briefe History of Their Lives and Memorable Actions, So Neere as Can Be Gathered Out of Antiquity*. Eliot's Court Press, London, 547 pp.

Gough, R. 1786. *Sepulchral Monuments in Great Britain*. Richard Gough, London, cciv + 78 pp.

Grafton, R. 1809. *Grafton's Chronicle; or, History of England (…)*, Vol. 1. J. Johnson; F.C. and J. Rivington; T. Payne; Wilkie and Robinson; Longman, Hurst, Rees and Orme; Cadell and Davies; and J. Mawman, London, 679 pp.

Gribling, B. 2017. *The Image of Edward the Black Prince in Georgian and Victorian England: Negotiating the Late Medieval Past*. Royal Historical Society Studies in History, Boydell & Brewer Ltd, Woodbridge, Suffolk, 171 pp.

Grose, F. & Astle, T. (eds), 1775. Edward the Black Prince. *In*: *The Antiquarian Repertory: A Miscellany, Intended to Preserve and Illustrate Several Valuable Remains of Old Times. Adorned with Elegant Sculptures*, Vol. 1. Francis Blyth and T. Evans, London, 169–172. (*Note*: The author of this article is noted as 'MO'.)

Guiffrey, J. 1894. *Inventaires de Jean Duc de Berry (1401–1416)*, Vol. 1. Ernest Leroux, Paris, France, cxciv + 347 pp.

Holmes, M.R. 1937. The crowns of England. *Archaeologia*, **86**, 73–90, https://doi.org/10.1017/S0261340900015356.

Hughes, J. 1706. *A Complete History of England: With the Lives of All the Kings and Queens Thereof; from the Earliest Account of Time, to the Death of His Late Majesty King William III (…)*, Vol. 1. Brab. Aylmer *et al.*, London, 640 pp.

Le Febvre, J. 1692. *Anciens Memoires du Quatorzieme Siecle (…)*. Baltazar Bellere, Douay, France, 433 pp.

Leland, J. 1774. *Joannis Lelandi Antiquarii de Rebus Britannicis Collectanea*, Vol. 4. Impensis Gul. & Jo. Richardson, London, 400 pp.

Llaguno Amirola, D.E. 1779. *Cronicas de los Reyes de Castilla (…) por D. Pedro Lopez de Ayala (…), que Comprende la Cronica del Rey Don Pedro*, Vol. 1. Don Antonio de Sancha, Madrid, Spain, 612 pp.

Melville, J. 1827. *Memoirs of His Own Life by Sir James Melville of Halhill: 1549–1593*. Bannatyne Club, Edinburgh, xxviii + 420 pp.

Mérimée, P. 1848. *Histoire de Don Pédre Ier, Roi de Castille*. Charpentier, Paris, France, 586 pp.

Mérimée, P. (transl. by Pearse, J.) 1849. *The History of Peter the Cruel, King of Castile and Leon*, Vol. 2. Richard Bentley, London, 379 pp.

Mirot, L. 1940. Études lucquoises, Galvano Trenta et les joyaux de la couronne. *Bibliothèque de l'Ecole des Chartes*, **101**(1), 116–156, https://doi.org/10.3406/bec.1940.452562.

Morand, F. 1876. *Chronique de Jean le Févre, Seigneur de Saint-Remy*, Vol. 1. Renouard, Paris, France, 393 pp.

Nichols, J. 1780. *A Collection of All the Wills, Now Known to be Extant, of the Kings and Queens of England, Princes and Princesses of Wales, and Every Branch of the Blood Royal, from the Reign of William the Conqueror, to that of Henry the Seventh Exclusive*. John Nichols, London, viii + 429 pp.

Nicolas, H. 1832. *History of the Battle of Agincourt and of the Expedition of Henry the Fifth into France in 1415*, 2nd edn. Johnson & Co., London, 106 pp.

Ogden, J. 2019. Gems and the gem trade in India. *In*: Jaffer, A. (ed) *Beyond Extravagance: A Royal Collection of Gems and Jewels*. Assouline, New York, New York, USA, 542–593.

Palgrave, F. 1836. *The Antient Kalendars and Inventories of the Treasury of His Majesty's Exchequer (…)*, Vols. 1–3. G. Eyre and A. Spottiswoode, London, cxlviii + 350 pp., 370 pp. and xiii + 491 pp.

Pedani, M.P. 2002. Balas rubies for the king of England (1413–15). *Electronic Journal of Oriental Studies*, **5**(7), 1–13.

Sandford, F. 1687. *The History of the Coronation of the Most High, Most Mighty, and Most Excellent Monarch, James II (…)*. Thomas Newcomb, London, xii + 135 pp.

Schmetzer, K. & Gilg, H.A. 2020. The late 14th-century royal crown of Blanche of Lancaster—History and gem materials. *Journal of Gemmology*, **37**(1), 26–64, https://doi.org/10.15506/JoG.2020.37.1.26.

Strachey, J. & Blyke, R. 1767–1777. *Rotuli Parliamentorum; Ut et Petitiones, et Placita in Parliamento*, Vol. 4. (No publisher given), 513 pp.

Stratford, J. 2012. *Richard II and the English Royal Treasure*. Boydell Press, Woodbridge, Suffolk, 470 pp.

Stratford, J. 2013. 'Par le special commandement du roy'. Jewels and plate pledged for the Agincourt expedition. *In*: Dodd, G. (ed) *Henry V: New Interpretations*. York Medieval Press, York, 157–170.

Tavernier, J.B. 1677. *Les Six Voyages de Jean Baptiste Tavernier (…) en Turquie, en Perse, et aux Indes (…)*, Vol. 2. Gervais Clouzier and Claude Barbin, Paris, France, 527 pp.

Taylor, F. & Roskell, J.S. (eds) 1975. *Gesta Henrici Quinti: The Deeds of Henry the Fifth*. Clarendon Press, Oxford, 256 pp.

Topham, J. (ed) 1787. *Liber Quotidianus Contrarotulatoris Garderobae, Anno Regni Regis Edwardi Primi Vicesimo Octavo A.D. MCCXCIX & MCCC*. Society of Antiquaries, London, lxx + 371 pp.

Trollope, E. (ed) 1884. King Henry VIII.'s Jewel Book. *In: Associated Architectural Societies' Reports and Papers*, Vol. 17, Pt. 2. James Williamson, Lincoln, 155–229.

Walpole, H. 1765. *Anecdotes of Painting in England; with Some Account of the Principal Artists; and Incidental Notes on Other Arts; Collected by the Late Mr. George Vertue*, Vol. 1, 2nd edn. Thomas Kirgate, Strawberry-Hill, Twickenham, xiii + 232 pp.

White, M.A. 2017. *Henrietta Maria and the English Civil Wars*. Routledge, Taylor & Francis Group, London, 238 pp.

Younghusband, G.J. 1921. *The Jewel House*. Herbert Jenkins, London, 256 pp.

Younghusband, G.J. & Davenport, C. 1919. *The Crown Jewels of England*. Cassell and Co., London, 84 pp.

Zurita y Castro, J. 1610. *Anales de la Corona de Aragon*, Vol. 6. Colegio de S. Vicente Ferrer por Lorenço de Robles, Aragon, Spain, 456 pp.

The Author

Dr Jack M. Ogden FGA
55 Florin Court, Charterhouse Square,
London EC1M 6EU
Email: jack@striptwist.com

Acknowledgements

Nigel Israel is thanked for scanning pages from two books in his extensive collection during the recent pandemic when I was unable to visit a library. Theodora Ogden helped with some translations from the early Spanish literature. I also extend my thanks to the anonymous reviewers of this article who made some very useful suggestions for its improvement. And a special thanks to the anonymous workers in libraries around the world who have scanned and made available online so many early texts and documents.

A Study of Emeralds from Davdar, North-Western China

Di Cui, Zongting Liao, Lijian Qi, Qian Zhong and Zhengyu Zhou

ABSTRACT: At the Davdar mine in Xinjiang, north-western China, emeralds are hosted mainly by carbonate, quartz-carbonate and quartz veins cutting metasedimentary rocks, and are associated with minerals such as hematite, dolomite, quartz, orthoclase and albite. Sixteen rough emeralds obtained during the authors' visit to the mining area in 2019 were studied by standard gemmological techniques and various spectroscopic methods (FTIR, Raman, UV-Vis-NIR and EPR), as well as LA-ICP-MS chemical analysis. The analysed samples were mostly coloured by Cr, and showed a wide range of Fe, V, Mg and alkali contents, along with relatively low Cs, Rb and Sc. UV-Vis-NIR spectra showed features at 370 nm (Fe^{3+}), 430 nm (Cr^{3+} with contributions from V^{3+} and possibly Fe^{3+}), 580–630 nm (Cr^{3+} and V^{3+}), 638 and 683 nm (Cr^{3+}), and 850 nm (Fe^{2+} and possibly Fe^{2+}–Fe^{3+} interactions). In addition, the more V-rich emeralds displayed a distinct V^{3+} absorption band at about 385–395 nm. Notably, the chemical composition of Davdar emeralds shows significant overlap with those from Panjshir, Afghanistan.

The Journal of Gemmology, **37**(4), 2020, pp. 374–392, https://doi.org/10.15506/JoG.2020.37.4.374

Davdar emeralds are sometimes described as 'emeralds of the Silk Road'. The deposit was discovered in around 2000 and the stones have appeared on the gem market since late 2003, but particularly since 2008 when the mines became more productive (Blauwet *et al.* 2005; Michelou & Pardieu 2009; Schwarz & Pardieu 2009; Marshall *et al.* 2012). The emeralds are notable for their attractive green colour, and in some cases they are quite transparent (e.g. Figure 1). The mine is located near Davdar (also spelled Dafdar or Dabdar) village in Taxkorgan Tajik Autonomous County, which is in the south-western part of Xinjiang near China's borders with Pakistan, Afghanistan and Tajikistan (Figure 2). The workings are located just east of Davdar village, at coordinates 37°20′52.48″ N, 75°25′42.56″ E and an elevation of about 3,600 m. Davdar is the second reported emerald occurrence in China, with the first being the Malipo (or Dyakou) deposit in Yunnan Province, where emeralds were discovered in the late 1980s during mining for tungsten (Xue *et al.* 2010; Hu & Lu 2019).

Previous studies have documented Davdar emeralds' chemical composition, fluid inclusions, stable isotope geochemistry and geographic origin characteristics (Schwarz & Pardieu 2009; Marshall *et al.* 2012; Saeseaw *et al.* 2014, 2019). However, the mining areas comprising the Davdar deposit (called Mine 1, Mine 2 and Mine 3 by the local workers) have not been fully described and studied in the field, although one of the occurrences was surveyed by Michelou & Pardieu (2009). During a field investigation of Davdar Mine 1 and Mine 2 by some of the authors (DC, LQ and QZ) in the summer of 2019, emeralds were obtained directly from the miners and collected *in situ*, and this article characterises them in detail.

HISTORY AND PRODUCTION

Mining activities initially developed during 2003–2005 in an area of a few square kilometres using bulldozers, hand tools and other equipment (Blauwet *et al.* 2005; Marshall *et al.* 2012). For several years the deposit was operated by Guimin Wong (Uyghur name = Ayineur Manglick), who obtained a legal mining permit in 2003 and set up the Kashi Junlin Mining Co. Ltd in 2004. The deposit is now owned by the local government, and there has been no mining since 2012, when activities

Figure 1: The fine-quality Davdar emeralds shown here were collected by local miners between 2009 and 2012. Most of the crystals weigh 0.4–0.6 g. Photo © Jia Maliding.

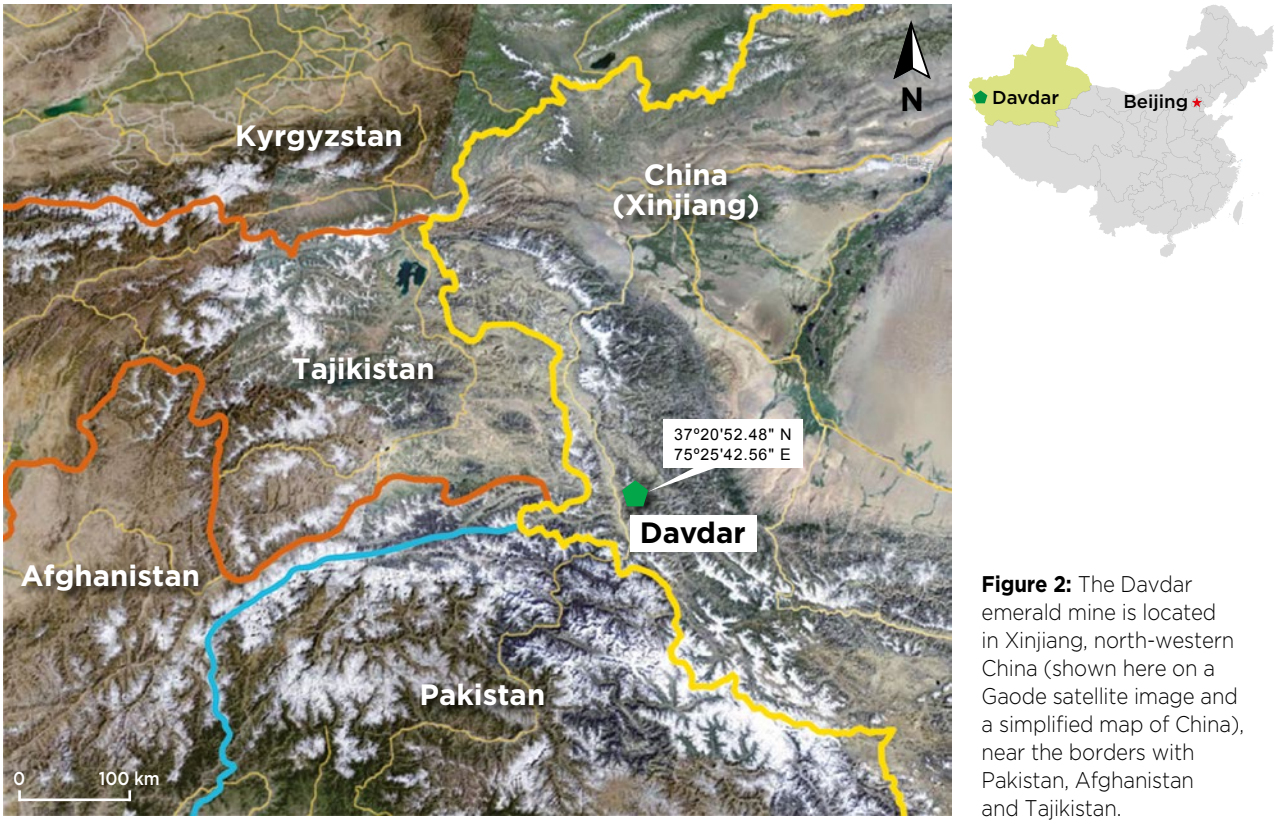

Figure 2: The Davdar emerald mine is located in Xinjiang, north-western China (shown here on a Gaode satellite image and a simplified map of China), near the borders with Pakistan, Afghanistan and Tajikistan.

were suspended due to regulations associated with a wildlife reserve in the area. In order for emerald mining and exploration to resume, new documents would need to be authorised by the local government.

The total output of rough emerald from Davdar is estimated at up to 25,000 carats (with gem-quality material constituting more than 10,000 carats), and the typical size range of fine-quality rough stones is 1–2 ct, although they may reach up to dozens of carats (Guimin and Alex Wong, pers. comm. 2020). The local miners and marketers have traditionally been from the Tajik ethnic group from the Xinjiang Uyghur Autonomous Region. Most Davdar emeralds have been traded into the local gem market near the town of Hongqilapu in the vicinity of China's borders with Pakistan, Afghanistan and Tajikistan. Guimin Wong currently sells Davdar emeralds from her stockpile in the gem markets of Ürümqi (the capital city of Xinjiang) and Shenzhen, China.

GEOLOGY

A geological survey of the Davdar emerald occurrence was performed in 2003–2004 by the Xinjiang Provincial Bureau of Geology and Mineral Resources (Brigade No. 2 2004). The deposit is located at the junction of the Karakorum-Kunlun-Pamir mountains and is underlain by the Early Silurian Wenquangou Group, which is bounded on the north-east by secondary structures related to the Taaxi Fault (Figure 3; Zhou *et al.* 2018). The Wenquangou Group is composed of siliciclastic rocks and sedimentary carbonates (e.g. pelitic siltstone, mudstone, quartz sandstone and minor conglomerate) with carbonate rock intercalations (Marshall *et al.* 2012). The emerald-bearing veins are hosted by metasedimentary units in which sandstone, dolomitic limestone and black carbonaceous slate are the main host rocks for the mineralisation (An 2006). Field observations by the present authors show

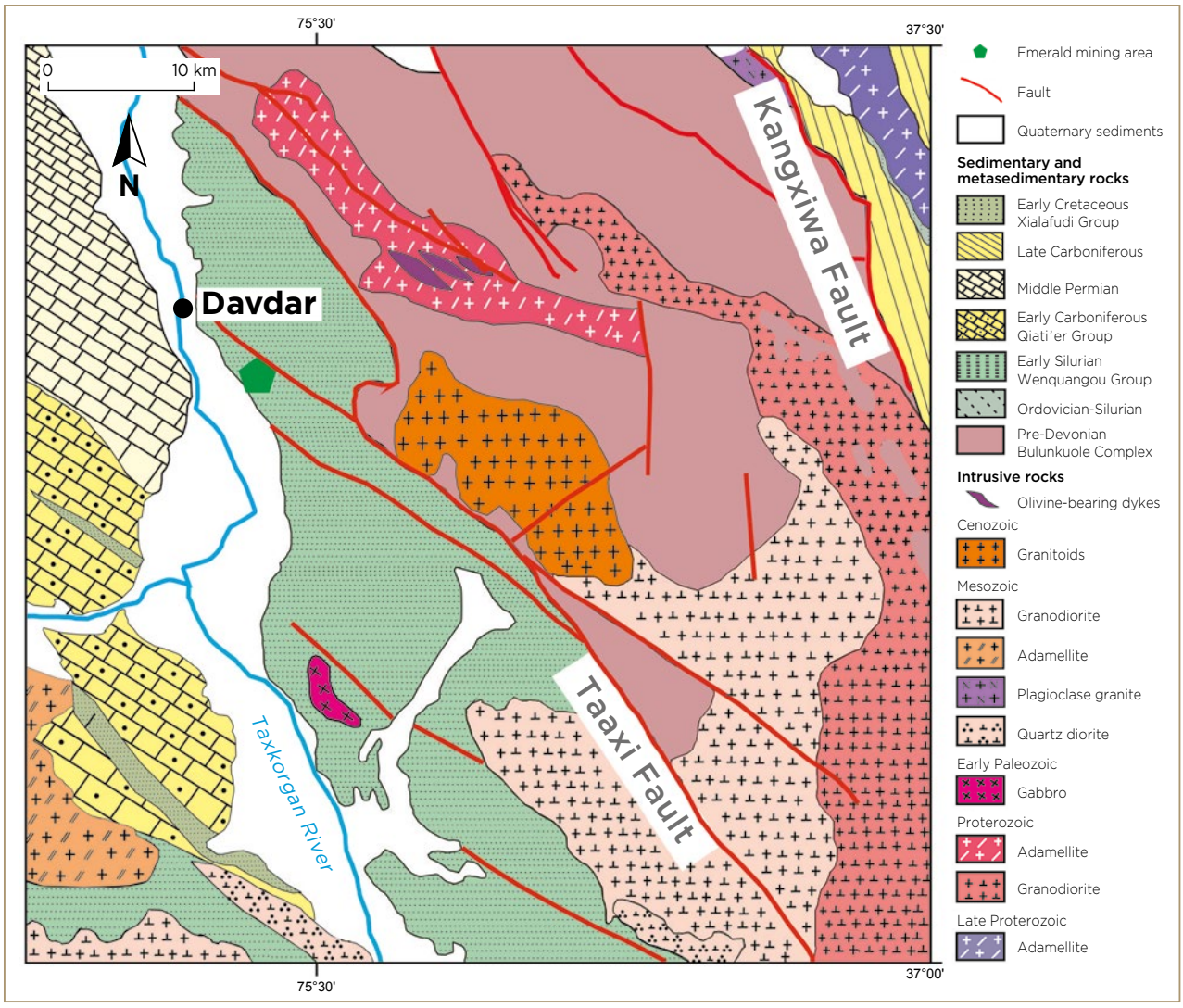

Figure 3: The Davdar emerald deposit is hosted by the Early Silurian Wenquangou Group, as shown in this simplified geologic map (modified from Zhou *et al.* 2018).

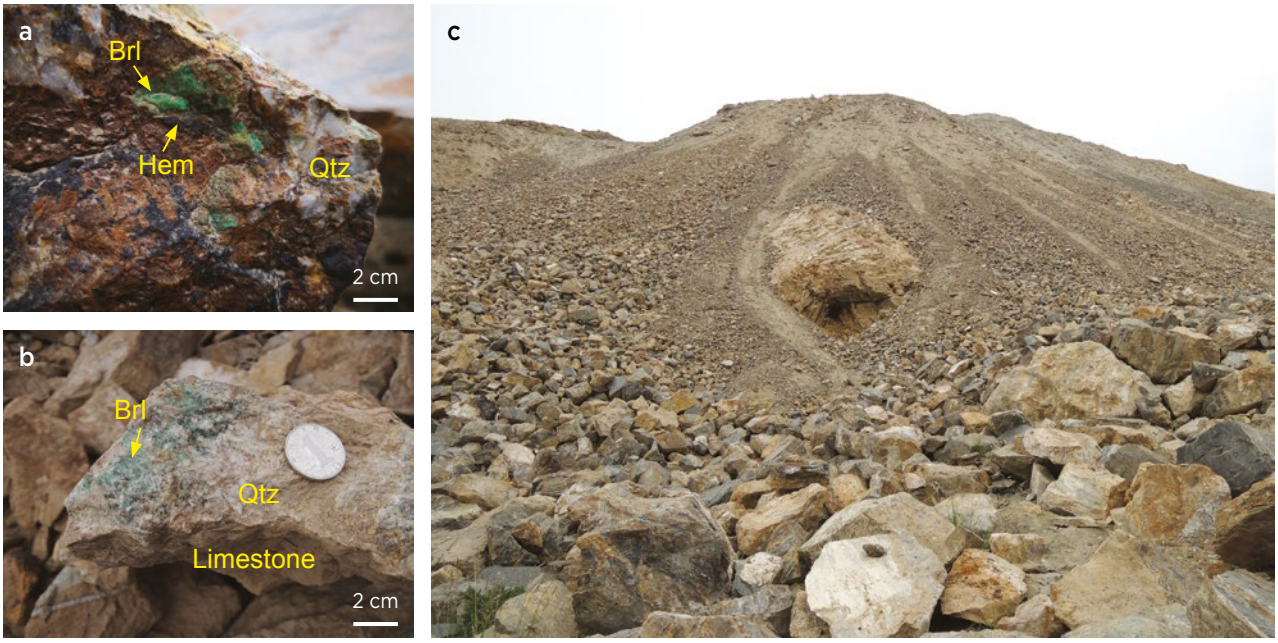

Figure 4: Characteristics of emerald mineralisation at the Davdar deposit are evident from (**a**) a quartz vein with minor accessory minerals such as hematite cross-cutting the host rock; (**b**) limestone with a vein surface containing non-gem-quality emerald and quartz; and (**c**) an outcrop with a small tunnel (approximately 1.5 × 1.0 m) at its base that has been mined for emeralds. Abbreviations: Brl = beryl (emerald), Hem = hematite and Qtz = quartz. Photos © L. Qi.

that the emerald-bearing veins are generally composed of quartz and carbonate minerals such as calcite associated with minor albite and hematite. The carbonate, quartz-carbonate and quartz veins are prospecting indicators for emerald mineralisation (Figure 4). Hematite, which is widely distributed in the veins, is regarded as another prospecting indicator by local miners.

Giuliani *et al.* (2019) noted similarities in the geographic and geologic environments between the emerald deposits in Davdar and in Panjshir, Afghanistan (located about 500 km to the west-south-west). Both are hosted by layered metasedimentary rocks (up to lower amphibolite facies) in veins that are predominantly composed of quartz and carbonate, and therefore they may share a similar genetic model. Giuliani *et al.* (2019) provisionally assigned both deposits to a type IIB (tectonic metamorphic-related) formation classification.

MATERIALS AND METHODS

Sixteen rough Davdar emerald samples (DC-1–DC-16) were chosen for testing. DC-1 through DC-13 were broken crystals obtained from local miners, and DC-14–DC-16 consisted of non-gem-quality emerald-bearing vein material obtained by the authors during their visit to the mining areas. Samples DC-1–DC-13 weighed 0.09–0.38 g, and they were cut and polished on two surfaces (parallel and perpendicular to the *c*-axis). Samples DC-14–DC-16 were cut and polished into slabs weighing 12.74, 20.37 and 18.17 g, respectively; they consisted of non-gem-quality emerald with hematite, carbonate, quartz and surrounding rock. The samples are pictured in Table I.

Microscopic features were observed and photographed using a GI-M6S91 gemmological microscope base manufactured by Nanjing Baoguang Technology Co. Ltd that was fitted with a Leica S9i digital stereo microscope equipped with a camera. RI measurements were acquired with a desktop refractometer for samples DC-1–DC-13, and SG values were obtained hydrostatically on these same emeralds. All samples were examined with standard 2–4 W long- and short-wave UV lamps and a Chelsea Colour Filter.

Spectroscopy was performed at the Laboratory of Gem and Technological Materials, Tongji University, Shanghai, China. Raman spectra were collected from all 16 samples with a Horiba Jobin Yvon LabRAM HR Evolution confocal micro-Raman spectrometer equipped with 325 and 532 nm lasers. The laser power was around 50 mW. Raman spectra of the emeralds were obtained in the 3800–3500 cm^{-1} range with the 325 nm laser using a grating of 1,800 grooves/mm. Raman spectra of accessory minerals were acquired in the 2000–100 cm^{-1} range with the 532 nm laser using a grating 600 grooves/mm, a scan time of 10 s, and two scans with the 50× objective of the microscope. Fourier-transform infrared (FTIR) transmission spectra were obtained for a representative sample (DC-1) with a Bruker Tensor 27 FTIR spectrometer. The nominal

Table I: Physical properties of Davdar emerald samples (photos © D. Cui).

Photo	Sample no.	Size (mm)	Weight (g)	Colour	Transparency	RI	Birefrin-gence	SG
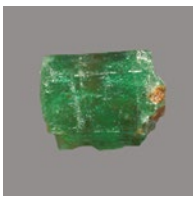	DC-1	4 × 4 × 6	0.15	Green	Translucent	1.578–1.586	0.008	2.56
	DC-2	7 × 6 × 7	0.40	Yellow-green	Translucent	1.580–1.587	0.007	2.57
	DC-3	5 × 4 × 2	0.11	Yellow-green	Translucent	1.581–1.588	0.007	2.61
	DC-4	4 × 5 × 2	0.09	Yellow-green	Translucent	1.577–1.584	0.007	2.62
	DC-5	3 × 4 × 4	0.11	Blue-green	Translucent	1.578–1.585	0.007	2.71
	DC-6	5 × 4 × 3	0.10	Blue-green	Transparent	1.575–1.582	0.007	2.70
	DC-7	3 × 4 × 4	0.25	Blue-green	Translucent	1.574–1.581	0.007	2.68
	DC-8	3 × 4 × 3	0.09	Yellow-green	Translucent	1.578–1.585	0.007	2.76

Photo	Sample no.	Size (mm)	Weight (g)	Colour	Transparency	RI	Birefringence	SG
	DC-9	4 × 3 × 2	0.09	Blue-green	Transparent	1.578–1.586	0.008	2.71
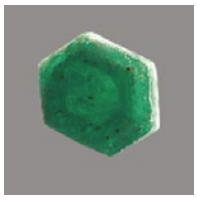	DC-10	4 × 3 × 4	0.10	Green	Translucent	1.578–1.585	0.007	2.65
	DC-11	6 × 4 × 3	0.14	Green	Translucent	1.580–1.588	0.008	2.70
	DC-12	3 × 3 × 4	0.10	Green	Translucent	1.579–1.586	0.007	2.62
	DC-13	7 × 7 × 3	0.38	Green	Translucent	1.576–1.583	0.007	2.57
	DC-14	23 × 20 × 7	12.74	Light green	Semi-translucent	—	—	—
	DC-15	27 × 22 × 10	20.37	Light green	Semi-translucent	—	—	—
	DC-16	36 × 24 × 8	18.17	Light green	Semi-translucent	—	—	—

resolution was 4 cm^{-1} and 32 scans were recorded. The scan speed was 10 kHz with a raster of 5 mm in the range of 8000–2000 cm^{-1}. Ultraviolet-visible-near infrared (UV-Vis-NIR) absorption spectra were obtained from all 16 samples with a GEM-3000 UV-Vis spectrometer manufactured by Guangzhou Flag Electronic Technology Co. The spectra were acquired at room temperature with a resolution of 1 nm, integration time of 110 milliseconds, average number of 20 times, smoothness of 1 and scan range of around 210–1000 nm.

Backscattered electron (BSE) imagery and chemical analysis of the accessory minerals in sample DC-13 were undertaken at the State Key Laboratory of Marine Geology of Tongji University using a JEOL JXA-8230 electron probe micro-analyser (EPMA) equipped with an energy-dispersive spectrometer. We used an accelerating voltage of 15 kV, a beam current of 10 nA and a beam diameter of 3 µm. Oxide compositions of the analysed minerals were calibrated against natural and synthetic mineral standards, and the ZAF procedure was used for data reduction.

Trace-element analysis of the 16 emeralds was conducted by laser ablation inductively coupled plasma mass spectrometry (LA-ICP-MS) using an Agilent 7900 ICP-MS combined with a Teledyne Cetac Analyte HE LA system at the Laboratory of Mineral Microanalysis in the Ore Deposit and Exploration Centre, Hefei University of Technology, Hefei, China. Detailed operating conditions for the instrumentation and data reduction were described by Zong *et al.* (2017). For this study, the spot size and frequency of the laser were set at 40 µm and 8 Hz, respectively. Data were calibrated against various reference glasses (NIST610, NIST612, NIST614, GSC-1G, GSD-1G and BCR-2G) without using an internal standard (Liu *et al.* 2008). Each analysis incorporated a background acquisition of approximately 40 s followed by 40 s of data acquisition from the sample. Six to nine spots were measured across colour-zoned samples (two to five spots for others). The samples were analysed on the same polished surfaces that were used for Raman spectroscopy.

Electron paramagnetic resonance (EPR) spectroscopy of sample DC-7 was performed with a Bruker EMX-8/2.7 electron-spin resonance spectrometer at the Test Centre of East China University of Science and Technology, Shanghai, China. The EPR measurements were made at room temperature using about 200 mg of powdered sample contained in a pure silica tube. Experimental conditions included a microwave frequency of 9.88 GHz, modulation frequency of 100 kHz, modulation amplitude of 4 G, microwave power of 2 mW, scan time of 42 s and spectral resolution of 1,024 points.

RESULTS

Standard Gemmological Properties

The standard gemmological properties of the 16 Davdar emeralds are listed in Table I. The samples ranged from semi-translucent to transparent and were light to dark blue-green to yellow-green. RI values were n_o = 1.584 ± 0.004 and n_e = 1.578 ± 0.004 with a birefringence of 0.007 ± 0.001, and SG ranged from 2.56 to 2.76. All of the samples were inert to both long- and short-wave UV radiation, and appeared green (i.e. showed no reaction) under the Chelsea filter while being illuminated with fibre-optic illumination.

Most of the emerald samples displayed colour zoning. Some were strongly colour zoned parallel to the hexagonal prism $\{10\bar{1}0\}$, and exhibited bands of near-colourless to green or yellowish green that showed variable thickness when viewed parallel to the *c*-axis (e.g. Figure 5).

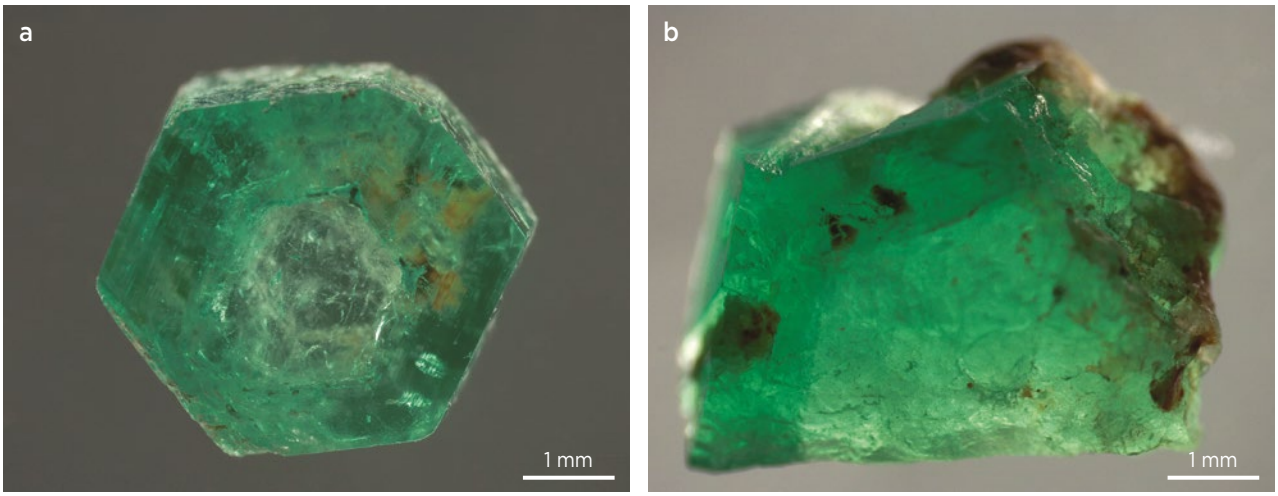

Figure 5: Colour zoning is evident when looking down the *c*-axis of Davdar emerald samples DC-4 (**a**) and DC-11 (**b**). Photos © D. Cui.

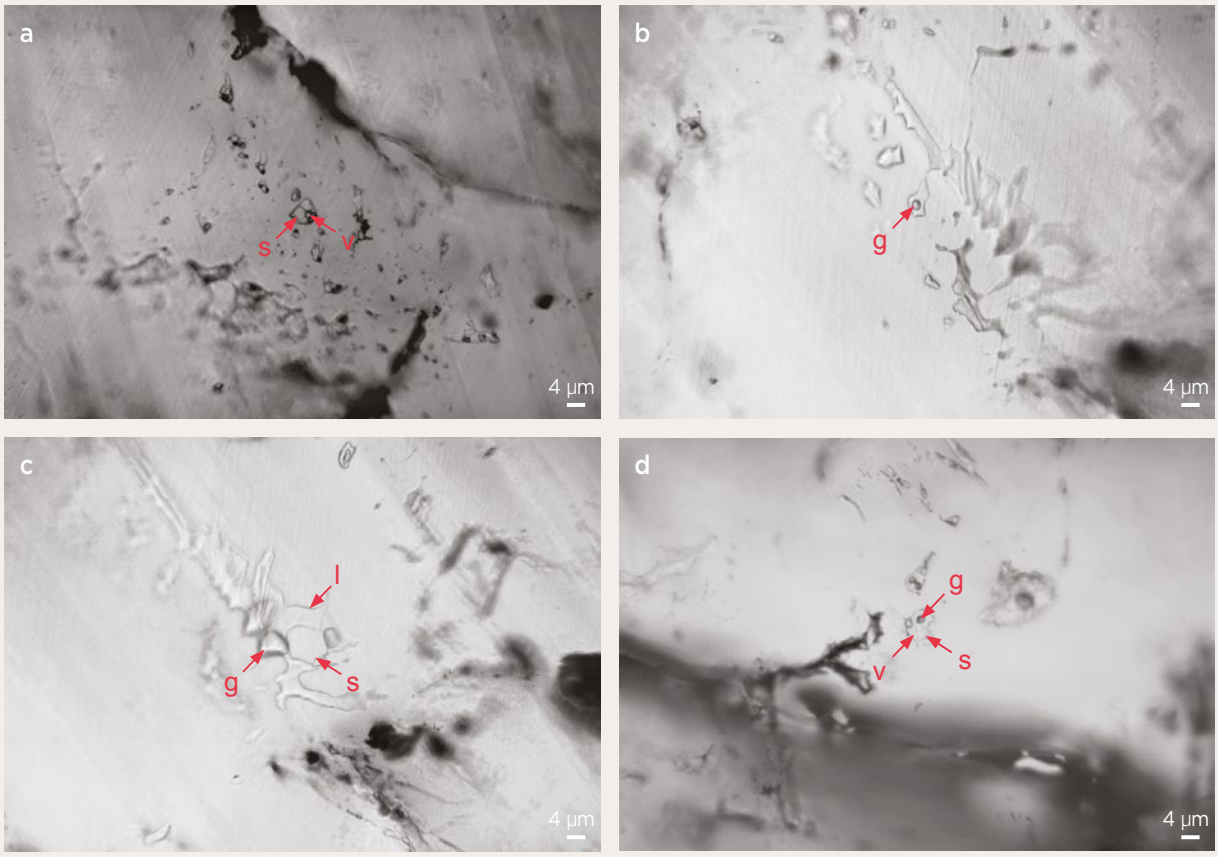

Figure 6: Two-phase (liquid + gas/vapour) and three-phase (liquid + solid + gas/vapour) inclusions are common in Davdar emeralds, as seen here in samples DC-9 (**a**–**c**) and DC-11 (**d**). Abbreviations: l = liquid, g = gas, s = solid and v = vapour. Photomicrographs © D. Cui in brightfield illumination.

Microscopy revealed abundant two-phase (liquid + vapour) and three-phase (liquid + vapour + solid) inclusions (Figure 6). They ranged from sub-microscopic to 10 µm, and most occurred in trails along partially healed fractures or formed isolated inclusions. The solid mineral within the three-phase inclusions might be halite (Marshall *et al.* 2012), but could not be discerned by Raman spectroscopy.

Minerals associated with the emeralds were observed microscopically and identified by Raman spectroscopy and BSE imaging as dolomite, quartz, orthoclase, albite and minor apatite (Figures 7 and 8a). In addition,

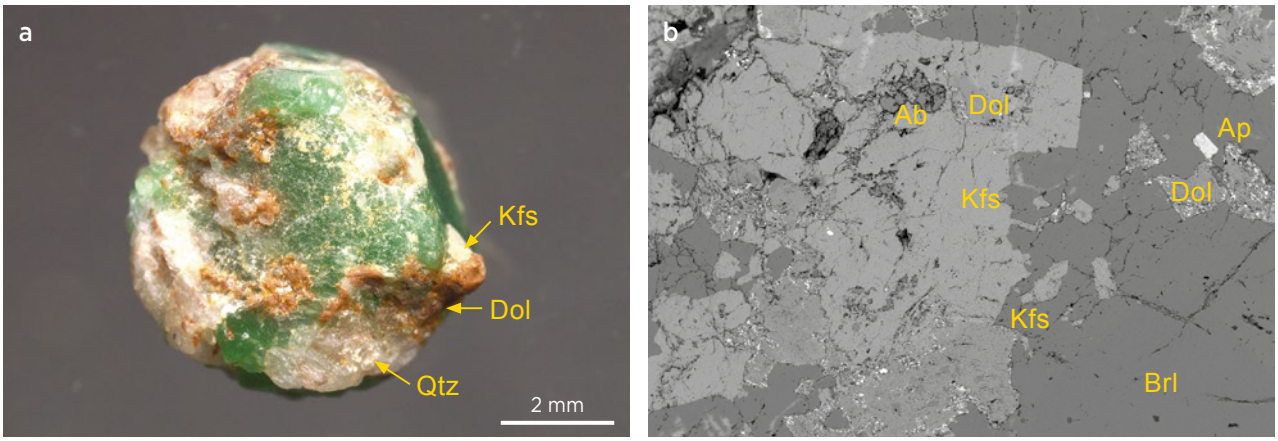

Figure 7: Associated minerals identified in Davdar emeralds include albite (Ab), apatite (Ap), dolomite (Dol), orthoclase (K-feldspar or Kfs) and quartz (Qtz). Sample DC-13 is seen here (**a**) before being partially polished (photo © D. Cui) and (**b**) on a polished surface using BSE imagery (image © Linmin Zhang).

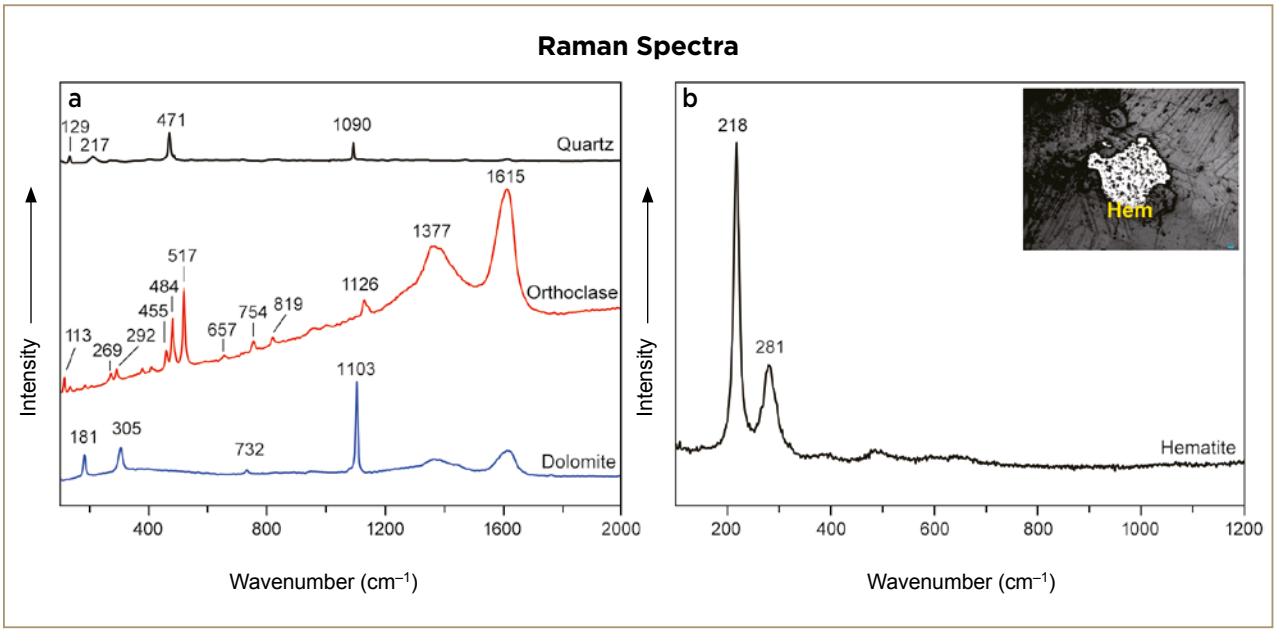

Figure 8: (**a**) Raman spectroscopy of some minerals associated with Davdar emerald sample DC-1 confirm their identity as quartz, orthoclase and dolomite. (**b**) In addition, hematite (Hem) was identified in sample DC-15 (photomicrograph © D. Cui).

hematite was identified by Raman spectroscopy (Figure 8b). EPMA analyses of these minerals in one sample are reported in Table II. Some emeralds with poor transparency contained what appeared to be a yellowish brown weathering product consisting of carbonates with hematite.

FTIR Spectroscopy

Representative FTIR spectra for E⊥c and E||c (Figure 9) showed weak bands in the ranges 4600–4000 cm^{-1} and 2900–2800 cm^{-1} associated with M-OH stretching vibrations and Cl^-, respectively (Shi 1999; Qi *et al.* 2002). A band at 2348 cm^{-1} is related to anti-symmetric

Table II: Electron microprobe analyses of accessory minerals at specific spots in sample DC-13.[a]

Oxides (wt.%)	Albite	Apatite	Dolomite	Dolomite	Orthoclase	Orthoclase
	DC-13-04	DC-13-02	DC-13-03	DC-13-06	DC-13-01	DC-13-05
SiO_2	69.26	nd	nd	nd	63.59	65.15
Al_2O_3	19.27	nd	nd	0.02	18.25	18.34
FeO[b]	nd	0.18	5.12	6.83	0.02	0.01
MnO	nd	0.01	0.46	0.26	nd	0.01
CuO	0.01	nd	0.01	0.01	0.04	nd
MgO	nd	0.02	13.73	16.64	nd	nd
CaO	0.05	55.21	34.46	29.19	0.05	0.04
Na_2O	11.55	0.06	0.01	0.02	0.72	0.67
K_2O	0.22	nd	0.02	0.01	16.93	16.93
P_2O_5	nd	41.26	0.07	0.15	0.04	nd
Total	100.36	96.75	53.87	53.11	99.63	101.14

[a] The accuracy of major elements is about 1%. Abbreviation: nd = not detected (<0.01 wt.%).
[b] All Fe is reported as FeO.

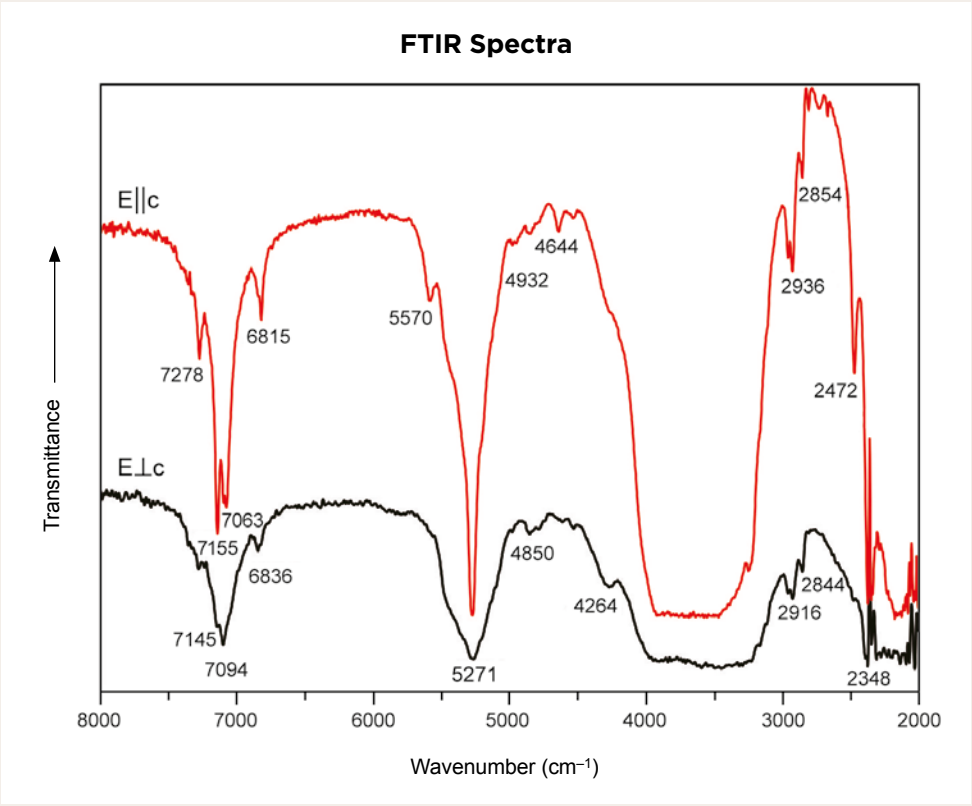

Figure 9: FTIR transmission spectra of representative Davdar emerald sample DC-1 in the range 8000–2000 cm^{-1} show features associated with type I and type II H_2O molecules, as well as other constituents. See Table III for band assignments.

stretching vibrations of CO_2 molecules (Yu *et al.* 2017). Strong bands near 7100 and 5200 cm^{-1} are attributed to double-frequency and frequency vibrations caused by type I and type II H_2O molecules in structural channels, as specified in Table III.

Raman Spectroscopy

Figure 10 illustrates representative Raman spectra of the core and rim of colour-zoned samples DC-4 and DC-12, measured in the range of OH^- and H_2O-molecule vibrations at 3500–3800 cm^{-1}. According to Huong *et al.* (2010), bands centred at approximately 3608 and 3598 cm^{-1} belong to type I H_2O (i.e. without an alkali ion nearby) and type II H_2O (i.e. with an alkali ion nearby), respectively. The positions of these bands can vary by a few wavenumbers. In this study, the features at 3613–3614 cm^{-1} (type I H_2O) and at 3601–3604 cm^{-1} (type II H_2O) showed significant intensity differences in the zoned samples, indicating relatively greater type II H_2O in the lighter-coloured core and more type I H_2O in the greener rim. However, the spectra of most of our samples showed that type II H_2O was dominant overall.

Table III: Principal FTIR vibrational bands in the 8000–2000 cm^{-1} range in Davdar emeralds.

Constituent	E||c	E⊥c	Mode of vibration (Qi *et al.* 2002; Yu *et al.* 2017)
Type I H_2O	7063	7145	Double-frequency vibration
Type II H_2O	7155	7094	Double-frequency vibration
Type I H_2O	5570	—	Frequency vibration
Type II H_2O	5271		Frequency vibration
CO_2	2348		Stretching vibration

Trace-Element Analysis

LA-ICP-MS data for the 16 emerald samples are summarised in Table IV. All of them contained abundant chromophore elements that varied over a relatively wide range: Cr = 1591–5919 ppmw, V = 454.5–12040 ppmw and Fe = 701.7–14700 ppmw. Some samples contained relatively high Cr and Fe, while others showed high V and low Fe. The Cr/V ratio ranged from 0.2 to 6.8. The emeralds contained comparatively low Rb and Cs, as well as traces of Ni and Ga. Mg ranged up to 12000 ppmw, averaging 7040 ppmw. Total alkali concentrations (Li + Na + K + Rb + Cs) averaged 8994 ppmw (2543–16070 ppmw); Na, K, Rb and Cs contents averaged 8478, 312, 20 and 26, respectively.

Table IV: Chemical composition of 16 Davdar emeralds obtained by LA-ICP-MS.*

Sample no.	DC-1	DC-2	DC-3	DC-4 rim	DC-4 core	DC-5	DC-6	DC-7	DC-8
Colour	Green	Yellow-green	Yellow-green	Yellow-green	Lt. ylo.-green	Blue-green	Blue-green	Blue-green	Yellow-green
No. analyses	2	2	6	7	2	2	3	2	3
Element (ppmw)									
Li	239.2–248.2	113.7–157.6	102.8–318.3	94.18–419.2	114.5–443.9	149.7–160.2	129.3–139.1	117.4–274.1	118.8–264.3
Na	8399–8811	8154–11440	7695–11300	8993–11690	9238–11000	7537–8189	6522–7399	8559–9869	6190–10150
Mg	9797–9953	6463–7128	6208–8061	6360–9398	7115–7940	4793–8673	5400–5541	10380–10600	4714–11180
K	279.1–285.9	163.2–220.7	212.6–318.3	235.5–395.1	221.0–295.8	304.6–1610	184.1–243.5	376.0–403.0	137.5–452.5
Sc	34.18–38.59	103.8–232.9	32.76–220.1	35.80–248.7	36.87–299.1	39.20–95.05	103.7–134.0	40.13–243.5	63.29–194.8
Cr	2347–2463	3335–3746	1674–4487	1790–5424	1781–4027	3902–4909	4143–4429	2746–3144	2152–4112
V	467.9–501.8	956.4–1169	707.7–1514	689.7–1443	682.1–1248	927.0–1067	883.6–928.6	567.4–1356	725.8–1528
Fe	5139–5323	8445–10700	4620–11650	5642–14700	5491–12760	7079–10350	6480–7171	6572–13980	6568–13440
Ga	17.49–19.38	25.27–28.96	19.32–37.39	19.39–33.83	19.54–33.79	40.35–76.45	25.10–29.54	19.30–39.95	22.88–37.81
Rb	17.29–19.86	16.53–20.75	20.65–32.31	22.04–39.69	20.09–30.56	23.40–42.12	10.41–14.02	21.75–32.47	11.48–29.19
Cs	26.00–26.59	22.13–30.65	24.70–40.60	23.46–43.93	21.33–37.24	27.68–33.69	15.18–17.79	27.08–39.89	23.60–38.06
Ni	19.82–20.75	14.91–15.64	18.38–22.03	16.53–20.20	17.14–20.68	20.65–76.02	18.60–22.00	19.44–24.44	13.42–24.76
Cr/V	4.7–5.3	3.2–3.5	2.2–3.4	1.9–3.9	2.6–4.3	4.2–4.6	4.7–4.8	2.3–4.8	2.1–3.2

Sample no.	DC-9	DC-10	DC-11	DC-12 rim	DC-12 core	DC-13	DC-14	DC-15	DC-16
Colour	Blue-green	Green	Green	Green	Lt. green	Green	Lt. green	Lt. green	Lt. green
No. analyses	2	2	3	4	5	5	5	5	5
Element (ppmw)									
Li	129.7–138.2	246.5–249.3	191.4–206.7	116.4–213.6	200.3–217.4	112.0–163.1	123.0–127.1	22.48–142.6	136.5–143.8
Na	5171–8217	8914–9099	4339–11960	7119–9670	8531–10110	9350–10710	7172–7836	2431–15360	5820–8518
Mg	6295–9490	9285–9354	3076–9017	4976–9800	5659–7846	8094–10550	5146–5478	2207–12000	4684–5182
K	432.8–850.2	262.9–432.8	109.6–311.0	162.8–282.2	222.7–477.2	329.4–527.1	169.9–189.0	67.6–506.8	176.0–729.1
Sc	71.88–186.9	33.45–35.52	37.14–88.66	30.55–202.8	27.25–33.55	18.39–260.0	227.9–268.1	131.1–279.8	221.9–298.8
Cr	3294–3313	2670–2739	3632–3818	3338–3598	2799–3148	1917–5193	2868–2894	1591–2738	2440–2759
V	770.8–1232	454.5–474.6	565.2–1020	523.2–1451	512.5–622.4	566.1–1233	11000–12040	4062–4918	8852–9802
Fe	7054–11270	5103–5652	7338–7408	5278–9399	4685–5383	4580–13360	1840–1982	701.7–3300	2205–3589
Ga	25.20–35.19	17.00–17.86	16.92–28.37	16.52–35.03	17.83–28.21	19.71–33.02	28.59–30.31	10.93–23.76	32.31–36.12
Rb	10.41–25.13	16.40–18.21	8.79–25.67	14.10–27.87	19.39–21.15	16.76–30.56	12.52–14.66	4.51–30.64	9.77–15.88
Cs	16.10–29.23	24.38–25.67	18.72–30.21	27.25–34.63	27.87–29.96	21.31–37.98	21.76–24.14	5.47–31.42	19.48–21.47
Ni	14.20–16.80	21.36–22.54	6.29–24.50	14.10–28.03	10.40–24.75	17.20–22.43	nd	nd	nd
Cr/V	2.7–4.3	5.8–5.9	3.7–6.4	2.5–6.8	5.1–5.5	2.7–5.5	0.2–0.3	0.3–0.6	0.2–0.3

* Except for zoned samples DC-4 and DC-12, spots were analysed in random locations. The accuracy is about 10%.
Abbreviations: nd = not detected, Lt. = light, ylo. = yellow.

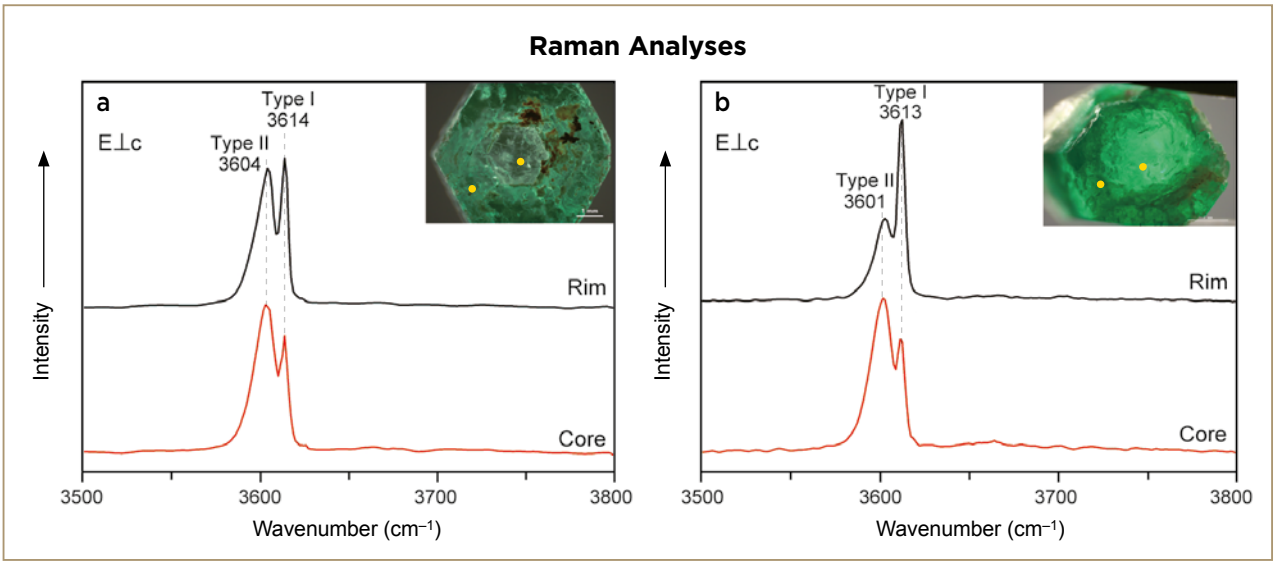

Figure 10: Raman spectra of colour-zoned Davdar emerald samples DC-4 (**a**) and DC-12 (**b**) display features characteristic of different proportions of type I and type II H_2O in the core and rim of each crystal. Inset photomicrographs © D. Cui; the yellow dots indicate the locations analysed.

Figure 11 shows the chemical zonation in colour-zoned samples DC-4 and DC-12. Their colour variations from core to rim were consistent with the contents of Cr and V. Overall, these were measured as 0.26–0.87 wt.% Cr_2O_3 and 0.10–0.20 wt.% V_2O_3 in DC-4, and 0.41–0.53 wt.% Cr_2O_3 and 0.08–0.21 wt.% V_2O_3 in DC-12. Higher concentrations of Cr and V together contributed to the greener colouration of the rims. It is also worth noting that the rims were low in alkalis, while the cores had higher alkali and Mg + Fe contents. The total content of Na_2O + K_2O in the rims of both samples ranged from 1.21 to 1.62 wt.% (again, see Table IV). Figure 10 demonstrates that the Raman intensity ratio I_{3604}/I_{3614} of sample DC-4 was higher in the core than the rim; the same trend was noted for sample DC-12. Therefore, as expected the type II H_2O Raman band increased in intensity together with the alkali content of the emerald cores.

UV-Vis-NIR Spectroscopy

UV-Vis-NIR spectra of relatively high-Fe Davdar samples (e.g. DC-1; Figure 12) displayed dominant Fe and Cr features. The broad absorption bands at 430 and 580–630 nm are due to Cr^{3+} with contributions from V^{3+} (Li & Zhu 2002; Saeseaw *et al.* 2014, 2019; Bai *et al.* 2019; Hu & Lu 2019). The peaks at 638 and 683 nm are also associated with Cr^{3+} (Saeseaw *et al.* 2014, 2019). Distinct Fe^{3+}

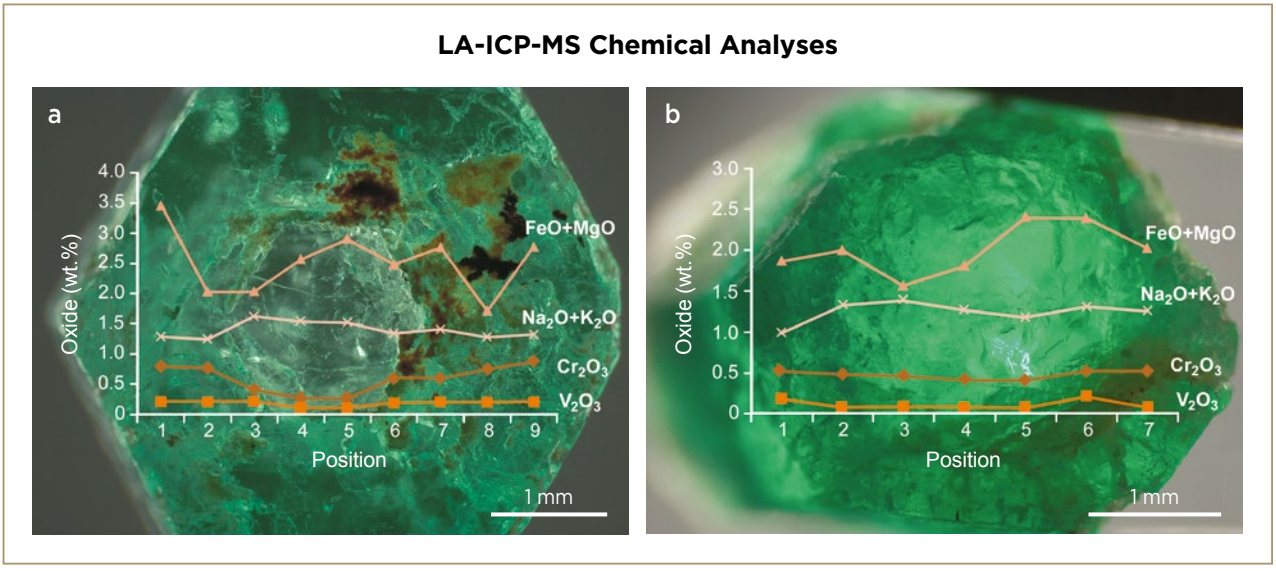

Figure 11: LA-ICP-MS data for selected oxides superimposed on photos of samples DC-4 (**a**) and DC-12 (**b**) illustrate how chemical composition varies with colour zoning across the emerald crystals. Photomicrographs © D. Cui.

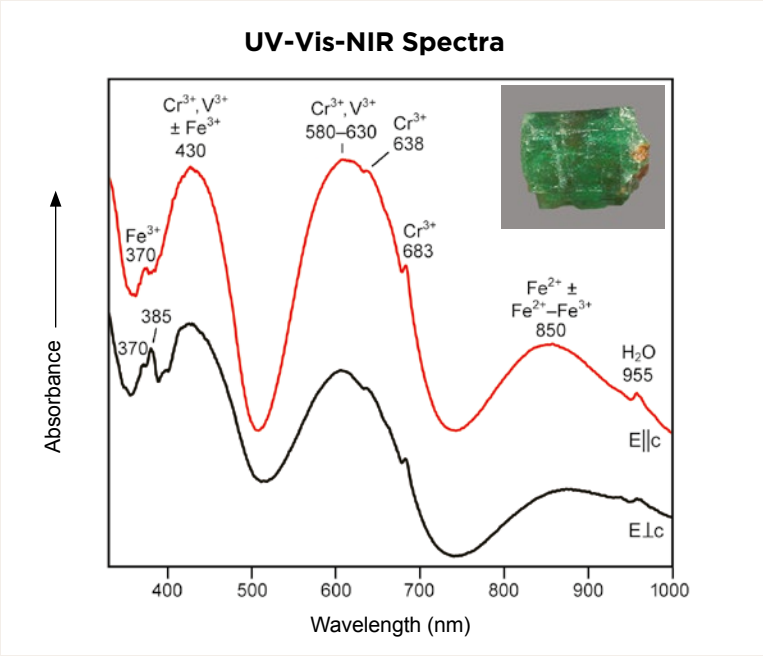

Figure 12: Polarised UV-Vis-NIR absorption spectra of high-Fe emerald sample DC-1 (containing an average of 2405 ppmw Cr, 485 ppmw V and 5231 ppmw Fe) show Fe^{2+}- and Fe^{3+}-related peaks, as well as Cr^{3+} and V^{3+} features, in both spectral orientations.

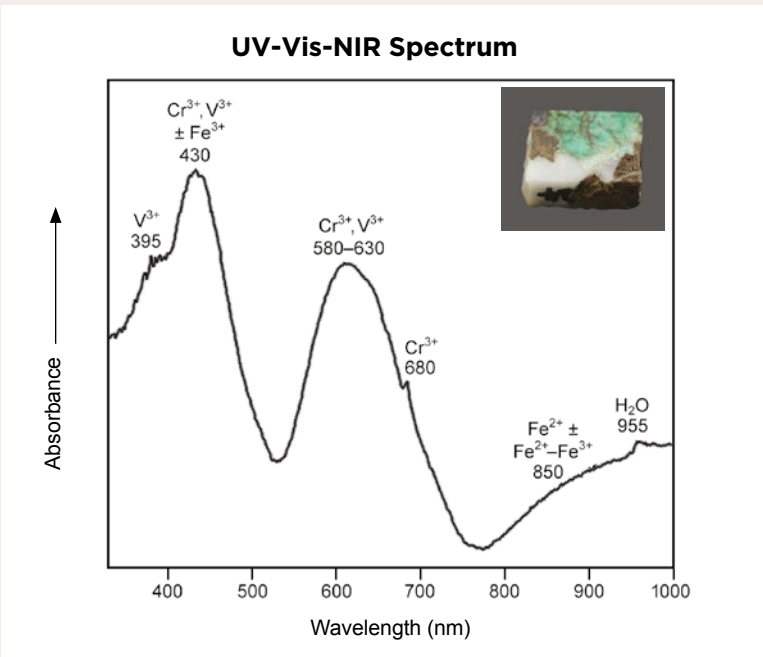

Figure 13: The UV-Vis-NIR absorption spectrum of high-V emerald sample DC-15, measured in a random direction, displays Cr- and V-dominant bands (with a shoulder at 395 nm due to V^{3+}), and Fe^{2+}- and Fe^{3+}-related features of variable intensity.

absorption occurred at around 370 nm and may also have contributed to the 430 nm band (Marfunin 1984; Zhang *et al.* 2012; Andersson 2019). Moreover, a weak, narrow Fe^{3+} band at about 385 nm was visible only for E⊥c polarisation, while the 370 nm Fe^{3+} feature could be observed in both the E⊥ c and E||c orientations. A band in the near-infrared region at around 850 nm is attributed to Fe^{2+} in octahedral (Khaibullin *et al.* 2003) or tetrahedral (Taran & Rossman 2001) structural sites. This Fe^{2+}-related feature is typically in the range of 810–830 nm (Taran & Vyshnevskyi 2019 and references therein), and the reason for the shift to 850 nm in our Davdar emeralds is unknown. Shao *et al.* (2014) proposed that this band (specifically at 842 nm) in Fe-rich Russian hydrothermal synthetic emerald may be caused by the combined effect of Fe^{2+} and Fe^{2+}–Fe^{3+} intervalence charge transfer. A peak at about 955 nm is related to the presence of H_2O (Wood & Nassau 1968).

Non-gem-quality Davdar emeralds containing relatively high amounts of V (samples DC-14–DC-16) showed UV-Vis-NIR absorption features comparable with previous studies (Figure 13; cf. Schwarz & Pardieu 2009; Saeseaw *et al.* 2014). The spectra displayed Cr^{3+}- and V^{3+}-dominant

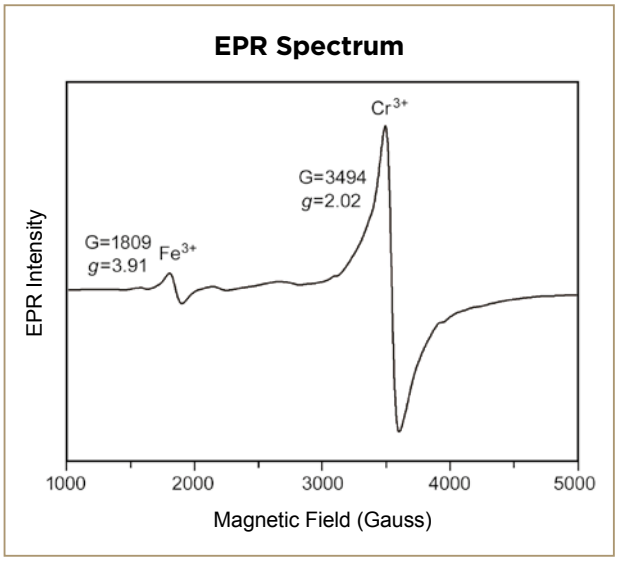

Figure 14: A representative powder EPR spectrum of emerald sample DC-7 shows signals for Cr^{3+} and Fe^{3+} centres.

features, along with bands of variable intensity related to Fe^{2+} and possibly Fe^{2+}–Fe^{3+} interactions. Schwarz and Pardieu (2009) noted that Davdar emeralds show intense Cr^{3+} and V^{3+} features, with a distinct V shoulder at about 380 nm. This shoulder was present in the absorption spectra of our high-V samples at around 385–395 nm (see, e.g., Figure 13). However, our spectra differed from data presented by Saeseaw *et al.* (2014), which showed the broad Fe^{2+}-related band but no Fe^{3+} in Davdar emeralds.

EPR Spectroscopy

EPR spectroscopy uses magnetic fields to measure the transitions between magnetic energy levels of transition metals with unpaired electrons (for more details, see Zhao 1991 and Pan & Nilges 2014). The interaction between the unpaired electrons and the applied magnetic field is described by its *g* value.

The representative EPR spectrum in Figure 14 displays the typical electronic paramagnetic signal of transition-metal ion substitutions in the X-band EPR. It presents two strong lines at about 3500 and 1800 G that are likely associated with the colouration mechanisms of Cr^{3+} and Fe^{3+}, respectively. The peak at about 3500 G ($g \approx 2$) can be assigned with some confidence to Cr^{3+} ions associated with the large zero-field splitting of Cr^{3+} ions (Ohkura *et al.* 1987). The peak at about 1800 G ($g \approx 4$) is probably related to paramagnetic behaviour corresponding to Fe^{3+} (Lin *et al.* 2013; Hu & Lu 2019). However, the Cr^{3+} centre might also be overlapped by Fe^{3+} ion-related centres for similar *g* factors (Hu & Lu 2019). Peaks centred at $g \approx 2$ were assigned to Fe^{3+} because of a classical spin Hamiltonian of a $3d^5$ ion in octahedral symmetry (Gaite *et al.* 2001). EPR spectra of Fe^{3+} have been reported previously by others who also proposed that these ions occupy Al^{3+} sites (Dvir & Low 1960; Blak *et al.* 1983; Ollier *et al.* 2015). Given the presence of vanadium in Davdar emeralds revealed by chemical analysis, V^{3+} might require low-temperature analytical conditions in order to be seen in the X-band EPR due to outer paired electrons (Hu & Lu 2019).

DISCUSSION

Chromophores in Davdar Emeralds

The concentrations of chromophores reported for Davdar emeralds show large ranges (see Table V). In this study, most of our samples contained more Cr than V, with Cr/V ratios of 1.9–6.8 (see Table IV). However, three non-gem-quality high-V samples had Cr/V ratios of 0.2–0.6. The UV-Vis-NIR spectra of these high-V emeralds displayed an absorption shoulder at about 385–395 nm (see, e.g., Figure 13), which has previously been assigned to V^{3+} in vanadium-doped synthetic emerald (Schmetzer *et al.* 2006). This absorption was also described as typical of high-quality Davdar emeralds with enriched V contents (Schwarz & Pardieu 2009; Saeseaw *et al.* 2014).

The AlO_6 octahedron is the structural unit that is key for the colouring of emerald because the ionic radii of Cr^{3+} (0.615 Å), V^{3+} (0.640 Å) and Fe^{3+} (~0.740 Å) are similar enough to that of Al^{3+} (0.535 Å) in the octahedral site to allow substitution (Shannon 1976). The substitution of Cr^{3+}, V^{3+}, Fe^{2+} and Fe^{3+} in the AlO_6 octahedra appears to follow the typical crystal-field behaviour that directly leads to colouration (Hu & Lu 2019). As suggested by Schwarz and Schmetzer (2002) and Schmetzer *et al.* (2006), yellowish green, green and bluish green emeralds reveal distinct absorption bands of

Table V: Summary of chemical composition data reported for Davdar emeralds.

Element (ppmw)	This study	Marshall *et al.* (2012)*	Saeseaw *et al.* (2014, 2019)	Schwarz & Pardieu (2009)
Cr	1591–5919	1231–4652	146–5630	1000–3000 (some 8000–9000)
V	455–12040	1428–2176	657–6960	1000–8000
Fe	701.7–14700	1166–2488	1170–6430	4000–11000
Cs	5.47–40.60	Not analysed	5.96–41.20	30–50 (some up to about 3000)

* Data of Marshall *et al.* (2012) have been recalculated as ppmw.

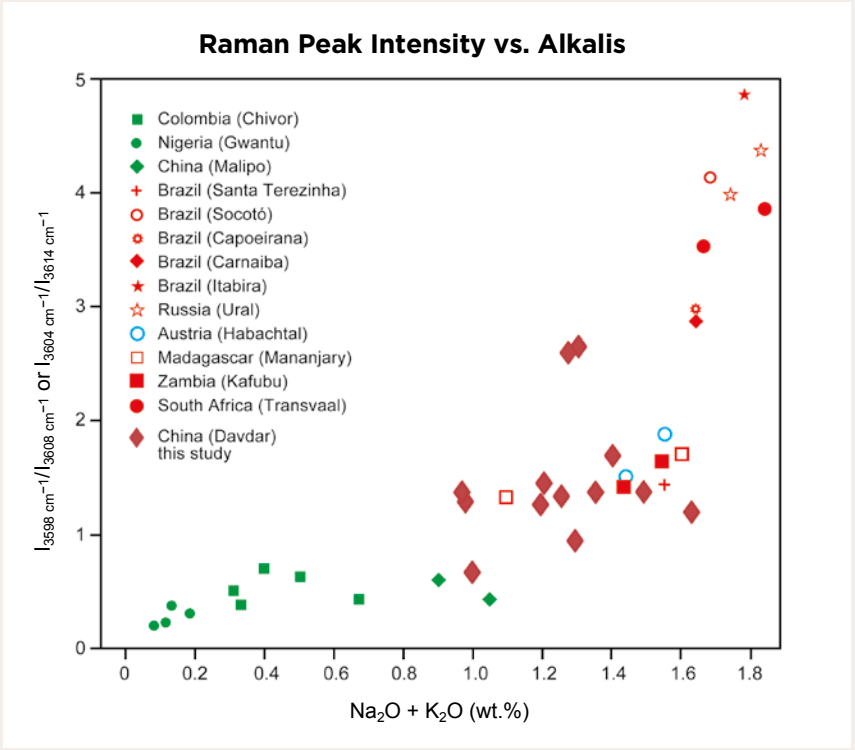

Figure 15: This plot shows the ratio of the Raman peak intensity (I) of the two water bands vs. the amount of alkalis (wt.% $Na_2O + K_2O$) for emeralds from various localities. The intensity ratios of the 3608 cm^{-1} (or 3614 cm^{-1}) and 3598 cm^{-1} (or 3604 cm^{-1}) bands are related to type I and type II water, respectively. The values for Davdar emeralds are from this study, and the other data are from Huong *et al.* (2010).

Cr, V or both in the red and blue-to-violet range. Considering the great variability of Cr, V and Fe concentrations in Davdar emeralds, Cr and V may sometimes occur in amounts necessary to yield the relatively saturated green colour of fine-quality emerald. While our high-Fe samples were mostly dominated by Cr, their bluish tinge could be associated with the presence of Fe.

Type I vs. Type II H_2O and Associated Alkali Content

Characteristics of channel water types can help provide useful information about the geographic origin of emerald. The FTIR spectra of our Davdar emeralds revealed that the bands for type II H_2O at 7155, 7094 and 5271 cm^{-1} were greater in intensity than those for type I H_2O at 7063, 7145 and 5570 cm^{-1}, in both the E||c and E⊥c directions (Figure 9; see also Table III for specific band assignments). Thus, the Davdar emeralds in this study were generally richer in type II H_2O. This is in contrast to the results obtained by Saeseaw *et al.* (2014), who recorded FTIR spectra for Davdar emeralds showing dominant type I H_2O with associated relatively low alkali contents (8840 ppmw total, on average, for the alkalis Li, Na, K, Rb and Cs).

Our samples contained total alkalis of around 9050 ppmw on average, with a range of 2540–16070 ppmw. Figure 15 illustrates that the total alkali concentration of Davdar emerald samples could be classified as 'medium' (1–2 wt.%) according to Karampelas *et al.* (2019), with a Raman peak intensity ratio I_{3604}/I_{3614} that was mostly >1 (i.e. 0.65–2.73), compared to low-alkali emeralds such as those from Colombia's Chivor mine, with an I_{3598}/I_{3608} ratio of <1 (Huong *et al.* 2010). The I_{3604}/I_{3614} ratio was >1 for all of our high-alkali Davdar samples, for which $Na_2O + K_2O$ = 1.18–1.62 wt.%. Only one Davdar spot analysis yielded a ratio of <1 (for $Na_2O + K_2O$ = 0.98 wt.%). We also found that as Mg + Fe concentrations and alkali cations increased, the type II H_2O band became more intense than the type I H_2O band.

A previous study (Qiao *et al.* 2019) showed a tentative correlation between water type and the contents of ($Na_2O + K_2O + Cs_2O$) and (MgO + FeO). In the emerald structure, the substitution of Al^{3+} by bivalent ions such as Mg^{2+}, Fe^{2+} or both requires a coupled substitution. The channels must then be occupied by alkali ions such as Na^+, Rb^+ and Cs^+ (usually Na^+), to balance the reduction in positive charge (Giuliani *et al.* 2019), as follows:

$$Al^{3+} = Mg^{2+} + Na^+_{(channel)}$$
$$Al^{3+} = Fe^{2+} + Na^+_{(channel)}$$

To summarise, the alkali content in emerald is controlled by the presence of $(Mg + Fe)^{2+}$ in the host rock or in the mineralising fluid (Qiao *et al.* 2019). Based on previous literature (Saeseaw *et al.* 2014), Davdar emeralds

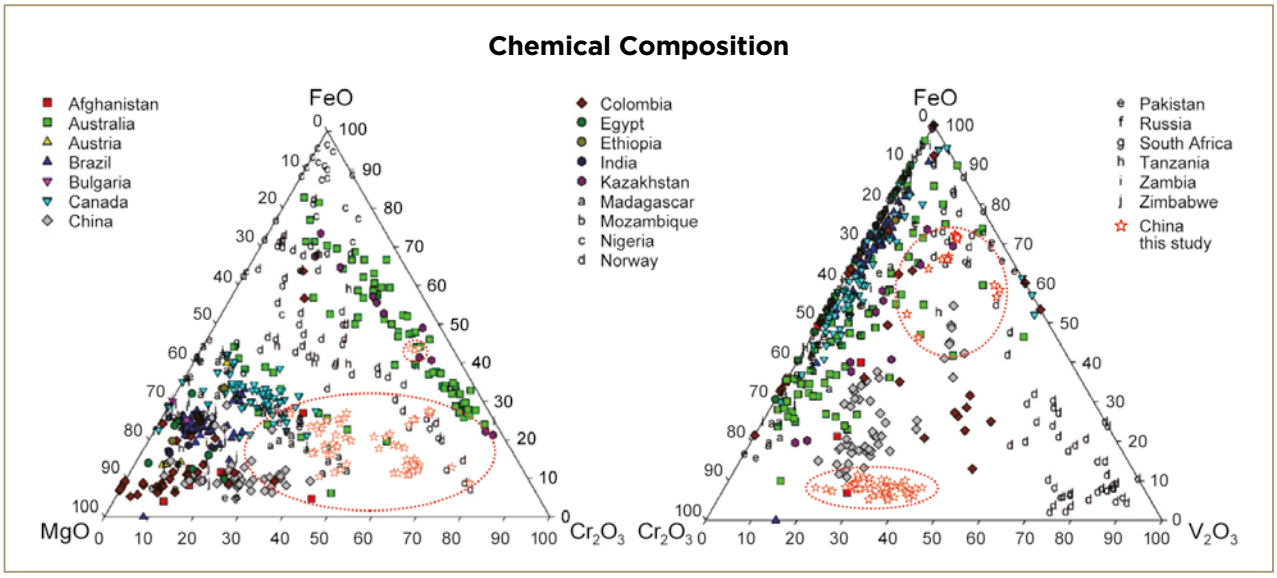

Figure 16: These ternary plots adapted from Giuliani *et al.* (2019) show emerald compositional data from worldwide localities with superimposed analyses of Davdar samples from this study.

are dominant in type I H_2O, suggesting they mineralised in an alkali-poor environment. However, our research shows that Davdar emeralds cannot be absolutely divided into being dominant in type I or type II H_2O, considering the variations in alkali-metal concentrations in their colour zones, which characterise multiple growth zones and the evolution of the mineralising environment (from alkali-rich to alkali-poor and from type II to type I H_2O). Overall, the alkali variations could be affected by the evolution of the mineralisation and the presence of local alkali-poor vs. alkali-rich environments.

Chemical Fingerprints of Davdar Origin

Our Davdar emerald samples showed relatively large ranges of Cr, V and Fe compared to those reported in previous studies (see Table V; Schwarz & Pardieu 2009; Marshall *et al.* 2012; Saeseaw *et al.* 2014, 2019), while the amount of Cs was similar to the results given by Saeseaw *et al.* (2014, 2019). The contents of Mg ranged from 2207 to 12000 ppmw, and Fe attained values up to 14700 ppm. Ternary diagrams of FeO–MgO–Cr_2O_3 and FeO–Cr_2O_3–V_2O_3 (Figure 16) show considerable overlap with data for emeralds from other localities, so these elements cannot be used to differentiate Davdar emeralds.

Emeralds appear to be sensitive to slight changes in their geological formation environments, which can impart unique trace-element signatures in material from different geographic localities (Saeseaw *et al.* 2019). Thus, variations in certain trace elements may be helpful for fingerprinting emeralds (Schwarz & Pardieu 2009; Saeseaw *et al.* 2014, 2019; Hu & Lu 2019). Figure 17 shows a plot of Fe vs. Ga data together with published data for emeralds from other deposits in Asia (Schwarz & Pardieu 2009; Zhang *et al.* 2012). This approach proved useful for separating Davdar emeralds from those of Pakistan, Russia and Malipo in China. However, it also confirmed the similarity of Davdar emeralds to those from Panjshir, Afghanistan, with a nearly complete overlap in their compositional fields. Plotting our Davdar emerald data on the Li vs. Cs diagram of Saeseaw *et al.* (2014) gave similar results (Figure 18). Davdar samples analysed in this study contained values for Li (22–444 ppmw) and Cs (5–41 ppmw) that commonly overlapped emeralds from Panjshir (78–268 ppmw Li and 11–97 ppmw Cs; Saeseaw *et al.* 2014, 2019).

Saeseaw *et al.* (2019) showed plots of Fe vs. Rb and Fe vs. Cs that appeared to be helpful for separating Davdar from Afghanistan emeralds, but the range of Fe contents obtained in this study varied too widely for such plots to be effective. Therefore, more research is needed for the reliable geochemical separation of emeralds from these two localities.

CONCLUSION

Davdar emeralds (e.g. Figure 19) formed in quartz-carbonate, carbonate and quartz veins with associated minerals such as hematite, dolomite, quartz, orthoclase and albite. Their chemical composition showed wide ranges of Fe, Cr and V (with mostly Cr>V), and relatively low Sc, Rb and Cs. Some non-gem-quality samples with V>Cr presented a distinct V absorption shoulder in their UV-Vis-NIR spectra. The chemical evolution of zoned Davdar emeralds indicates that they precipitated from

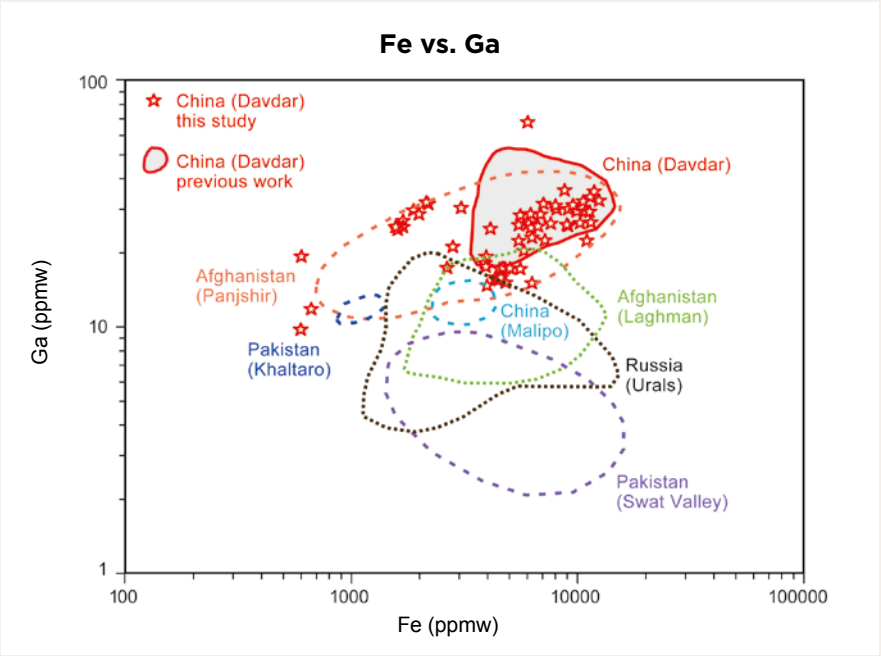

Figure 17: A logarithmic plot of Fe vs. Ga in emeralds from Davdar with compositional fields from some emerald deposits in Asia (from Schwarz & Pardieu 2009 and Zhang *et al.* 2012) shows the similarity of Davdar emeralds to those from Panjshir, Afghanistan.

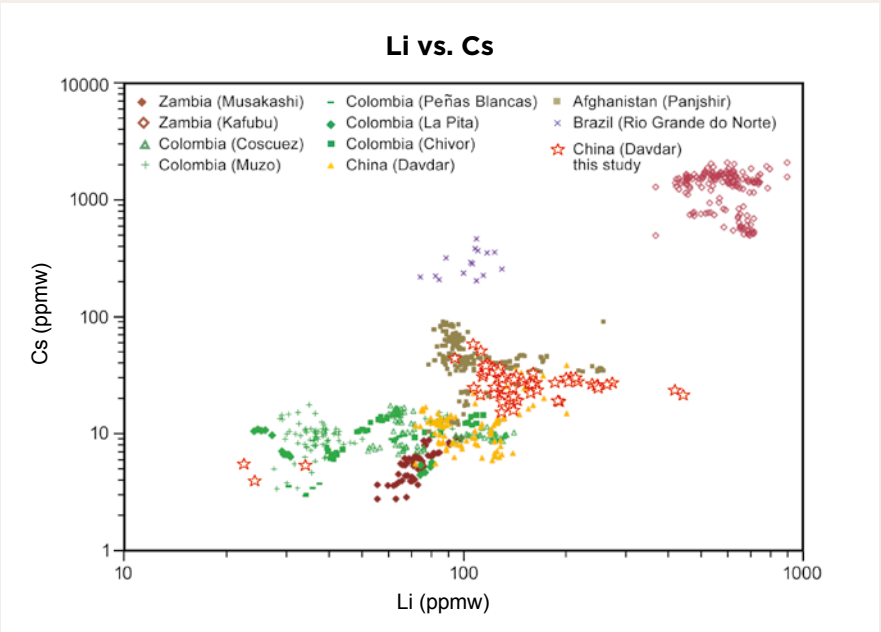

Figure 18: A logarithmic plot of Li vs. Cs in emeralds from various localities from Saeseaw *et al.* (2014)—with data from this study added for Davdar emeralds—also shows the similarity in chemical composition between stones from Davdar and Panjshir.

alkali-rich to alkali-poor conditions. Most samples were dominated by type II H_2O in their structural channels, although type I H_2O was more abundant in the rims of zoned samples. LA-ICP-MS data for Fe, Ga, Cs, Li and Sc offer useful information for differentiating Davdar emeralds from those of other localities except, in some cases, material from Panjshir, Afghanistan.

Figure 19: These diamond-set earrings feature Davdar emeralds (1.80 and 1.60 ct) and show the potential of this deposit to produce attractive gem-quality material. Courtesy of Fan Yaozeng; photo © Z. Zhou.

REFERENCES

An, Y.X. 2006. Geological characteristics of the emerald deposit in Taxkorgan, Xinjiang. *Xinjiang Nonferrous Metals*, **29**(2), 9–10, https://doi.org/10.16206/j.cnki.65-1136/tg.2006.02.003 (in Chinese).

Bai, F., Pan, H. & Li, X. 2019. Replacement degree of Al^{3+} and Cr/V ratio in high-V emeralds from Malipo, Yunnan, China. *Arabian Journal of Geosciences*, **12**, article 377 (9 pp.), https://doi.org/10.1007/s12517-019-4465-2.

Blak, A.R., Isotani, S. & Watanabe, S. 1983. Optical absorption and electron spin resonance in blue and green natural beryl: A reply. *Physics and Chemistry of Minerals*, **9**(6), 279–280, https://doi.org/10.1007/bf00309581.

Blauwet, D., Quinn, E. & Muhlmeister, S. 2005. Gem News International: New emerald deposit in Xinjiang, China. *Gems & Gemology*, **41**(1), 56–57.

Brigade No. 2, 2004. 1:50,000 *Geological Survey Internal Report of Davdar Emerald and Crystal Mine in Taxkorgan, Xinjiang*. Xinjiang Bureau of Geology and Mineral Resources, Ürümqi, China, 40 pp. (in Chinese).

Dvir, M. & Low, W. 1960. Paramagnetic resonance and optical spectrum of iron in beryl. *Physical Review*, **119**(5), 1587–1591, https://doi.org/10.1103/PhysRev.119.1587.

Gaite, J.M., Izotov, V.V., Nikitin, S.I. & Prosvirnin, S.Y. 2001. EPR and optical spectroscopy of impurities in two synthetic beryls. *Applied Magnetic Resonance*, **20**(3), 307–315, https://doi.org/10.1007/bf03162283.

Giuliani, G., Groat, L.A., Marshall, D., Fallick, A.E. & Branquet, Y. 2019. Emerald deposits: A review and enhanced classification. *Minerals*, **9**, article 105 (63 pp.), https://doi.org/10.3390/min9020105.

Hu, Y. & Lu, R. 2019. Unique vanadium-rich emerald from Malipo, China. *Gems & Gemology*, **55**(3), 338–352, https://doi.org/10.5741/gems.55.3.338.

Huong, L.T., Häger, T. & Hofmeister, W. 2010. Confocal micro-Raman spectroscopy: A powerful tool to identify natural and synthetic emeralds. *Gems & Gemology*, **46**(1), 36–41, https://doi.org/10.5741/gems.46.1.36.

Karampelas, S., Al-Shaybani, B., Mohamed, F., Sangsawong, S. & Al-Alawi, A. 2019. Emeralds from the most important occurrences: Chemical and spectroscopic data. *Minerals*, **9**, article 561 (29 pp.), https://doi.org/10.3390/min9090561.

Khaibullin, R.I., Lopatin, O.N., Vagizov, F.G., Bazarov, V.V., Bakhtin, A.I., Khaibullin, I.B. & Aktas, B. 2003. Coloration of natural beryl by iron ion implantation. *Nuclear Instruments and Methods in Physics Research Section B: Beam Interactions with Materials and Atoms*, **206**, 277–281, https://doi.org/10.1016/s0168-583x(03)00744-4.

Li, Q. & Zhu, X. 2002. Colouration mechanism and VIS, IR spectra of emerald from Malipo, Yunnan Province. *Journal of Gems & Gemmology*, **4**(1), 23–26 (in Chinese with English abstract).

Lin, J., Chen, N., Huang, D. & Pan, Y. 2013. Iron pairs in beryl: New insights from electron paramagnetic resonance, synchrotron X-ray absorption spectroscopy, and ab initio calculations. *American Mineralogist*, **98**(10), 1745–1753, https://doi.org/10.2138/am.2013.4472.

Liu, Y., Hu, Z., Gao, S., Günther, D., Xu, J., Gao, C. & Chen, H. 2008. *In situ* analysis of major and trace elements of anhydrous minerals by LA-ICP-MS without applying an internal standard. *Chemical Geology*, **257**(1–2), 34–43, https://doi.org/10.1016/j.chemgeo.2008.08.004.

Marfunin, A.S. 1984. *Introduction to Mineral Physics*. Geological Publishing House, Beijing, China (in Chinese).

Marshall, D., Pardieu, V., Loughrey, L., Jones, P. & Xue, G. 2012. Conditions for emerald formation at Davdar, China: Fluid inclusion, trace element and stable isotope studies. *Mineralogical Magazine*, **76**(1), 213–226, https://doi.org/10.1180/minmag.2012.076.1.213.

Michelou, J.C. & Pardieu, V. 2009. A glimpse of the new fine emerald deposit at Xinjiang's Davdar mine. *InColor*, No. 10, 26–30.

Ohkura, H., Hashimoto, H., Mori, Y., Chiba, Y. & Isotani, S. 1987. The luminescence and ESR of a synthetic emerald and the natural ones mined from Santa Terezinha in Brazil. *Japanese Journal of Applied Physics*, **26**(9), Part 1, 1422–1428, https://doi.org/10.1143/jjap.26.1422.

Ollier, N., Fuchs, Y., Cavani, O., Horn, A.H. & Rossano, S. 2015. Influence of impurities on Cr^{3+} luminescence properties in Brazilian emerald and alexandrite. *European Journal of Mineralogy*, **27**(6), 783–792, https://doi.org/10.1127/ejm/2015/0027-2484.

Pan, Y. & Nilges, M.J. 2014. Electron paramagnetic resonance spectroscopy: Basic principles, experimental techniques and applications to Earth and planetary sciences. *Reviews in Mineralogy and Geochemistry*, **78**, 655–690, https://doi.org/10.2138/rmg.2014.78.16.

Qi, L., Xia, Y. & Yuan, X. 2002. Channel-water molecular pattern and ^{1}H, ^{23}Na NMR spectra representation in synthetic red beryl. *Journal of Gems & Gemmology*, **4**(3), 8–16, https://doi.org/10.15964/j.cnki.027jgg.2002.03.004 (in Chinese with English abstract).

Qiao, X., Zhou, Z., Schwarz, D.T., Qi, L., Gao, J., Nong, P., Lai, M. *et al.* 2019. Study of the differences in infrared spectra of emerald from different mining areas and the controlling factors. *Canadian Mineralogist*, **57**(1), 65–79, https://doi.org/10.3749/canmin.1800042.

Saeseaw, S., Pardieu, V. & Sangsawong, S. 2014. Three-phase inclusions in emerald and their impact on origin determination. *Gems & Gemology*, **50**(2), 114–132, https://doi.org/10.5741/gems.50.2.114.

Saeseaw, S., Renfro, N.D., Palke, A.C., Sun, Z. & McClure, S.F. 2019. Geographic origin determination of emerald. *Gems & Gemology*, **55**(4), 614–646, https://doi.org/10.5741/gems.55.4.614.

Schmetzer, K., Schwarz, D., Bernhardt, H.-J. & Häger, T. 2006. A new type of Tairus hydrothermally-grown synthetic emerald, coloured by vanadium and copper. *Journal of Gemmology*, **30**(1), 59–74, https://doi.org/10.15506/JoG.2006.30.1.59.

Schwarz, D. & Schmetzer, K. 2002. The definition of emerald – The green variety of beryl colored by chromium and/or vanadium. *In*: Giuliani, G., Jarnot, M., Ottaway, T., Sinkankas, J. & Staebler, G. (eds) *Emeralds of the World – The Legendary Green Beryl*. Lapis International LLC, East Hampton, Connecticut, USA, 74–78.

Schwarz, D. & Pardieu, V. 2009. Emeralds from the Silk Road countries – A comparison with emeralds from Colombia. *InColor*, No. 12, 38–43.

Shannon, R.D. 1976. Revised effective ionic radii and systematic studies of interatomic distances in halides and chalcogenides. *Acta Crystallographica*, **A32**, 751–767, https://doi.org/10.1107/s0567739476001551.

Shao, H., Qi, L., Zhong, Q. & Zhou, Y. 2014. Study on characteristics of iron-rich hydrothermal synthetic emerald from Russia. *Journal of Gems & Gemmology*, **16**(1), 26–34, https://doi.org/10.15964/j.cnki.027jgg.2014.01.002 (in Chinese with English abstract).

Shi, G. 1999. FTIR features of Guilin hydrothermally-grown synthetic emerald and its significance. *Journal of Gems & Gemmology*, **1**(1), 40–46, https://doi.org/10.15964/j.cnki.027jgg.1999.01.010 (in Chinese with English abstract).

Taran, M.N. & Rossman, G.R. 2001. Optical spectroscopic study of tuhualite and a re-examination of the beryl, cordierite, and osumilite spectra. *American Mineralogist*, **86**(9), 973–980, https://doi.org/10.2138/am-2001-8-903.

Taran, M.N. & Vyshnevskyi, O.A. 2019. Be, Fe^{2+}-substitution in natural beryl: An optical absorption spectroscopy study. *Physics and Chemistry of Minerals*, **46**(8), 795–806, https://doi.org/10.1007/s00269-019-01040-2.

Wood, D.L. & Nassau, K. 1968. The characterization of beryl and emerald by visible and infrared absorption spectroscopy. *American Mineralogist*, **53**(5–6), 777–800.

Xue, G., Marshall, D., Zhang, S., Ullrich, T.D., Bishop, T., Groat, L.A., Thorkelson, D.J., Giuliani, G. *et al*. 2010. Conditions for Early Cretaceous emerald formation at Dyakou, China: Fluid inclusion, Ar-Ar, and stable isotope studies. *Economic Geology*, **105**(2), 339–349, https://doi.org/10.2113/gsecongeo.105.2.339.

Yu, X., Hu, D., Niu, X. & Kang, W. 2017. Infrared spectroscopic characteristics and ionic occupations in crystalline tunneling system of yellow beryl. *JOM*, **69**(4), 704–712, https://doi.org/10.1007/s11837-017-2266-1.

Zhang, P., Schwarz, D. & Lu, T. 2012. Chapter 3: Emerald. *In*: *Geographic Origin Determination of Coloured Gemstones*. Geological Press, Beijing, China, 392 pp. (in Chinese).

Zhao, M.G. 1991. Chapter 4: Optical, magnetic properties and EPR theory of paramagnetic crystals. *In*: *Theory on Crystal Field and Electron Paramagnetic Resonance*. Science Press, Beijing, China, 204–216 (in Chinese).

Zhou, Z.-J., Tang, H.-S., Wu, Y.-S., Li, Q.-G., Chen, Y.-J. & Chen, Z.-L. 2018. Geology, geochemistry and genesis of the Zankan iron deposit in the West Kunlun orogen, Xinjiang, China. *Ore Geology Reviews*, **100**, 334–346, https://doi.org/10.1016/j.oregeorev.2017.09.009.

Zong, K., Klemd, R., Yuan, Y., He, Z., Guo, J., Shi, X., Liu, Y., Hu, Z. *et al*. 2017. The assembly of Rodinia: The correlation of early Neoproterozoic (ca. 900 Ma) high-grade metamorphism and continental arc formation in the southern Beishan orogen, southern Central Asian Orogenic Belt (CAOB). *Precambrian Research*, **290**, 32–48, https://doi.org/10.1016/j.precamres.2016.12.010.

The Authors

Di Cui, Dr Zongting Liao, Lijian Qi, Dr Qian Zhong and Dr Zhengyu Zhou
State Key Laboratory of Marine Geology, Tongji University, Shanghai 200092, China; School of Ocean and Earth Science, Tongji University, Shanghai 200092, China; Laboratory of Gem and Technological Materials, Tongji University, Shanghai 200070, China
Emails: adamszzyu@126.com (Dr Zhengyu Zhou) or liaozt@tongji.edu.cn (Dr Zongting Liao)

Acknowledgements

The authors sincerely thank Dr Dietmar Schwarz and two anonymous reviewers for their constructive comments. We also acknowledge Zhangtai Bao, Lipin Chang, Paerhati, Yaozeng Fan and Jia Maliding for assistance with fieldwork and sample collection. Special thanks to Guimin Wong and her son Alex for providing information on Davdar emerald production. Further thanks go to Ling Li, Yan Zhou, Fangyue Wang, Lifang Zhou and Lingmin Zhang for their help with gem testing. This research was supported by special funding from the Shanghai Science and Technology Commission (15DZ2283200, 18DZ2281300) and the Gem Discipline Development Fund.

Characterisation of Pink-to-Red Spinel from Four Important Localities

Chawalit Chankhantha, Ratthaphon Amphon, Habib Ur Rehman and Andy H. Shen

ABSTRACT: Most pink-to-red spinel that is currently available on the global gem market originates from moderate- to high-grade metamorphic rocks. For this study, we characterised 60 such spinels from Myanmar, Tajikistan, Tanzania and Vietnam. They ranged from pink to red with orange or blue modifiers due to combinations of the chromophores Cr^{3+}, V^{3+} and Fe^{2+}. The most common mineral inclusions in the samples from Myanmar, Vietnam and Tanzania were apatite crystals and graphite platelets, and we also observed zircon in the spinels from Tanzania. Octahedral negative crystals and partially healed fractures were present in samples from all four origins, while dislocations/needles were found only in those from Tanzania and Vietnam. Linear discriminant analysis of chemical data obtained by LA-ICP-MS was performed using seven elements (Ti, V, Cr, Fe, Zn, Ga and Sn) and provided potential criteria for separating spinels from these four important localities.

The Journal of Gemmology, **37**(4), 2020, pp. 393–403, https://doi.org/10.15506/JoG.2020.37.4.393

Most gem-quality spinel is $MgAl_2O_4$ with the substitution of various minor-to-trace elements in the structural sites (Bowles *et al.* 2011). So-called *normal spinel* has the composition AB_2O_4, where A (Mg^{2+}) refers to the tetrahedral site and B (Al^{3+}) is the octahedral site. Another structural form of spinel is *inverse spinel*, for which the formula is written as $B(AB)O_4$, as seen in the structure of magnetite (Deer *et al.* 1992).

Gem-quality spinel (e.g. Figure 1) occurs mainly in East Africa, Central Asia and South East Asia. Most of the deposits are hosted in marble that has undergone metamorphism to amphibolite–granulite facies. In East Africa, gem spinel occurs in marbles and calc-silicate rocks that belong to the Neoproterozoic Mozambique Belt formed during the Pan-African orogeny (750–450 million years ago; Keller 1992; Balmer *et al.* 2017). Central Asia's spinel deposits are hosted by the Himalayan mountain belt, which formed during the Tertiary collision (since 45 million years ago) of the Indian Plate northward into the Eurasian Plate. This geologic activity resulted in massive

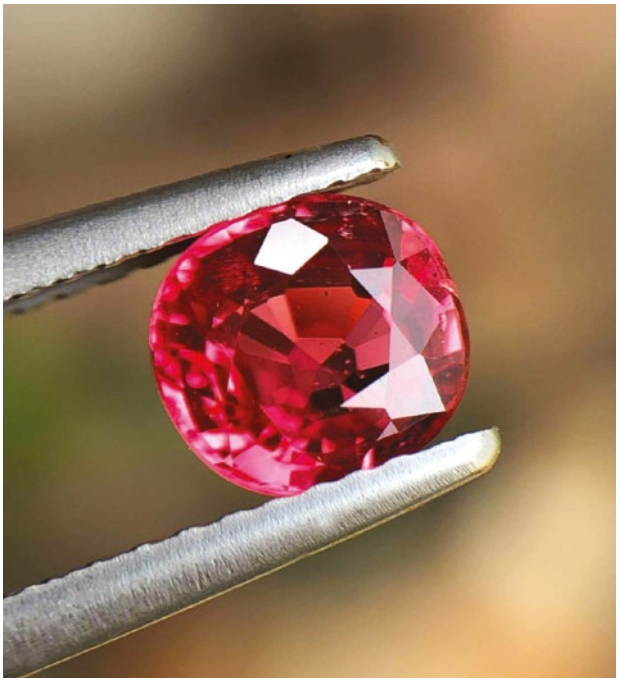

Figure 1: This 1.23 ct spinel is from Mogok, Myanmar. Photo courtesy of Poetry Gems & Jewelry, Chiang Mai, Thailand.

marble units that contain ruby, spinel and other gems (Garnier *et al.* 2008). Spinel deposits in South East Asia are found in various types of marble units that resulted from the metamorphism of an ancient carbonaceous platform. Regional metamorphism of these marbles (i.e. in Vietnam and Myanmar) took place during the Indosinian (250–240 million years ago) and Himalayan orogenies (Lepvrier *et al.* 2008; Huong *et al.* 2012).

Although small quantities of gem spinel have been mined in Sri Lanka, Madagascar, Pakistan, Nepal and Kenya (Okrusch *et al.* 1976; Shigley *et al.* 1990), most of the production in the pink-to-red colour range that is available today comes from four major localities: Myanmar, Tajikistan, Tanzania and Vietnam. In Myanmar, spinel has been mined from both primary and secondary deposits in the Mogok area, situated in the north-eastern part of the Mogok metamorphic belt, adjacent to the north-south trending Shan Scarp and Sagaing Fault (Chhibber 1934; Thein 2008; Themelis 2008). In addition, spinel is occasionally found in skarns (contact zones between carbonate rocks and magmatic intrusions) and in placer deposits of the Namya (or Nanyaseik) area in northern Myanmar (Aung & Zin 2018). In Tajikistan, spinel was first discovered at the historical Kuh-i-Lal mine, hosted by the Goran metamorphic series in the south-western Pamir Mountains (Hubbard *et al.* 1999). The spinel deposits mostly consist of enstatite-forsterite rocks associated with magnesian skarns (Kievlenko 2003). In Tanzania, spinel mining takes place in the Mahenge area, mainly at Ipanko (Pardieu & Hughes 2008; Kukharuk & Manna 2019). Vietnamese red-to-pink spinel occurs as crystals disseminated in marble units in the Luc Yen area, Yen Bai Province. The deposits are located in the Lo Gam tectonic zone and are hosted by the Thac Ba and An Phu metasedimentary sequences (Garnier *et al.* 2005; Pham Van *et al.* 2013).

In the current gem market, the price of pink-to-red spinels from Myanmar (e.g. Figure 1) is higher than those from other sources. It is therefore important to be able to identify the geographical origin of spinel in this colour range. Although a few reports on the geographical origin of gem spinel have been published (Malsy & Klemm 2010; Giuliani *et al.* 2017), multivariate statistical methods such as linear discriminant analysis have not been applied previously. In this study, we investigate the separation of pink-to-red spinel from Myanmar, Tajikistan, Tanzania and Vietnam using gemmological characteristics, internal features, spectroscopic data and multivariate statistical analysis of chemical data.

MATERIALS AND METHODS

We examined a total of 60 samples consisting of 15 spinels from each of four localities: Myanmar, Tajikistan, Tanzania and Vietnam (Figure 2 and Table I). The

Figure 2: Sixty pink-to-red spinels were studied for this article, including 15 from each of four localities: Myanmar (top row), Tajikistan (second row), Tanzania (third row) and Vietnam (bottom two rows). See Table I for weight ranges. Photo by C. Chankhantha.

Table I: Gemmological properties of the studied spinels.*

Property	Myanmar (Mogok)	Tajikistan (Kuh-i-Lal)	Tanzania (Mahenge)	Vietnam (Luc Yen)
Weight (ct)	0.54–3.01	0.19–0.84	0.77–2.95	0.92–6.95
Colour	Red to pink	Pink to purplish pink	Pink to red, some slightly orangey	Orangey pink to purplish pink and pink-red
Diaphaneity	Transparent	Transparent	Transparent to semi-transparent	Transparent
RI	1.716–1.720	1.712–1.714	1.715–1.720	1.714–1.720
SG	3.59–3.61	3.58–3.60	3.60–3.62	3.59–3.61

* All samples fluoresced moderate to strong red to long-wave UV radiation and were inert or fluoresced weak red to short-wave UV.

samples from Myanmar were cabochons and those from Tanzania were faceted, while the others mostly consisted of broken pieces with polished windows.

The samples were examined using standard gemmological instruments for their RI and hydrostatic SG values. Fluorescence was viewed under long-wave (366 nm) and short-wave (254 nm) UV radiation. Microscopic observations and photomicrography of internal features were recorded using a Leica M205 A microscope equipped with transmitted lighting and fibre-optic illumination. Mineral inclusions were identified using a Bruker Senterra R200-L Raman micro-spectrometer equipped with a 532 nm laser (20 mW laser output power and spot size of 50 µm). The Raman spectra were interpreted using OriginPro 2018 software and compared to spectra in the RRUFF database.

Ultraviolet-visible (UV-Vis) absorption spectra were collected from two samples from each locality using a Jasco MSV-5200 spectrometer, in the range 250–800 nm, with a slit width of 2.0 mm, a data interval of 1.0 nm and scan speed of 266.75 nm/min.

Chemical analyses of five samples from each locality were performed using laser ablation inductively coupled plasma mass spectrometry (LA-ICP-MS) at Wuhan Sample Solution Analytical Technology Co. Ltd with an Agilent 7700 Series ICP-MS coupled with a GeoLas Pro 193 nm excimer laser. The laser employed a 5 Hz pulse rate and a 44 µm diameter spot size. Reference materials included USGS glasses (BCR-2G, BHVO-2G and BIR-1G) and NIST glass (SRM 610), and ^{29}Si was used as the normalised element to calculate the concentrations of 55 elements with ICPMSDataCal software (Liu *et al.* 2008).

Multivariate statistical analysis of the LA-ICP-MS chemical data was performed by linear discriminant analysis (LDA) using the IBM SPSS Statistics software package (version 26). LDA is a statistical tool that aims to maximise between-class variance while minimising within-class variance in order to group information and provide reliable, accurate classification criteria (Fisher 1936; McLachlan 2004; Guo *et al.* 2007).

RESULTS AND DISCUSSION

The gemmological properties of the spinels are summarised in Table I. The Myanmar samples were predominantly red, while those from Tajikistan were pink to purplish pink. The spinels from Tanzania were pink to red (some with a slightly orangey cast), and those from Vietnam were orangey pink to purplish pink and pink-red. The tone of the stones ranged from light to medium and the saturation was pale to moderate. No colour zoning was observed. The samples were mostly transparent, although some from Tanzania appeared cloudy due to numerous tiny inclusions.

Gemmological Properties

The RI of the samples varied from 1.712 to 1.720 and the SG range was 3.58–3.62 (Table I). The lowest RI and SG values were measured for the spinels from Tajikistan. All samples were isotropic without anomalous birefringence, and all displayed moderate to strong red fluorescence to long-wave UV radiation and were weak red or inert under short-wave UV radiation. These properties are consistent with those of gem-quality spinels reported in the literature (Malsy & Klemm 2010; Bowles *et al.* 2011).

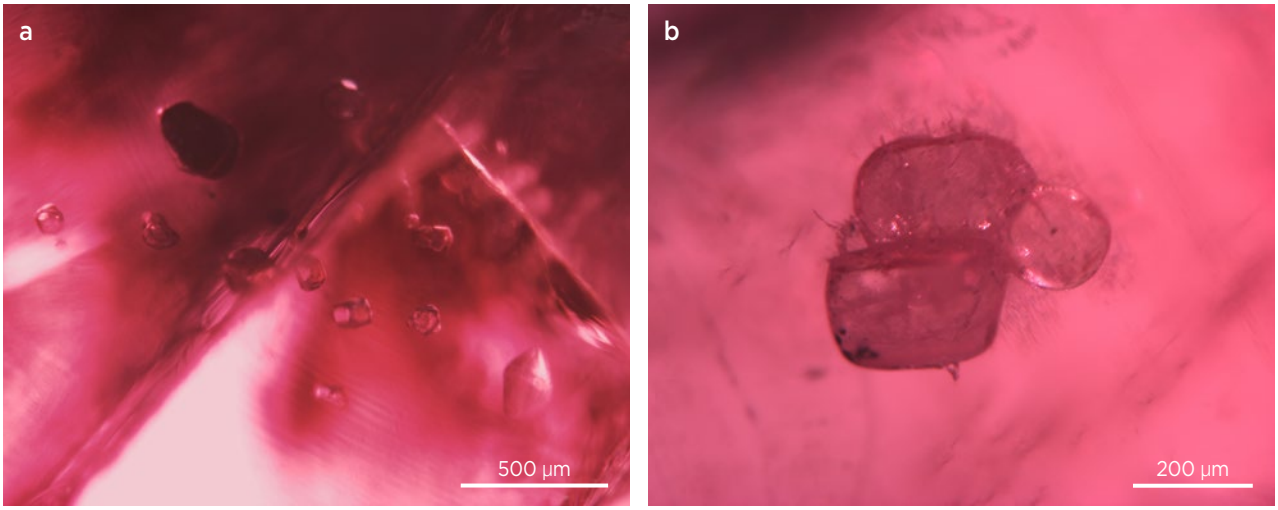

Figure 3: Apatite inclusions are seen here in spinels from (**a**) Myanmar and (**b**) Vietnam, and were also noted in the Tanzanian samples. Photomicrographs by C. Chankhantha.

Microscopic Features

The internal characteristics of spinel from various localities have been reported previously by different researchers (e.g. Gübelin & Koivula 1986; Malsy & Klemm 2010; Phyo *et al.* 2019). In our samples, colourless apatite (Figure 3) occurred as single crystals and clusters in the spinels from Myanmar, Tanzania and Vietnam. Black graphite platelets (Figure 4) were also found in the samples from these localities. The graphite was derived from the metamorphism of organic substances (Giuliani *et al.* 2008). The spinels from Tajikistan contained only some negative crystals and 'fingerprints' (Figure 5), and these features were also seen in samples from the three other localities. In our samples we did not observe any apatite crystals with graphite attached to their surface, sometimes known as 'belly button' inclusions (Gübelin & Koivula 2005).

The spinels from Tanzania commonly contained numerous short needles or particles oriented parallel to octahedral {111} directions (Figure 6), giving them a somewhat cloudy appearance. These needles or particles were possibly caused by the exsolution of högbomite, as previously mentioned by Schmetzer and Berger (1992). Some of the Tanzanian samples also contained zircon inclusions that were usually surrounded by a tension crack (Figure 7).

The most common inclusions in our samples from Vietnam were dislocation needles, usually oriented along crystallographic directions (Figure 8a), which appear to be diagnostic for spinel from this locality (Malsy & Klemm 2010; Hughes *et al.* 2019). Some of the Vietnamese samples also contained planar arrays of octahedral negative crystals (Figure 8b).

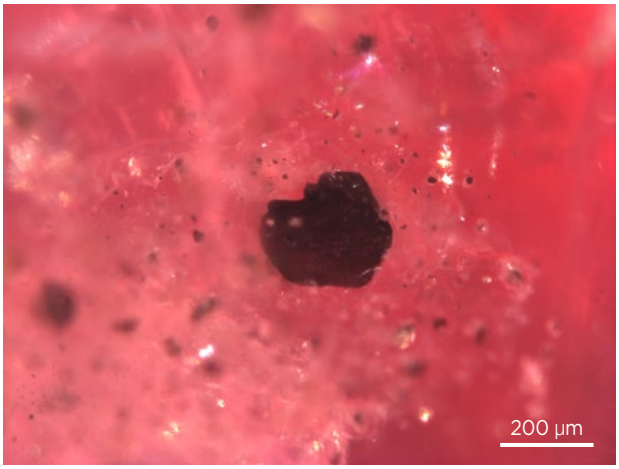

Figure 4: Graphite platelets, shown here in a spinel from Tanzania, were observed in samples from Myanmar and Vietnam. Photomicrograph by C. Chankhantha.

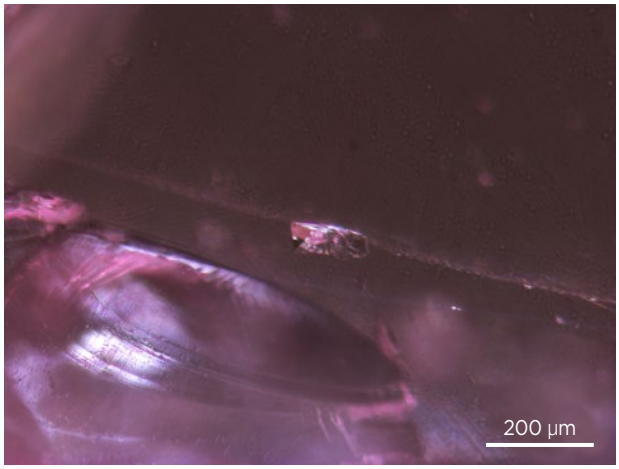

Figure 5: This negative crystal with a 'fingerprint' is typical of the relatively few inclusions seen in our spinel samples from Tajikistan. Photomicrograph by C. Chankhantha.

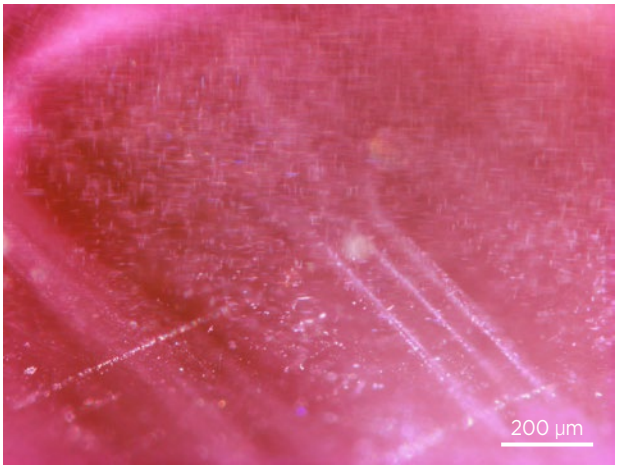

Figure 6: Numerous short needles oriented parallel to octahedral {111} directions contribute to a cloudy appearance exhibited by some of our Tanzanian spinels. Photomicrograph by C. Chankhantha.

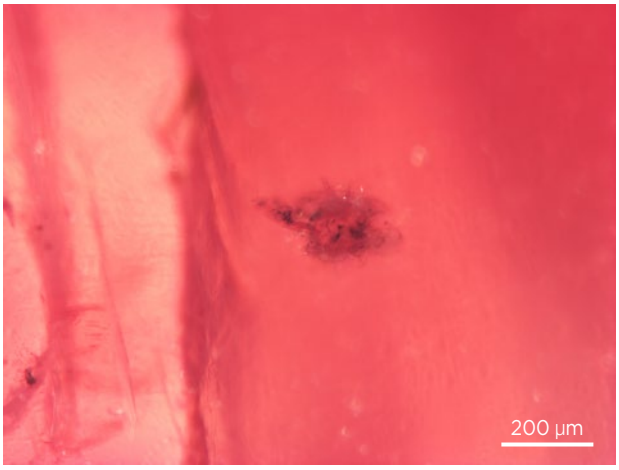

Figure 7: Zircon crystals occurred in some of the spinels from Tanzania. This one is surrounded by a tension crack. Photomicrograph by C. Chankhantha.

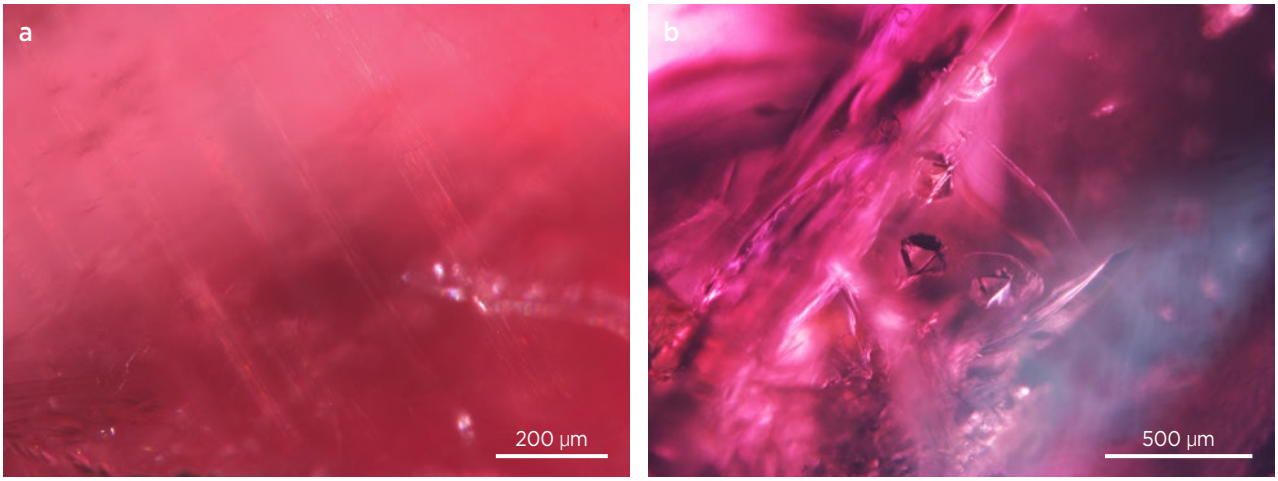

Figure 8: (**a**) Parallel dislocation needles aligned in crystallographic directions appear to be a diagnostic feature of Vietnamese spinel. (**b**) Octahedral negative crystals are present in this Vietnamese spinel. Photomicrographs by C. Chankhantha.

UV-Vis Absorption Spectra

All of the spinel samples revealed well-known Cr^{3+} absorption bands at 392, 415 and 538 nm (Figure 9). Some had an orangey hue, probably due to V^{3+} (Kleišmantas & Daukšytė 2016), although the absorption bands of Cr^{3+} and V^{3+} are generally superimposed (Schmetzer *et al.* 1989; Malsy & Klemm 2010; Andreozzi *et al.* 2019). Also present in the spectra was a peak at 372 nm due to Fe^{2+}.

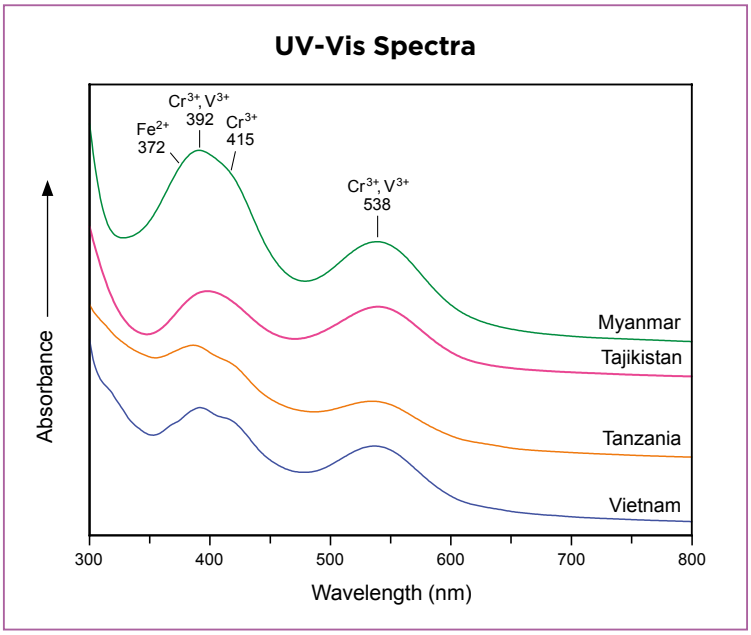

Figure 9: Representative UV-Vis absorption spectra of spinel from all four localities reveal absorption bands related to Cr^{3+}, V^{3+} and Fe^{2+}.

Table II: Chemical composition of the studied spinels, as determined by LA-ICP-MS.*

Element (ppmw)	Myanmar (Mogok)	Tajikistan (Kuh-i-Lal)	Tanzania (Mahenge)	Vietnam (Luc Yen)
Ti	441–1270 (923)	107–197 (156)	70.7–97.5 (83.2)	24.8–157 (106)
V	560–1050 (870)	261–432 (336)	513–1520 (1040)	525–1600 (969)
Cr	9130–15600 (12900)	280–475 (409)	871–2640 (1840)	772–3460 (1940)
Fe	657–2010 (1140)	2160–4250 (3190)	2470–4300 (3330)	4630–11600 (7920)
Ni	6.22–40.6 (18.3)	nd–3.65 (0.87)	3.01–16.0 (12.5)	nd–42.1 (20.6)
Zn	482–4320 (2210)	589–755 (676)	3450–5520 (4640)	200–1460 (674)
Ga	61.0–226 (165)	159–316 (231)	153–214 (181)	81.4–238 (152)
Sn	24.9–38.9 (30.3)	42.1–53.6 (49.0)	29.0–43.5 (35.4)	46.6–58.5 (52.4)

* Average amounts are shown in parentheses; nd = not detected.

Chemical Composition

LA-ICP-MS data for the studied spinels are summarised in Table II. The chromophores Cr, V and Fe were present in various concentrations, whereas Ti, Ni, Ga and Sn were generally low. In addition, Zn was present in significant amounts.

The red Burmese spinels contained the highest contents of Cr, and Ti was also somewhat elevated, as compared to data for the other three localities. The Tanzanian spinels showed the highest Zn contents (3450–5520 ppm), which could be considered characteristic of material from this deposit. Next highest in Zn were the Burmese spinels, ranging from 482 to 4320 ppm. This is consistent with some studies that have shown Zn to be higher in Mogok spinels compared to those from Tajikistan and Vietnam (Malsy & Klemm 2010). The concentrations of Ga and Sn in our spinels did not vary in any significant way. The pink spinels from Tajikistan showed low to moderate values for Ti, Fe and Zn along with the lowest average concentrations of Cr and Ni among the four deposits. The Luc Yen spinels had the highest average Fe content (7920 ppm).

Discrimination of the pink-to-red spinels from the four localities was initially attempted by plotting V+Cr, Fe and Zn in a ternary diagram (Figure 10). While our samples from Myanmar and Tanzania could be distinguished from the other localities, the spinels from Vietnam and Tajikistan showed some overlap and thus require another method of separation.

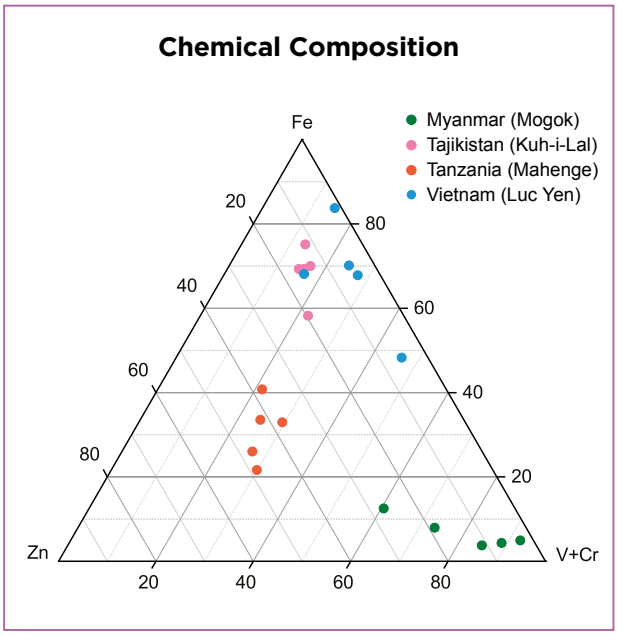

Figure 10: This ternary plot of V+Cr, Fe and Zn shows separate groupings for spinels from Myanmar and Tanzania, but considerable overlap for samples from Vietnam and Tajikistan.

Linear Discriminant Analysis

LDA has been applied to country-of-origin determination for various gem materials, such as corundum (Pornwilard *et al.* 2011; Giuliani *et al.* 2020; Krebs *et al.* 2020), Cu-bearing tourmaline (Blodgett & Shen 2011), nephrite jade (Luo *et al.* 2015, 2018; Yu *et al.* 2018) and peridot (Zhang *et al.* 2019). We applied LDA to our spinel data using the elements Ti, V, Cr, Fe, Zn, Ga and Sn as possible independent variables. (Nickel was not included in the final data processing since we found that it did not provide any significant effect on the LDA results). Calculations based on these seven variables yielded three linear discriminant functions (DFs):

$$DF1 = (Cr \times 0.001) + (Zn \times 0.001) - (Ga \times 0.003) - (Sn \times 0.121) + 0.056$$

$$DF2 = (Ti \times 0.002) + (V \times 0.004) - (Cr \times 0.001) + (Zn \times 0.001) - (Ga \times 0.015) - (Sn \times 0.049) - 0.923$$

$$DF3 = (Ti \times 0.001) + (V \times 0.003) + (Fe \times 0.001) + (Ga \times 0.008) + (Sn \times 0.139) - 13.757$$

When evaluating LDA results, the so-called eigenvalue provides an indication of the effectiveness of the discriminant functions for differentiating groups (Norušis 1990). In this work, the eigenvalue was highest for DF1 (37.053), followed by DF2 and DF3 (13.761 and 5.091, respectively). All three DFs were selected to build the classification model, in order to provide better separation between groups.

Two- and three-dimensional scatter diagrams produced from these DFs successfully separated our spinel samples into four discriminant areas according to the different localities (Figures 11 and 12). Cross-validation indicated that these results were nearly 100% accurate. Nevertheless, the present analyses of our samples provide only a preliminary data set, and further chemical data should be evaluated with this technique. LDA could provide a complementary tool to determine the geographic origin of spinel samples, but such distinctions should also include other factors to increase precision, such as gemmological and internal characteristics.

Comparison of Spinel Geological Environments and Compositions

Gem-quality spinel typically forms during moderate- to high-grade metamorphism in various lithologies, including calc-silicate rocks and marbles (e.g. Balmer *et al.* 2017) or skarns (e.g. Gorghinian *et al.* 2013). Spinel is also found in placers derived from these rocks (e.g. Thein 2008). The concentrations of elements such as Fe, Zn, Cr and V in spinel are controlled by the local geological environment (e.g. based on their abundance in either the initial protolith or in the host marble; Giuliani *et al.* 2017; Pham Van *et al.* 2018).

In Myanmar, spinel is typically found in granulite-facies marbles in the Mogok Metamorphic Belt formed during the Himalayan orogeny (Iyer 1953; Giuliani *et al.* 2017). These marbles are comprised of calcite, dolomite,

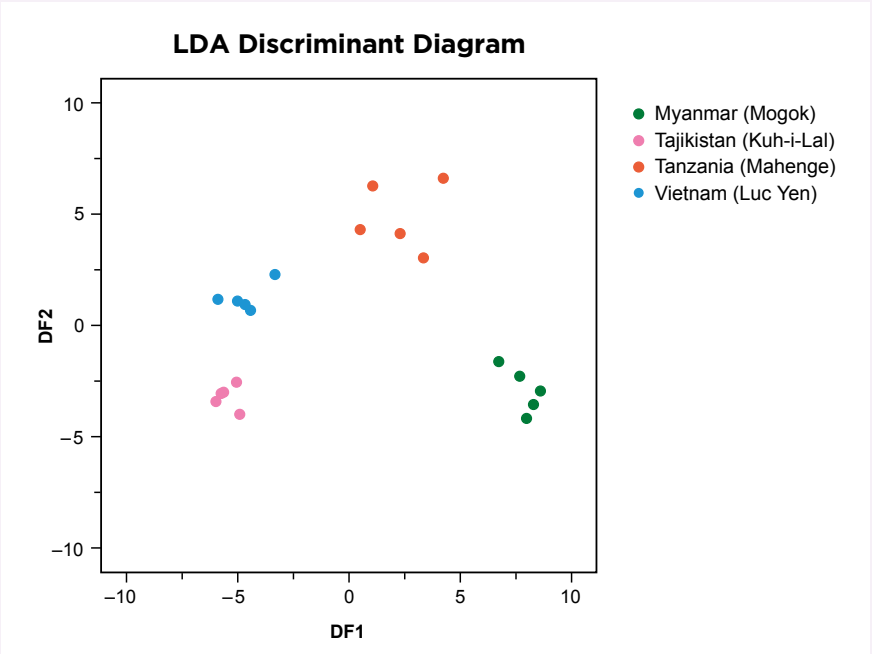

Figure 11: A two-dimensional plot of two of the linear discriminant functions obtained by LDA displays four groupings that distinguish pink-to-red spinels from the different localities.

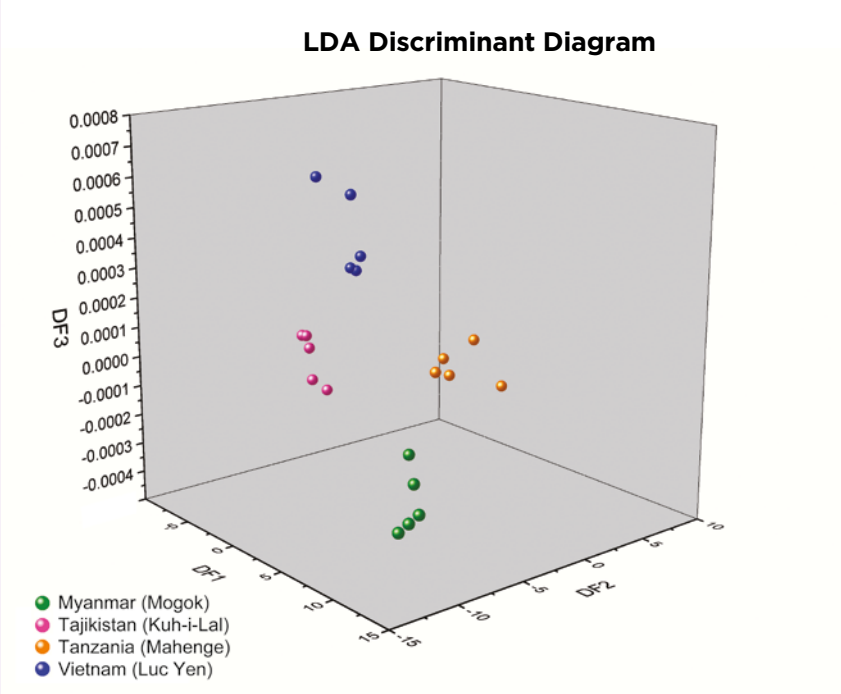

Figure 12: A three-dimensional plot of all three linear discriminant functions obtained by LDA also shows a clear separation for the pink-to-red spinels from the four localities.

diopside, chondrodite, pargasite, clinohumite, forsterite, phlogopite, apatite, dravite, pyrite and graphite (Zaw *et al.* 2015). The Burmese spinels in this study typically contained relatively low Fe (657–2010 ppm), consistent with the nature of the marble host rock. It has been proposed that such Fe-poor spinels originated from pure marbles (Themelis 2008), while the Cr chromophore came from relicts of nearby initial magmatic rocks (Schwarz *et al.* 2008) or entered the sedimentary basin as impurities in clays (Garnier *et al.* 2008) prior to metamorphism. The red colouration of spinel is intensified by Cr content, and our Mogok spinels contained elevated Cr (up to 15600 ppm) compared to our samples from the other localities (again, see Table II). In addition, the Ti content of our Mogok spinels (441–1270 ppm) was higher than our samples from elsewhere.

In Tajikistan, spinel mineralisation at Kul-i-Lal is hosted by enstatite-forsterite rocks associated with magnesian skarns (Hubbard *et al.* 1999; Kievlenko 2003), and either formed during upper amphibolite- to granulite-facies metamorphism or derived from a metasomatic by-product of fluid infiltration during contact metamorphism (Giuliani *et al.* 2017). The relatively low Cr and V concentrations in our spinels from this source—which probably are related to the composition of the host rocks—are consistent with their lighter colour compared to the other samples.

In the Mahenge area of Tanzania, spinel crystallised in dolomitic marbles that underwent granulite-facies metamorphism (approximately 750–850°C at 9.5–12 kbar) within the Neoproterozoic Mozambique Belt (Möller *et al.* 2000; Hauzenberger *et al.* 2007; Giuliani *et al.* 2015). The mineral assemblage is characterised by corundum-calcite-plagioclase-phlogopite ± dolomite, pargasite, sapphirine, titanite and tourmaline (Balmer *et al.* 2017). The Mahenge spinels in this study are characterised by significantly greater Zn (3450–5520 ppm) than in those from the other three localities. The Zn could have been derived from the decomposition of biotite (Tajčmanová *et al.* 2009) or the breakdown of staurolite (Stoddard 1979; Spry 1982).

In Luc Yen, Vietnam, spinel formed in calcitic to dolomitic marbles within the Lo Gam tectonic zone, which forms the eastern part of the Red River shear zone (Pham Van 1996; Garnier *et al.* 2005). The marbles contain calcite, dolomite, forsterite, clinohumite, pargasite, phlogopite and chlorite (Hofmeister 2001). Although the mineralisation at Luc Yen is similar to that of Mogok, and likewise took place during the Himalayan orogeny, the chemical composition of Luc Yen spinel differs significantly by its higher Fe contents (4630–11600 ppm), which exceeded the values obtained for our samples from the other three localities.

Despite the limited amount of data obtained in this study for each specific locality, the chemical results appear to be typical for these geological settings when compared to some previous studies (Malsy & Klemm 2010; Giuliani *et al.* 2017).

CONCLUSIONS

Pink-to-red spinels (e.g. Figure 13) make up a significant part of the coloured stone market, and most of the production comes from marble-hosted deposits. The pink-to-red spinels examined for this study from Myanmar (Mogok), Tajikistan (Kuh-i-Lal), Tanzania (Mahenge) and Vietnam (Luc Yen) showed overlapping gemmological characteristics except that the RI range of samples from Tajikistan was lower than the values obtained for the other localities. Many of the internal features in our spinels from the four localities were similar, but some could be indicative of specific origins, such as the short needles in the Mahenge material and the dislocation needles in the Luc Yen spinels.

Elements such as Ti, V, Cr, Fe and Zn can be factors in spinel origin determination. Among the samples from the four localities examined in this study, those from Mahenge were highest in Zn, whereas the Mogok spinels were relatively Ti rich and Fe poor, and the Luc Yen spinels were generally Fe rich. Nevertheless, compositional overlap can be a problem for spinel origin determination. Statistical analysis by LDA of seven elements (Ti, V, Cr, Fe, Zn, Ga and Sn) was successful at separating our spinel samples according to their four localities. Although only a limited dataset was obtained in this study, our results suggest that LDA could be a useful diagnostic tool for origin determination of pink-to-red spinels when combined with gemmological properties and internal features.

Figure 13: These spinels are from Myanmar (left, 2.39 ct and centre, 1.83 ct) and Tanzania (right, 3.34 ct). Courtesy of RareSource, Chattanooga, Tennessee, USA; photo by Orasa Weldon.

REFERENCES

Andreozzi, G.B., D'Ippolito, V., Skogby, H., Hålenius, U. & Bosi, F. 2019. Color mechanisms in spinel: A multi-analytical investigation of natural crystals with a wide range of coloration. *Physics and Chemistry of Minerals*, **46**(4), 343–360, https://doi.org/10.1007/s00269-018-1007-5.

Aung, H.L. & Zin, T.T. 2018. Exploring gemstones in northern part of Myanmar. *In*: Lin, J.W., Pan, J.S., Chu, S.C. & Chen, C.M. (eds.) *Genetic and Evolutionary Computing*. ICGEC 2017, Advances in Intelligent Systems and Computing, **579**, Springer, Singapore, 182–188, https://doi.org/10.1007/978-981-10-6487-6_22.

Balmer, W.A., Hauzenberger, C.A., Fritz, H. & Sutthirat, C. 2017. Marble-hosted ruby deposits of the Morogoro region, Tanzania. *Journal of African Earth Sciences*, **134**, 626–643, https://doi.org/10.1016/j.jafrearsci.2017.07.026.

Blodgett, T. & Shen, A. 2011. Application of discriminant analysis in gemology: Country-of-origin separation in colored stones and distinguishing HPHT-treated diamonds. *Gems & Gemology*, **47**(2), 145.

Bowles, J.F.W., Howie, R.A., Vaughan, D.J. & Zussman, J. 2011. *Rock-Forming Minerals—Non-Silicates: Oxides, Hydroxides and Sulphides*, Vol. 5A, 2nd edn. The Geological Society, London, 920 pp.

Chhibber, H.L. 1934. *The Geology of Burma*. Macmillan and Co. Ltd, London, xxviii + 538 pp.

Deer, W.A., Howie, R.A. & Zussman, J. 1992. *An Introduction to the Rock-Forming Minerals*, 2nd edn. Longman Scientific & Technical, Harlow, Essex, 696 pp.

Fisher, R.A. 1936. The use of multiple measurements in taxonomic problems. *Annals of Eugenics*, **7**(2), 179–188, https://doi.org/10.1111/j.1469-1809.1936.tb02137.x.

Garnier, V., Ohnenstetter, D., Giuliani, G., Maluski, H., Deloule, E., Phan Trong, T., Pham Van, L. & Hoang Quang, V. 2005. Age and significance of ruby-bearing marble from the Red River shear zone, northern Vietnam. *Canadian Mineralogist*, **43**(4), 1315–1329, https://doi.org/10.2113/gscanmin.43.4.1315.

Garnier, V., Giuliani, G., Ohnenstetter, D., Fallick, A.E., Dubessy, J., Banks, D., Vinh, H.Q., Lhomme, T. *et al*. 2008. Marble-hosted ruby deposits from Central and Southeast Asia: Towards a new genetic model. *Ore Geology Reviews*, **34**(1–2), 169–191, https://doi.org/10.1016/j.oregeorev.2008.03.003.

Giuliani, G., Ohnenstetter, D., Palhol, F., Feneyrol, J., Boutroy, E., De Boissezon, H. & Lhomme, T. 2008. Karelianite and vanadian phlogopite from the Merelani Hills gem zoisite deposits, Tanzania. *Canadian Mineralogist*, **46**(5), 1183–1194, https://doi.org/10.3749/canmin.46.5.1183.

Giuliani, G., Martelat, J.-E., Ohnenstetter, D., Feneyrol, J., Fallick, A.E. & Boyce, A.J. 2015. Les gisements de rubis et de spinelle rouge de la Ceinture Métamorphique Néoprotérozoique Mozambicaine. *Revue de Gemmologie*, No. 192, 11–18 (in French with English abstract).

Giuliani, G., Fallick, A.E., Boyce, A.J., Pardieu, V. & Pham Van, L. 2017. Pink and red spinels in marble: Trace elements, oxygen isotopes, and sources. *Canadian Mineralogist*, **55**(4), 743–761, https://doi.org/10.3749/canmin.1700009.

Giuliani, G., Groat, L., Fallick, A., Pignatelli, I. & Pardieu, V. 2020. Ruby deposits: A review and geological classification. *Minerals*, **10**(7), article 597 (83 pp.), https://doi.org/10.3390/min10070597.

Gorghinian, A., Mottana, A., Rossi, A., Oltean, F.M., Esposito, A. & Marcelli, A. 2013. Investigating the colour of spinel: 1. Red gem-quality spinels ("balas") from Ratnapura (Sri Lanka). *Rendiconti Lincei*, **24**(2), 127–140, https://doi.org/10.1007/s12210-013-0223-7.

Gübelin, E.J. & Koivula, J.I. 1986. *Photoatlas of Inclusions in Gemstones*. ABC Edition, Zurich, Switzerland, 532 pp.

Gübelin, E.J. & Koivula, J.I. 2005. *Photoatlas of Inclusions in Gemstones*, Vol. 2. Opinio Publishers, Basel, Switzerland, 829 pp.

Guo, Y., Hastie, T. & Tibshirani, R. 2007. Regularized linear discriminant analysis and its application in microarrays. *Biostatistics*, **8**(1), 86–100, https://doi.org/10.1093/biostatistics/kxj035.

Hauzenberger, C.A., Sommer, H., Fritz, H., Bauernhofer, A., Kröner, A., Hoinkes, G., Wallbrecher, E. & Thöni, M. 2007. SHRIMP U–Pb zircon and Sm–Nd garnet ages from the granulite-facies basement of SE Kenya: Evidence for Neoproterozoic polycyclic assembly of the Mozambique Belt. *Journal of the Geological Society*, **164**(1), 189–201, https://doi.org/10.1144/0016-76492005-081.

Hofmeister, W. 2001. Modelling some mineralizations of typical Vietnamese gem deposits. *International Workshop on Material Characterization by Solid State Spectroscopy: Gems and Minerals of Vietnam*, Hanoi, Vietnam, 4–10 April, 10–18.

Hubbard, M.S., Grew, E.S., Hodges, K.V., Yates, M.G. & Pertsev, N.N. 1999. Neogene cooling and exhumation of upper-amphibolite-facies 'whiteschists' in the southwest Pamir Mountains, Tajikistan. *Tectonophysics*, **305**(1–3), 325–337, https://doi.org/10.1016/s0040-1951(99)00012-8.

Hughes, E.B., Koivula, J.I., Renfro, N., Manorotkul, W. & Hughes, R.W. 2019. Spinel inclusions, an exercise in aesthetics. *InColor*, No. 43, 66–73.

Huong, L.T.-T., Häger, T., Hofmeister, W., Hauzenberger, C., Schwarz, D., Pham Van, L., Wehrmeister, U., Nguyen Ngoc, K., & Nguy Tuyet, N. 2012. Gemstones from Vietnam: An update. *Gems & Gemology*, **48**(3), 158–176, https://doi.org/10.5741/GEMS.48.3.158.

Iyer, L.A.N. 1953. *The Geology and Gem-stones of the Mogok Stone Tract, Burma*. Geological Survey of India, Calcutta, Delhi, India, 100 pp.

Keller, P.C. 1992. *Gemstones of East Africa*. Geoscience Press, Tucson, Arizona, USA, 144 pp.

Kievlenko, E.Y. 2003. *Geology of Gems*. Ocean Pictures Ltd, Littleton, Colorado, USA, 468 pp.

Kleišmantas, A. & Daukšytė, A. 2016. The influence of Vietnam and Sri Lanka spinel mineral chemical elements on colour. *Chemija*, **27**(1), 45–51.

Krebs, M., Hardman, M., Pearson, D., Luo, Y., Fagan, A. & Sarkar, C. 2020. An evaluation of the potential for determination of the geographic origin of ruby and sapphire using an expanded trace element suite plus Sr–Pb isotope compositions. *Minerals*, **10**(5), article 447 (37 pp.), https://doi.org/10.3390/min10050447.

Kukharuk, M. & Manna, C. 2019. The spinels of Mahenge, Tanzania. *InColor*, No. 43, 54–58.

Lepvrier, C., Nguyen Van, V., Maluski, H., Phan Truong, T. & Tich Van, V. 2008. Indosinian tectonics in Vietnam. *Comptes Rendus Geoscience*, **340**(2–3), 94–111, https://doi.org/10.1016/j.crte.2007.10.005.

Liu, Y., Hu, Z., Gao, S., Günther, D., Xu, J., Gao, C. & Chen, H. 2008. *In situ* analysis of major and trace elements of anhydrous minerals by LA-ICP-MS without applying an internal standard. *Chemical Geology*, **257**(1–2), 34–43, https://doi.org/10.1016/j.chemgeo.2008.08.004.

Luo, Z., Yang, M. & Shen, A.H. 2015. Origin determination of dolomite-related white nephrite through iterative-binary linear discriminant analysis. *Gems & Gemology*, **51**(3), 300–311, https://doi.org/10.5741/gems.51.3.300.

Luo, Z., Shen, A.H. & Chen, M. 2018. Quantitative identification of green nephrite from five major origins in Asia and North America. *Gems & Gemology*, **54**(3), 259–260.

Malsy, A. & Klemm, L. 2010. Distinction of gem spinels from the Himalayan mountain belt. *CHIMIA International Journal for Chemistry*, **64**(10), 741–746, https://doi.org/10.2533/chimia.2010.741.

McLachlan, G.J. 2004. *Discriminant Analysis and Statistical Pattern Recognition*. John Wiley & Sons Inc., Hoboken, New Jersey, USA, 526 pp.

Möller, A., Mezger, K. & Schenk, V. 2000. U–Pb dating of metamorphic minerals: Pan-African metamorphism and prolonged slow cooling of high pressure granulites in Tanzania, East Africa. *Precambrian Research*, **104**(3–4), 123–146, https://doi.org/10.1016/s0301-9268(00)00086-3.

Norušis, M.J. 1990. *SPSS/PC+ Advanced Statistics 4.0 for the IBM PC/XT/AT and PS/2*. SPSS Inc., Chicago, Illinois, USA, 372 pp.

Okrusch, M., Bunch, T.E. & Bank, H. 1976. Paragenesis and petrogenesis of a corundum-bearing marble at Hunza (Kashmir). *Mineralium Deposita*, **11**(3), 278–297, https://doi.org/10.1007/bf00203079.

Pardieu, V. & Hughes, R.W. 2008. Spinel: Resurrection of a classic. *InColor*, No. 8, 10–18.

Pham Van, L. 1996. Preliminary results of the study on the genesis and the forming condition of corundum at Luc Yen mine. *Journal of Geology, Series A*, No. 252, 71–74.

Pham Van, L., Pardieu, V. & Giuliani, G. 2013. Update on gemstone mining in Luc Yen, Vietnam. *Gems & Gemology*, **49**(4), 233–246, https://doi.org/10.5741/gems.49.4.233.

Pham Van, L., Giuliani, G., Fallick, A.E., Boyce, A.J. & Pardieu, V. 2018. Trace elements and oxygen isotopes of gem spinels in marble from the Luc Yen - An Phu areas, Yen Bai Province, North Vietnam. *Vietnam Journal of Earth Sciences*, **40**(2), 165–177, https://doi.org/10.15625/0866-7187/40/2/12241.

Phyo, M.M., Franz, L., Bieler, E., Balmer, W. & Krzemnicki, M.S. 2019. Spinel from Mogok, Myanmar—A detailed inclusion study by Raman microspectroscopy and scanning electron microscopy. *Journal of Gemmology*, **36**(5), 418–435, https://doi.org/10.15506/JoG.2019.36.5.418.

Pornwilard, M.M., Hansawek, R., Shiowatana, J. & Siripinyanond, A. 2011. Geographical origin classification of gem corundum using elemental fingerprint analysis by laser ablation inductively coupled plasma mass spectrometry. *International Journal of Mass Spectrometry*, **306**(1), 57–62, https://doi.org/10.1016/j.ijms.2011.06.010.

Schmetzer, K. & Berger, A. 1992. Lamellar inclusions in spinels from Morogoro area, Tanzania. *Journal of Gemmology*, **23**(2), 93–94, https://doi.org/10.15506/JoG.1992.23.2.93.

Schmetzer, K., Haxel, C. & Amthauer, G. 1989. Colour of natural spinels, gahnospinels and gahnites. *Neues Jahrbuch für Mineralogie, Abhandlungen*, **160**(2), 159–180.

Schwarz, D., Pardieu, V., Saul, J.M., Schmetzer, K., Laurs, B.M., Giuliani, G., Klemm, L., Malsy, A.-K. *et al*. 2008. Rubies and sapphires from Winza, central Tanzania. *Gems & Gemology*, **44**(4), 322–347, https://doi.org/10.5741/gems.44.4.322.

Shigley, J.E., Dirlam, D.M., Schmetzer, K. & Jobbins, E.A. 1990. Gem localities of the 1980s. *Gems & Gemology*, **26**(1), 4–31, https://doi.org/10.5741/gems.26.1.4.

Spry, P.G. 1982. An unusual gahnite-forming reaction, Geco base-metal deposit, Manitouwadge, Ontario. *Canadian Mineralogist*, **20**(4), 549–553.

Stoddard, E.F. 1979. Zinc-rich hercynite in high-grade metamorphic rocks: A product of dehydration of staurolite. *American Mineralogist*, **64**(7–8), 736–741.

Tajčmanová, L., Konopásek, J. & Košler, J. 2009. Distribution of zinc and its role in the stabilization of spinel in high-grade felsic rocks of the Moldanubian domain (Bohemian massif). *European Journal of Mineralogy*, **21**(2), 407–418, https://doi.org/10.1127/0935-1221/2009/0021-1899.

Thein, M. 2008. Modes of occurrence and origin of precious gemstone deposits of the Mogok Stone Tract. *Journal of the Myanmar Geosciences Society*, **1**(1), 75–84.

Themelis, T. 2008. *Gems & Mines of Mogok*. Self-published, 352 pp.

Yu, J., Hou, Z., Sheta, S., Dong, J., Han, W., Lu, T. & Wang, Z. 2018. Provenance classification of nephrite jades using multivariate LIBS: A comparative study. *Analytical Methods*, **10**(3), 281–289, https://doi.org/10.1039/c7ay02643a.

Zaw, K., Sutherland, L., Yui, T.-F., Meffre, S. & Thu, K. 2015. Vanadium-rich ruby and sapphire within Mogok gemfield, Myanmar: Implications for gem color and genesis. *Mineralium Deposita*, **50**(1), 25–39, https://doi.org/10.1007/s00126-014-0545-0.

Zhang, Z., Ye, M. & Shen, A.H. 2019. Characterisation of peridot from China's Jilin Province and from North Korea. *Journal of Gemmology*, **36**(5), 436–446, https://doi.org/10.15506/JoG.2019.36.5.436.

The Authors

Chawalit Chankhantha,[1,2] Ratthaphon Amphon,[1] Habib Ur Rehman[1] and Prof. Andy H. Shen[1,*]

[1] Gemmological Institute and Center for Innovative Gem Testing Technology (CIGT), China University of Geosciences, No. 388 Lumo Rd., 430074 Wuhan, China

[2] Department of Industrial Promotion, Ministry of Industry, Rama 6 Rd., Ratchathewi, 10400 Bangkok, Thailand

* Email: shenxt@cug.edu.cn

Acknowledgements

Special thanks to Pattama Danchalermnon for supplying some specimens and to Poetry Gems & Jewelry for providing the photo in Figure 1. This paper is CIGT contribution CIGTWZ-2020031. The authors acknowledge the financial support of a grant (CIGTXM-S201842) from CIGT. We also thank the three anonymous reviewers for their helpful comments.

Flower-Shaped Trapiche Ruby from Mong Hsu, Myanmar: A Revised Growth Mechanism

Isabella Pignatelli, Gaston Giuliani, Christophe Morlot, Michel Cathelineau and Shang I (Edward) Liu

ABSTRACT: Two polished slices of flower-shaped trapiche ruby from Mong Hsu were analysed by X-ray computed tomography and X-ray micro-fluorescence. They are characterised by the presence of a core overgrown by two layers of ruby (with the outer one forming the 'petal' shape), and these three domains were previously attributed by Liu (2015) to a multi-stage growth mechanism. The present research indicates that these specimens show textural sector zoning associated with chemical sector zoning. In agreement with literature data, three different growth sectors are identified: a pinacoidal growth sector (corresponding to the core) and two sets of dipyramidal growth sectors with different inclinations with respect to the *c*-axis. The core, middle and outer layers are thus growth sectors of the same crystal, and no successive stages are needed to explain their formation. Therefore, the growth model proposed for other trapiche rubies from Myanmar also applies to the formation of these flower-shaped specimens. The distinctive shape of these rubies is due to weathering of the growth sectors and the sector boundaries.

The Journal of Gemmology, **37**(4), 2020, pp. 404–415, https://doi.org/10.15506/JoG.2020.37.4.404

The Mong Hsu marble-hosted ruby deposits in Myanmar are famous for producing non-trapiche (Smith & Surdez 1994; Peretti *et al.* 1995, 1996) and trapiche rubies (Schmetzer *et al.* 1996; Sunagawa *et al.* 1999). Mong Hsu rubies have a number of prominent features that differ from those of the Mogok deposits, including their crystal habits, the presence of a dark violet to blue core surrounded by a red rim, colour banding, small twin lamellae and the presence of OH groups revealed by infrared spectroscopy (Smith & Surdez 1994; Smith 1995). In the present article, we examine two unusual flower-shaped trapiche rubies from Mong Hsu (Figure 1)—previously described by Liu (2015)—in order to re-evaluate the mechanism of their formation.

Non-trapiche rubies from Mong Hsu show various habits (Smith & Surdez 1994; Peretti *et al.* 1995), and are bounded by pinacoidal *c* {0001} faces and hexagonal dipyramidal faces $\{hh\bar{2}hl\}$, sometimes associated with small rhombohedral *r* $\{10\bar{1}1\}$ faces. Second-order *a* $\{11\bar{2}0\}$ prism faces have also been observed in some samples. The smaller dipyramidal faces are *n* $\{22\bar{4}3\}$, whereas the larger dipyramidal ones have often been reported as *v* $\{44\bar{8}1\}$ or *ω* $\{14\ 14\ \overline{28}\ 3\}$, and less commonly as *z* $\{22\bar{4}1\}$ or *w* $\{11\bar{2}1\}$. The $\{14\ 14\ \overline{28}\ 3\}$ indices are too high for smooth faces, and it is possible that they consist of alternating microsteps between $\{11\bar{2}0\}$ and {0001} faces (Sunagawa 1995; Sunagawa *et al.* 1999). The most common habits are characterised by the presence of *c*, *n*, *r* and *ω* or *v*, as shown in Figure 2; other habits are rarely encountered (Smith & Surdez 1994). A growth sector corresponds to each face and is indicated by the same Miller indices.

Trapiche rubies from Mong Hsu were described in detail by Schmetzer *et al.* (1996, 1999). The trapiche

Figure 1: Two flower-shaped trapiche rubies (each slice is about 5–7 mm diameter and 1.0–1.5 mm thick) from Mong Hsu were analysed for this study: samples FS02 (left) and FS03 (right). Photos reproduced from Liu (2015).

pattern is easily recognisable in sections cut perpendicular to the crystallographic *c*-axis (Figure 3). It consists of gemmy portions generally corresponding to the hexagonal dipyramidal growth sectors, which are separated by yellowish to white sector boundaries of fluid and solid inclusions such as fine-grained calcite, dolomite and K-Al-Fe-Ti silicates mixed with corundum and secondary Fe-bearing minerals formed during the weathering process (Schmetzer *et al*. 1999; Sunagawa *et al*. 1999; Garnier *et al*. 2002a, b). In some sections, these boundaries extend from the corners of a hexagonal core (i.e. pinacoidal growth sector). The presence and size of the core depend on the position of the slice along the crystal (Pignatelli *et al*. 2019). In sections cut near the ends of a crystal, the core is larger, while slices cut between an end and the centre have a smaller core. If the section passes through the centre of the crystal, then there is no core and the sector boundaries intersect in a central point. The colour of both the core and surrounding growth sectors is due to the presence of chromophores in the corundum structure (i.e. Cr, V and Ti; Peretti *et al*. 1996; Schmetzer *et al*. 1999; Garnier *et al*. 2002a, b).

Trapiche rubies are also characterised by the presence of tube-like voids filled by solids, liquid and gas. These voids originate from the core or sector boundaries and develop into the growth sectors (Schmetzer *et al*. 1996; Sunagawa *et al*. 1999). Primary and secondary fluid inclusions are similar in both trapiche and non-trapiche rubies, and the fluids belong to the CO_2-H_2S-COS-S_8-AlO(OH) system (Giuliani *et al*. 2018). Variations in density of the carbonic phase reflect differences in fluid pressure in the metamorphic marble system. These variations lead to changes in the driving-force conditions during the growth of the rubies and allow for the formation of the trapiche texture (Giuliani *et al*. 2018; Pignatelli *et al*. 2019).

Liu (2015) described flower-shaped trapiche rubies from Mong Hsu that do not show the classical trapiche pattern because their core is surrounded by two layers of ruby sectors. Weathering of the outer sectors gave them

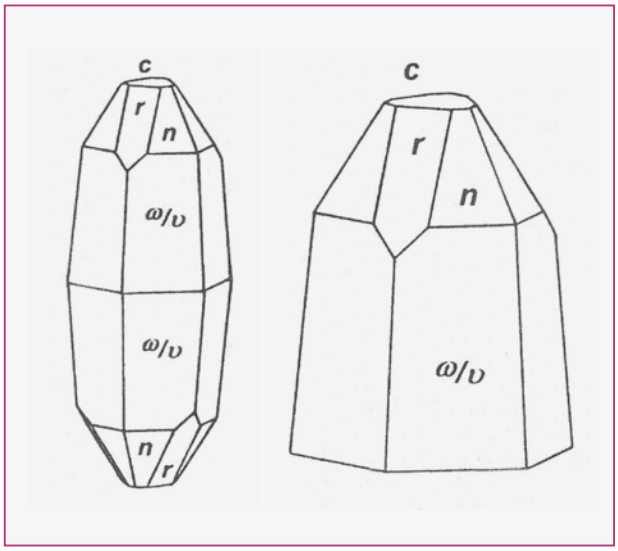

Figure 2: The most common habits of rubies from Mong Hsu are characterised by the presence of *c*, *n*, *r* and *ω* or *υ* faces (modified from Smith & Surdez 1994); other habits are rarely encountered.

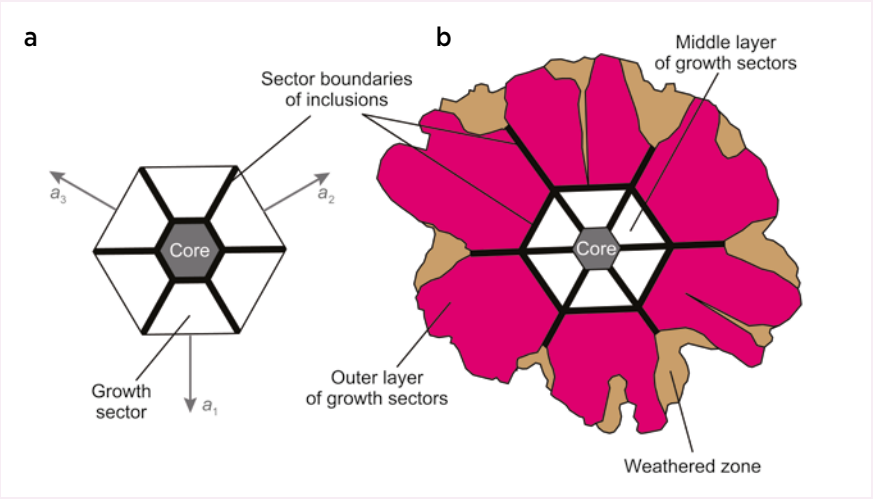

Figure 3: This schematic representation of the trapiche texture seen in a section perpendicular to the *c*-axis illustrates the difference between a classical trapiche ruby (**a**) and a flower-shaped trapiche ruby (**b**).

their characteristic 'petal' shape. In the present study, slices of two of these flower-shaped trapiche rubies (again, see Figure 1) were examined by optical microscopy, X-ray computed tomography (CT) and X-ray micro-fluorescence (XRF). The insights provided allow us to infer the growth mechanism of these peculiar ruby specimens.

MATERIALS AND METHODS

A total of five flower-shaped trapiche rubies were obtained in the cities of Yangon (in 2011) and Mogok (in 2013) by one of the authors (Liu 2015). These samples were 5–7 mm in diameter and 1.0–1.5 mm thick, and were cut and polished as slices perpendicular to the *c*-axis. Two of these samples (FS02 and FS03) were examined for this study.

CT scanning is a non-destructive technique that has been used to reveal unseen rubies within their host rock (Bouts 2014), as well as three-dimensional (3D) interior details of trapiche rubies (Morlot *et al.* 2016; Richard *et al.* 2019). For the present study, CT data were collected with a Phoenix Nanotom S scanner, using resolutions of 3.75 and 3.23 µm/voxel, and an X-ray tube tension of 75 kV. The Nanotom tomography produced files with voxel (3D pixel) resolutions between 30 and 0.6 µm/voxel as a function of the sample size.

Virtual cross-sections were extracted from these to yield textural details (e.g. porosity) and to detect the presence of phases with different densities in the samples. VGStudio and Avizo 9.5 software were used to calculate the volume occupied by the porosity, cavities and solid inclusions, which were identified using a segmentation process based on their contrast in the tomographic images. This contrast is due to differences in their attenuation coefficient, which depends on the kinds of atoms, radiation and the cross sections of X-ray interactions with matter.

XRF mapping was performed using a Bruker M4 Tornado spectrometer. The system has an Rh X-ray tube with polycapillary optics, providing an X-ray beam with a diameter of 25–30 µm on the sample. The X-ray tube was operated at 50 kV and 200 µA, and X-rays were detected by a 30 mm^2 XFlash silicon drift detector with an energy resolution up to 135 eV. All analyses were done under a vacuum of 20 mbar. Semi-quantitative element maps were generated for Cr, Fe, V and Ti for ruby, and K, Si and Ca for other minerals within areas of the samples measuring 4 × 4 mm over a period of 60 s. Data acquisition and processing were carried out using Bruker software supplied with the instrument (Flude *et al.* 2017).

Scanning electron microscopy (SEM) and electron probe micro-analysis (EPMA) were not employed in this study because the carbon coating necessary for these analyses would be difficult to remove due to the porosity of the samples.

RESULTS

Textural Description

Optical Observation. Both of the flower-shaped ruby samples FS02 and FS03 were characterised by a central hexagonal area (corresponding to the 'disc' of aster-type flowers) surrounded by radiating 'petals'. The specimens consisted of the following textural zones (Figures 1 and 3b):

- A small hexagonal core, 0.38–0.43 mm across, free of solid inclusions and deep red in colour. The core appeared darker than the surrounding ruby sectors

and was delimited by sector boundaries with a high concentration of inclusions.

- A hexagonal zone around the core, referred to by Liu (2015) as the 'middle layer'. It was 1.53–2.38 mm across and formed by six trapezoidal sectors separated by yellowish to white sector boundaries. The latter extended from the corners of the core towards the outer zone of the crystal, along ‹10$\bar{1}$0› directions. The outer extent of the middle layer was delimited by a thin corona of inclusions of similar aspect and colour to those of the six sector boundaries cross-cutting the whole ruby.
- An 'outer layer' surrounding the middle layer. It consisted of six wider sectors, irregular in size and shape, separated by the sector boundaries. These six sectors showed various degrees of weathering, giving them the appearance of heart-shaped or clothes peg-shaped petals (Liu 2015).

Visual observations also revealed that the sector boundaries of inclusions had a herringbone pattern similar to that observed in trapiche emeralds (Pignatelli *et al*. 2015). The boundaries contained a complex mineralogical assemblage that was difficult to identify due to the small sizes of the individual minerals.

Eye-visible elongated tube-like voids were almost perpendicular to the hexagonal dipyramidal faces of the crystals. They followed the sector boundaries and extended from them into the layers without any directional disturbances.

CT Scans. The tomographic investigations showed in detail the sector boundaries of inclusions and their distribution in both samples. The CT images confirmed that the inclusions surrounded the core and developed from its corners outward towards the growth sectors (Figure 4). The CT images through FS03 also showed a gradually tapered shape of the core (Figure 4b). The

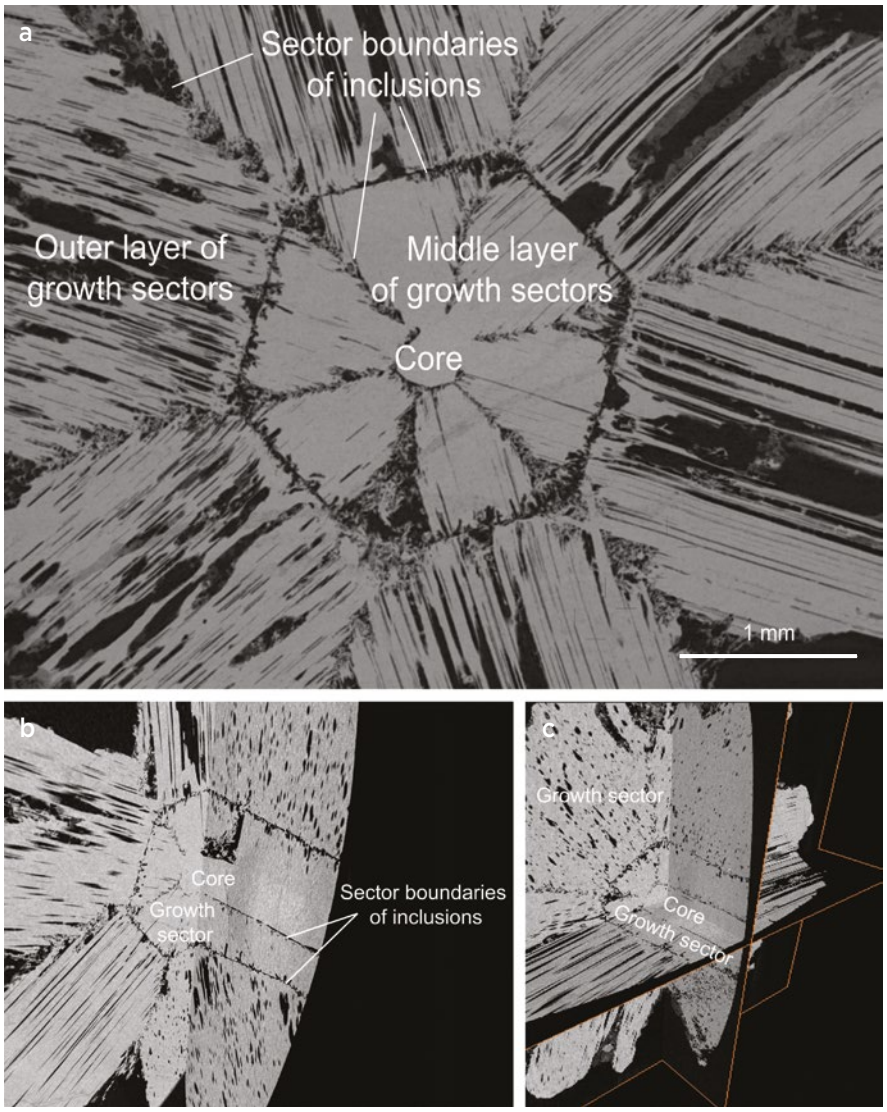

Figure 4: CT images of sample FS03 show the spatial distribution of the core, middle and outer layers. (**a**) The image of a section perpendicular to the *c*-axis shows the spatial relationship between the core, growth sectors and sector boundaries. (**b**) A combination of two cross-section images, oriented perpendicular and parallel to the *c*-axis, shows that the size of the core slightly decreases from the lower right to the upper left in the image parallel to the *c*-axis. (**c**) A combination of three images—the section perpendicular to the *c*-axis with two sections parallel to the *c*-axis—shows the tube-like voids are oriented approximately perpendicular to the face of each growth sector.

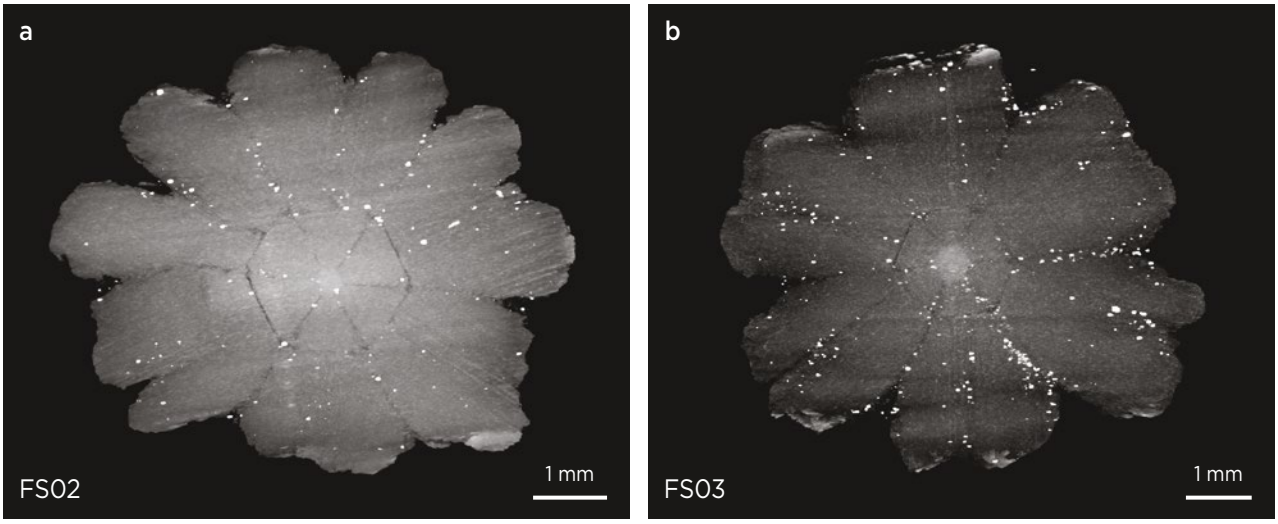

Figure 5: These CT images show the distribution of solid inclusions (white) in samples FS02 (**a**) and FS03 (**b**). The volume occupied by these inclusions is less than 0.01% of the total volume of each sample. These inclusions are scarce within the growth sectors and are mostly concentrated along the sector boundaries. Most of the solid inclusions in the growth sectors are in the areas where weathering occurred.

cores of both samples could be seen by slight contrast differences in the CT images (Figure 5). Higher contrast was evident in the core of FS03 (Figure 5b), probably due to its greater concentration of transition metals.

The distribution of solid inclusions in the two samples was also shown by the CT scans (again, see Figure 5). These inclusions were more numerous in sample FS03, and their diameter varied between 16 and 188 µm. The volume occupied by solid inclusions in samples FS02 and FS03 was calculated as 29.73 and 37.35 mm^3, respectively —less than 0.01 % of the total volume of each specimen.

Solid inclusions were scarce within the growth sectors of both samples; they were concentrated mostly along the sector boundaries. Those within growth sectors seemed to be more abundant in areas where weathering occurred. There was no correlation between the positions and the sizes of solid inclusions in the different growth sectors (Figure 5).

The CT images confirmed the presence of tube-like voids in the growth sectors (Figure 6), which crossed both the middle and outer layers without any deviations or perturbations. Some were straight, while others became curved near the edges of the crystal and resembled a feathered headdress (Figure 6a, b). In sections parallel to the *c*-axis, straight tube-like voids seemed to be perpendicular to the outer face of each growth sector (Figures 4c and 6c).

The porosity of each sample, as shown for example by the slices in Figure 7, represented 4.3% and 14% of the total volume of samples FS02 and FS03, respectively. The zones of higher porosity were the main locus for weathering.

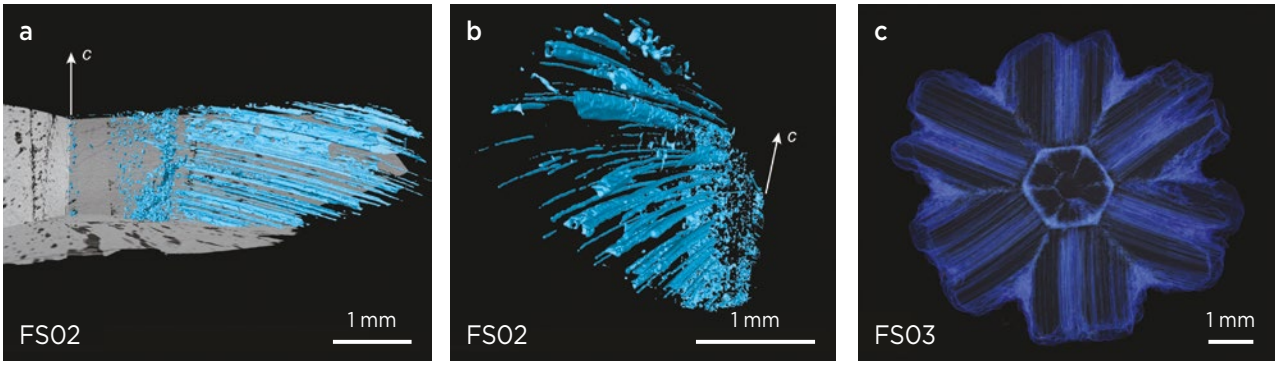

Figure 6: CT images of tube-like voids in the growth sectors show that some of them become curved near the edges of sample FS02 (**a** and **b**). The tube-like inclusions are generally straight and almost perpendicular to the growth sectors, as seen in FS03 (**c**).

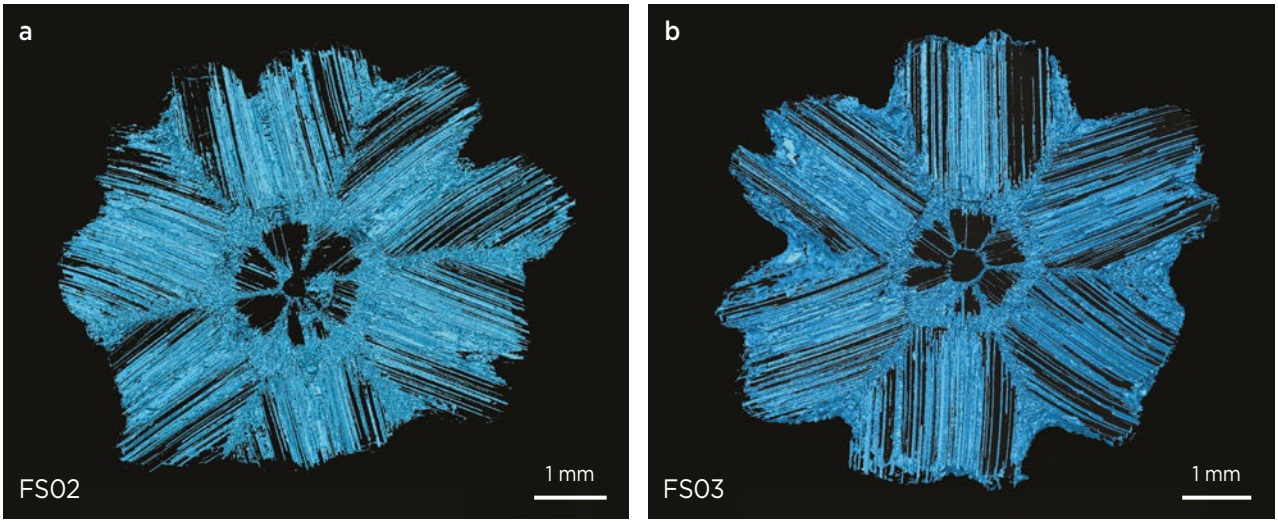

Figure 7: CT images show areas of high porosity and voids in samples FS02 (**a**) and FS03 (**b**). The porosity corresponds to 4.3% and 14% of the entire sample volume of FS02 and FS03, respectively. Note that while Figure 6c shows only the tube-like inclusions, here Figure 7b shows the porosity plus other kind of voids, including the tube-like ones.

XRF Mapping

XRF mapping of the two samples characterised the chemical zoning and colour variations in the core, sector boundaries and two growth layers. The compositional maps in Figure 8 (FS02) and Figure 9 (FS03) show the distribution of the main chromophores detected in the two rubies (i.e. Cr, V, Fe and Ti). The slightly curved surface of each sample prevented complete and regular chemical compositional mapping because it caused distortion in imaging the distribution of the elements, as shown by Figure 8b. Useful elemental mapping was therefore only possible for the central portion of each sample, but the analysed area still encompassed both of the layers adjacent to the core (although only the inner part of the outer layer).

Sample FS02. This specimen revealed a clear pattern of Cr among the different textural zones (Figure 8b, c). The distribution of Cr, V and Ti underscored the growth history of the ruby from the centre to the periphery, indicating that no twin lamellae were present, and thus it is a single, untwinned crystal.

High Cr concentrations were found in the core and in the outermost part of the middle layer (Figure 8b), whereas lower Cr concentrations were found in growth sectors of the outer layer. The Cr concentrations at the outermost borders of the crystal (visible in Figure 8b) are not discussed here because they could be artefacts due to the slightly curved surface. For this reason, we focus on compositional maps from the inset area indicated on Figure 8b. These maps (Figure 8c–f) reveal the following features:

- The core was rich in V and Cr, without any Fe or Ti.
- The middle layer was divided into two distinct areas: one closer to the core that was poor in Cr and an outer area rich in Cr. The Cr-poor area also showed greater V, as well as Ti, that gradually increased inward toward the core. The outer Cr-rich zone contained low V and no Ti.
- The outer layer was characterised by low Cr and moderate V, while Ti was low to absent.
- The entire area was very poor in Fe; this element was mainly concentrated along the sector boundaries and in fractures.

Sample FS03. This specimen yielded very different compositional maps (Figures 9c–f) from those observed for sample FS02:

- Cr was concentrated in the middle layer, nearly absent from the core and absent from the outer layer.
- V was present in very low concentrations throughout the sample, more or less equivalent to the background noise of the analysis.
- The core and both layers were Fe-free. Higher Fe concentrations were located in the sector boundaries surrounding the middle layer.
- Ti was somewhat elevated in the core and decreased in the middle layer.

Solid Inclusions. These were present along the sector boundaries in both the middle and outer layers (see Figure 5). In the absence of SEM and EPMA investigations, the nature of these inclusions was determined from the XRF data (e.g. for sample FS02, as shown in Figure 10c–f).

The Si and Ca maps show the presence of silicates and carbonates along the sector boundaries. The K and Si maps show concentrations of these elements in a fracture cross-cutting the sample (Figure 10b); they probably correspond to the presence of phyllosilicates or K-feldspar. The Ti and V maps in Figure 8 clearly show rounded Ti- and V-rich solid inclusions (possibly V-bearing rutile). The sector boundaries of inclusions were underscored by higher concentrations of Fe and Ca in the absence of Cr and Ti. The main component of these areas was Fe, which was also regularly distributed in the tube-like voids, suggesting the presence of iron oxides or hydroxides formed during the weathering process.

DISCUSSION

The flower-shaped trapiche rubies from Mong Hsu show a textural sector zoning as already described in the literature for other trapiche minerals, such as emerald, tourmaline, andalusite, staurolite and garnet (Rice & Mitchell 1991; Rice *et al*. 2006; Wilbur & Ague 2006; Schmetzer *et al*. 2011; Pignatelli *et al*. 2015). The textural sector zoning is characterised by the presence of inclusions along the boundaries between neighbouring growth sectors (Andersen 1984). The textural zoning can be associated with chemical sector zoning, when growth

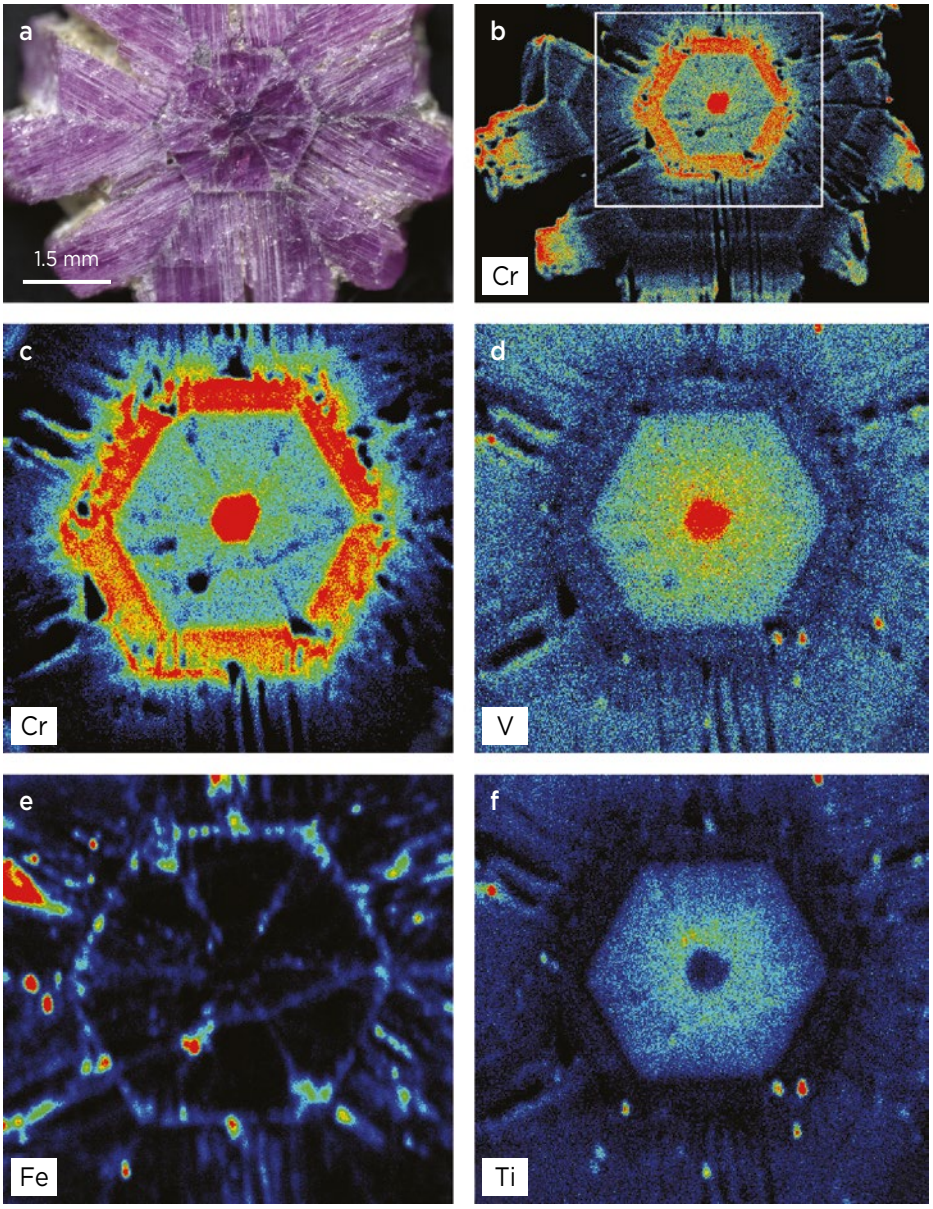

Figure 8: (**a**) The slightly curved surface of the flower-shaped trapiche rubies, here shown on sample FS02, caused artefacts when mapping the trace-element distribution of the sample. For this reason, we considered only the data within the white inset in (**b**). The XRF maps show the distribution of Cr (**c**), V (**d**), Fe (**e**) and Ti (**f**). The colours in the maps indicate the concentration of an element along a spectral scale from most (red) to least (blue). The red areas seen in the outer layer for Cr in (b) are likely artefacts resulting from the curved surface of the sample. Photo (a) by M. Cathelineau.

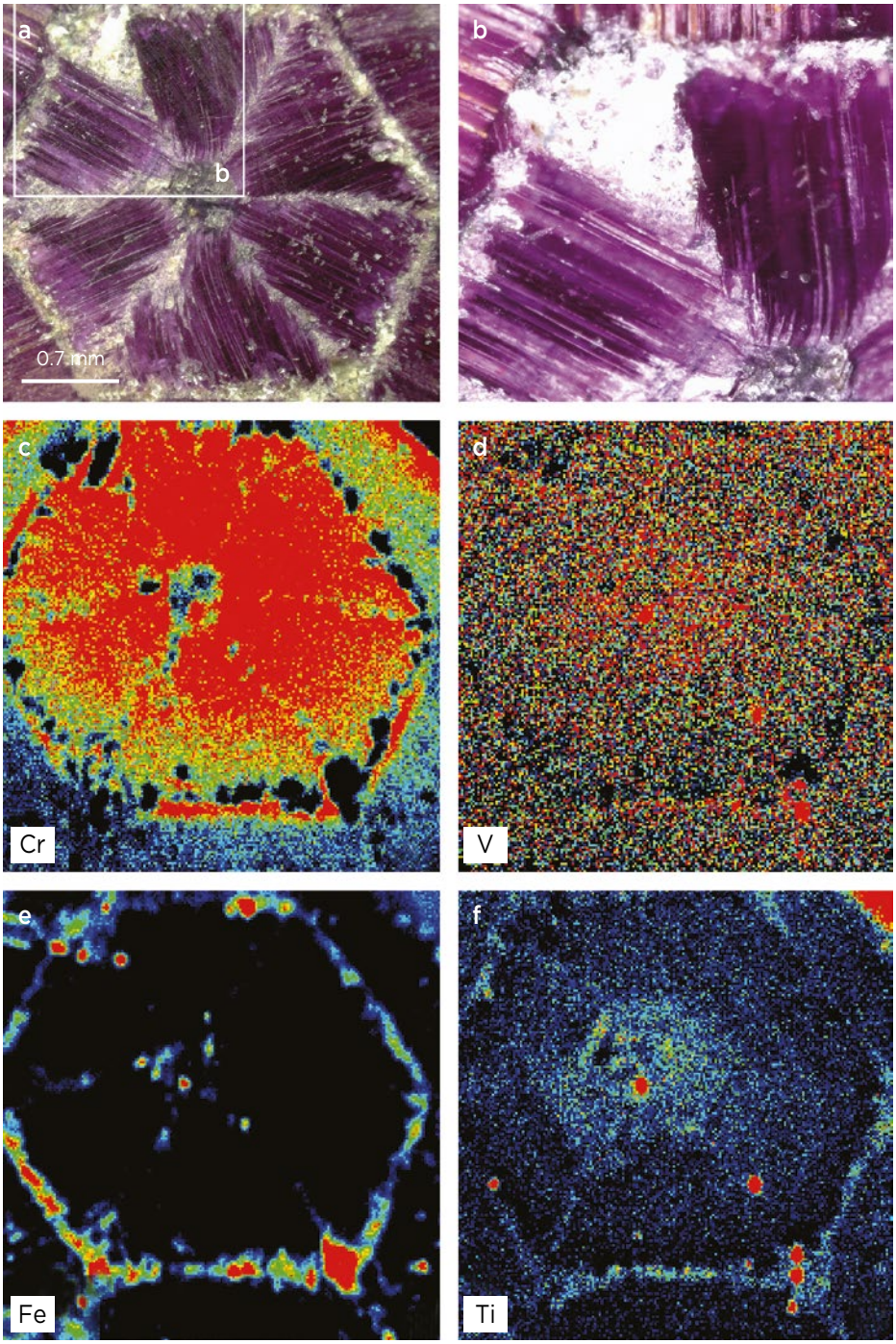

Figure 9: (**a**) The central region of sample FS03 was also investigated by XRF mapping. (**b**) This enlarged portion of the core and middle layer shows in more detail the tube-like voids in the growth sectors, as well as the herringbone pattern of the sector boundaries of inclusions. The XRF maps show the distribution of Cr (**c**), V (**d**), Fe (**e**) and Ti (**f**). The colours in the maps indicate the concentration of an element along a spectral scale from most (red) to least (blue). Photos (a, b) by M. Cathelineau.

sectors that are not crystallographically equivalent have different compositions. For the two flower-shaped rubies examined here, our CT and XRF results indicate the presence of both types of zoning. In sample FS03, the chemical zoning allows for the distinction of at least three types of growth sectors: first, the Ti-bearing and Cr-poor core, which corresponds to a pinacoidal {0001} sector. The growth sectors in the middle layer are richer in Cr than those in the outer layer (Figure 9c). According to the most common habits observed in rubies from Mong Hsu, there should be two groups of dipyramidal growth sectors having different inclinations with respect to the *c*-axis (Smith & Surdez 1994; Peretti *et al.* 1995). Their exact indexation is hampered by the fact that these flower-shaped trapiche ruby specimens are polished slices, so their crystal habit is no longer recognisable. As the presence of rhombohedral $\{10\bar{1}1\}$ sectors could not be confirmed, we omitted them from our 3D model of the crystal habit (Figure 11a). Even if the $\{10\bar{1}1\}$ sectors were present, their size would be small and their projection would fall along the directions of sector boundaries, which would make them difficult to see considering the

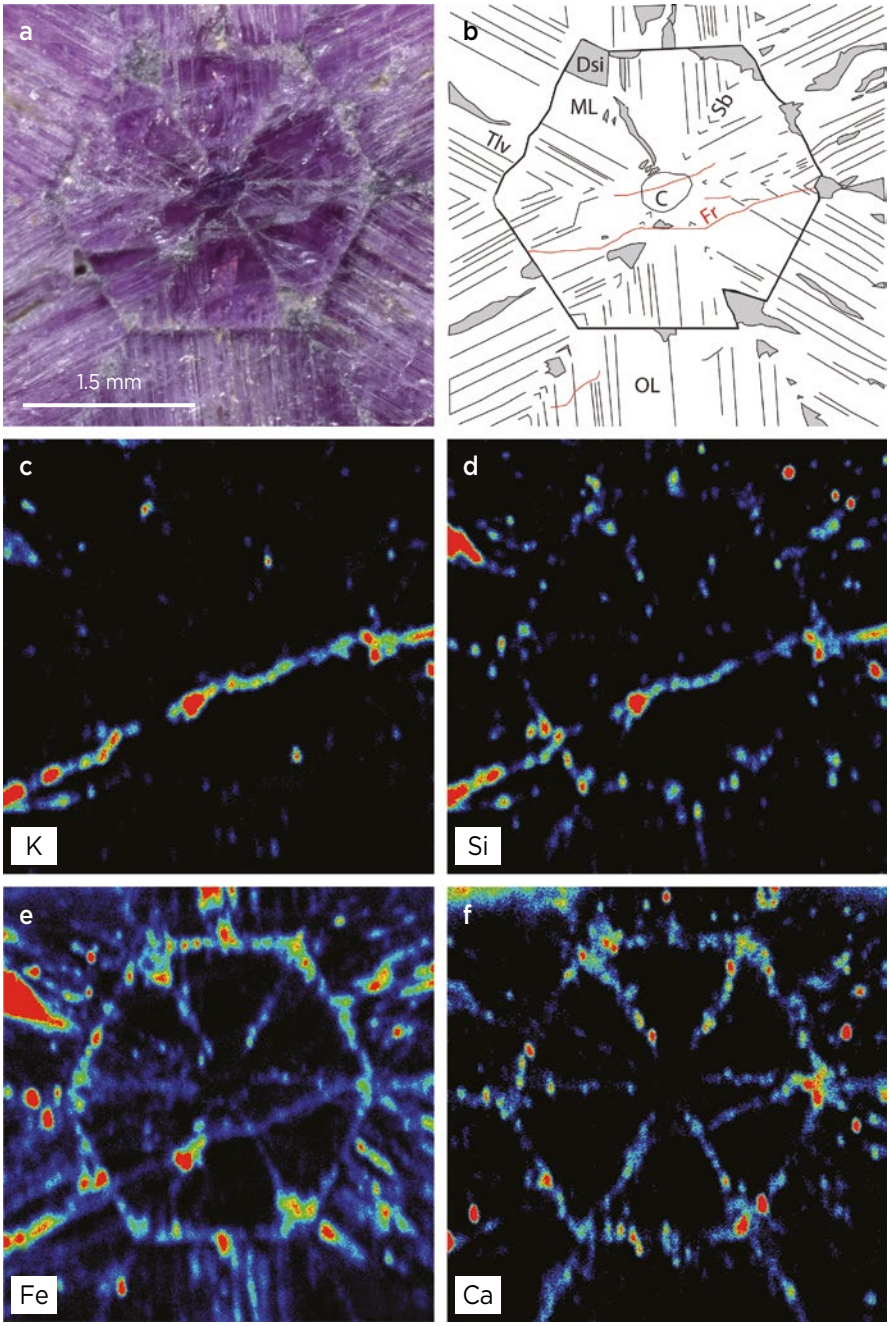

Figure 10: XRF maps of sample FS02 show the chemical composition of its solid inclusions along sector boundaries and in a fracture. (**a**) This photo of the sample shows the area mapped. (**b**) A corresponding drawing shows the inclusions associated with the trapiche texture (in grey) and the weathering of the crystal. Late meteoric fluids were concentrated in fractures (shown in red) and infiltrated at the corners of the growth sectors and along tube-like voids. Most of the solid inclusions (e.g. Fe-oxides/hydroxides) are concentrated in these weathered zones. The abbreviations in the drawing are C = core, ML = middle layer, OL = outer layer, Sb = sector boundaries, Tlv = tube-like voids and Dsi = dissolution and infilling by late solids of the tube-like voids and parts of the sector boundaries. XRF maps show the distribution of K (**c**), Si (**d**), Fe (**e**) and Ca (**f**). The colours in the maps indicate the concentration of an element along a spectral scale from most (red) to least (blue). Photo (a) by M. Cathelineau.

concentrations of inclusions and porosity in those areas.

Sample FS03 was not cut through the centre of the crystal; if it were, no core would be visible (Figure 11b). Instead, it corresponds to a cross-section shifted along the *c*-axis, which is confirmed by the CT images showing that the size of the core slightly decreases along a cross-section of the slice. Both the dipyramidal and pinacoidal growth sectors are recognisable in this cross-section (Figure 11c), which closely reproduces the chemical sector zoning observed in the XRF maps.

The same conclusion can be reached for sample FS02 which, like FS03, has three types of growth sectors: a pinacoidal one corresponding to the core and two groups of dipyramidal growth sectors—one for the middle layer and the other for the outer layer. However, the Cr zoning on the XRF map could be misleading and could lead us to suppose the presence of additional growth sectors in the middle layer. This is excluded by CT data, which underscore the absence of sector boundaries of inclusions and porosity between the Cr-poor and Cr-rich zones within the middle layer. Thus, the variation in Cr within this layer is due to growth banding resulting from fluctuations in growth rates, which can favour the incorporation of impurities.

A considerable concentration of tube-like voids is present within the growth sectors of these trapiche rubies.

Two possible mechanisms have been reported in the literature to explain the presence of these voids in trapiche minerals. Both mechanisms involve the formation of dislocations:

(1) Tube-like voids can form by dissolution along dislocation bundles if the supersaturation of the growth medium decreased after crystal growth (Scandale & Zarka 1982; Authier & Zarka 1994). These dislocations are perpendicular to the front of each growth sector and proceed with it during growth.

(2) Tube-like voids could also form from dislocations due to the trapping of syngenetic solid inclusions. In this case, the dislocations start from the inclusions and can propagate straight, oriented close to the growth direction of the sector in which they lie, but they usually have a non-crystallographic direction (Klapper 2000, 2010).

The first mechanism seems to agree with the observations of this study and those reported for other trapiche rubies from Myanmar (Schmetzer *et al.* 1999; Sunagawa *et al.* 1999).

Some tube-like voids appeared curved in proximity to the edges of the crystal, as shown in Figures 6a and 6b. This could be due to the fact that ruby FS02 was likely deformed under pressure during the final phase of its growth. Thus, the curvature of the tube-like voids results from the fact that the dislocations modified their directions during the formation of the crystal, adopting new directions for which their energy was minimal within the growth layer. The deformation could be related to local tectonic constraints happening during regional metamorphism and, thus, during trapiche growth in rock lithology of different competence such as marble, calc-silicate and schist.

The flower shape of the analysed trapiche rubies is due to weathering, which affected both the growth sectors and the sector boundaries. In the growth sectors, the weathered zones created V- or U-shaped inlets, as previously observed in Colombian trapiche emeralds (Bernauer 1933). The yellowish colour of the sector

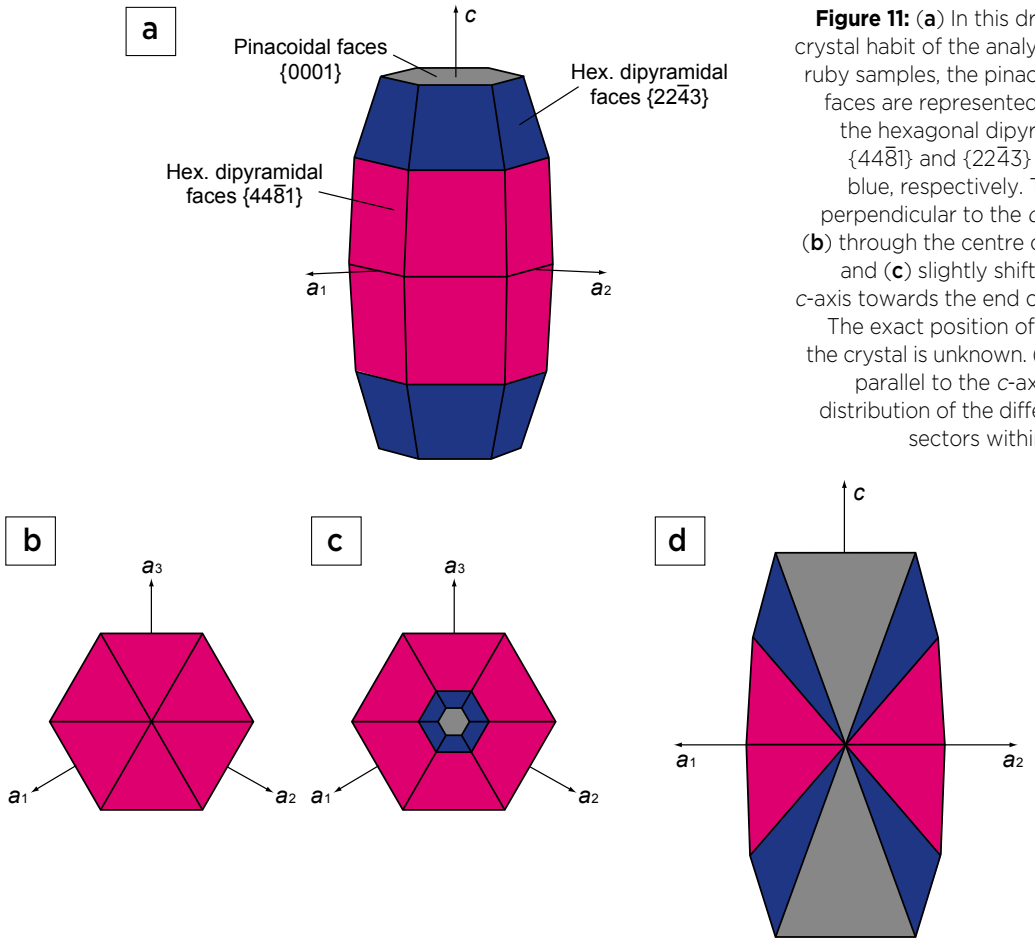

Figure 11: (**a**) In this drawing of the crystal habit of the analysed trapiche ruby samples, the pinacoidal {0001} faces are represented in grey, and the hexagonal dipyramidal faces {44$\bar{8}$1} and {22$\bar{4}$3} are pink and blue, respectively. Two sections perpendicular to the *c*-axis are cut (**b**) through the centre of the crystal and (**c**) slightly shifted along the *c*-axis towards the end of the crystal. The exact position of each slice in the crystal is unknown. (**d**) A section parallel to the *c*-axis shows the distribution of the different growth sectors within the crystal.

boundaries is also due to weathering, which is associated with the deposition of iron oxides/hydroxides, as shown by the Fe distribution in the XRF maps (Figures 8e and 10e) and also described by Sunagawa *et al*. (1999). Weathering was favoured by the porosity of the boundaries, as underlined by the CT data, and as reported previously for trapiche ruby and emerald (Schmetzer *et al*. 1999; Garnier *et al*. 2002a, b; Pignatelli *et al*. 2015).

The complex mineralogical assemblage within the sector boundaries consists of carbonates, K-Si minerals, Fe-oxides/hydroxides and a Ti-bearing mineral (probably V-rutile) according to previous data on trapiche rubies from the same locality (Garnier *et al*. 2002a, b and reference therein). The K-Si minerals are present in a fracture and could be related to micas or K-feldspar as described by Garnier *et al*. (2002a, b).

The difference between the texture shown by these flower-shaped trapiche specimens and classical trapiche rubies has been attributed to multi-stage formation (Liu 2015). This formation hypothesis consists of five stages. During the first three stages, a flower-shaped ruby formed as a classical trapiche (according to the growth model proposed by Sunagawa *et al*. 1999), during which the core, middle layer and sector boundaries developed. Then two additional stages resulted in the formation of the sector boundaries and growth sectors of the outer layer. Based on the XRF and CT data collected in the current study, the middle and outer layers are different growth sectors of the same crystal, and all sectors formed together. Thus, no additional stages are needed for their formation, and the genetic model proposed by Sunagawa *et al*. (1999) for classical trapiche rubies from Myanmar is also applicable to flower-shaped trapiche rubies.

CONCLUSION

The two samples of flower-shaped trapiche rubies from Mong Hsu described in this study show both textural and chemical sector zoning. CT scanning and XRF mapping revealed the presence of three types of growth sectors: a pinacoidal one, which corresponds to the core of each sample, and two sets of dipyramidal growth sectors forming the middle and outer layers. The growth sectors are characterised by variations in trace-element composition, as shown by XRF maps.

The formation mechanism of these flower-shaped trapiche rubies is the same as proposed for other trapiche crystals from Mong Hsu, according to the model developed by Sunagawa *et al*. (1999), without adding further growth stages. However, such flower-shaped specimens are rare because the ruby must be sliced at a location perpendicular to the *c*-axis where both sets of dipyramidal growth sectors are present, whereas most sections contain only one of them (cf. Peretti *et al*. 1995). In comparison with other trapiche ruby samples, the appearance of the flower-shaped rubies is due to the combination of: (1) the crystal habit (i.e. the number of faces and growth sectors) and the position of the slice within the host crystal; and (2) the weathering of the growth sectors and sector boundaries, giving the aspect of clothes-peg-shaped petals.

REFERENCES

Andersen, T.B. 1984. Inclusion patterns in zoned garnets from Magerøy, north Norway. *Mineralogical Magazine*, **48**(346), 21–26, https://doi.org/10.1180/minmag.1984.048.346.03.

Authier, A. & Zarka, A. 1994. X-ray topographic study of the real structure of minerals. *In*: Marfunin, A.S. (ed) *Advanced Mineralogy—Volume 1: Composition, Structure, and Properties of Mineral Matter: Concepts, Results, and Problems*. Springer-Verlag, Berlin, Germany, 221–233, https://doi.org/10.1007/978-3-642-78523-8_12.

Bernauer, F. 1933. Las llamadas maclas múltiples de esmeraldas de Muzo y sus anomalías ópticas. *Compilacíon de los Estudios Geológicos Oficiales en Colombia – 1917 a 1933*, **1**(4), 199–221.

Bouts, A. 2014. Detection of ruby crystals in marble host rock by X-ray computed tomography. *Journal of Gemmology*, **34**(1), 50–54, https://doi.org/10.15506/JoG.2014.34.1.50.

Flude, S., Haschke, M. & Storey, M. 2017. Application of benchtop micro-XRF to geological materials. *Mineralogical Magazine*, **81**(4), 923–948, https://doi.org/10.1180/minmag.2016.080.150.

Garnier, V., Ohnenstetter, D., Giuliani, G. & Schwarz, D. 2002a. Rubis trapiches de Mong Hsu, Myanmar. *Revue de Gemmologie A.F.G.*, No. 144, 5–12.

Garnier, V., Ohnenstetter, D., Giuliani, G., Blanc, P. & Schwarz, D. 2002b. Trace-element contents and cathodoluminescence of "trapiche" rubies from Mong Hsu, Myanmar (Burma): Geological significance. *Mineralogy and Petrology*, **76**(3–4), 179–193, https://doi.org/10.1007/s007100200040.

Giuliani, G., Dubessy, J., Pignatelli, I. & Schwarz, D. 2018. Fluid inclusions study of trapiche and non-trapiche rubies from the Mong Hsu deposit, Myanmar. *Canadian Mineralogist*, **56**(5), 691–703, https://doi.org/10.3749/canmin.1800013.

Klapper, H. 2000. Generation and propagation of dislocations during crystal growth. *Materials Chemistry and Physics*, **66**(2–3), 101–109, https://doi.org/10.1016/s0254-0584(00)00342-4.

Klapper, H. 2010. Generation and propagation of defects during crystal growth. *In*: Dhanaraj, G., Byrappa, K., Prasad, V. & Dudley, M. (eds) *Springer Handbook of Crystal Growth*. Springer-Verlag, Heidelberg, Germany, 93–132, https://doi.org/10.1007/978-3-540-74761-1_4.

Liu, E. 2015. Gem Notes: Flower-shaped trapiche ruby from Mong Hsu, Myanmar. *Journal of Gemmology*, **34**(8), 660–662.

Morlot, C., Pignatelli, I., Giuliani, G., Sterpenich, J., Boiron, M.C., Ohnenstetter, D., Andriamamonjy, A., Raoul, J. *et al*. 2016. La tomographie à rayons X et ses applications en gemmologie : Exemples de l'émeraude trapiche et du grenat démantoïde. *Revue de Gemmologie A.F.G.*, No. 198, 13–18.

Peretti, A., Schmetzer, K., Bernhardt, H.-J. & Mouawad, F. 1995. Rubies from Mong Hsu. *Gems & Gemology*, **31**(1), 2–26, https://doi.org/10.5741/gems.31.1.2.

Peretti, A., Mullis, J. & Mouawad, F. 1996. The role of fluorine in the formation of colour zoning in rubies from Mong Hsu, Myanmar (Burma). *Journal of Gemmology*, **25**(1), 3–19, https://doi.org/10.15506/JoG.1996.25.1.3.

Pignatelli, I., Giuliani, G., Ohnenstetter, D., Agrosi, G., Mathieu, S., Morlot, C. & Branquet, Y. 2015. Colombian trapiche emeralds: Recent advances in understanding their formation. *Gems & Gemology*, **51**(3), 222–259, https://doi.org/10.5741/gems.51.3.222.

Pignatelli, I., Giuliani, G., Morlot, C. & Pham, V.L. 2019. The texture and chemical composition of trapiche ruby from Khoan Thong, Luc Yen mining district, northern Vietnam. *Journal of Gemmology*, **36**(8), 726–746, https://doi.org/10.15506/JoG.2019.36.8.726.

Rice, A.H.N. & Mitchell, J.I. 1991. Porphyroblast textural sector-zoning and matrix displacement. *Mineralogical Magazine*, **55**(380), 379–396, https://doi.org/10.1180/minmag.1991.055.380.08.

Rice, A.H.N., Habler, G., Carrupt, E., Cotza, G., Wiesmayr, G., Schuster, R., Sölva, H. *et al*. 2006. Textural sector-zoning in garnet: Theoretical patterns and natural examples from Alpine metamorphic rocks. *Austrian Journal of Earth Sciences*, **99**, 70–89.

Richard, A., Morlot, C., Créon, L., Beaudoin, N., Balistky [*sic*], V.S., Pentelei, S., Dyja-Person, V., Giuliani, G. *et al*. 2019. Advances in 3D imaging and volumetric reconstruction of fluid and melt inclusions by high resolution X-ray computed tomography. *Chemical Geology*, **508**, 3–14, https://doi.org/10.1016/j.chemgeo.2018.06.012.

Scandale, E. & Zarka, A. 1982. Sur l'origine des canaux dans les cristaux. *Journal of Applied Crystallography*, **15**(4), 417–422, https://doi.org/10.1107/s0021889882012291.

Schmetzer, K., Hänni, H.A., Bernhardt, H.-J. & Schwarz, D. 1996. Trapiche rubies. *Gems & Gemology*, **32**(4), 242–250, https://doi.org/10.5741/gems.32.4.242.

Schmetzer, K., Beili, Z., Yan, G., Bernhardt, H.-J. & Hänni, H.A. 1999. Element mapping of trapiche rubies. *Journal of Gemmology*, **26**(5), 289–301, https://doi.org/10.15506/JoG.1999.26.5.289.

Schmetzer, K., Bernhardt, H.-J. & Hainschwang, T. 2011. Chemical and growth zoning in trapiche tourmaline from Zambia — A re-evaluation. *Journal of Gemmology*, **32**(5), 151–173, https://doi.org/10.15506/JoG.2011.32.5.151.

Smith, C.P. & Surdez, N. 1994. The Mong Hsu ruby: A new type of Burmese ruby. *Jewel Siam*, **4**(6), 82–98.

Smith, C.P. 1995. A contribution to understanding the infrared spectra of rubies from Mong Hsu, Myanmar. *Journal of Gemmology*, **24**(5), 321–335, https://doi.org/10.15506/JoG.1995.24.5.321.

Sunagawa, I. (ed) 1995. *Morphology of Crystals: Part B: Fine Particles, Minerals and Snow*. Terra Scientific Publishing Company and Kluwer Academic Publishers, Tokyo, Japan, 378 pp.

Sunagawa, I., Bernhardt, H.-J. & Schmetzer, K. 1999. Texture formation and element partitioning in trapiche ruby. *Journal of Crystal Growth*, **206**(4), 322–330, https://doi.org/10.1016/s0022-0248(99)00331-0.

Wilbur, D.E. & Ague, J.J. 2006. Chemical disequilibrium during garnet growth: Monte Carlo simulations of natural crystal morphologies. *Geology*, **34**(8), 689–692, https://doi.org/10.1130/G22483.1.

The Authors

Dr Isabella Pignatelli, Christophe Morlot and Dr Michel Cathelineau
Université de Lorraine,
GeoResources UMR 7359 CNRS-UL, BP 70239,
54506 Vandœuvre-lès-Nancy cedex, France
Email: isabella.pignatelli@univ-lorraine.fr

Dr Gaston Giuliani
Université Paul Sabatier,
GET/IRD, UMR CNRS-IRD-CNES 5563,
14 avenue Edouard Belin, 31400 Toulouse, France
and
Université de Lorraine, CRPG UMR 7358 CNRS-UL,
15 rue Notre-Dame-des-Pauvres, BP 20, 54501
Vandœuvre-lès-Nancy cedex, France

Dr Shang I (Edward) Liu
The Gemmological Association of Hong Kong,
P.O. Box 97711, Tsim Sha Tsui, Kowloon,
Hong Kong

Update on Emeralds from the Mananjary-Irondro Area, Madagascar

Vincent Pardieu, Supharart Sangsawong, Léonard Cornuz, Victoria Raynaud and Sarocha Luetrakulprawat

ABSTRACT: Emerald deposits in eastern Madagascar near Mananjary were discovered in the 1970s by Jeannot Andrianjafy and have yielded some high-quality emeralds. There are currently a few mining sites being worked by Andrianjafy's children. This article characterises emerald samples that were collected in 2019 at two of the deposits—Ambodivandrika and Ambatomaneno, in the northern and southern parts of the area, respectively—where the mineralisation occurs in schist associated with pegmatites. The samples from each deposit showed some significant differences in their internal features and trace-element composition (i.e. alkalis and others such as Mn, Zn and Ga). Emeralds from both mines share many characteristics with those from other schist-type deposits, such as in Zambia, Brazil and elsewhere.

The Journal of Gemmology, **37**(4), 2020, pp. 416–425, https://doi.org/10.15506/JoG.2020.37.4.416

For the past three decades, Madagascar has supplied some attractive emeralds to the gem trade. Most of the deposits are situated on the eastern side of the island in the Mananjary-Ifanadiana area near Irondro, about 50 km south-west of the coastal city of Mananjary.

Levat (1912) first mentioned the occurrence of emerald in Madagascar, and Sinkankas (1981) described small grains found in secondary deposits along with kyanite in the Mananjary-Ifanadiana area. Hänni and Klein (1982) characterised emeralds from the Ankadilalana mine (known today as Ambodibakoly) near the town of Kianjavato, and Chikayama (1989), Campbell (1991) and Kleyenstüber (1991) also documented emeralds from the Mananjary area. Schwarz and Henn (1992) described the Morafeno mining area, and Thomas (1993) also visited several emerald prospects in the Mananjary region. Ranorosoa (1993) studied the Mananjary area for her thesis work, and Schwarz (1994) described the internal features of emeralds from various deposits there. Pezzotta (1999) mentioned Mananjary emeralds and nearby gem-bearing pegmatites, and Cheilletz *et al.* (2001) showed the relation between emerald mineralisation at Mananjary and at another genetically different deposit in southern Madagascar. Chan Peng (2003) built models for the formation of the Mananjary emerald deposits, Moine *et al.* (2004) investigated the composition of the mineralising fluids, and Vapnik *et al.* (2006) examined the formation of the deposits based on fluid inclusions. Clanin (2012) described emerald mining activities near Mananjary in 1991 and reported that the mineralisation was hosted by biotite-amphibolite schist intruded by pegmatites.

In March 2018 and December 2019, author VP visited the Mananjary area in order to collect emerald reference samples, first for the Bahrain Institute for Pearls and Gemstones (DANAT) in 2018 (Karampelas *et al.* 2019), and then in 2019 for his private reference collection. The samples described in this article were collected during that second visit (e.g. Figure 1).

The Mananjary deposits have been controlled by Le Quartz Cie since the first emerald fragments were discovered near the village of Morafeno in the 1970s by Jeannot Andrianjafy, a Malagasy gem merchant and

prospector. After securing mining licences and making some alliances with the local 'kings' (Pardieu 2018a), Andrianjafy explored the region further. Within 10 years he discovered more than 15 deposits on both the north and south sides of the road linking Fianarantsoa to Mananjary (Pardieu 2020a). He has worked these deposits with his family under Le Quartz Cie for the past 50 years (Pardieu 2018b). Some additional mining activities in the area have also been undertaken by a few other Malagasy mining ventures, more or less in partnership with foreign financers (e.g. Clanin 2012).

GEOLOGY

The emeralds of the Mananjary area occur as euhedral crystals in phlogopite ± hornblende schists within altered amphibolite bodies. The deposits are situated in rocks of the Manampotsy Group, suggesting a uniform genetic context for the whole area (Chan Peng 2003; Tucker *et al.* 2012). Emerald and fluorine-rich phlogopite formed between hornblende grains or replaced Cr-bearing amphibolite due to alteration by K-F-Be-rich hydrothermal fluids. The mineralisation occurred spatially 'at the contact between pegmatite and lenticular bodies of hornblendites' (Vapnik *et al.* 2006, p. 143), and the associated alteration created a sharp reaction front composed of a distinctive mineralogical assemblage: hornblende, phlogopite, plagioclase, calcite, quartz, chlorite and emerald. The inclusions found in the emeralds reflect their growth environment, which suggests pegmatitic interaction (fluorite, tourmaline) with the amphibolite (magnesite; Gübelin & Koivula 2008).

The emerald-bearing rocks were metamorphosed and folded twice; the first deformation produced flat recumbent eastward-verging folds, and then east-west shortening created vertical folds along a north-south trend (Moine *et al.* 2004). Deformed orthogneiss in the area is related to magmatism that occurred 800 million years ago (Ma; Handke *et al.* 1999), while the pegmatites and veins associated with emerald mineralisation were emplaced during the Pan-African tectono-metamorphic event at around 530–500 Ma (Markl *et al.* 2000), or 490 ± 8 Ma based on the age dating of the associated phlogopite ($^{40}Ar/^{39}Ar$ method; Cheilletz *et al.* 2001). The pressure-temperature conditions were estimated at 8 ± 1 kbar and 700 ± 30°C for rocks of the Mananjary area (Chan Peng 2003), and 1.5 kbar and 250–450°C for emerald genesis (Vapnik *et al.* 2006).

Figure 1: Two rough emeralds from Ambodivandrika, Madagascar (left 0.2 g and right 3.45 g) that were studied for this article are shown with a faceted pear-shape emerald (0.86 ct), also reportedly from Madagascar. The faceted stone is courtesy of Asia Lounges, Bangkok, Thailand; photo by Arjuna Irsutti.

The key process for the formation of the emerald deposits was the introduction of mantle-derived CO_2-rich fluids along the Ifanadiana-Angavo mega-shear zone (15 km west of the emerald-bearing area) and the presence of crustal H_2O-rich fluids related to the pegmatites and veins (Vapnik *et al*. 2006). Therefore, Madagascar's emerald deposits may be classified as being associated with pegmatites in mafic-ultramafic rock, in a tectonic-magmatic context (i.e. type IA, as described by Giuliani *et al*. 2018, 2019). Other worldwide emerald deposits categorised similarly include Itabira-Nova Era in Brazil, the Kafubu area of Zambia and the Kenticha pegmatite field in Ethiopia.

MINING AND PRODUCTION

The Mananjary-Irondro emerald-producing area is mainly active during the dry season from May to December. Then with heavy rains the mining usually ceases. In 2018 mining stopped earlier, in September, because of a presidential election that took place in November.

In the southern part of the deposit area, near Morafeno village, the main active operation is at Ambatomaneno, on the top of a hill (see Figures 2 and 3). It is an open-pit operation, and during author VP's 2019 visit there were 18 miners, led by Patricia Andrianjafy (daughter of Jeannot Andrianjafy). They were working with a bulldozer and

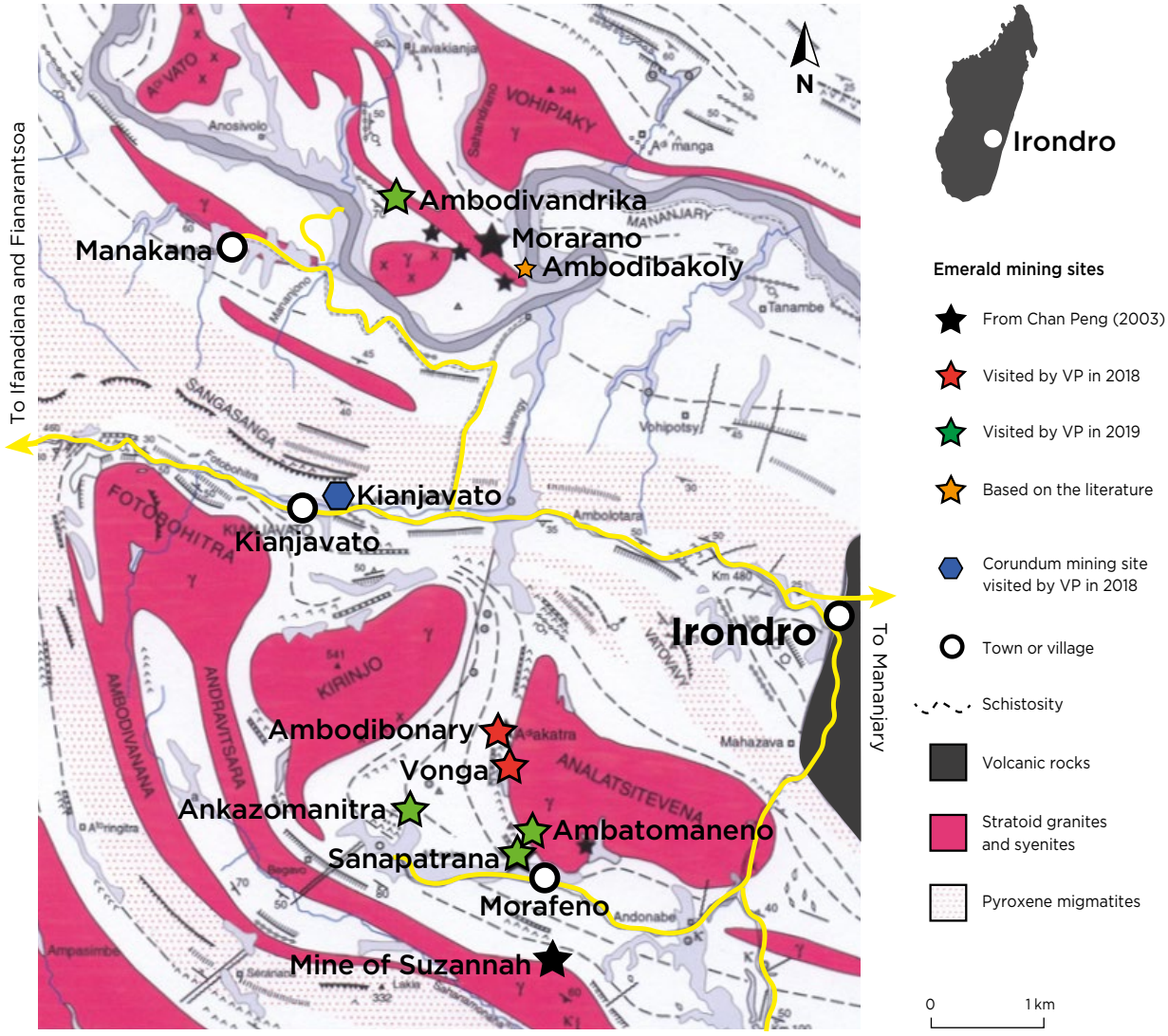

Figure 2: This geological map of the Mananjary region (modified after Chan Peng 2003) shows the locations of the deposits visited by author VP in 2018 and 2019, as well as other emerald mines and a corundum deposit that lies in between the two emerald areas.

Figure 3: This aerial drone view (looking south-east) of the southern part of the emerald-producing area shows the Le Quartz Cie mining camp in the foreground. In the background, on top of the hill on the left, is the Ambatomaneno emerald mine. On the right are the tailings of the dormant Sanapatrana mine. Photo by V. Pardieu.

some hand tools, but no explosives, as a deliberate choice not to damage the emeralds. They extracted emeralds from weathered rocks composed of mica-rich layers associated with pegmatites. The production was mainly composed of light bluish green emeralds (e.g. Figure 4) up to about 20 g.

The Sanapatrana open-pit mine near Ambatomaneno (again, see Figures 2 and 3) has been inactive for several years. Sanapatrana reportedly produced more than 7 tonnes of emeralds since its discovery in 1984. Just west of these pits is the Ankazomanitra mine, where Patricia Andrianjafy is prospecting. No mining activity was seen at Ambodibonary or Vonga (Figure 2), where Jean Luc Andrianjafy (father of Jeannot) has been working in recent years.

North of the Kianjavato-Irondro road, Patricia Andrianjafy was also working at Ambodibakoly (Figure 2) with, reportedly, the support of an investor from Dubai, but

Figure 4: Samples from the recent production at Ambatomaneno display the light bluish green colour typical of emeralds from this mine. The stones shown here range up to approximately 1 g. Photo by V. Pardieu.

Figure 5: This aerial drone view (looking south-east) shows Christian Andrianjafy's camp (centre foreground) and the Ambodivandrika emerald mine (white cliff over a burned area). Other emerald mines are also visible (as areas lacking vegetation) in the same alignment as on the geological map in Figure 2. Photo by V. Pardieu.

author VP was not able to visit that mine. However, mining was witnessed at Ambodivandrika (Figure 5), where Christian Andrianjafy (another son) was working with 19 people, also using only hand tools to avoid damaging the emeralds. As at Ambatomaneno, mining was taking place in weathered mica-rich rocks intruded by pegmatites; the emeralds were associated with phenakite and, reportedly, alexandrite. More than 1 kg of emeralds were seen by author VP, including some highly transparent material showing good colour and clarity, and some fine emerald crystal specimens over 20 g (e.g. Figure 6).

Figure 6: These rough emeralds and crystal specimen (about 8 cm long) are from recent production at Ambodivandrika. The rough material (0.2 to 0.4 g) has been clipped to remove included portions. The area of the crystal near the termination is well formed and very clean, while the rest of the stone is much more included. Photo by V. Pardieu.

MATERIALS AND METHODS

Eight emeralds obtained from Ambodivandrika in the northern part of the mining area and seven emeralds from Ambatomaneno in the southern part were studied for this article (Figure 7). These samples were classified as 'D-type' (obtained from a miner but not at the mine) and 'C-type' (obtained at the mine but without witnessing the mining of the specific stones), respectively, according to the cataloguing system of Pardieu (2009, 2020b). They consisted of broken pieces and partial crystals that weighed 0.08–3.45 g and ranged from pale to intense bluish green. Two samples (i.e. one from each mining area) were prepared with windows polished perpendicular to the *c*-axis for spectroscopy.

The emeralds were characterised at ICA | GemLab in Bangkok, Thailand. Photomicrographs of internal features were captured with a Canon EOS 750D camera using darkfield, brightfield, diffused and oblique illumination, together with a fibre-optic light source when necessary. Standard gemmological data were collected from seven samples. Refractive indices were obtained with a refractometer produced by World Jewelry Tools Co. Ltd (Bangkok, Thailand), SG was measured hydrostatically with a calibrated Mettler Toledo JP1203C electronic balance, fluorescence was checked with long-wave (365 nm) and short-wave (254 nm) UV radiation, and a GIA polariscope was used to observe optic character.

Ultraviolet-visible-near infrared (UV-Vis-NIR) spectra were collected on the two windowed samples using a Jasco V-770 spectrophotometer with a resolution of

Figure 7: The 15 emeralds shown here were characterised for this study. The samples on the left are from Ambodivandrika (0.13–3.45 g) and those on the right are from Ambatomaneno (0.08–1.54 g). Some of the latter samples appear pale-coloured due to their shallow thickness. Photo by Nutnicha Sripadungcharoen.

2.0 nm. Fourier-transform infrared (FTIR) spectroscopy was performed on all samples using a Thermo Nicolet iS50 FTIR spectrometer equipped with an XT-KBr beam splitter and DTGS-KBr detector operating with a 4× beam condenser. The resolution was 4 cm^{-1}.

Chemical analyses of all samples were obtained using laser ablation inductively coupled plasma mass spectrometry (LA-ICP-MS) with a Thermo Fisher Scientific iCAP Q ICP-MS coupled with a Q-switched Nd:YAG laser operating at a wavelength of 213 nm. The analytical parameters included a laser spot size of 40 µm in diameter, a fluence of around 10 J/cm^2 and a 10 Hz repetition rate. NIST 610 and NIST 612 glasses were used for calibration standards. The time-resolved signal was processed with Qtegra ISDS software using silicon (^{29}Si) as the internal standard, applying a theoretical value of 31.35 wt.% for beryl.

RESULTS AND DISCUSSION

The emeralds from Ambodivandrika were relatively intense bluish green, while those from Ambatomaneno were generally paler bluish green. Standard gemmological testing yielded RIs of n_o = 1.591 ± 0.001 and n_e = 1.583 ± 0.001, with a birefringence of 0.009 ± 0.001. The SG values were 2.75 ± 0.02. No systematic differences were noted in the RI and SG values between emeralds from the two different mining areas. A doubly refractive reaction was observed with the polariscope. The samples were inert to both long- and short-wave UV radiation.

Samples from both areas had black to brown micaceous material on their outer surfaces. Examination with a gemmological microscope revealed that the emeralds from Ambodivandrika were relatively clean, while those from Ambatomaneno appeared somewhat cloudy. Internal features in the Ambodivandrika samples included reddish brown and black dendritic inclusions (Figure 8a), as also seen in emeralds from the Kafubu area in Zambia (Zwaan *et al.* 2005; Saeseaw *et al.* 2014) and in other schist-hosted emeralds (Hänni *et al.* 1987). They also contained elongate colourless inclusions with concentric equatorial fractures (Figure 8b), similar to those seen in Brazilian emeralds from Nova Era (Hänni *et al.* 1987).

The samples from Ambatomaneno contained irregular two-phase (fluid-gas) inclusions with relatively large bubbles (Figure 8c), similar to those documented in emeralds from Shakiso in Ethiopia (Renfro *et al.* 2017) and the Belmont mine in Brazil (Hänni *et al.* 1987). Iridescent platelets were seen in one Ambatomaneno sample (Figure 8d), similar to those commonly encountered in Russian emeralds (Palke *et al.* 2019). Overall, there was some overlap in the internal features seen in the samples from Ambodivandrika and Ambatomaneno. Although fluorite, tourmaline and magnesite have been reported previously in Madagascar emeralds (Gübelin & Koivula 2008), these were not seen in our samples.

The UV-Vis-NIR spectra (Figure 9) revealed electronic transitions of Cr and Fe. The most prominent features were Cr^{3+} absorption bands at about 430, 600, 639 and 683 nm, Fe^{3+} absorption at 372 nm, and the broad feature at 810 nm that is due to Fe^{2+} and possibly Fe^{2+}–Fe^{3+} interactions, typical of schist-hosted emeralds (Saeseaw *et al.* 2014, 2019). The Cr^{3+} absorptions were more pronounced in the Ambodivandrika sample. Both spectra are similar to those of schist-type emeralds from other localities such as Brazil, Ethiopia, Russia and Zambia (Karampelas *et al.* 2019).

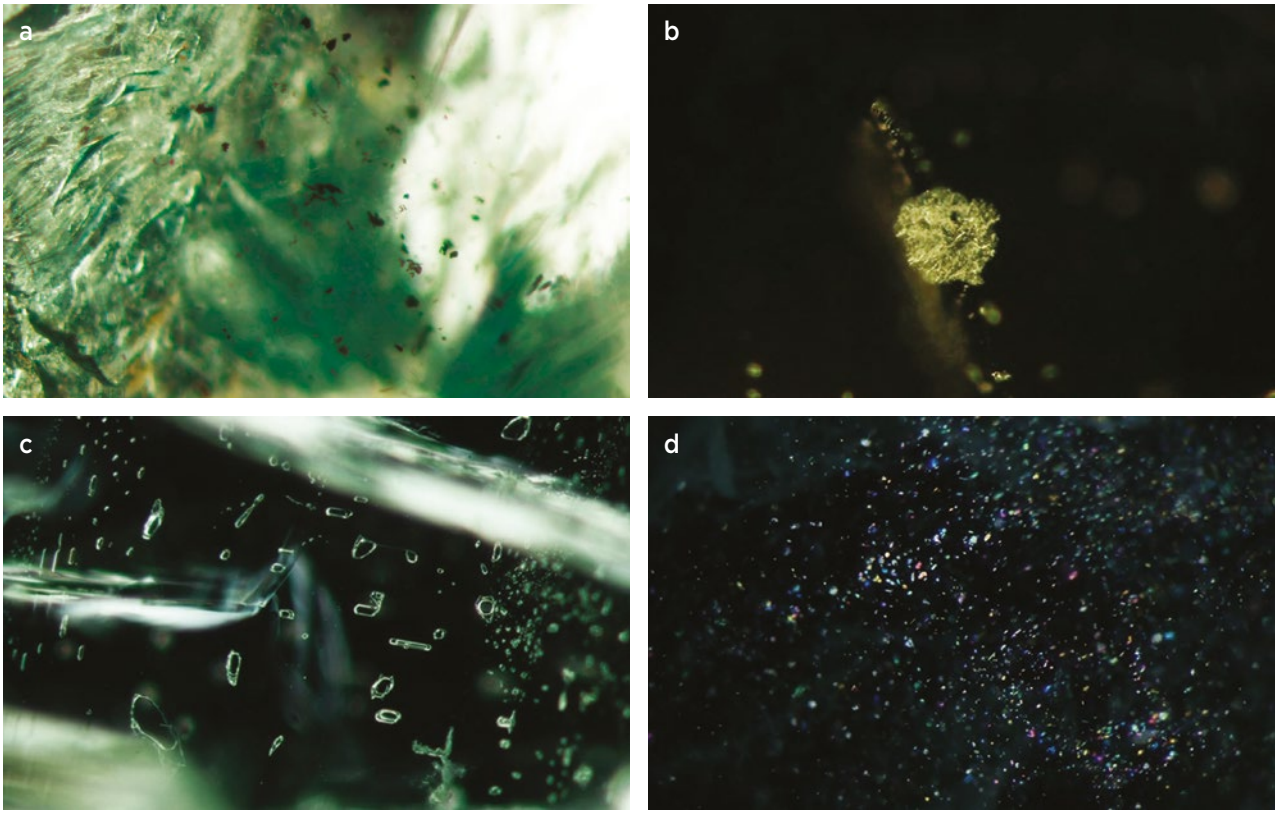

Figure 8: Microscopic examination of the Madagascar emerald samples reveals various internal features. Emeralds from Ambodivandrika contain reddish brown and black dendritic inclusions (**a**, image width 1.4 mm), and may also display elongate colourless inclusions with concentric equatorial fractures (**b**, image width 1.5 mm). Emeralds from Ambatomaneno show irregular-shaped two-phase inclusions with large bubbles (**c**, image width 14.8 mm), and may also contain iridescent reflective platelets (**d**, image width 2.2 mm). Photomicrographs by S. Luetrakulprawat.

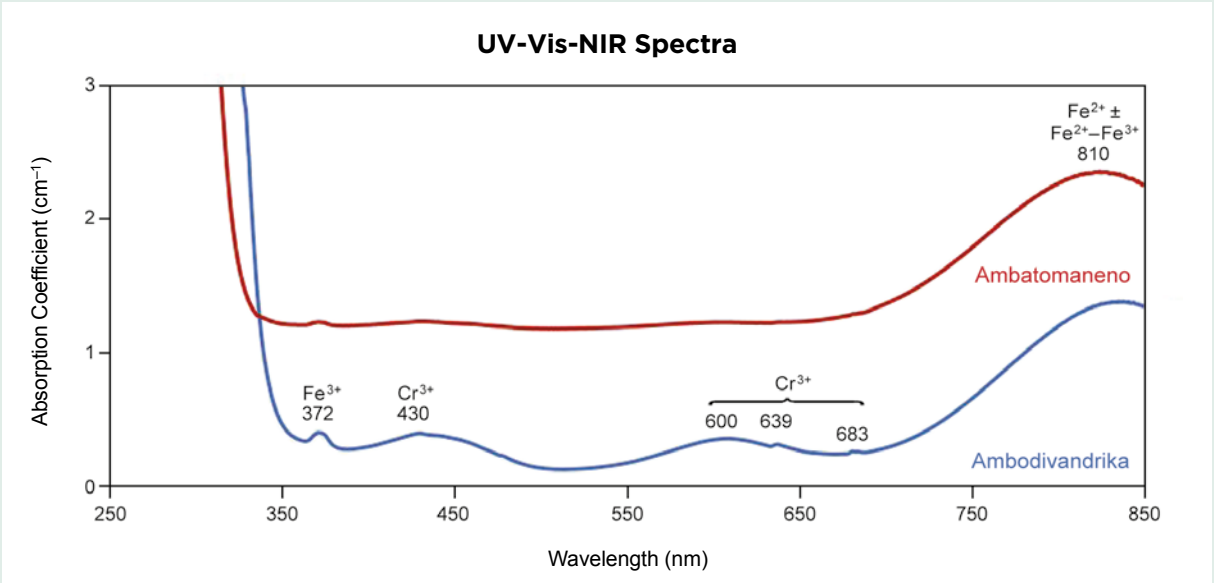

Figure 9: UV-Vis-NIR spectra (for the o-ray) of the Madagascar emeralds reveal typical features for Cr^{3+}, Fe^{2+} and Fe^{3+}, with weaker Cr^{3+} features in the Ambatomaneno samples. The top spectrum is offset vertically for clarity.

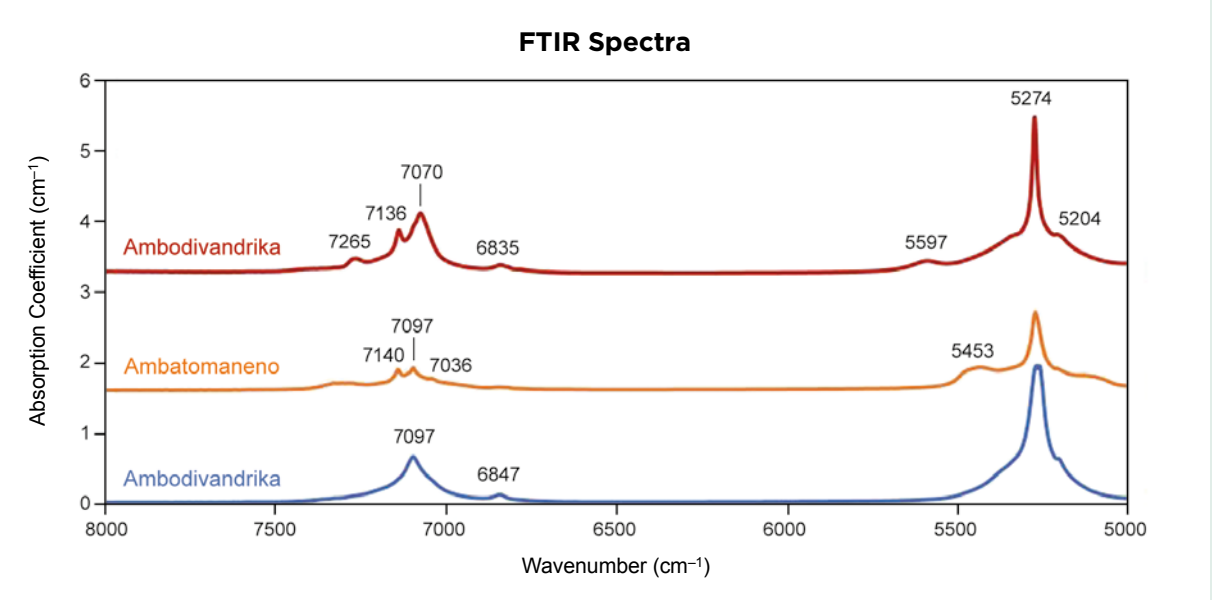

Figure 10: FTIR spectra of the Madagascar emeralds show three basic patterns, but they all reveal a series of water-related bands at 7500–6500 cm^{-1} and at around 5270 cm^{-1}. The spectra are offset vertically for clarity.

The FTIR spectra (Figure 10) showed three different patterns of water-related bands from 7500 to 6500 cm^{-1} and at around 5270 cm^{-1} (Saeseaw *et al.* 2014).

LA-ICP-MS analysis (Table I) revealed minor amounts of Mg, Na, Fe, K and Cr, as well as traces of Li, Sc, V, Mn, Co, Ni, Zn, Ga, Rb and Cs. The chromophores Cr, V and Fe were present in significant amounts, particularly Fe. The Cr/V ratio was relatively high compared to

Table I: LA-ICP-MS analyses of the studied emeralds from Madagascar.[a]

Element (ppm)	Ambodivandrika (8 samples)			Ambatomaneno (7 samples)		
	Min.–Max.	Average	Median	Min.–Max.	Average	Median
Li	56–129	108	112	35–65	55	57
Na_2O (wt.%)	1.67–2.05	1.84	1.80	0.54–1.48	1.25	1.34
MgO (wt.%)	2.69–3.15	2.95	2.97	0.93–2.49	2.09	2.26
K	592–2510	1758	1950	935–3020	2046	1960
Sc	24–48	35	33	19–66	42	38
V	96–118	107	108	52–99	79	86
Cr	1120–1590	1341	1325	232–983	559	545
Mn	4–14	10	11	9–19	15	16
Fe	9790–11100	10500	10500	3320–10400	8498	9370
Co	2–4	3	3	2–3	3	3
Ni	23–33	27	26	9–33	20	20
Zn	9–15	11	11	29–47	36	35
Ga	5–8	7	6	10–17	13	13
Rb	139–210	171	168	44–79	60	63
Cs	508–853	654	660	97–202	129	108
Cr/V	11–15	12	13	5–11	7	6
Na_2O/MgO	0.57–0.73	0.62	0.60	0.56–0.67	0.60	0.59
Total alkalis (wt.%)[b]	1.54–1.73	1.63	1.63	0.51–1.38	1.16	1.21

[a] Three spots were measured on each sample.
[b] Total alkalis = Sum of the concentrations of Li + Na + K + Rb + Cs.

that for emeralds from other localities (cf. Karampelas *et al*. 2019). In addition, the alkali contents (Na, K, Rb and Cs) of these samples were rather high, whereas Li was relatively low compared to other type IA emerald occurrences (e.g. Ethiopia, Russia, Zimbabwe and Zambia; Giuliani *et al*. 2019). Comparing samples from the two mining areas, the emeralds from Ambodivandrika showed significantly higher contents of most trace elements than those from Ambatomaneno, particularly for alkalis such as Na, Rb and Cs. However, the contents of K, Mn, Zn and Ga were slightly higher in emeralds from Ambatomaneno. These trends probably reflect differences in the chemical signature of the local geology between the two mining areas.

CONCLUSIONS

The recent visits by author VP to the emerald deposits near Mananjary enabled the study of reference samples obtained on site at two different mines in the southern and northern parts of the emerald-mining region. The samples from Ambodivandrika were relatively cleaner and more intense bluish green than those from Ambatomaneno. Internal features in the Ambodivandrika emeralds generally consisted of reddish brown and black dendritic inclusions as well as elongate colourless inclusions with concentric equatorial fractures, while the Ambatomaneno samples mainly contained two-phase (fluid-gas) inclusions and iridescent thin films, with some overlap between the samples from the two mining areas. The emeralds from Ambodivandrika generally contained more trace-element impurities than those from Ambatomaneno.

This study shows that emeralds from different deposits in eastern Madagascar may show some significant differences in their inclusions and chemical composition, and therefore Malagasy emeralds deserve more detailed study. The deposits appear to have good potential for the additional production of fine, light to deep green emeralds with good transparency.

REFERENCES

Campbell, I.C.C. 1991. A report on one of a number of emeralds from Madagascar. *South African Gemmologist*, **5**(1), 8–15.

Chan Peng, J.-C. 2003. *Modalités de formation des gisements d'émeraude de la région de Mananjary – est de Madagascar*. Unpublished PhD thesis, Université Paul Sabatier, Toulouse, France, 155 pp.

Cheilletz, A., Sabot, B., Marchand, P., De Donato, P., Taylor, B., Archibald, D., Barres, O. & Andrianjaffy, J. 2001. Emerald deposits in Madagascar: Two different types for one mineralizing event. *European Union of Geosciences XI General Assembly*, Strasbourg, France, 547.

Chikayama, A. 1989. Gemstones from Madagascar. *XXII International Gemmological Conference*, Tremezzo, Italy.

Clanin, J. 2012. *The Fundamentals of Mining for Gemstones and Mineral Specimens*. New England Historical Publications, Massachusetts, USA, 402 pp.

Giuliani, G., Groat, L.A. & Marshall, D.D. 2018. Emerald deposits in the 21st century. *InColor*, No. 40, 22–32.

Giuliani, G., Groat, L.A., Marshall, D., Fallick, A.E. & Branquet, Y. 2019. Emerald deposits: A review and enhanced classification. *Minerals*, **9**, article 105 (63 pp.), https://doi.org/10.3390/min9020105.

Gübelin, E.J. & Koivula, J.I. 2008. *Photoatlas of Inclusions in Gemstones*, Vol. 3. Opinio Publishers, Basel, Switzerland, 672 pp.

Handke, M.J., Tucker, R.D. & Ashwal, L.D. 1999. Neoproterozoic continental arc magmatism in west-central Madagascar. *Geology*, **27**(4), 351–354, https://doi.org/10.1130/0091-7613(1999)027<0351:Ncamiw>2.3.Co;2.

Hänni, H.A. & Klein, H.H. 1982. Ein Smaragdvorkommen in Madagaskar. *Zeitschrift der Deutschen Gemmologischen Gesellschaft*, **31**(1/2), 71–77.

Hänni, H.A., Schwarz, D. & Fischer, M. 1987. The emeralds of the Belmont mine, Minas Gerais, Brazil. *Journal of Gemmology*, **20**(7), 446–456, https://doi.org/10.15506/JoG.1987.20.7.446.

Karampelas, S., Al-Shaybani, B., Mohamed, F., Sangsawong, S. & Al-Alawi, A. 2019. Emeralds from the most important occurrences: Chemical and spectroscopic data. *Minerals*, **9**, article 561 (29 pp.), https://doi.org/10.3390/min9090561.

Kleyenstüber, A. 1991. Observation of inclusions in a Madagascar emerald and their possible implications. *South African Gemmologist*, **5**(2), 4–9.

Levat, D. 1912. *Richesses Minérales de Madagascar*. H. Dunod et E. Pinat, Paris, France, 359 pp.

Markl, G., Bäuerle, J. & Grujic, D. 2000. Metamorphic evolution of Pan-African granulite facies metapelites from southern Madagascar. *Precambrian Research*, **102**(1–2), 47–68, https://doi.org/10.1016/s0301-9268(99)00099-6.

Moine, B., Chan Peng, C. & Mercier, A. 2004. Rôle du fluor dans la formation des gisements d'émeraude de Mananjary (est de Madagascar). *Comptes Rendus Geoscience*, **336**, 513–522, https://doi.org/10.1016/j.crte.2003.12.013.

Palke, A.C., Lawley, F.J., Vertriest, W., Wongrawang, P. & Katsurada, Y. 2019. The Russian emerald saga: The Mariinsky Priisk mine. *InColor*, No. 44, 36–46.

Pardieu, V. 2009. Concise field report—Volume 1: Pailin, Cambodia (Dec 2008 – Feb 2009). Gemological Institute of America, Bangkok, Thailand, 35 pp., www.gia.edu/doc/Field-Report_Pailin.pdf.

Pardieu, V. 2018a. "Ants and Kings: Part 1: Kings": Emeralds from Mananjary, Madagascar. YouTube, www.youtube.com/watch?v=qUioeFyvY_o, accessed 6 December 2018.

Pardieu, V. 2018b. Emerald deposits near Mananjary, Madagascar. Overview by a field gemologist. *InColor*, No. 40, 95–97.

Pardieu, V. 2020a. Ants and Kings: Emeralds from Mananjary Madagascar: "Ants and Kings" (Part 02: Ants). YouTube, www.youtube.com/watch?v=7S0PB-FC3ZQ, accessed 10 April 2020.

Pardieu, V. 2020b. Field gemology: The evolution of data collection. *InColor*, No. 46, 36–42.

Pezzotta, F. 1999. Madagascar—*A Mineral and Gemstone Paradise*. extraLapis English No. 1, Christian Weise Verlag, Munich, Germany, and Lapis International, East Hampton, Connecticut, USA, 98 pp.

Ranorosoa, N. 1993. *Étude du gisement d'émeraude de Mananjary (Madagascar)*. Diplôme d'Université de Gemmologie (DUG) thesis, University of Nantes, 118 pp. (in French).

Renfro, N., Sun, Z., Nemeth, M., Vertriest, W., Raynaud, V. & Weeramonkhonlert, V. 2017. Gem News International: A new discovery of emeralds from Ethiopia. *Gems & Gemology*, **53**(1), 114–116.

Saeseaw, S., Pardieu, V. & Sangsawong, S. 2014. Three-phase inclusions in emerald and their impact on origin determination. *Gems & Gemology*, **50**(2), 114–132, https://doi.org/10.5741/gems.50.2.114.

Saeseaw, S., Renfro, N.D., Palke, A.C., Sun, Z. & McClure, S.F. 2019. Geographic origin determination of emerald. *Gems & Gemology*, **55**(4), 614–646, https://doi.org/10.5741/gems.55.4.614.

Schwarz, D. 1994. Emeralds from the Mananjary region, Madagascar: Internal features. *Gems & Gemology*, **30**(2), 88–101, https://doi.org/10.5741/gems.30.2.88.

Schwarz, D. & Henn, U. 1992. Emeralds from Madagascar. *Journal of Gemmology*, **23**(3), 140–149, https://doi.org/10.15506/JoG.1992.23.3.140.

Sinkankas, J. 1981. *Emerald and Other Beryls*. Chilton Book Co., Radnor, Pennsylvania, USA, 665 pp.

Thomas, A. 1993. The emerald mines of Madagascar. *South African Gemmologist*, **7**(1), 3–11.

Tucker, R.D., Peters, S.G., Roig, J.Y., Théveniaut, H. & Delor, C. 2012. *Notice Explicative des Cartes Géologique et Métallogéniques de la République de Madagascar à 1/1,000,000*. Ministry of Mines, Antananarivo, Madagascar, 257 pp.

Vapnik, Y., Moroz, I., Roth, M. & Eliezri, I. 2006. Formation of emeralds at pegmatite-ultramafic contacts based on fluid inclusions in Kianjavato emerald, Mananjary deposits, Madagascar. *Mineralogical Magazine*, **70**(2), 141–158, https://doi.org/10.1180/0026461067020320.

Zwaan, J.C., Seifert, A.V., Vrána, S., Laurs, B.M., Anckar, B., Simmons, W.B., Falster, A.U., Lustenhouwer, W.J. *et al.* 2005. Emeralds from the Kafubu area, Zambia. *Gems & Gemology*, **41**(2), 116–148, https://doi.org/10.5741/gems.41.2.116.

The Authors

Vincent Pardieu
VP Consulting SPC, Office 714, Building 469, Road 1705, Block 317, Diplomatic Area, Manama, Kingdom of Bahrain
Email: vince@fieldgemology.org

Dr Supharart Sangsawong FGA and Sarocha Luetrakulprawat
ICA | GemLab, 6th Fl., Jewelry Trade Center, Silom Road, Bangrak, Bangkok, Thailand 10500

Léonard Cornuz
CREALP (Centre de Recherche sur l'Environnement Alpin), 8 rue du Rhone, 1950 Sion, Switzerland

Victoria Raynaud
Raynaud & Prim, Bangkok, Thailand

Acknowledgements

The authors thank the Andrianjafy family and people from Le Quartz Cie in Madagascar for their welcome at the mine. We also thank Kenneth Scarratt and his colleagues at the ICA | GemLab in Bangkok for their help and support.

Gem-A Notices

COVID-19 NOTICE

In this unprecedented year, we continue to see the effects of the COVID-19 pandemic impacting global economies, businesses and individual livelihoods, which have challenged our very way of life. Our great Association has also seen the impact of the pandemic on our finances and business activities. Despite these uncertainties, Gem-A's management team and staff have continued to work tirelessly to support the Association's core functions of education and membership. While this has meant some internal changes to our business operations, as announced in Membership communications from Gem-A's CEO Alan Hart FGA DGA, we would like to reassure our Members that the Association remains strong and resilient. Through the various operational measures undertaken over the past six months, we will see the uncertain times through and be in a position to improve, grow and flourish in the future.

GEM-A GRADUATION AND PRESENTATION OF AWARDS

Due to the global pandemic, Gem-A made a very difficult decision to cancel the Gem-A Graduation and Presentation of Awards that was scheduled to take place in November 2020. For the January 2020 examinations, 233 students passed our Gemmology and Diamond Diploma examinations, and 16 of them passed with Distinction. Every year over our long history we have celebrated our graduates, some of whom come from across the globe to attend the awards ceremony in London and become part of our prestigious gemmology community. Last year we celebrated our 2019 graduates with a ceremony at the Royal Institution of Great Britain (e.g. see photo).

Although times have changed and social distancing rules mean that we cannot meet in person for now, we would like to give our heartiest congratulations to our January 2020 graduates. Due to the postponement of the Gem-A June examinations until September 2020, this graduate list and the 2020 Prize and Medal winners will be announced in the following issue of *The Journal* (Vol. 37, No. 5, 2021). Next year, we look forward to holding a combined 2020/2021 Gem-A Graduation and Presentation of Awards at London's historic Church House.

GEMMOLOGY DIPLOMA PASSES

Azra Aadil, Sri Lanka
Nicole J. Ahline, United States of America
Jean-Marie Albanese, France
Musharraf Ali Anver, Sri Lanka
Nalin Prasantha Ariyadasa, Sri Lanka
Tianxing Bai, P.R. China
Yuan Bai, P.R. China
Anouska Banks, United Kingdom
Yang Bao, P.R. China
José Silva Baptista, Portugal
Manon Bigot, France
Min Cao, P.R. China
Qiaoqiao Cao, P.R. China
Wing Sum Nicole Chan, Hong Kong (S.A.R.)
Chi-Lan Chang, Taiwan (R.O.C.)
Chin-Cheng Chang, Taiwan (R.O.C.)
Yu-Hsien Vivian Chang, Taiwan (R.O.C.)
Mutong Che, P.R. China
Anqi Chen, P.R. China
Gang Chen, P.R. China
Jun Chen, P.R. China
Kanglin Chen, P.R. China
Shuming Chen, P.R. China
Xin Chen, P.R. China
Xu Chen, P.R. China
Xingyu Chi, P.R. China
Kris Chien, P.R. China
Cheung Choi, Hong Kong (S.A.R.)
Shiyuan Cui, P.R. China
Tong Cui, P.R. China
Xinyi Deng, P.R. China
Ruoke Ding, P.R. China
Naimeng Dong, P.R. China
Hana Downing, United Kingdom
Joëlle Dufour, Canada
Qianyu Fan, P.R. China
Yue Fan, P.R. China
Jia Feng, P.R. China
Jiaqi Feng, P.R. China
Quan Shun Feng, P.R. China
Fazzari Nathalie Marie France, Madagascar
Cordelia Jane Fraser, United Kingdom
Fangfang Fu, P.R. China
Lanying Fu, P.R. China
Fang Gao, P.R. China
Jingya Gao, P.R. China
Tianyuan Gao, P.R. China
Xiang Gao, P.R. China
Yujia Gao, P.R. China
Yuxuan Gao, P.R. China
Julie Gau, France
Xiuhua Gong, P.R. China
Gandi He, P.R. China
Jing He, P.R. China
Rundi He, P.R. China
Zhaoran He, P.R. China
Wei Ting Hsu, Taiwan (R.O.C.)
Danyan Hu, P.R. China
Xing Ji, P.R. China
Ying Jia, P.R. China
Yusi Jia, P.R. China
Bohan Jiang, P.R. China
Mingming Jiao, P.R. China
Lucy Jupp, United Kingdom
Barbara Kentish Barnes, United Kingdom
Kitty Annelike India Kimber, United Kingdom
Ying-Hui Kuo, Taiwan (R.O.C.)
Yu-Po Lee, Taiwan (R.O.C.)
Jinlian Lei, P.R. China
Kam Fai Leung, Hong Kong (S.A.R.)
Jing Li, P.R. China
Lanbing Li, P.R. China
Ling Li, P.R. China
Qianmin Li, P.R. China
Wei Hao Li, Taiwan (R.O.C.)
Xiangyi Li, P.R. China

Xuyang Li, P.R. China
Yan Li, P.R. China
Dandan Liang, P.R. China
Haoran Lin, P.R. China
Jiaying Lin, P.R. China
Zhaoying Lin, P.R. China
Jie Liu, P.R. China
Lina Liu, P.R. China
Niya Liu, P.R. China
Qiuhua Liu, P.R. China
Tianlin Liu, P.R. China
Zhengyu Long, P.R. China
Yifan Lu, P.R. China
Yingrong Lu, P.R. China
Junyue Luo, P.R. China
Tianyu Luo, P.R. China
Aung Ko Lwin, Myanmar
Ke Ning Ma, P.R. China
Shijing Ma, P.R. China
Xingyi Mao, P.R. China
Myrna-Ivy Martinet, France
Ian Bruce McLeod, United Kingdom
Ran Meng, P.R. China
Lydia Micallef, United Kingdom
Fabienne Michaud, France
Fei Mo, P.R. China
Yunfei Mo, P.R. China
Fathima Tasneema Mohamed, Sri Lanka
Chao Peng, P.R. China
Hui Peng, P.R. China
Yizhou Qian, P.R. China
Ying Ren, P.R. China
Yuenan Ren, P.R. China
Anna Robertson, United Kingdom
Afat Rustamova-Ferris, United Kingdom
Valentina Scuderini, United Kingdom
Sarah Marie Suzanne Senzer, Canada
Yanran Shang, P.R. China
Min Hua Shi, Hong Kong (S.A.R.)
Than Than Soe, Myanmar
Michaela Stephan, United States of America
Laura Suades Vall, United Kingdom
Ling Sun, P.R. China
Ning Sun, P.R. China
Sufang Sun, P.R. China
Susi Taylor, United Kingdom
De Jack Teh, Malaysia
Po Chun The, P.R. China
Ying-Shuo Tseng, Taiwan (R.O.C.)
Lung Shing William Wai, P.R. China
Bo-Syong Wang, Taiwan (R.O.C.)
Chuchu Wang, P.R. China
Dan Wang, P.R. China
Han Wang, P.R. China
Jing-Yi Wang, Taiwan (R.O.C.)
Lijuan Wang, P.R. China
Lin Wang, P.R. China
Luwei Wang, P.R. China
Siyu Wang, P.R. China
Xiaohui Wang, P.R. China
Yanzhou Wang, P.R. China
Yimeng Wang, P.R. China
Yu Wang, P.R. China
Helena Waudby, United Kingdom
Zhen Wei, P.R. China
He Weng, P.R. China
Madison Rose Whitman, United States of America
Dongyuan Wu, P.R. China
Lanxi Wu, P.R. China
Yueqin Wu, P.R. China
Zhenhuan Wu, P.R. China
Jingwen Xiao, P.R. China
Guangbing Xing, P.R. China
Ning Xu, P.R. China
Sihan Xu, P.R. China
Kang Yang, P.R. China
Puyue Yang, P.R. China
Tian Zhen Yang, P.R. China
Xia Yang, P.R. China
Jingya Ye, P.R. China

Xinyi Ye, P.R. China
Ting-Hsuan Yen, Taiwan (R.O.C.)
Mingshu Yin, P.R. China
Mengying Yu, P.R. China
Yue Yu, P.R. China
Lei Zhang, P.R. China
Li Zhang, P.R. China
Yamin Zhang, P.R. China
Yang Zhang, P.R. China
Yang Yang Zhang, P.R. China
Yiwu Zhang, P.R. China
Yongli Zhang, P.R. China
Yu Qi Zhang, P.R. China
Yue Zhang, P.R. China
Yuhui Zhang, P.R. China
Kehan Zhao, P.R. China
Meiqiao Zhao, P.R. China
XiaoChuan Zhao, P.R. China
Xuenan Zhao, P.R. China
Ziqi Zhao, P.R. China
Ziyan Zhao, P.R. China
Zhou Zhou, P.R. China
Hong Zhu, P.R. China
Xiaoxin Zhu, P.R. China
Ruiyan Zuo, P.R. China

GEMMOLOGY DIPLOMA PASSES WITH MERIT

Zi Wen Bao, P.R. China
Dongxu Chen, P.R. China
Juglair Léa, France
Yihan Li, P.R. China
Xin Liu, P.R. China
Yuning Liu, P.R. China
Hongyu Lyu, P.R. China
Yuanmeng Song, P.R. China
Chen Wang, P.R. China
Xinxin Xiao, P.R. China
Xinyue Xu, P.R. China
Nan Zhang, P.R. China

GEMMOLOGY DIPLOMA PASSES WITH DISTINCTION

Renping Cheng, P.R. China
Xinying Shi, P.R. China
Ziyi Wang, P.R. China
Siyi Zhu, P.R. China

DIAMOND DIPLOMA PASSES

Sorrel Auger-Cerrone, United Kingdom
Damon Andrew Neish Barker, United Kingdom
Ting Yan Chiu, Hong Kong (S.A.R.)
Etienne Du Toit, United Kingdom
Edward John Evans, United Kingdom
Ka Yee Keung, Hong Kong (S.A.R.)
Kin Man Kong, P.R. China
Bo-Xuan Lin, Taiwan (R.O.C.)
Yu-Hung Lin, Taiwan (R.O.C.)
Yuen Hoi Ling Helen, Hong Kong (S.A.R.)
Mei Sze Olive Lo, P.R. China
Chiemi Sasajima, Italy
Po-Jui Ting, Taiwan (R.O.C.)
Jen-Hao Tung, Taiwan (R.O.C.)
Chi Him Jerome Wai, P.R. China
Helena Waudby, United Kingdom
Ching Yip Wong, Hong Kong (S.A.R.)
Wenxian Xu, P.R. China

DIAMOND DIPLOMA PASSES WITH MERIT

John Nils Axelson, United Kingdom
Astrid Bosshard Schreckenberg, Switzerland
Fung Yee Chan, Hong Kong (S.A.R.)
Robert Patrick Hart, United Kingdom
Ka Yee Leung, Hong Kong (S.A.R.)
Laura Suades Vall, United Kingdom

DIAMOND DIPLOMA PASSES WITH DISTINCTION

Rebecca Sophie Block, United Kingdom
Patricia Campion, United Kingdom
Valeria Di Cola, United Kingdom
Carolyn Harrington, United Kingdom
Su Myat Htet, Myanmar
Katrina Hughes, United Kingdom
Ceylan Ismail, United Kingdom
Leyla Ismail, United Kingdom
Amanda Pollarolo, United Kingdom
Masumi Sakai, Japan
Stacie Anne Tayler, United Kingdom
Joanna Wyganowska, United Kingdom

MEMBERSHIP RENEWAL NOTICE

Gem-A Members are at the heart of everything we do. In this unprecedented year, the support and well wishes conveyed by our Members have reinforced our efforts to do everything possible to maintain our great Association and its core functions of education and membership. At the end of October we started our annual Membership renewal run, and your support has never been more important than now. Head over to the Gem-A website to securely pay for your annual Membership. Renew before 31 December 2020 to benefit from the early-bird fee of £110. We have streamlined our payment options by introducing GoCardless and PayPal subscription services. We also still accept bank transfers, but due to the current pandemic we kindly discourage you from sending cheques, and we are unable to take payments over the phone. If you need assistance with your renewal, Gem-A's Membership Secretary is available via email at membership@gem-a.com. Through your Membership renewal, you will be able to continue enjoying Gem-A's quarterly publications and other benefits, including being part of a highly regarded and well-respected global network of gemmology professionals.

GIFTS TO THE ASSOCIATION

Gem-A is most grateful to our generous donors, who support continued research and teaching:

Christopher P. Smith, USA, for developing and donating a customised database for recording information on all of Gem-A's stone samples and literature, and making it accessible to Gem-A USA.

GEM-A ANNUAL GENERAL MEETING 2020

Due to the current pandemic and social distancing rules, the Gem-A Council made the decision to hold the Gem-A Annual General Meeting (AGM) online for the very first time. The 2020 AGM will be held on 16 December 2020 at 17:00 GMT. Members have received notification by email to register for the AGM and receive secure online access to submit their votes on the AGM resolutions. The results from the online voting will be announced at the AGM. The online AGM will provide a safe and effective opportunity for Members globally to participate and vote on the resolutions of the Association. For those who cannot attend, the AGM will be recorded and uploaded to the Members area of the Gem-A website.

A WEBINAR WITH THE EDITOR

Go behind the scenes at *The Journal of Gemmology* by tuning in to our ongoing webinar series with Editor-in-Chief Brendan Laurs FGA, on 27 January 2021 at 17:00 GMT.

Join us as we hear Brendan discuss the current issue of *The Journal* with Gem-A's CEO Alan Hart FGA DGA. To register your place, head to https://linktr.ee/gemaofgb. Did you miss our previous sessions of Gem-A Live with Brendan? Head to Gem-A's YouTube Channel and watch them now: www.youtube.com/c/GemAOfficialChannel.

Learning Opportunities

Note: Event dates and formats are subject to change depending on the COVID-19 situation.

CONFERENCES AND SEMINARS

23rd FEEG Symposium—25th Anniversary
~~23–24 January 2021~~ Postponed to January 2022
Paris, France
www.feeg-education.com/symposium

NAJA 55th Ace© It Virtual Conference
30–31 January 2021
Online
www.najaappraisers.com/html/conferences.html

AGTA Gemfair Tucson
2–7 February 2021
Tucson, Arizona, USA
https://agta.org/agta-gem-fair-tucson
Note: Includes a seminar programme

Hong Kong International Jewellery Show
3–7 March 2021
Hong Kong
https://event.hktdc.com/fair/hkjewellery-en/HKTDC-Hong-Kong-International-Jewellery-Show

10th National Opal Symposium
31 March–1 April 2021
Coober Pedy, Australia
www.opalsymposium.org

17th Annual Sinkankas Symposium – Agate & Chalcedony
April or May 2021 (exact date TBA)
Carlsbad, California, USA
https://sinkankassymposium.net

American Gem Society Conclave
26–28 April 2021
Louisville, Kentucky, USA
www.conclave2021.americangemsociety.org

Swiss Gemmological Society Conference
30 May–1 June 2021
St Gallen, Switzerland
http://gemmologie.ch/en/current

JCK Las Vegas
4–7 June 2021
Las Vegas, Nevada, USA
https://lasvegas.jckonline.com
Note: Includes a seminar programme

14th International Conference on New Diamond and Nano Carbons (NDNC)
6–10 June 2021
Kanazawa, Japan
www.ndnc2020.org

Diamonds – Source to Use 2021
9–11 June 2021
Johannesburg, South Africa
www.saimm.co.za/saimm-events/upcoming-events/diamonds-source-to-use-2020

Jewellery in Texts: Texts in Jewellery
19 June 2021
London
www.societyofjewelleryhistorians.ac.uk/news

NAJ Summit
19–21 June 2021
Northampton, East Midlands
www.naj.co.uk/summit
Note: Includes the IRV Valuers' Conference (19–21 June) and the JBN Retail Jewellers' Congress (21 June)

Jewellery & Gem ASIA Hong Kong
24–27 June 2021
Hong Kong
https://exhibitions.jewellerynet.com/6jg

Sainte-Marie-aux-Mines Mineral & Gem Show
24–27 June 2021
Sainte-Marie-aux-Mines, France
www.sainte-marie-mineral.com
Note: Includes a seminar programme

MJSA Expo
August 2021 (exact dates TBA)
New York, New York, USA
https://mjsa.org/eventsprograms/mjsa_expo
Note: Includes a seminar programme

NAJA 55th Ace© It Mid-Year Conference
14–17 August 2021
Location TBA
www.najaappraisers.com/html/conferences.html

9th International Conference Mineralogy and Museums
24–26 August 2021
Sofia, Bulgaria
www.bgminsoc.bg
Note: Gem minerals and archaeogemmology are among the topics that will be covered.

3rd European Mineralogical Conference (emc2020)
29 August–2 September 2021
Krakow, Poland
https://emc2020.ptmin.eu
Sessions of interest: The Geology of Gem Deposits: A Session in Honour of Gaston Giuliani; Materials Sciences and Archaeometry for Cultural Heritage

13th Annual Portland Jewelry Symposium
September 2021 (exact dates TBA)
Portland, Oregon, USA
https://portlandjewelrysymposium.com

31st International Conference on Diamond and Carbon Materials
5–9 September 2021
Palma, Mallorca, Spain
www.elsevier.com/events/conferences/international-conference-on-diamond-and-carbon-materials

3rd International Conference on Tourmaline (TUR2021)
9–11 September 2021
Elba Island, Italy
www.tur2021.com

OTHER EDUCATIONAL OPPORTUNITIES

Gem-A Workshops and Courses
Gem-A, London
https://gem-a.com/education

Lectures with The Society of Jewellery Historians
Society of Antiquaries of London, Burlington House
www.societyofjewelleryhistorians.ac.uk/current_lectures

- Jonathan Boyd—I Can't String a Sentence Together: Jewellery and Words/Words and Jewellery
  26 January 2021
- Jack Ogden—The Black Prince's Ruby: Investigating the Legend
  23 February 2021
- Carol Michaelson—Chinese Jade Jewellery and Ornaments from the Neolithic to the Present
  27 April 2021
- Gonçalo de Vasconclo e Sousa—Portuguese Jewellery
  25 May 2021
- Karl Schmetzer—The Late 14th-Century Royal Crown of Blanche of Lancaster
  22 June 2021
- Charlotte Gere—Colour in Victorian Jewellery
  28 September 2021
- Three Speakers TBA—New Research on Jewellery
  26 October 2021
- Ute Decker—Sculptural Minimalism & Fairtrade Gold – Philosophy, Provenance and Process
  23 November 2021

New Media

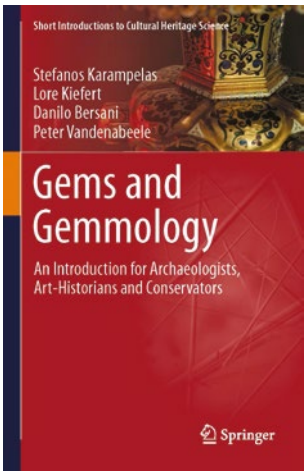

Gems and Gemmology: An Introduction for Archaeologists, Art-Historians and Conservators

By Stefanos Karampelas, Lore Kiefert, Danilo Bersani and Peter Vandenabeele, 2020. Short Introductions to Cultural Heritage Science series, Springer, Cham, Switzerland, 112 pages, illus., ISBN 978-3030354480 or e-ISBN 978-3030354497, https://doi.org/10.1007/978-3-030-35449-7. EUR62.39 hardcover or EUR50.28 eBook.

It is common in archaeological circles that an excavator or curator might lovingly describe a piece of jewellery, a Greek gold necklace perhaps, and then simply say something such as 'set with red stones'. The general lack of familiarity with gems and gemmology among archaeologists and art historians is self-evident, and a simple introductory text aimed at this target audience has been long-awaited. This book, sadly, is not it.

The first impression of the book is that it is quite brief, at only 112 pages and with just four chapters covering 'Gems Through the Ages', 'Gem Analysis', 'Gem Treatments, Synthetics and Imitations' and 'Archaeometrical Questions (Case Studies)'. Further perusal of the book shows that it has minimal visual appeal. Surely a book introducing art historians and archaeologists to gems and their study should be visually attractive and inspiring, especially when there are so many remarkable historic pieces and a wealth of interesting gems to draw from. Examples might include 4,000-year-old lapis lazuli beads from Mesopotamia; Roman jewellery containing diamonds, sapphires, amethysts, etc.; and early faceted gems in Medieval treasuries. However, the authors provide just three illustrations of gems that date to before around 1200 AD. By comparison, numerous illustrations show gemmological equipment, FTIR spectra, trace-element plots, etc. I am not convinced that a 112-page introductory text needs, for example, to describe the parts per million of boron in blue diamonds. The archaeologist, curator or conservator only needs to know what is possible with modern laboratory equipment, with clear examples.

The detailed coverage of 'classical' gemmological tools—such as the loupe, refractometer, polariscope, and so on—should have placed more emphasis on the use of the loupe. It is the most essential and portable of equipment, and seems more relevant in a brief introduction than, say, talking about the K and L levels of electrons. It is useful to know that advanced laboratory equipment can distinguish between ancient emeralds from Egypt and Pakistan, but for the archaeologist it would also be useful to know more simply that a non-Egyptian source might be suggested by the brighter-green, better-clarity and typically differently polished emeralds that began to be seen in some later Roman jewellery.

The four authors are all top experts in their fields, but none is a specialist in jewellery or gem history, and this is where gaps become particularly noticeable. The historical bits often seem to rely on older secondary sources and typically gemmological rather than archaeological or historical ones. This gives a somewhat outdated view of the subject. As an example, the book states that the Egyptian emerald mines were worked from 'at least 2000 BCE'. This is an old misunderstanding that was laid to rest in Egyptological circles at least as far back as the 1960s (in fact, there is no evidence for emerald use in Egypt before about 300 BCE). The book has a brief discussion of nomenclature issues with the quartz varieties, but no mention of a seminal work that specifically addresses these in an archaeological/historical context: Margaret Sax's 'The recognition and nomenclature of quartz materials with specific reference to engraved gemstones' (*Jewellery Studies*, **7**, 1996, 63–72). The chapter on treatments, synthetics and imitations is very much oriented to recent work, with no mention of the heat treatment of carnelian, for example, that dates back more than 4,000 years, or the heat crackling and dyeing of rock crystal in surviving Roman and Renaissance examples.

The book largely ignores the considerable recent research on early lapidary techniques, from how diamond chips were used in drilling and engraving other gem materials (by at least 500 BCE) to the introduction

of emery as an abrasive (probably by about 2000 BCE), before which sand was the primary option. Lapidary techniques might seem peripheral to gemmology, but you cannot study early gems without at least a framework for how they were worked. To give a simple example, a faceted sapphire bead cannot be Bronze Age. It is odd to say, as this book does, that gem cutting 'radically improved after the industrial revolution' (i.e. 1700s) but totally ignore the huge leap in lapidary work that came with the introduction of continuous rotary motion powered by the crank and flywheel in the 15th century.

The chapter on 'Archaeometrical Questions (Case Studies)' devotes almost 10% of the book's length to a fairly in-depth look at the gems set in Medieval and Renaissance treasures in Einsiedeln Abbey and the Basel Cathedral Treasury, both in Switzerland. Very interesting, but the book is aimed at 'students who need an introduction…and professionals who want to refresh their knowledge'. Where are the case studies of gemmological examinations of such things as humbler beads and little engraved gems, which can be no less illustrative of 'gemmology' but represent the types of gems most likely to be encountered by students and professionals?

Conservators are also included in the target audience given in the book's subtitle, but there is no chapter that covers the challenges of the degradation of some gem materials, a subject equally important to the excavating archaeologist. Durability is a defining feature of a gem, alongside beauty and rarity, but the durability of older gems, particularly long-buried ones, cannot always be taken for granted and thus beauty is threatened. Even garnets in archaeological objects can show surface etching caused by weathering, and there can be considerable selective etching of the different colour bands in agates that have spent millennia underground. Pearls and amber are particularly affected by long burial. At one extreme, pearls can disappear completely; at the other is the precipitation of calcite onto their surfaces. It is surprising for a book on gems partly aimed at conservators to lack a chapter tackling important issues that can impact such objects' conservation.

At the start of this review, I mentioned an archetypical archaeologist or art historian labelling a gem as a 'red stone'. That is better than making an uneducated guess at its identity. What they need is a guide that allows them to make a more educated and provisional suggestion of identity, helps them to understand why correct identification is important, and tells them in an inspirational way of the potentials for gemmology and gemmological science in their fields. They are still waiting.

Dr Jack M. Ogden FGA
London
United Kingdom

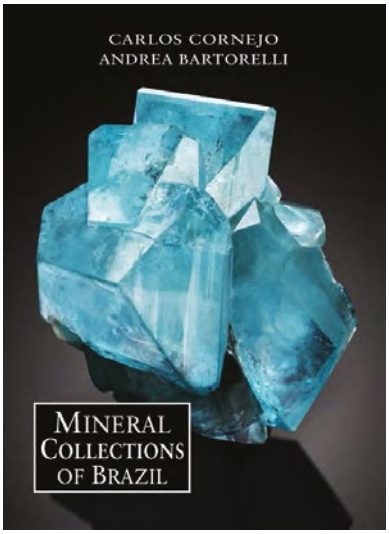

Mineral Collections of Brazil/ Coleçóes Minerais do Brasil

By Carlos Cornejo and Andrea Bartorelli, 2020. Solaris Edições Culturais, São Paulo, Brazil, solarised@terra.com.br, 792 pages, illus., ISBN 978-8589820134 (English) or ISBN 978-8589820127 (Portuguese). USD120.00 hardcover.

This comprehensive and monumental 792-page book follows a previous work by the same authors titled *Minerals & Precious Stones of Brazil* that was published in 2010. In the words of co-author Carlos Cornejo, 'With this book, we seek to highlight…Brazilian mineralogy, gemmology and palaeontology, leaving a historical record not only of the specimens, but also of the people who extract, collect, study, and preserve them.... In essence, this book is about presenting the most beautiful, interesting or rare pieces of collectors, institutions and mineralogical museums in Brazil' (p. 6). Co-author Andrea Bartorelli added that, where possible, sponsorship from the book's participants helped cover the cost of the respective chapters. The authors were surprised by 'the eager turnout of over 70 private collectors, museums and public institutions' (p. 7), which allowed this greatly expanded edition to include collections consisting of fossils, meteorites, lithic artefacts, faceted gemstones and jewellery.

The table of contents lists 75 sections comprising six main chapters. The book starts with an introduction consisting of a preface by each author and a review of

important mineralogical discoveries reported in various European publications, beginning with the early 16th century. Included as the book's first illustration is an image from Conrad Gesner's 1565 *De Omni Rerum Fossilium* that concerns Brazilian green tourmaline. The historical review also covers subjects such as 'The gold fever that conquered Brazil', the diamond cycle, José Bonifácio de Andrada e Silva (Brazil's first and foremost mineralogist), mineralogical collections and many other interesting topics. The introduction is wonderfully illustrated with images of people, important finds, mines, crystals and gemstones (including many historic photographs), providing a good background before moving on to the various important collectors and collections.

The first chapter, titled 'Mineralogical Collections', is organised alphabetically by name of the collector, beginning with Álvaro Lúcio, who is well known in the USA as a participant at the Tucson gem shows for decades. For each person whose collection is documented in this section, we get a glimpse into why and what they collect, along with a history of their acquisitions. Each person provides interesting stories about their collections, alongside photos of their favourite or important pieces. The chapter finishes with a one-page table on page 329 that provides a chronological listing of 72 Brazilian type-minerals (i.e. those first discovered in Brazil) that was compiled by Daniel Atencio. It starts with chrysoberyl (documented in 1789) and ends with breyite (described in 2018).

The following chapter covers 'Public Museums and Private Collections', starting with the geoscience museum at the University of San Paulo (USP). This well-documented section covers the history, collections and some of the finer specimens at 12 different Brazilian museums. My personal favourite is the 'Owl's Eye' agate at the USP museum that is shown on page 337.

The next chapter, titled 'Mineralogists and Geologists', includes Daniel Atencio (who created the list of Brazilian type-minerals mentioned above), Paulo and Marizilda Sinátora das Neves, Antonio Luciano Gandini, Gilson Essenfelder, Wendell E. Wilson, Thomas Campbell and Odúlio José Marensi de Moura.

This is followed by the chapter 'Mines, Miners and Mineral Traders'. This section includes Brazilian traders as well as foreign dealers, such as Americans Daniel Trinchillo and Robert Lavinsky, Italian Marco Tironi, and others. Localities described in this chapter are the Pederneira and Cruzeiro tourmaline mines and the Laranjeiras emerald mine. Many photos of famous specimens illustrate this chapter.

The next chapter, 'Meteorites and Tektites', includes Wilton Pinto de Carvalho's 'PhD in meteorites', followed by sections on André Moutinho and Carlo Bottelli. Again, this section is well illustrated with fine photographs, including some of the people discussed.

The final chapter is titled 'Gems, Stone-Cutting and Jewelry'. It features a large variety of colour photographs of objects that have made Brazil famous worldwide in the gem and jewellery trade. Diamond, emerald, tourmaline, topaz and beryl appear on page after page, with some stones mounted in beautiful jewellery by Brazilian designers.

This book is an amazing attempt to cover nearly all aspects of Brazil's gems, minerals, fossils, meteorites, collectors, mines and museums. I believe it mostly succeeds, and I give it high praise. I do think the very heavy (1.2 kg) book might have been more effective as two volumes, although that might have made it too expensive.

For anyone who loves gems, minerals or jewellery—or Brazil—this book is exciting and full of excellent information not usually found in a single reference.

Bill Larson FGA
Pala International
Fallbrook, California, USA

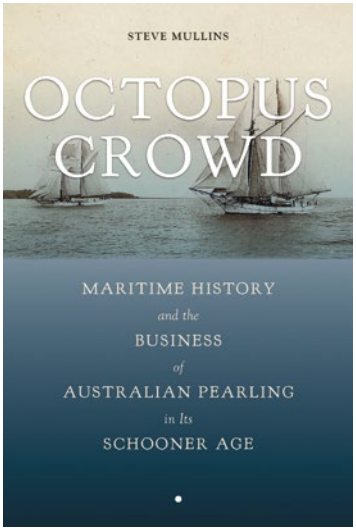

Octopus Crowd: Maritime History and the Business of Australian Pearling in Its Schooner Age

By Stephen Mullins, 2019. University of Alabama Press, Tuscaloosa, Alabama, USA, www.uapress.ua.edu/product/Octopus-Crowd,7074.aspx, 336 pages, illus., ISBN 978-0817320249 (print) or 978-0817392383 (eBook). USD54.95 hardcover or eBook.

This book describes pearling in the area encompassed by the Coral, Arafura and Timor Seas (north of Australia) from the mid-19th century to the first quarter of the 20th century (around the end of World War I), and the commercial appearance of saltwater cultured pearls. During this period, the area was an important source of natural nacreous saltwater pearls, in addition to the waters of the Arabian Gulf and off Central America. In the Australian waters, *Pinctada maxima* bivalves were fished (in which larger natural pearls could be found compared to those obtained elsewhere). Natural pearls averaged 12% of the value of Australian pearling production, and the other 88% came from the inner nacreous part of the shell ('mother-of-pearl'), which was of great interest for the button industry during this period.

The book is well written and includes an important list of notes and a bibliography, but with few, mostly archival, figures. It focuses on the evolution from skin divers to full-dress helmet divers, and on the development from non-specific vessels to pearling luggers about 9–12 m long and the schooners that carried them. The parallel changes from shore-based pearling to floating stations (sometimes called 'floating sweatshops' because of the working conditions)—where 100-tonne schooners remained at sea for months and ferried about a dozen pearling luggers together with full-dress helmet divers—increased the pearling companies' profits.

Changes in the pearling workforce according to the region and time period are also described. In Western Australia, local aborigines were employed initially, with Indonesians (usually referred to as 'Malays') increasing over time. In the Torres Strait, the workforce initially was composed of South Sea Islanders, indigenous Torres Strait Islanders and Melanesians, which were gradually replaced by Malays, Filipinos (or 'Manilamen'), Japanese and Sri Lankans. The book offers several insights into workforce changes, worker rights, mistreatment of workers, conflicts with the indigenous peoples and related legislation. Information is also provided about resource depletion, cyclones that devastated pearling operations, politics and jurisdictions shaped by the pearling industry.

Details about 'pearl king' James Clark, Australia's most influencial pearler and head of the powerful Clark Combination syndicate, enliven the book. The syndicate was also named the 'Octopus Crowd', after cartoonists of the day used the octopus to caricature the money grubbers, and from this comes the title of the book.

Following the book's introduction are 10 chapters. Chapters 1, 2 and 3 describe the early development of pearling on Australia's north-east coast, which extended to the Torres Strait (between Australia and New Guinea) during the 1860s and 1870s. They also cover how pearling became an important industry for Queensland at the start of the 1880s, as well as development of the passage to Western Australia and the floating pearling stations during the mid-1880s.

Chapter 4 considers the legislation challenges created by these floating stations, as they were beyond the three-mile limit of shore-based operations. It goes on to describe how, towards the end of the 1880s, some pearlers returned to the Torres Strait, while others went to the Netherlands East Indies (a Dutch colony in Southeast Asia), triggering discussions between the British and the Dutch. Chapters 5, 6 and 7 revisit the Torres Strait during the 1890s, where opposition ongoing between shore-based pearlers and floating-station owners also involved legislation that outlawed foreigners from owning or leasing pearling luggers.

Chapters 8, 9 and 10 describe the introduction of the 'White Australia' policy in 1901, the challenges to large operations of securing a workforce, the move of the Clark Combination syndicate to the Netherlands East Indies, the transformation of this region due to the pearling operations, the consequences to the market linked with World War I and the return of the Clark Combination to Western Australia. Then, the book's conclusion describes the end of the 'schooner age' and beginning of the syndicate that formed around the end of World War I, mainly due to changes in Australia's socio-political landscape that no longer supported small pearling operations.

Although the book does not focus on natural pearl fishing, it will be interesting for gemmologists who want to know more about the sociological issues of the industry. It well represents the evolving situations of the region during this period of time, with notes and references to help the reader dig further if desired.

Dr Stefanos Karampelas
Basel, Switzerland

Other Book Titles

CULTURAL HERITAGE

Relicarios: The Forgotten Jewels of Latin America
By Martha J. Egan and Carol Eastes, 2020. SF Design LLC/Fresco Books, Santa Fe, New Mexico, USA, 276 pages, ISBN 978-1934491744. USD75.00 hardcover.

DIAMOND

Diamonds Across Time
Ed. by Usha R. Balakrishnan, 2020. World Diamond Museum, London, 432 pages, ISBN 978-7818380485402. GBP95.00 hardcover.

GENERAL REFERENCE

Gems
Ed. by François Farges, 2020. Rizzoli, New York, New York, USA, 304 pages, ISBN 978-2081512955. USD45.00 hardcover.

Mineralogy – An Introduction to Minerals, Rocks and Mineral Deposits
By Martin Okrusch and Hartwig Frimmel, 2020. Springer-Verlag, Berlin and Heidelberg, Germany, 981 pages, ISBN 978-3662573143 (print) or ISBN 978-3662573167 (eBook), https://doi.org/10.1007/978-3-662-57316-7. EUR72.79 (hardcover + eBook) or EUR58.84 (eBook only).

The Pinch Collection at the Canadian Museum of Nature
By Michael Bainbridge, 2020. Lithographie, Arvada, Colorado, USA, 288 pages, ISBN 978-0983632382. USD60.00 hardcover.

JEWELLERY AND *OBJETS D'ART*

Andrew Grima: The Father of Modern Jewellery
By William Grant, 2020. ACC Art Books, Woodbridge, Suffolk, 336 pages, ISBN 978-1788841061. GBP65.00 hardcover.

Beautiful Creatures: Jewelry Inspired by the Animal Kingdom
By Marion Fasel, 2020. Rizzoli, New York, New York, USA, 160 pages, ISBN 978-0847868407. USD35.00 hardcover.

Chinese Contemporary Jewelry Design
By Bifei Cao, 2020. Schiffer Publishing, Atglen, Pennsylvania, USA, 320 pages, ISBN 978-0764360282. USD60.00 hardcover.

The Circle and the Line: The Jewelry of Betty Cooke
By Jeannine Falino and Eleanor Hughes, 2020. D. Giles Ltd, London, 96 pages, ISBN 978-1911282778. GBP24.95 hardcover.

Coveted: Art and Innovation in High Jewelry
By Melanie Grant, 2020. Phaidon Press, New York, New York, USA, 208 pages, ISBN 978-1838661496. USD$89.95 hardcover.

Dior Joaillerie: The A to Z of Victoire de Castellane
By Victoire de Castellane and Olivier Gabet, 2020. Rizzoli, New York, New York, USA, 440 pages, ISBN 978-0847863365. USD150.00 hardcover.

Renaissance Treasures from the Edmond Foulc Collection
By Jack Hinton, 2020. Yale University Press for the Philadelphia Museum of Art, New Haven, Connecticut, USA, 64 pages, ISBN 978-0876332948. USD15.00 softcover.

Stardust: The Work and Life of Jeweler Extraordinaire Frédéric Zaavy
By Gilles Hertzog, John Taylor and Dianne Dubler, 2020. Officina Libraria, Rome, Italy, 240 pages, ISBN 978-8833671031. EUR65.00 hardcover.

A Study of Navajo Concha Belts
By Donald Richards and Karen Richards, 2020. Schiffer Publishing, Atglen, Pennsylvania, USA, 576 pages, ISBN 978-0764359644. USD89.99 hardcover.

SOCIAL STUDIES

The Political Economy of the Kimberley Process
By Nathan Munier, 2020. Cambridge University Press, New York, New York, USA, ISBN 978-1108839709 (print), 978-1108884877 (online) or 978-1108881036 (eBook), https://doi.org/10.1017/9781108884877. USD99.99 hardcover or USD80.00 eBook.

SYNTHETICS AND SIMULANTS

Laboratory Grown Diamonds, 3rd edn.
By Dusan Simic and Branko Deljanin, 2020. Gemmological Research Industries Inc., Vancouver, British Columbia, Canada, 188 pages, ISBN 978-177369200. USD49.95 softcover.

Literature of Interest

COLOURED STONES

Application of EMPA-XRD-SEM to study the mineralogical characteristics of turquoise from Xichuan, Henan Province. X. Li, Z. Xian, J. Fan, Z. Zhang, J. Guo, Z. Gao and Z. Wen, *Rock and Mineral Analysis*, **38**(4), 2019, 373–381 (in Chinese with English abstract).

Be, Fe^{2+}-substitution in natural beryl: An optical absorption spectroscopy study. M.N. Taran and O.A. Vyshnevskyi, *Physics and Chemistry of Minerals*, **46**, 2019, 795–806, https://doi.org/10.1007/s00269-019-01040-2.

The beryl group – An overview. H.A. Hänni, *Journal of the Gemmological Association of Hong Kong*, **61**, 2020, 48–54, www.gahk.org/journal/2020/a11.pdf.*

Blue or green? Turquoise–planerite species from Carico Lake valley in Nevada, the United States: Evidence from Raman spectroscopy. M. Dumańska-Słowik, A. Wesełucha-Birczyńska, L. Natkaniec-Nowak, A. Gaweł, A. Włodek and K. Kulmaczewska, *Journal of Raman Spectroscopy*, **51**(2), 2019, 346–356, https://doi.org/10.1002/jrs.5761.

Cause analysis of chatoyancy of sapphires from Shandong, China. J. Yu, X. He and Z. Lu, *RSC Advances*, **9**(42), 2019, 24420–24427, https://doi.org/10.1039/c9ra03585k.*

Characterization of hydrous mineral inclusions in ruby and sapphire by infrared spectroscopy and microscopic confocal laser Raman spectroscopy. P. Ning, T. Zhang, H. Ma, J. Xie, T. Ding, H. Li and R. Liang, *Rock and Mineral Analysis*, **38**(6), 2019, 640–648 (in Chinese with English abstract).

Classification of precious matrix opals of Australia. E. Akhmetshin and V. Filippov, *Australian Gemmologist*, **27**(3), 2020, 102–107.

Deep purple vesuvianite (idocrase) from Pakistan. H.A. Hänni, L. Franz and H. Wang, *Australian Gemmologist*, **27**(3), 2020, 136–139.

Explanation of the colour change in alexandrites. F. Xie, Y. Cao, C. Ranchon, A. Hart, R. Hansen, J.E. Post, C.W. Whitney, E. Dawson-Tarr, A.J. Drew and D.J. Dunstan, *Scientific Reports*, **10**, 2020, article 6130 (6 pp.), https://doi.org/10.1038/s41598-020-62707-3.*

Faceted eudialyte: A gemmology data capture. J.-M. Arlabosse and S. Cerutti, *Gemmology Today*, September 2020, 60–63, www.worldgemfoundation.com/GTSEPTEMBER2020DV.*

Garnets from Val d'Ala rodingites, Piedmont, Italy: An investigation of their gemological, spectroscopic and crystal chemical properties. V. Diella, R. Bocchio, N. Marinoni, F. Caucia, M.I. Spalla, I. Adamo, A. Langone and L. Mancini, *Minerals*, **9**(12), 2019, article 728 (18 pp.), https://doi.org/10.3390/min9120728.*

The gemmological & mineralogical characterisation of a "single crystal jadeite". Y. Liu, L. Guo, T. Ding, W. Han, J. Huang, F. Zhu and T. Lu, *Journal of the Gemmological Association of Hong Kong*, **61**, 2020, 77–83, www.gahk.org/journal/2020/a16.pdf (in Chinese with English abstract).*

Hydrogen and oxygen stable isotope ratios of dolomite-related nephrite: Relevance for its geographic origin and geological significance. K. Gao, T. Fang, T. Lu, Y. Lan, Y. Zhang, Y. Wang and Y. Chang, *Gems & Gemology*, **56**(2), 2020, 266–280, https://doi.org/10.5741/GEMS.56.2.266.*

Improvements to the analytical protocol of lapis lazuli provenance: First study on Myanmar rock samples. G. Vaggelli, L. Es Sebar, A. Borghi, R. Cossio, A. Re, F. Fantino and A. Lo Giudice, *European Physical Journal Plus*, **134**, 2019, article 104 (15 pp.), https://doi.org/10.1140/epjp/i2019-12523-4.

Libyan desert glass in prehistory, antiquity and the present. J. Štubňa, *Gemologický spravodajca/Gemmological Newsletter*, **10**(1), 2020, 5–23, www.gu.fpv.ukf.sk/images/GS/2020_1_stubna_a.pdf (in Slovak with English abstract).*

The nature and origin of pigments in black opal from Lightning Ridge, New South Wales, Australia. J.R. Herrmann, R. Maas, P.F. Rey and S.P. Best, *Australian Journal of Earth Sciences*, **66**(7), 2019, 1027–1039, https://doi.org/10.1080/08120099.2019.1587643.

Prismatine chromifère du Kenya [Chromiferous prismatine from Kenya]. J.-M. Arlabosse and A. Delaunay, *Revue de Gemmologie A.F.G.*, No. 209, 2020, 10–13 (in French).

Study of the differences in infrared spectra of emerald from different mining areas and the controlling factors. X. Qiao, Z. Zhou, D.T. Schwarz, L. Qi, J. Gao, P. Nong, M. Lai, K. Guo *et al.*, *Canadian Mineralogist*, **57**(1), 2019, 65–79, https://doi.org/10.3749/canmin.1800042.

CULTURAL HERITAGE

Chinese jades: Selections from the Yale University Art Gallery. D.P. Leidy, *Arts of Asia*, **50**(3), 2020, 22–31, www.artsofasianet.com/admin/save_file.php?attach_id=fc21eb7eaddef9cc08178d0ccf03b0d4.*

Emperor Yongzheng's repository of jades. W. Ming, *Arts of Asia*, **50**(3), 2020, 32–39.

Jade collection from the Museum of Far Eastern Antiquities, Sweden. M.D. Lee and J.C.S. Lin, *Arts of Asia*, **50**(3), 2020, 65–75.

"Old fei cui of the Ming & Qing dynasties" - What is it really? M.C.M. Ou Yang, *Journal of the Gemmological Association of Hong Kong*, **61**, 2020, 85–88, www.gahk.org/journal/2020/a17.pdf.*

Some English jade collections. R. Kerr, *Arts of Asia*, **50**(3), 2020, 40–49.

Use of variscite as a gemstone in the Late Bronze Age Royal Tomb at Qatna, Syria. Y. Abe, A. Nakamura, S. Suzuki, K. Tantrakarn, I. Nakai, J. Zöldföldi and P. Pfälzner, *Journal of Archaeological Science: Reports*, **27**, 2019, article 101994 (6 pp.), https://doi.org/10.1016/j.jasrep.2019.101994.

DIAMONDS

A defect study and classification of brown diamonds with deformation-related color (Part 1). T. Hainschwang, F. Notari and G. Pamies, *Minerals*, **10**(10), 2020, article 903 (38 pp.), https://doi.org/10.3390/min10100903.*

A defect study and classification of brown diamonds with non-deformation-related color (Part 2). T. Hainschwang, F. Notari and G. Pamies, *Minerals*, **10**(10), 2020, article 914 (35 pp.), https://doi.org/10.3390/min10100914.*

Features of the phonon wing of the luminescence of diamond. S.I. Zienko and D.S. Slabkovskii, *Technical Physics Letters*, **45**(6), 2019, 537–539, https://doi.org/10.1134/s1063785019060166.

Luminescence of natural diamond in the NIR range. E. Vasilev, G. Kriulina and I. Klepikov, *Physics and Chemistry of Minerals*, **47**, 2020, article 31 (8 pp.), https://doi.org/10.1007/s00269-020-01099-2.

Naturally colored yellow and orange gem diamonds: The nitrogen factor. C.M. Breeding, S. Eaton-Magaña and J.E. Shigley, *Gems & Gemology*, **56**(2), 2020, 194–219, https://doi.org/10.5741/GEMS.56.2.194.*

Nitrogen in diamond. M.N.R. Ashfold, J.P. Goss, B.L. Green, P.W. May, M.E. Newton and C.V. Peaker, *Chemical Reviews*, **120**(12), 2020, 5745–5794, https://doi.org/10.1021/acs.chemrev.9b00518.

Spectroscopic features of natural and HPHT-treated yellow diamonds. M.Y. Lai, C.M. Breeding, T. Stachel and R.A. Stern, *Diamond and Related Materials*, **101**, 2020, article 107642 (8 pp.), https://doi.org/10.1016/j.diamond.2019.107642.

FAIR TRADE

Ethical guidelines for Burmese amber acquisitions. A. Peretti, *Journal of Applied Ethical Mining of Natural Resources and Paleontology (PMF Journal)*, No. 1, 2020, 4–78, www.pmf.org/s/PMF-Journal-No1_2020-08-10.pdf.*

The journey of ethics – A review of responsible sourcing developments in the gem sector. L.E. Cartier, *InColor*, No. 46, 2020, 66–71, www.gemstone.org/incolor/46.*

GEM LOCALITIES

Connecting with the world of work: Focus on mining in Canada / Les liens avec le monde professionel: Focus sur l'exploitation minière au Canada. Gem Academy of Canada (EGM), *Gemmology Today*, September 2020, 37–42, www.worldgemfoundation.com/GTSEPTEMBER2020DV (in English and French).*

Gemstones of Greece: Geology and crystallizing environments. P. Voudouris, C. Mavrogonatos,

I. Graham, G. Giuliani, A. Tarantola, V. Melfos, S. Karampelas *et al.*, *Minerals*, **9**(8), 2019, article 461 (29 pp.), https://doi.org/10.3390/min9080461.*

The genetic linkage between the Yuanjiang marble-hosted ruby deposit and Cenozoic tectonic evolution of the Ailao Shan-Red River shear zone (southwest China). T. Yang, X. Sun, G. Shi, D. Li and H. Zhou, *Journal of Asian Earth Sciences*, **177**, 2019, 38–47, https://doi.org/10.1016/j.jseaes.2019.03.010.

Geology of the Chernogorskoe gem-quality scapolite deposit (central Pamirs, Tajikistan). A.K. Litvinenko, S.B. Moiseeva, S.A. Odinaev and V.A. Utenkov, *Geology of Ore Deposits*, **61**(5), 2019, 481–493, https://doi.org/10.1134/s1075701519050040.

History of the Chivor emerald mine, Part II (1924–1970): Between insolvency and viability. K. Schmetzer, G. Martayan and A.R. Blake, *Gems & Gemology*, **56**(2), 2020, 230–257, https://doi.org/10.5741/GEMS.56.2.230.*

King cobras, gold and diamonds [alluvial mining in Sierra Leone]. B.C.K. Koroma, *Gemmology Today*, September 2020, 72–76, www.worldgemfoundation.com/GTSEPTEMBER2020DV.*

Rebrand to restart [emeralds from Swat, Pakistan]. C. Evans, *Journal of the Gemmological Association of Hong Kong*, **61**, 2020, 94–95, www.gahk.org/journal/2020/a19.pdf.*

The tsavorite (gem quality green vanadium grossular) minerogenetic system in East Africa: A case of metamorphic partial melting and lateral secretion. W.L. Pohl, *Arabian Journal of Geosciences*, **12**(19), 2019, article 612 (6 pp.), https://doi.org/10.1007/s12517-019-4744-y.

The where of mineral names: Tanzanite, a variety of zoisite, Merelani Hills, Simanjiro District, Manyara region, Tanzania. B. Cairncross, *Rocks & Minerals*, **95**(5), 2020, 458–462, https://doi.org/10.1080/00357529.2020.1771156.

INSTRUMENTATION AND TECHNOLOGY

Dark secrets [GemPen Darkroom]. L. Langeslag, *Gemmology Today*, September 2020, 77–81, www.worldgemfoundation.com/GTSEPTEMBER2020DV.*

FTIR in gem testing • A pink sapphire lesson. R. Hughes and W. Manorothkul, *Journal of the Gemmological Association of Hong Kong*, **61**, 2020, 61–63, www.gahk.org/journal/2020/a13.pdf.*

Gem color determination: From visual analysis to instrumental evaluation. A.N. Chertov, E.V. Gorbunova, A.S. Kushkoeva, A.A. Alekhin, V.S. Peretyagin, N.A. Pavlenko and E.A. Sycheva, *Measurement Techniques*, **62**(8), 2019, 686–691, https://doi.org/10.1007/s11018-019-01679-x.

Long-wave ultraviolet torches • A gemmologist's new best friend. E.B. Hughes, *Journal of the Gemmological Association of Hong Kong*, **61**, 2020, 57–59, www.gahk.org/journal/2020/a12.pdf.*

Multiview generative adversarial network and its application in pearl classification. Q. Xuan, Z. Chen, Y. Liu, H. Huang, G. Bao and D. Zhang, *IEEE Transactions on Industrial Electronics*, **66**(10), 2019, 8244–8252, https://doi.org/10.1109/tie.2018.2885684.

JEWELLERY HISTORY

Analyse gemmologique de la bague dite du couronnement de l'impératrice Joséphine [Gemmological analysis of the so-called coronation ring of Empress Josephine]. G. Riondet and G. Panczer, *Revue de Gemmologie A.F.G.*, No. 209, 2020, 20–23 (in French).

La *Grande Table des Orsini* : Un chef d'oeuvre gemmologique des collections royales [The Great Table of the Orsinis: A gemmological masterwork in the royal collection]. F. Farges and P.-J. Chiapperro, *Revue de Gemmologie A.F.G.*, No. 209, 2020, 24–31 (in French).

Mughal emerald in European jewelry. I.V. Pozhidaeva, *Oriental Courier*, Nos. 1–2, 2020, 203–215, https://doi.org/10.18254/s268684310010400-8.*

LAPIDARY TOPICS

Characteristics of modern Chinese jade carvings: The nephrite jade works that won the Tiangong Awards from 2003 to 2014. M. Wang and G. Shi, *Arts of Asia*, **50**(3), 2020, 88–102.

A coloured gemstone buyer's guide to cut styles. J.K. Prim, *Australian Gemmologist*, **27**(3), 2020, 108–113.

Évolution et révolution dans la technique de taille du diamant. Différentes étapes de la technique de taille du diamant du XVème siècle à nos jours. En couverture [Evolution and revolution in diamond-cutting technique. Different steps in diamond-cutting methods from the 16th century to our time. An overview]. E. Vleeschdraeger, *Revue de Gemmologie A.F.G.*, No. 209, 2020, 14–19 (in French).

Round brilliant cut beauty and light performance part 2. M.D. Cowing, *Gemmology Today*, September 2020, 86–94, www.worldgemfoundation.com/GTSEPTEMBER2020DV.*

MISCELLANEOUS

The collaborative interdependence in the local production arrangement of gems and jewels in south of Brazil. L.F.F. Filho, A.R. Mozzato and K.B.B. Fritz, *International Journal of Strategic Business Alliances*, **6**(4), 2019, 233–250, https://doi.org/10.1504/ijsba.2019.102618.

Diamonds versus precious metals: What gleams most against USD exchange rates? R. Bedoui, K. Guesmi, S. Kalai and T. Porcher, *Finance Research Letters*, **34**, 2020, article 101253 (9 pp.), https://doi.org/10.1016/j.frl.2019.08.001.

Hidden treasure: Collecting the literature of jade. R.W. Hughes and E.J. Hoffman, *Arts of Asia*, **50**(3), 2020, 76–87.

NEWS PRESS

Lab-grown and natural diamond industries end hostilities, as declining jewelry demand threatens all. P.N. Danziger, *Forbes*, 19 July 2020, www.forbes.com/sites/pamdanziger/2020/07/19/lab-grown-and-natural-diamond-factions-settle-hostilities-as-declining-jewelry-demand-threatens-all.*

Some paleontologists seek halt to Myanmar amber fossil research. L. Joel, *New York Times*, www.nytimes.com/2020/03/11/science/amber-myanmar-paleontologists.html.*

Sustainable mining: 'The handprint is just as important as the footprint'. K. Matthams, *Forbes*, 29 July 2020, www.forbes.com/sites/katematthams/2020/07/29/sustainable-mining-handprint-as-important-as-footprint.*

ORGANIC/BIOGENIC GEMS

An attempt to correlate the physical properties of fossil and subfossil resins with their age and geographic location. P. Stach, G. Martinkutė, P. Šinkūnas, L. Natkaniec-Nowak, P. Drzewicz, B. Naglik and M. Bogdasarov, *Journal of Polymer Engineering*, **39**(8), 2019, 716–728, https://doi.org/10.1515/polyeng-2019-0159.

Baltic amber or Burmese amber: FTIR studies on amber artifacts of eastern Han Dynasty unearthed from Nanyang. D. Chen, Q. Zeng, Y. Yuan, B. Cui and W. Luo, *Spectrochimica Acta Part A: Molecular and Biomolecular Spectroscopy*, **222**, 2019, article 117270 (5 pp.), https://doi.org/10.1016/j.saa.2019.117270.

Elephants never forget, should art museums remember too? Historic ivory collections as ambassadors for conservation education. C. Good, P. Tyrrell, Z. Zhou and D.W. Macdonald, *Biodiversity and Conservation*, **28**(6), 2019, 1331–1342, https://doi.org/10.1007/s10531-019-01735-6.*

PEARLS

Non-spherical pearl layers in the Polynesian 'black-lipped' *Pinctada margaritifera*: The non-nacreous deposits compared to microstructure of the shell growing edge. J.P. Cuif, Y. Dauphin, G. Luquet, O. Belhadj, S. Rouzière, M. Salomé, M. Cotte, A. Somogyi *et al.*, *Aquaculture Research*, **51**(2), 2019, 506–522, https://doi.org/10.1111/are.14395.

Potential combinations of mabé, keshi and cultured pearl production from colourful hatchery-produced *Pinctada margaritifera*. C.-L. Ky, N. Leclerc, F. Broustal, S. Nakasai and D. Devaux, *Aquaculture*, **505**, 2019, 235–241, https://doi.org/10.1016/j.aquaculture.2019.02.057.

Sea of Cortez cultured pearls. C. Lüle, *GemGuide*, **39**(5), 2020, 8–9.

What's in a name? *Pinctada albina*, the Shark Bay pearl shell. L.J. Rennie, *Australian Gemmologist*, **27**(3), 2020, 114–118.

SIMULANTS

Gemmological characteristics of a feicui jade imitation. H. Zhu, H. Liu, R. Du, X. Zhao, Z. Wuang, X. Ding and S. Chen, *Superhard Material Engineering*, **32**(2), 2020, 59–63 (in Chinese with English abstract).

I want to believe [fakes and imitations]. N. Zolotukhina, *Gemmology Today*, September 2020, 27–76, www.worldgemfoundation.com/GTSEPTEMBER2020DV.*

Simulated malachite with barium sulphate as the major constituent. Y. Kim, *Journal of the Gemmological Association of Hong Kong*, **61**, 2020, 66–69, www.gahk.org/journal/2020/a14.pdf.*

SYNTHETICS

High NV density in a pink CVD diamond grown with N_2O addition. A. Tallaire, O. Brinza, P. Huillery, T. Delord, C. Pellet-Mary, R. Staacke, B. Abel, S. Pezzagna *et al.*, *Carbon*, **170**, 2020, 421–429, https://doi.org/10.1016/j.carbon.2020.08.048.

Identification of amethysts and synthetic amethysts by X-ray powder diffraction technology. X. Jin, Z. Liang, W. Cai, H. Wu, G. Yang, X. Chen and J. Wang, *Superhard Material Engineering*, **32**(2), 2020, 39–42 (in Chinese with English abstract).

Photoluminescence studies of nitrogen-vacancy and silicon-vacancy centers transformation in CVD diamond. Y. Zhang, K. Wang, S. Ding, Y. Tian, J. Li and Y. Chai, *Journal of Physics: Condensed Matter*, **32**, 2020, article 34LT01 (5 pp.), https://doi.org/10.1088/1361-648X/ab8987.

Separation of natural from laboratory-grown diamond using time-gated luminescence imaging. Colin D. McGuinness, A.M. Wassell, P.M.P. Lanigan and S.A. Lynch, *Gems & Gemology*, **56**(2), 2020, 220–229, https://doi.org/10.5741/GEMS.56.2.220.*

Under the microscope: Colour instability in CVD diamonds. N. Del Re, *Jewellery Business*, February 2020, 42–44.

TREATMENTS

Artificial colour in diamonds with a focus on HPHT treatment of natural diamonds. M.C. Casamento, *Australian Gemmologist*, **27**(3), 2020, 119–133.

Conclusive comparison of gamma irradiation and heat treatment for color enhancement of rubellite from Mozambique. B. Phichaikamjornwut, S. Pongkrapan, S. Intarasiri and D. Bootkul, *Vibrational Spectroscopy*, **103**, 2019, article 102926 (9 pp.), https://doi.org/10.1016/j.vibspec.2019.102926.

Optical whitening and brightening of pearls: A fluorescence spectroscopy study. C. Zhou, T.-H. Tsai, N. Sturman, N. Nilpetploy, A. Manustrong and K. Lawanwong, *Gems & Gemology*, **56**(2), 2020, 258–265, https://doi.org/10.5741/GEMS.56.2.258.*

The UV-Vis spectral study on thermal treatment of yellowish-green apatite. J. Zhang, T. Shao and A.H. Shen, *Spectroscopy and Spectral Analysis*, **40**(1), 2020, 147–151 (in Chinese with English abstract).

COMPILATIONS

***G&G* Micro-World.** Böhmite in corundum • Chabazite in Ethiopian opal • Fluorophlogopite in Burmese spinel • Unusual-shaped rutile in Russian emerald • Sapphire with negative crystal containing mobile graphite daughter crystal • 'Windmills' in sphalerite • Trapiche-like pattern in Pakistani emerald • Pyrite in quartz. *Gems & Gemology*, **56**(2), 2020, 292–297, www.gia.edu/gg-issue-search?ggissueid=1495318944465&articlesubtype=microworld.*

Gem News International. Purplish pink diaspore from Afghanistan • Fossil ivory carved by Lee Downey • 'Fragility of the Eternal' kunzite • Petrified wood from the Russian Far East • 85 g rough Cu-bearing tourmaline from Mozambique • Natrolite from Indonesia • Field trip to Crater of Diamonds, USA • Greenish blue glass imitating gem silica • Marble imitation of rough jadeite. *Gems & Gemology*, **56**(2), 2020, 298–316, www.gia.edu/gg-issue-search?ggissueid=1495318944465&articlesubtype=gni.*

Lab Notes. Cat's-eye andradite • Quench-crackled dyed blue chalcedony resembling Larimar • Irradiated blue diamond with interesting DiamondView image • Diamond with multiple radiation stains • Hemimorphite resembling Paraíba tourmaline • Purple Montana sapphire • Sapphire with negative crystal containing a mobile CO_2 bubble • Mozambique pink sapphire • HPHT-processed CVD synthetic diamonds with low color grades • HPHT synthetic pink diamond with unstable color. *Gems & Gemology*, **56**(2), 2020, 281–291, www.gia.edu/gg-issue-search?ggissueid=1495318944465&articlesubtype=labnotes.*

**Article freely available for download, as of press time*

Thank You, Guest Reviewers

The following individuals served as guest reviewers during the past publication year. A special thanks is extended to each one of them for lending their expertise to reviewing manuscripts submitted to *The Journal*. Together with the Associate Editors, these individuals have enhanced the quality of *The Journal* through their knowledge and professionalism.

Shigeru Akamatsu
Japan Pearl Promotion Society, Toba, Japan

Dr Dmitriy Belakovskiy
Fersman Mineralogical Museum, Moscow, Russia

Prof. Bruce Cairncross
University of Johannesburg, South Africa

Dr Alessandra Costanzo
National University of Ireland Galway

Dr Kyle Ewart
TRACE Wildlife Forensics Network, Sydney, Australia

Prof. Edward S. Grew
University of Maine, Orono, Maine, USA

Nigel B. Israel
London

Harold Killingback
Brooke, Rutland, East Midlands

Dr Shang I (Edward) Liu
The Gemmological Association of Hong Kong

Dr Dominic Mok
Asian Gemmological Institute and Laboratory Ltd, Hong Kong

Dr Illia Mysiura
V. N. Karazin Kharkiv National University, Kharkiv, Ukraine

Dr Myint Myat Phyo
Swiss Gemmological Institute SSEF, Basel, Switzerland

Nathan D. Renfro
Gemological Institute of America, Carlsbad, California, USA

William R. Rohtert
William Rohtert Consulting LLC, Phoenix, Arizona, USA

Prof. José Sasián
University of Arizona, Tucson, Arizona, USA

Erik Schoonhoven
Amsterdam, The Netherlands

Jeremy Shepherd
Pearl Paradise, Los Angeles, California, USA

Dr Lawrence W. Snee
Global Gems and Geology, Lake Mary, Florida, USA

Martin P. Steinbach
Steinbach – Gems with a Star, Idar-Oberstein, Germany

Dr Rolf Tatje
Duisburg, Germany

Dr Zuowei Yin
Gemological Institute, China University of Geosciences, Wuhan, China

Don't forget to renew your Gem-A Membership!

We've made it easier for you to renew your membership with us.

If you renew before 31st December 2020 you only pay £110*

*(£135 thereafter)

Pay Using **PayPal, GoCardless,** or **Bank Transfer**

By paying with **GoCardless** or **PayPal Subscription**, payment is taken automatically every year so you no longer have to worry about not renewing on time and missing your issues.

To renew, simply log in to the Gem-A website: **https://gem-a.com/log-in** and choose the payment method you wish to use.
Don't want to subscribe? You can still log in and make a one-off payment.